Characterisation of Hot Jupiter Atmospheres with Phase-Resolved Emission Spectra

Jingxuan Yang
Hertford College
University of Oxford

A thesis submitted for the degree of
Doctor of Philosophy

Michaelmas 2024

Acknowledgements

I thank my supervisor, Patrick Irwin, for the helpful guidance and feedback throughout this thesis project. I thank the NIRSpec GTO Program collaboration, in particular Nicolas Crouzet, for providing the unpublished *JWST* NIRSpec/G395H emission spectra of WASP-43b analysed in Chapter 7. I thank Vivien Parmentier for providing his general circulation model of WASP-43b used in this thesis. I thank Shang-Min Tsai for providing the chemical models presented in Chapter 6. I thank Juan Alday, Joanna Barstow, Mark Hammond, and Anjali Piette for their fruitful collaborations and scientific insights. I would also like to thank Oxford's planetary science community for their much-appreciated company. Finally, I would like to thank my family for their unwavering support.

Abstract

Hot Jupiters are gaseous giant planets with orbital periods of less than ten days. They are currently the only class of exoplanets that can be characterised with high-quality spectroscopic observations over multiple orbital phases owing to their large radii and high atmospheric temperatures. Constraints on their atmospheric properties, such as molecular abundance and thermal structure, give us insight into how planetary atmospheres behave under extreme conditions and help us understand their formation and evolution pathways.

This thesis uses infrared emission spectra observed at multiple orbital phases with space telescopes to characterise the atmosphere of the hot Jupiter WASP-43b, which is a planet roughly twice the mass of Jupiter orbiting a solar metallicity K star with an orbital period of just 19.5 hours. I analyse data taken with four instruments, spanning roughly 1-10 μm in wavelength: (1) *HST*/WFC3; (2) *Spitzer*/IRAC; (3) *JWST* MIRI/LRS; and (4) *JWST* NIRSpec/G395H. To extract information from the data, I develop a method to fit emission spectra at multiple orbital phases simultaneously and an open-source spectral retrieval code.

I report the detection of key molecules in the atmosphere of WASP-43b: H_2O, CO_2, CO, NH_3, HCN, and H_2S, and place a strict upper bound on the abundance of CH_4. The retrieved molecular abundance suggests that the atmosphere of WASP-43b has a super-solar metallicity and a super-solar C/O ratio. The results of this thesis are critical inputs for atmospheric models of WASP-43b and offer insights into the planet's formation history. The high atmospheric metallicity and C/O ratio rule out gas-accretion-dominated formation at large orbital radius followed by disc-free migration. Instead, these constraints suggest that processes such as pebble drift and accretion and in situ heavy element enrichment likely played important roles in the formation history of WASP-43b.

Contents

List of Figures

Chapter 1

Introduction

1.1 Motivation

Exoplanetary astronomy has grown rapidly since the first exoplanet detections in the early 1990s (Wolszczan & Frail, 1992; Wolszczan, 1994; Mayor & Queloz, 1995). Astronomical surveys have since revealed that planets are common around stars in the Galaxy (Winn & Fabrycky, 2015). There are now more than five thousand confirmed exoplanets, as shown in Figure 1.1. One class of exoplanets, known as hot Jupiters, is of particular observational and theoretical interest. They are gaseous giant planets similar to Jupiter in bulk density but orbit their stars with periods of less than 10 days, typically with a semi-major axis of less than 0.05 AU. Hot Jupiters are thought to orbit roughly 1% of Sun-like stars, accounting for about 10% of the overall giant planet occurrence rate (Cumming et al., 2008; Wright et al., 2012). Despite their relative rarity, hot Jupiters are a key focus for exoplanetary studies for several reasons. Firstly, the atmospheres of hot Jupiters are ideal targets for spectroscopic characterisation. The proximity to their host stars gives rise to hot and extended atmospheres with large atmospheric scale heights, resulting in favourable planet-to-star flux ratios and prominent spectral features. Furthermore, the abundance of important volatile molecules such as water can be readily constrained as they exist in the gaseous phase in the observable region of hot Jupiter atmospheres, unlike on Jupiter and Saturn, where many volatile molecules are sequestered deep below the cloud decks. Secondly, the existence of hot Jupiters offers valuable insight into planetary formation. Traditional formation models, such as core accretion and gravitational instability, struggle to fully explain the formation of giant planets on such short orbits without significant orbital migration, thereby necessitating a revision of the mechanisms governing planetary systems' formation and evolution. Finally, hot Jupiters are unique case studies for atmospheric science. The extreme conditions in their atmospheres make them natural laboratories for studying atmospheric chemistry and dynamics under conditions not found in the Solar System.

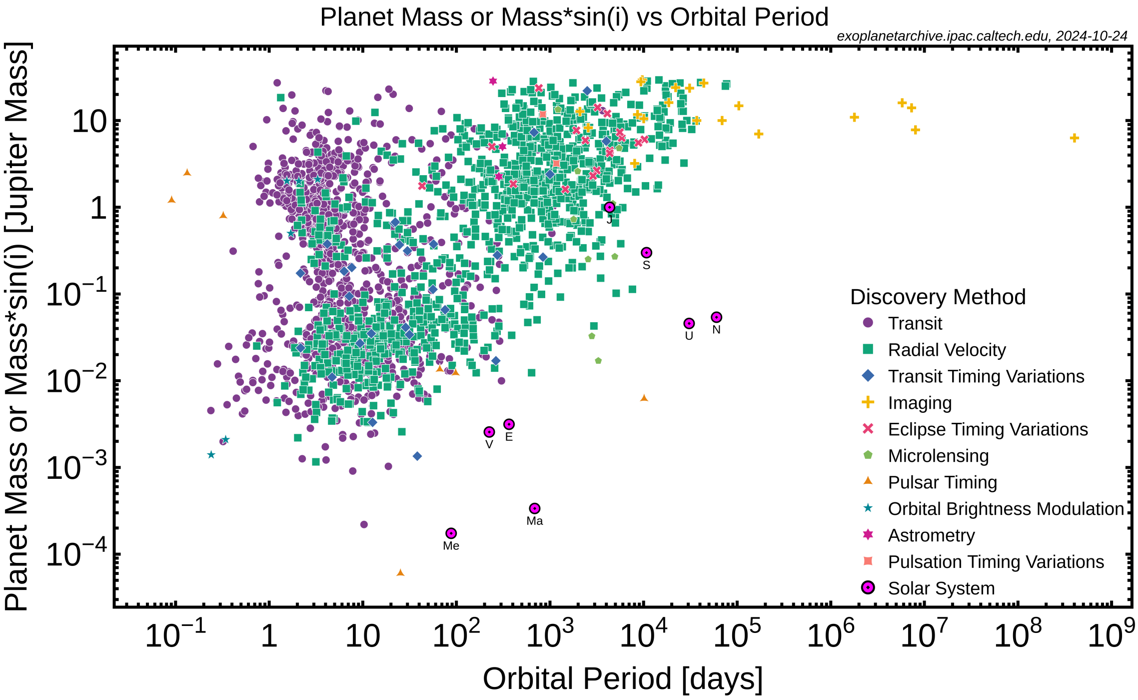

Figure 1.1: Distribution of confirmed exoplanets in the mass versus orbital period space. Dotted circles mark the Solar System planets for reference. Hot Jupiters occupy the upper left corner: they have orbital periods of less than 10 days and masses comparable to Jupiter's. Image credits: NASA Exoplanet Archive.

1.2 Scientific Themes

Observational characterisation is central to the study of hot Jupiters. This thesis aims to constrain the atmospheric properties of hot Jupiters by analysing observations taken with state-of-the-art space telescopes such as the Hubble Space Telescope (*HST*) and the James Webb Space Telescope (*JWST*). In particular, this thesis studies low-resolution phase-resolved emission spectra of transiting hot Jupiters, which are emission spectra observed at multiple orbital phases (also known as spectroscopic phase curve observation). The geometry of phase-resolved emission spectroscopy for a transiting hot Jupiter is shown in Figure 1.2. Since hot Jupiters have tiny semi-major axes, we expect them to be tidally locked to their hot stars so that their self-rotation is in sync with their orbital rotation (Gladman et al., 1996). As a result, hot Jupiters have permanent daysides that always face the host stars and permanent nightsides that are always in the shadow. For a transiting hot Jupiter, we can simply relate the central longitude of the observed hemisphere to the orbital phase of the planet, as illustrated by Figure 1.2. Therefore, phase-resolved emission spectra can allow us to easily map out the atmospheric conditions across the entire planet. Figure 1.3 shows an example of a phase curve observation binned to a single wavelength; for a full spectroscopic phase curve observation, we would see similar curves for each of the observed wavelength channels.

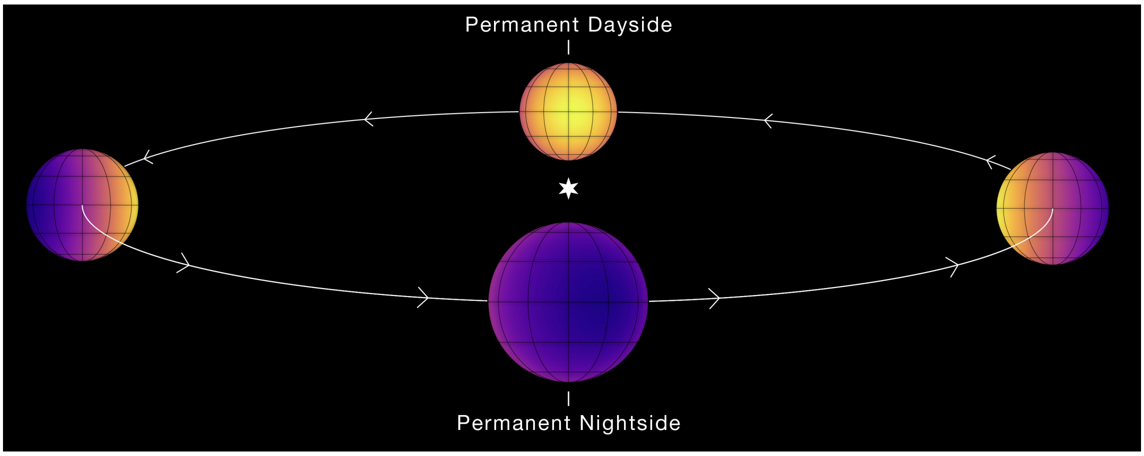

Figure 1.2: Illustration of the tidally locked orbit of a transiting hot Jupiter. Due to the tidal locking, hot Jupiters have permanent daysides and nightsides. An observer sees different hemispheres of a transiting hot Jupiter through an entire orbital period. The self-rotation phase of the planet is in sync with its orbital rotation phase. Image credits: NASA, ESA, CSA, Ralf Crawford, Taylor Bell, Joanna Barstow, Michael Roman.

This thesis contributes to the field of hot Jupiter science in three ways. First, this thesis provides tools to retrieve information from hot Jupiter emission spectra, including a novel parametric atmospheric temperature model that can fit emission spectra observed at multiple orbital phases simultaneously (Yang et al., 2023) and an open source radiative transfer and atmospheric retrieval code (Yang et al., 2024a). Next, this thesis applies these tools to three sets of phase-resolved emission spectra of the hot Jupiter WASP-43b taken with space telescopes. Finally, this thesis investigates how the inferred atmospheric properties of WASP-43b can be used to constrain its formation history. The remainder of this chapter details these scientific themes.

1.2.1 Retrieval of Information from Emission Spectra

The spectral appearance of giant planets is set by the opacity structure and the thermal structure of their atmospheres. By fitting spectra generated from atmospheric

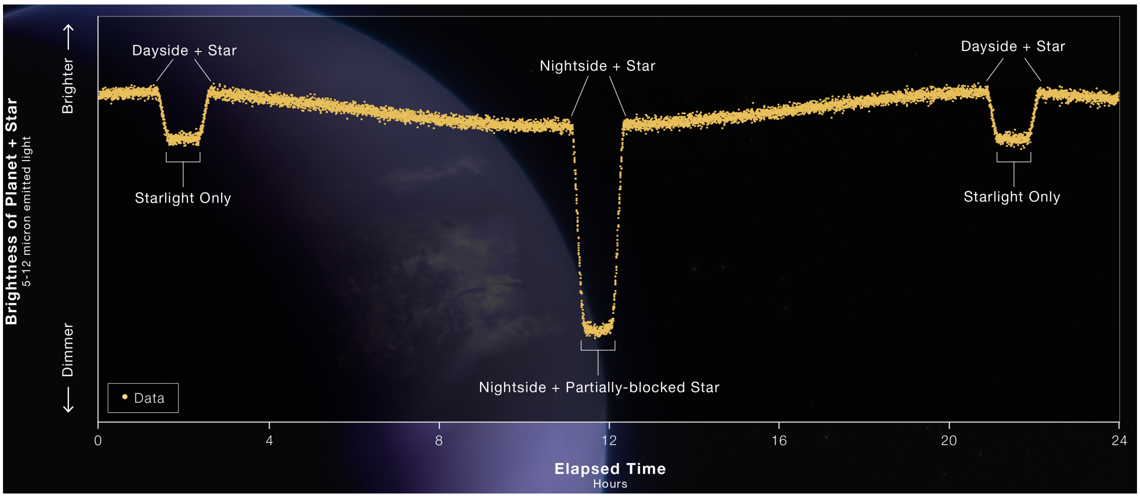

Figure 1.3: An example of a phase curve observation, where the combined brightness of the star and the planet is plotted against time. Since the dayside of the planet is hotter than the nightside, the combined brightness varies with time as the planet rotates. The two shallower dips in brightness correspond to secondary eclipses, where the planet goes behind the host star so that the radiation from the planet is no longer visible. The deeper dip in brightness corresponds to a primary transit, where the planet goes in front of the host star and blocks off a fraction of stellar light. Image credits: NASA, ESA, CSA, Ralf Crawford, Taylor Bell, Joanna Barstow, Michael Roman.

models to observations, we can constrain their atmospheric properties. The process of inferring atmospheric properties from spectroscopic observations is known as atmospheric retrieval (Rodgers, 1976; Irwin et al., 2008; Madhusudhan & Seager, 2009) and is detailed in Chapter 4. The atmospheres of hot Jupiters are ideal targets for spectroscopic observations because they have large atmospheric scale heights, defined as

$$H = \frac{k_B T}{mg}, \tag{1.1}$$

where k_B is the Boltzmann constant, T is the atmospheric temperature, m is the mean molecular weight of the atmosphere, and g is the gravitational acceleration. Larger atmospheric scale heights generally correspond to larger observed spectral features. Two observing geometries are widely used to characterise the atmospheres of hot Jupiters: (1) transmission spectroscopy, which measures the stellar light filtered through the planetary limb during primary transits (e.g., Sing et al., 2016); (2) eclipse spectroscopy, which extracts the dayside emission spectra by monitoring the combined stellar and planetary flux during secondary eclipses (e.g., Lee et al., 2012; Mansfield et al., 2021). Such observations have been done at both high spectral resolution from ground-based facilities (e.g., Brogi & Line, 2019) and at lower resolution using space telescopes (e.g., Wakeford et al., 2017), resulting in numerous atomic and molecular detections, including atomic species such as sodium (Charbonneau et al., 2002; Snellen et al., 2008), potassium (Nikolov et al., 2015), iron (Hoeijmakers et al., 2018), and molecular species such as H_2O (Evans et al., 2016; Yang et al., 2024b), CO_2 (Alderson et al., 2023), CO (de Kok et al., 2013; Lesjak et al., 2023), CH_4 (Barman et al., 2015; Bell et al., 2023b; Sing et al., 2024), SiO_2 (Grant et al., 2023), and SO_2 (Powell et al., 2024; Dyrek et al., 2024).

This thesis studies how to retrieve the atmospheric properties of hot Jupiters from emission spectra. In particular, this thesis analyses low-resolution phase-resolved emission spectra, which are emission spectra observed at multiple orbital phases by space telescopes and can enable detailed atmospheric characterisation of hot Jupiters (see Figure 1.2). This thesis contributes to the field of atmospheric retrievals in two ways. Firstly, this thesis introduces a novel parametric atmospheric temperature model that can fit emission spectra observed at multiple orbital phases simultaneously, which can mitigate the degeneracy between thermal structure and molecular abundance in the analysis of low-resolution emission spectra and boost the signal-to-noise ratio of the data. Secondly, this thesis presents a spectral simulation and atmospheric retrieval software named NEMESISPY (Yang et al., 2024a), developed based on the Fortran NEMESIS library of Irwin et al. (2008). These tools enable the atmospheric retrievals performed in the thesis, which reveal key insight into the atmospheric properties of hot Jupiters.

1.2.2 Characterising the Atmosphere of WASP-43b

WASP-43b is a transiting hot Jupiter around a K7V star discovered by Hellier et al. (2011) as part of the Wide Angle Search for Planets (WASP) survey. It has a mass of roughly two Jupiter masses and a radius of approximately one Jupiter radius. WASP-43b orbits its host star in just over 19.5 hours, making it a prime target for phase curve observations as its entire orbit can be observed in a short time span. Furthermore, as WASP-43 is a K star with an effective temperature of around 4500 kelvin and a radius of roughly 0.7 solar radii, the planet-to-star flux ratio of WASP-43b is larger compared to a similarly irradiated hot Jupiter around an F or a G star, yielding a more favourable signal-to-noise ratio. The observability of WASP-43b makes it a target of both observational and theoretical interest. There is a wealth of scientific studies on WASP-43b, spanning telescopic observations (Czesla et al., 2013; Blecic et al., 2014; Kreidberg et al., 2014; Stevenson et al., 2014, 2017; Weaver et al., 2020; Fraine et al., 2021; Scandariato et al., 2022; Lesjak et al., 2023; Murphy et al., 2023;

Bell et al., 2024), atmospheric retrievals (Changeat & Al-Refaie, 2020; Feng et al., 2020; Irwin et al., 2020; Cubillos et al., 2021; Chubb & Min, 2022; Dobbs-Dixon & Blecic, 2022; Yang et al., 2023; Taylor & Parmentier, 2023; Yang et al., 2024b) and atmospheric modelling (Kataria et al., 2015; Keating & Cowan, 2017; Mendonça et al., 2018a,b; Venot et al., 2020; Helling et al., 2020; Carone et al., 2020; Schneider et al., 2022; Teinturier et al., 2024).

By using the custom-built NEMESISPY radiative transfer and atmospheric retrieval code (Yang et al., 2024a), this thesis constrains the atmospheric properties of WASP-43b by analysing three sets of phase-resolved emission spectra: (1) the *HST*/WFC3 + *Spitzer*/IRAC observation in Chapter 5; (2) the *JWST*/MIRI observation in Chapter 6; (3) the *JWST*/NIRSpec observation in Chapter 7. Additionally, this thesis analyses a panchromatic dayside emission spectrum in Chapter 8, which is generated from the eclipse spectra of the above three data sets. The atmospheric retrievals reveal the presence of key molecules including H_2O ($> 12\sigma$), CO_2 ($> 13\sigma$), CO ($> 7\sigma$), NH_3 ($> 6\sigma$), HCN ($> 4\sigma$), and H_2S ($> 2.8\sigma$), and rule out the presence of CH_4 at detectable abundance. Furthermore, the retrieval results constrain the atmospheric temperature profile of WASP-43b across a wide pressure range. Overall, the retrieved atmospheric chemical abundance points to metal enrichment and a super-solar C/O ratio in the atmosphere of WASP-43b. These results provide the foundation for further investigation into the atmospheric chemistry and formation history of WASP-43b.

1.2.3 Constraining the Formation History of WASP-43b

Understanding the formation of giant planets is a key focus of planetary science. The elemental abundance in a hot Jupiter's atmosphere may constrain its formation history (Dawson & Johnson, 2018; Madhusudhan, 2019; Fortney et al., 2021). For example, atmospheric heavy element enrichment ('metallicity') and carbon-to-oxygen elemental abundance ratio (C/O ratio) are thought to be important tracers of the formation history (Öberg et al., 2011; Madhusudhan et al., 2014; Mordasini et al., 2016; Madhusudhan et al., 2017). Past studies have also explored the roles of nitrogen abundance (Piso et al., 2016; Cridland et al., 2020; Turrini et al., 2021; Ohno & Fortney, 2023a,b), sulphur abundance (Crossfield, 2023), and the abundance of refractory elements (Chachan et al., 2023). The key insight that links the elemental abundance of a planet to its formation history is that the partition of molecules in solid and gas phases changes radically across icelines in the protoplanetary disc, where major volatile species such as H_2O, CO_2, and CO condense. Therefore, depending on whether the formation of the planet is gas accretion dominated or solid accretion dominated, their final metallicity and C/O ratio are indicative of their formation location and pathway (Madhusudhan et al., 2014, 2017; Mordasini et al., 2016). A more detailed discussion on the link between the formation mechanisms and the present day composition of hot Jupiters is given in Chapter 8.4.

The atmospheric metal enrichment and super-solar C/O ratio of WASP-43b constrained in this thesis hold important clues to its formation scenario. These constraints rule out the formation scenarios where the accretion is purely gas-dominated, which would result in solar/sub-solar metallicity with a solar/super-solar C/O ratio, assuming that the protoplanetary disc had the same composition as the star WASP-43, which is of solar metallicity. Furthermore, it is difficult to explain these abundance constraints without a combination of in situ metal enrichment, planetesimal accretion or pebble drift and evaporation (Mollière et al., 2022; Morbidelli et al., 2023). These results are among the first works that show the feasibility of constraining formation mechanism with atmospheric retrievals (Line et al., 2021; Fu et al., 2024), and continuing efforts on this front will help us better understand the origin of hot Jupiters and giant planets in general.

1.3 Thesis Outline

The remainder of this thesis is organised as follows. Chapters 2, 3, and 4 describe the methodology of this thesis, whereas Chapters 5, 6, 7 and 8 describe the atmospheric retrieval results.

Chapter 2 describes how emission spectra in this thesis are calculated and presents the radiative transfer and atmospheric retrieval software NEMESISPY, which I have developed for this thesis project.

Chapter 3 introduces parametric atmospheric temperature models that can be used to fit emission spectra of hot Jupiters, including a novel 2D atmospheric temperature model.

Chapter 4 outlines the process of retrieving information from spectroscopic observations, known as atmospheric retrievals, including the statistical methods used for parameter inference and model comparison.

Chapter 5 employs the novel 2D temperature model introduced in Chapter 3 to simultaneously fit emission spectra observed at multiple orbital phases. The retrieval scheme is used to constrain the atmospheric properties of WASP-43b using a combined *HST* + *Spitzer* data set, yielding a detection of H_2O.

Chapter 6 applies the novel 2D temperature model introduced in Chapter 3 to constrain the atmospheric properties of WASP-43b using phase-resolved emission spectra observed with the Mid-Infrared Instrument (MIRI) onboard the *JWST*. The retrieval results confirm the detection of H_2O in Chapter 5, reveal tentative evidence of NH_3, CO and CO_2, and rule out the presence of CH_4 at detectable abundance.

Chapter 7 performs a phase-by-phase retrieval analysis on phase-resolved emission spectra of WASP-43b observed with the Near Infrared Spectrograph (NIRSpec) onboard the *JWST*. The retrieval results reveal the presence of CO, CO_2, H_2S, and confirm the detection of H_2O in Chapters 5 and 6.

Chapter 8 analyses a panchromatic dayside emission spectrum of WASP-43b generated from the data sets used in Chapters 5, 6 and 7. The retrievals yield the detection of H_2O, CO, CO_2, NH_3, H_2S, HCN, and a non-detection of CH_4. The retrieved molecular abundances suggest that the atmosphere of WASP-43b is metal-enriched and has a close-to-unity C/O ratio, though the uncertainty on the metallicity is large. The metallicity and C/O ratio suggest that pebble drift likely played an important role in the formation of WASP-43b.

Chapter 9 discusses the limitations of the results presented in this thesis.

Chapter 10 concludes the thesis.

Chapter 2

Calculating Emission Spectra

Partial contents of this chapter have been published in Monthly Notices of the Royal Astronomical Society under Yang et al. (2023), and in the Journal of Open Source Software under Yang et al. (2024a).

Emission spectra are an essential tool in the study of planetary atmospheres. They can reveal the chemical composition, temperature structure, and physical processes at play in the atmosphere. This chapter delves into the physical theory and computational methods required to calculate the emission spectra of exoplanetary atmospheres, with a particular focus on hot Jupiters. On the theoretical side, Section 2.1 outlines the quantum mechanical principles governing photon-matter interactions on the microscopic scale. Section 2.2 introduces the radiative transfer equation, which provides a macroscopic account of how radiation travels through a planetary atmosphere, thereby explaining the origin of atmospheric emission spectra. On the computational side, Section 2.3 explains the correlated-k method, which significantly speeds up radiative transfer calculation. Section 2.4 details a method for calculating the disc-integrated emission spectra of exoplanets. Finally, Section 2.5 presents the open source radiative transfer code NEMESISPY, which I have developed based on the NEMESIS library of Irwin et al. (2008). All spectral calculations presented in this thesis are performed using the NEMESISPY library.

Since this thesis focuses on hot Jupiters, this chapter does not consider the spectral contribution from a liquid or solid surface and assumes that the observed spectral features of hot Jupiters originate purely in the atmosphere. For terrestrial planets such as the Earth, it is also possible to see absorption and emission features due to land or ocean surfaces.

2.1 Atomic and Molecular Spectroscopy

Spectroscopy is the study of how matter interacts with light. Atoms and molecules can absorb or emit light subject to a set of physical rules, which give rise to the emission and absorption lines in the spectra of stellar and planetary objects. This section uses the theory of atomic and molecular spectroscopy to explain the features of these spectral lines.

The fundamental fact of spectroscopy is that the energy levels of atoms and molecules are quantised, meaning they come in discrete values. An atom or a molecule can only absorb or emit photons with energies corresponding to the difference between two energy levels. An atom or molecule can absorb a photon and move to a higher energy level or emit a photon and move to a lower energy level. The photon's wavelength λ and frequency ν is related to the energy level difference δE by the Planck relation

$$\delta E = h\nu = \frac{hc}{\lambda}, \tag{2.1}$$

where h is the Planck's constant and c is the speed of light in vacuum. Each species of atoms or molecules, such as hydrogen, water, or carbon dioxide, has a unique set of energy levels; consequently, each species absorbs and emits light at a unique set of wavelengths. Therefore, spectral lines enable the identification of atoms and molecules from the observed spectra of atmospheres.

Atomic spectral lines are related to electronic transitions, which occur when electrons in an atom move between different energy levels. The corresponding photons generally have wavelengths in the ultraviolet and visible range of the electromagnetic spectrum. Numerous atomic species have been observed in the spectra of hot Jupiters. For example, sodium has a doublet line[1] at around 589 nm, which has been observed in multiple hot Jupiters (Charbonneau et al., 2002; Sing et al., 2008; Huitson et al., 2012; Nikolov et al., 2014; Casasayas-Barris et al., 2017; Seidel et al., 2023). Other atomic species detected in the spectra of hot Jupiters[2] include potassium (Sing et al., 2015; Sedaghati et al., 2016) and iron (Gibson et al., 2020). Molecules, in addition to the electronic degree of freedom, have two additional degrees of freedom related to the vibrational and rotational motions. This is because molecules, unlike atoms, can rotate around their centre of mass and vibrate along the bonds that connect the constituent atoms. Vibrational transitions typically occur in the infrared, whereas

---

[1] A doublet line originates from the splitting of an electronic energy level due to spin-orbit interaction.

[2] Note that some of the detections listed here are for planets known as 'ultra hot Jupiters' because of their exceptionally high dayside temperatures.

rotational transitions typically occur in the microwave or far-infrared region. Vibrational transitions can happen in conjunction with rotational transitions, which result in the rotational-vibrational (ro-vibrational) bands of spectral lines, with the bands centred on the vibrational frequency. Electronic transitions are generally irrelevant for molecules, as molecules tend not to have stable excited electronic states. Molecules observed in the spectra of hot Jupiters include, for example, H_2O (Kreidberg et al., 2014; Yang et al., 2023, 2024b) and CO (Rodler et al., 2013; van Sluijs et al., 2023; Lesjak et al., 2023).

Spectral 'lines' have finite width due to several broadening mechanisms. While the energy levels determine the wavelengths of spectral lines, line-broadening mechanisms determine their shape. At the most basic level, the quantum mechanical energy-time uncertainty couples the uncertainty in the lifetime of an excited state Δt to the uncertainty in its energy ΔE, such that the product of the two uncertainties is bounded below:

$$\Delta E \Delta t \geq \frac{h}{4\pi}. \tag{2.2}$$

Since excited states have finite lifetimes, there are finite uncertainties in their energy levels, which lead to a broadening of spectral lines. This broadening mechanism is known as natural broadening, which by itself gives rise to a Lorentzian line profile. The effects of natural broadening are negligible in the context of exoplanetary spectra. Secondly, collisions between particles also limit the lifetimes of energy levels, thus broadening spectral lines due to the uncertainty principle. This broadening mechanism is known as collisional broadening, or pressure broadening, as the broadening increases with atmospheric pressure. Collisional broadening, like natural broadening, gives rise to a Lorentzian line profile. Thirdly, atoms and molecules are in thermal motion when they absorb and emit photons. Thus, the frequency of the emitted or absorbed photons is shifted depending on the particles' motion relative to the observer. This broadening mechanism is known as Doppler broadening and positively correlates with temperature. If the particles' velocities follow the Maxwell-Boltzmann distribution, then Doppler broadening gives rise to a Gaussian line profile. Doppler broadening is significant in the spectra of hot Jupiter due to the high temperatures in their atmospheres. When both Doppler and collisional broadening are significant, the resultant line shape is a convolution of the two broadening effects, known as the Voigt line profile.

The mathematical forms of spectral line profiles are given by a distribution function $f(\nu)$ (e.g., Goody & Yung, 1995). Consider first pure Doppler broadening. Assuming LTE, the random molecular motions are described by the Maxwell-Boltzmann distribution. Therefore, the distribution of the relative velocity u between the absorber and the observer is given by (Goody & Yung, 1995):

$$p(u) = \sqrt{\frac{m}{2\pi k_B T}} \exp\left(-\frac{mu^2}{2k_B T}\right), \tag{2.3}$$

where m is the particle mass, k_B is the Boltzmann constant, and T is the temperature. For a line centred at ν_0, pure Doppler broadening results in a line profile given by a Gaussian distribution

$$f_D(\nu) = \frac{1}{\alpha_D \sqrt{\pi}} \exp\left(-\frac{(\nu - \nu_0)^2}{\alpha_D^2}\right), \tag{2.4}$$

where the Doppler line width α_D is defined as

$$\alpha_D = \frac{\nu_0}{c} \sqrt{\frac{k_B T}{m}}. \tag{2.5}$$

For pure collisional broadening, the line profile is given by the Lorentzian distribution function

$$f_L(\nu) = \frac{1}{\pi} \frac{\alpha_L}{(\nu - \nu_0)^2 + \alpha_L^2}, \tag{2.6}$$

where α_L is the collision-broadening width and depends on both the pressure and the temperature. The combination of both Doppler broadening and collision broadening is modelled by a convolution of the Gaussian line profile and the Lorentzian line profile, which is the Voigt profile given by

$$f_V(\nu) = \frac{a}{\pi^{3/2} \alpha_D} \int_{-\infty}^{\infty} dy \frac{e^{-y^2}}{(\nu' - y)^2 + a^2}, \tag{2.7}$$

where $\nu' = (\nu - \nu_0)/\alpha_D$, and $a = \alpha_L/\alpha_D$.

2.2 The Radiative Transfer Equation

Having reviewed the theory of how light interacts with matter on the microscopic level, let us now turn to the topic of radiative transfer, which is the physical process by which light is absorbed, emitted, and scattered as it propagates through a macroscopic medium, such as a planetary atmosphere. The basic physical quantity describing a radiation field is the spectral radiance (e.g., Goody & Yung, 1995), which is the energy flux in a given direction per unit area perpendicular to the given direction, per unit solid angle, per unit time, per unit frequency interval (or per unit wavelength interval). The spectral radiance is also referred to as specific intensity and has the SI unit $\mathrm{Wm^{-2}sr^{-1}Hz^{-1}}$. As a beam of radiation travels through the atmosphere, the atmospheric constituents can modify it through processes of absorption, scattering, and emission. Absorption attenuates the beam, whereas emission enhances it. Scattering can either attenuate the beam by scattering radiation out of it or enhance it by scattering ambient radiation into it.

The radiative transfer equation describes the change in the intensity of radiation as it moves through a medium. Consider a beam of spectral radiance I_λ travelling through an elemental volume, where λ denotes the wavelength dependency of the spectral radiance. The elemental change in I_λ is given by

$$\delta I_\lambda = -\delta I_\lambda^{\mathrm{abs}} - \delta I_\lambda^{\mathrm{sca,out}} + \delta I_\lambda^{\mathrm{sca,in}} + \delta I_\lambda^{\mathrm{em}}, \tag{2.8}$$

where $\delta I_\lambda^{\mathrm{abs}}$ is the loss due to absorption, $\delta I_\lambda^{\mathrm{sca,out}}$ is the loss due to scattering, $\delta I_\lambda^{\mathrm{sca,in}}$ is the gain due to scattering, and $\delta I_\lambda^{\mathrm{em}}$ is the gain due to emission. Equation (2.8) is the basic form of the radiative transfer equation; in-depth treatment of its analytic and numerical solutions can be found in textbooks such as Goody & Yung (1995).

This thesis assumes that the atmosphere is in local thermodynamic equilibrium (LTE). Under LTE, both the radiative properties of the particles and the distribution of particle energies are linked to the same local temperature. Low-resolution emission spectra observed using space telescopes typically probe pressures between 1 bar and 1 mbar in the atmospheres of hot Jupiters (for example, see the transmission weighting function in Figures 5.2 and 6.5) , where the collisional timescale is short compared to the radiative timescale, so LTE is a valid assumption. Now, consider a beam of radiation travelling through a layer of atmosphere of elemental thickness δz along a slant path at zenith angle θ. Lambert's law gives the change in the spectral radiance due to absorption at wavelength λ:

$$\delta I_\lambda^{\mathrm{abs}}(z) = -\alpha I_\lambda(z) = -I_\lambda(z) k_\lambda(z) \rho_a(z) \sec\theta \delta z = -I_\lambda(z) \frac{k_\lambda(z)\rho_a(z)}{\mu} \delta z, \tag{2.9}$$

where α is the absorptivity of the elemental layer, $\rho_a(z)$ is the number density of the absorbers (SI unit: m^{-3}), $k_\lambda(z)$ is the absorption cross-section of the absorbers (SI unit: m^2), and $\mu = \cos\theta$. Assuming LTE, it can be shown via Kirchhoff's law of thermal radiation that the radiation emitted along the slant path is

$$\delta I_\lambda^{\mathrm{em}} = B_\lambda(T(z))\frac{k_\lambda(z)\rho_a(z)}{\mu}\delta z, \tag{2.10}$$

where $T(z)$ is the temperature of the atmospheric layer, and B_λ is the Planck function given by

$$B_\lambda(T) = \frac{2hc^2}{\lambda^5}\frac{1}{e^{hc/(\lambda k_B T)} - 1}, \tag{2.11}$$

h being the Planck constant, k_B the Boltzmann constant, and c the speed of light. Note that the Planck function describes the black body radiation.

If we neglect the change in spectral radiance due to scattering, Equation (2.8) simplifies to

$$\delta I_\lambda = -\delta I_\lambda^{\mathrm{abs}} + \delta I_\lambda^{\mathrm{em}}. \tag{2.12}$$

Substituting Equations (2.9) and (2.10) into Equation (2.12), we obtain the radiative transfer equation in a non-scattering atmosphere:

$$\delta I_\lambda = -I_\lambda(z)\frac{k_\lambda(z)\rho_a(z)}{\mu}\delta z + B_\lambda(T(z))\frac{k_\lambda(z)\rho_a(z)}{\mu}\delta z. \tag{2.13}$$

Note that δI_λ is completely specified by the temperature and composition profiles of the atmosphere, which determines $T(z)$, $k_\lambda(z)$, and $\rho_a(z)$. The dominant contributions to the scattering term in Equation (2.8) in giant planet atmospheres are scattering due to aerosols and Rayleigh scattering due to the bulk H_2/He atmosphere. Rayleigh scattering is negligible in the infrared wavelengths studied in this thesis, and aerosols are not included in the atmospheric retrievals in this thesis. Therefore, this thesis neglects the scattering component in the radiative transfer calculations.

We can integrate Equation (2.13) to calculate the spectral radiance emerging at the top of the atmosphere, which specifies the emission spectrum. Consider a finite atmospheric layer with the layer base at z_0 and the layer top at z_1. Let the spectral radiance at the layer base and the layer top be $I_{\lambda,0}$ and $I_{\lambda,1}$, respectively. Let us define some useful quantities. The optical thickness (or optical depth) τ_λ of the layer is given by

$$\tau_\lambda(z_0, z_1) = \int_{z_0}^{z_1} k_\lambda(z)\rho_a(z)dz, \tag{2.14}$$

which is a measure of how opaque the layer is. For radiation propagating along on a slant path defined by $\mu = \cos\theta$, the optical path χ_λ is given by

$$\chi_\lambda(z_0, z_1) = \frac{\tau_\lambda}{\mu}. \tag{2.15}$$

The transmission $\mathcal{T}_\lambda$ is defined as

$$\mathcal{T}_\lambda(z_0, z_1, \mu) = \exp\Big(-\frac{\tau_\lambda(z_0, z_1)}{\mu}\Big) = \exp(-\chi_\lambda(z_0, z_1)), \tag{2.16}$$

which gives the fraction of incident spectral radiance that is transmitted through the atmospheric layer defined by (z_0, z_1) in the direction specified by μ. Integrating Equation (2.13) after rewriting it in terms of optical thickness, we see that the spectral radiance at the top of the layer is

$$I_{\lambda,1} = I_{\lambda,0}\mathcal{T}_\lambda(z_0, z_1, \mu) + \int_{z_0}^{z_1} B(\lambda, T(z))\frac{d\mathcal{T}_\lambda(z, z_1, \mu)}{dz}dz. \tag{2.17}$$

By evaluating Equation (2.17) at the top of the atmosphere, we can obtain the emission spectra of hot Jupiters. Note that the derivative of the transmission $\mathcal{T}_\lambda$ informs us about where in the atmosphere an observation is sensitive to, as it determines from where the radiation of the observed spectrum originates in the atmosphere. We define $\frac{d\mathcal{T}_\lambda(z,z_1,\mu)}{dz}$ as the transmission weighting function. The transmission weighting function can be equivalently defined using the pressure coordinate as the derivative of the transmission with respect to pressure.

2.3 The Correlated-*k* Method

Solving the radiative transfer equation can be computationally intensive. This is because gaseous opacities are generally rapidly varying functions of wavelength due to the multitude of spectral lines. Evaluating quantities related to gaseous opacities thus requires many quadrature points for standard numerical evaluation schemes. Consider radiation propagating in a homogeneous medium along a path consisting of absorber amount m (SI unit: m^{-2}), where the absorber amount here is defined as the number density of the absorber, ρ_a, integrated over the path length. The mean transmission $\overline{\mathcal{T}}$ in the wavelength bin $[\lambda, \lambda + \Delta\lambda]$ is given by

$$\overline{\mathcal{T}}(m) = \frac{1}{\Delta\lambda}\int_{\lambda}^{\lambda+\Delta\lambda} \exp(-k(\lambda)m)d\lambda, \tag{2.18}$$

where $k(\lambda)$ is the absorption cross-section (SI unit: m^2). The most direct approach to evaluating (2.18) is the line-by-line method, which computes the absorption cross-section by taking into account every spectral line above some cut-off intensity in

$[\lambda, \lambda + \Delta\lambda]$ for all relevant molecules and atoms. While accurate, this approach can be intractable due to the sheer number of spectral lines that need to be accounted for.

In atmospheric retrievals where we fit the observed spectrum with model spectra generated from an atmospheric model, exploring a large region of the model parameter space is desirable. Therefore, it is imperative to have a numerical scheme that can calculate atmospheric spectra efficiently and accurately. This thesis uses the correlated-k method (Lacis & Oinas, 1991) to speed up radiative transfer calculations, following Irwin et al. (2008). Consider the mean transmission $\overline{\mathcal{T}}$, which is the key quantity that links opacity structure and thermal structure in thermal emission calculations. As mentioned previously, the cross-section k is a rapidly varying function of λ, so it is computationally expensive to numerically calculate Equation (2.18). However, since the ordering of k in the wavelength bin $[\lambda, \lambda + \Delta\lambda]$ does not affect the value of Equation (2.18), we are free to sort k in ascending order within a wavelength bin, which gives a monotonic distribution of k that is easier to handle in quadrature schemes, as shown in Figure 2.1.

Mathematically, let the cumulative frequency distribution of k be $g(k)$, then the inverse of $g(k)$, which we denote as $k(g)$, is well-defined and monotonic. The function $k(g)$ is called the k-distribution and can be tabulated on a grid of pressures and temperatures for each spectrally active molecule before radiative transfer calculations. During radiative transfer calculations, we can combine the k-distributions of multiple gases into a single k-distribution with the random-overlapping-line approximation (Lacis & Oinas, 1991), which assumes that the spectral lines of different gases overlap randomly. Such approximation gives residuals insignificant compared with measurement error in the modelling of exoplanet spectra, as found by Irwin et al. (2020) and Mollière et al. (2015).

To calculate $\overline{\mathcal{T}}$ for an inhomogenous path, we first split the path into multiple sub-paths that are sufficiently homogeneous, then model each sub-path with the absorber-amount weighted sub-path properties. In the monochromatic case, the transmission of each sub-path can be multiplied together to give the transmission of the total path. However, to use the k-distribution technique where we have reordered opacity, we need to additionally assume that the wavelength regions of high opacity are correlated for all sub-paths, which is the correlated-k approximation. Using the k-distribution technique, the mean transmission of a sub-path as defined in Equation (2.18) can be

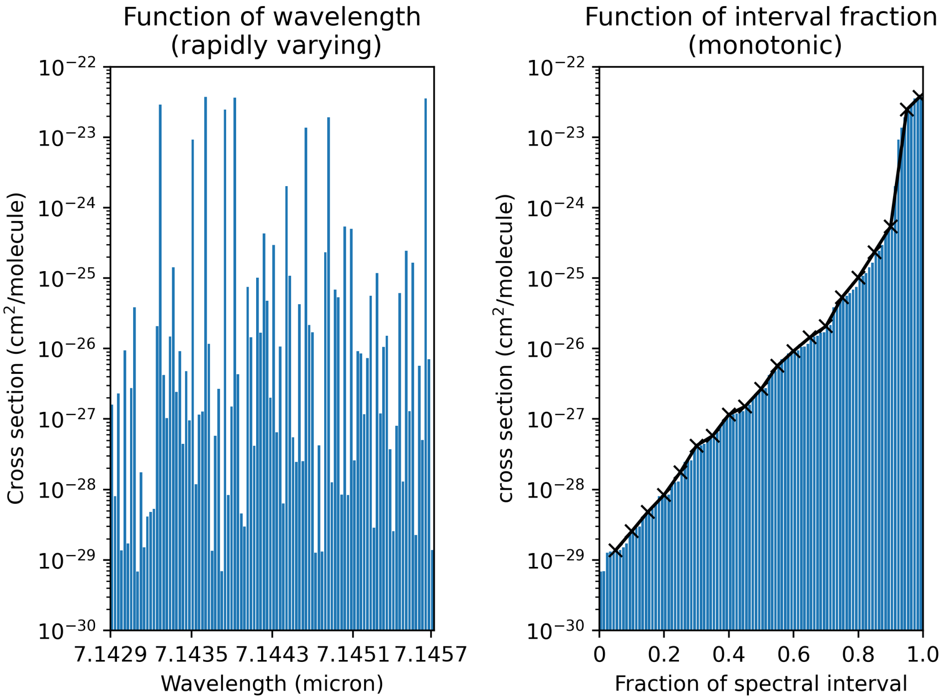

Figure 2.1: Re-ordering of opacity in the correlated-k method. The plot on the left shows methane lines around 7.14 μm at 296 K obtained from the HITRAN database, with line broadening processes neglected for clarity. The cross-sections are rearranged in ascending order to give the k-distribution in the right plot, together with the sampled quadrature points (black asterisks) for a 20-point numerical Gaussian integration.

well-approximated with a Gaussian quadrature scheme:

$$\overline{\mathcal{T}}(m) = \sum_{i=1}^{N_g} \exp(-k_i m)\Delta g_i, \tag{2.19}$$

where k_i is the ith quadrature point, Δg_i the corresponding weight, and N_g the number of quadrature points. The total transmission of an inhomogenous path is then

$$\overline{\mathcal{T}}(m) = \sum_{i=1}^{N_g} \exp\big(-\sum_{j=1}^{N_{\text{layer}}} k_{ij} m_j\big)\Delta g_i, \tag{2.20}$$

where we have multiplied the transmission of all N_{layer} layers together. This thesis uses k-distribution look-up tables ('k-tables') with $N_g = 20$, following Irwin et al. (2008). To calculate an emission spectrum using the correlated-k method, we only need to substitute Equation (2.20) into Equation (2.17) and then evaluate for all relevant wavelength bins.

2.4 A Disc-Integration Method

This section introduces a method for calculating the disc-integrated emission spectra of exoplanets given by Irwin et al. (2020). The disc-averaged spectral radiance of a planetary atmosphere for a distant observer is

$$\bar{I}(\lambda) = \frac{1}{\pi}\int_{\phi=0}^{2\pi}\int_{\mu=0}^{1} I(\lambda,\mu,\phi)\mu d\mu d\phi, \tag{2.21}$$

where $\mu = \cos(\theta)$ is the cosine of the zenith angle θ, and ϕ is the azimuth angle. Note that the zenith angle is defined as the angle between the local normal of the atmosphere and the line of sight, and the azimuth angle is the angle from a reference direction on the projected disc.

For a spatially inhomogeneous atmosphere where the spectral radiance I varies as a function of location on the visible disc, Equation (2.21) must be evaluated numerically. Atmospheric retrievals usually need to calculate many model spectra to explore the parameter space of an atmospheric model, so it is important to have a numerical integration scheme for Equation (2.21) that is both accurate and computationally inexpensive. In the numerical method of Irwin et al. (2020), the zenith integration with respect to μ is done with a Gauss-Lobatto quadrature scheme with N_μ quadrature points, while the azimuthal integration with respect to ϕ is done with a Trapezium rule quadrature scheme with N_ϕ quadrature points. For the trapezium

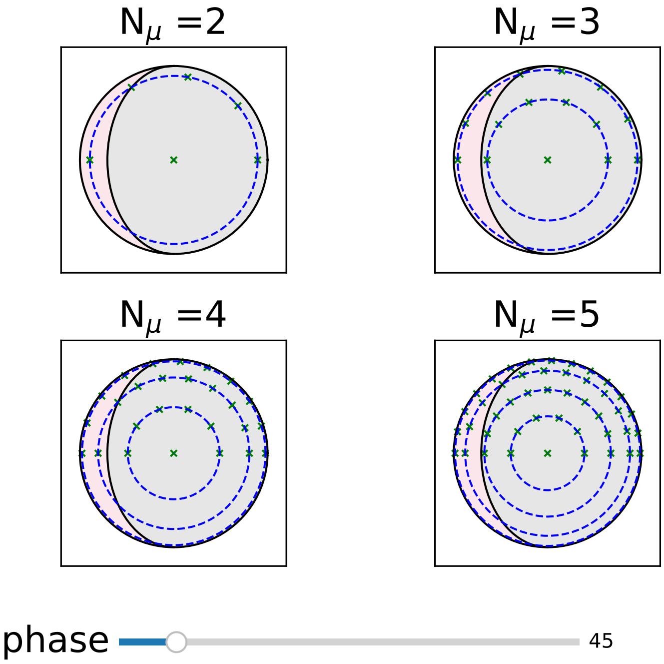

Figure 2.2: The disc-integration scheme of Irwin et al. (2020). The orbital phase shown here is 45°, where 0° corresponds to the primary transit and 180° the secondary eclipse. The illuminated dayside region visible to the observer is shaded in pink, whereas the nightside region is shaded in grey. The crosses mark the quadrature points for disc-integration, and the dashed circles mark the positions of the zenith angle quadratures. The integration scheme is shown for four different values of N_μ.

rule integration, the quadrature points are placed on circles corresponding to each zenith quadrature point such that the arc length between neighbouring points is approximately R_{plt}/N_μ, where R_{plt} is the planetary radius. Overall, the Irwin et al. (2020) numerical integration scheme for Equation (2.21) is given by:

$$\bar{I}(\lambda) = 2\sum_{i}^{N_\mu}\sum_{j}^{N_\phi} I(\lambda, \mu_i, \phi_{ij})\mu_i \Delta\mu_i w_{ij}, \tag{2.22}$$

where μ_i are the Lobatto quadrature points for the zenith integration, $\Delta\mu_i$ are the corresponding quadrature weights, ϕ_{ij} are the Trapezium rule quadrature points for the azimuth integration (which are different for each zenith angle), and w_{ij} are the Trapezium rule quadrature weights for the jth azimuthal angle and the ith zenith angle. Furthermore, if a zenith angle quadrature circle crosses the day/night terminator, then the nearest azimuth quadrature point is adjusted to be on the day/night terminator, as shown in Figure 2.2. To model the emission spectra of transiting hot Jupiters, this thesis assumes that the planet's orbit is exactly edge-on and that the atmosphere is symmetric about the equatorial plane, which is defined as being in the orbital plane, following the approach of Irwin et al. (2020). As a result, we only need to evaluate the integration over half of the visible disc and multiply the result by a factor of two. The quadrature points for $N_\mu = 2, 3, 4, 5$ are shown in Figure 2.2. The error introduced by assuming an exactly edge-on orbit is secondary as transiting planets have nearly edge-on orbits. The symmetry about the equatorial plane is based on GCM simulations of hot Jupiters (Parmentier et al., 2016; Amundsen et al., 2016; Mendonça, 2020; Roman et al., 2021), which exhibit negligible differences between the northern and southern hemispheres. A possible scenario where the assumption of north-south symmetry is not appropriate is given by the GCM simulations of Cho et al. (2021), which suggest that the atmospheres of hot Jupiter may be highly turbulent, and the atmospheric thermal structures may exhibit significant time variability that breaks the north–south symmetry. Nonetheless, there is currently no evidence that WASP-43b exhibits such significant time variability (Murphy et al., 2023).

2.5 Software Development: NEMESISPY

The final section of this chapter introduces the NEMESISPY software package that I have developed to calculate the emission spectra of exoplanets (Yang et al., 2024a). NEMESISPY is a Python package developed to perform parametric atmospheric modelling and radiative transfer calculation for the retrievals of exoplanetary spectra. The software implements the theory and computational methods covered in this chapter. It is a recent development of the well-established Fortran NEMESIS library of Irwin et al. (2008), which has been applied to the atmospheric retrievals of both solar system planets and exoplanets employing numerous different observing geometries (Lee et al., 2012; Teanby et al., 2012; Barstow et al., 2014, 2016; Krissansen-Totton et al., 2018; Barstow, 2020; Irwin et al., 2020; James et al., 2023). NEMESISPY can easily interface with Bayesian inference algorithms to retrieve atmospheric properties from spectroscopic observations (Chapter 4 gives details on Bayesian inference). To date, the NEMESISPY retrieval pipeline has been used to analyse *HST*/WFC3 and *Spitzer*/IRAC observation of a hot Jupiter (Yang et al., 2023, discussed in Chapter 5), *JWST*/MIRI observation of a hot Jupiter (Yang et al., 2024b, discussed in Chapter 6), *JWST*/NIRSpec observation of a hot Jupiter (discussed in Chapter 7), *JWST*/NIRSpec observation of a super-Earth (Banerjee et al., 2024), in addition to several other projects in preparation.

NEMESISPY has several positive attributes as an exoplanetary retrieval pipeline. Firstly, NEMESISPY is significantly faster than the original Fortran NEMESIS library. This is due to the extensive code refactoring in the development of NEMESISPY, as well as the employment of a just-in-time compiler (Lam et al., 2015), which compiles the most computationally expensive routines to machine code at run time to mitigate the speed disadvantage of Python as an interpreted language. For a typical retrieval performed in this thesis project, NEMESISPY is about a factor of ten faster than NEMESIS, which is a crucial improvement as exoplanetary retrievals typically utilise computationally intensive statistical inference algorithms that compute hundreds of thousands of model spectra. Secondly, NEMESISPY inherits the correlated-k (Lacis & Oinas, 1991) radiative transfer routine from the Fortran NEMESIS library (Irwin et al., 2008), which has been extensively validated against other radiative transfer codes (Barstow et al., 2020). Thirdly, NEMESISPY implements several parametric atmospheric temperature models. These routines are particularly useful for retrieving spectroscopic phase curves of hot Jupiters. Additionally, NEMESISPY contains several general-purpose routines for atmospheric modelling and spectral simulations. The modular nature of the package means that subroutines can be easily called on their own. The combination of accelerated computational speed, well-tested core radiative transfer routines, and modular design is ideal for tackling the influx of *JWST* data of exoplanets.

NEMESISPY is fully open source and can be downloaded from GitHub[3] or the

---

[3] `https://github.com/Jingxuan97/nemesispy2022`

Python Package Index (PyPI)[4]. NEMESISPY is also listed on the Astrophysics Source Code Library[5] and the NASA GSFC Exoplanet Modeling and Analysis Center[6].

---

[4] `https://pypi.org/project/nemesispy/`

[5] `https://ascl.net/2411.030`

[6] `https://emac.gsfc.nasa.gov?cid=2409-001`

Chapter 3

Atmospheric Thermal Structure

Partial contents of this chapter have been published in Monthly Notices of the Royal Astronomical Society under Yang et al. (2023).

As the spectral appearance of hot Jupiters depends on their atmospheric thermal structure, we need to model their atmospheric temperature in order to retrieve information from their emission spectra. This thesis employs two one-dimensional parametric temperature-pressure (TP) profiles to model the thermal structure of hot Jupiters, as described in Section 3.1. Furthermore, this thesis introduces a novel two-dimensional parametric atmospheric temperature model that can be used to fit several phase-resolved emission spectra simultaneously, which is described in Section 3.2.

3.1 1D Temperature-Pressure (TP) Profiles

The temperature-pressure (TP) profile of a planetary atmosphere is determined by a combination of factors such as stellar irradiation, atmospheric composition, internal heat flux, and atmospheric dynamics. The fundamental physical processes that determine the shape of the TP profile are radiative heat transport and convection. As explained in Chapter 2, in particular by Equation (2.17), the TP profile of an atmosphere is directly linked to its emission spectrum: absorption and emission features arise when different layers of the observable atmosphere are emitting radiation at different temperatures. Modelling the TP profile is thus an important task in the atmospheric retrievals of hot Jupiters. This section introduces two one-dimensional TP profiles that are commonly used to fit the emission spectra of exoplanets (e.g., Gandhi & Madhusudhan, 2018; Bell et al., 2024). Section 3.1.1 introduces the Guillot (2010) TP profile, which assumes radiative equilibrium. Section 3.1.2 introduces the Madhusudhan & Seager (2009) TP profile, which is more flexible than the Guillot (2010)

TP profile and can approximate a wide range of temperature structures calculated with more sophisticated models. Retrieval studies that use 1D TP profiles typically use the same profile for the entire portion of the atmosphere under consideration. For disc-integrated emission spectra, the retrieved 1D TP profile thus represents an 'average profile'.

3.1.1 Guillot (2010) TP Profile

Guillot (2010) proposed an analytic radiative equilibrium TP profile for irradiated atmospheres. The profile partitions the radiation field into two independent components: an upwelling thermal component and a downwelling visible component, each parametrised by a mean opacity. The exact form of the Guillot (2010) TP profile used in this thesis is given by Equation (29) of Guillot (2010):

$$T^4 = \frac{3T_{\mathrm{int}}^4}{4}\Big(\frac{2}{3}+\tau\Big) + \frac{3T_{\mathrm{irr}}^4}{4} f \Big[\frac{2}{3} + \frac{1}{\gamma\sqrt{3}} + \Big(\frac{\gamma}{\sqrt{3}} - \frac{1}{\gamma\sqrt{3}}\Big)\mathrm{e}^{-\gamma\tau\sqrt{3}}\Big], \tag{3.1}$$

where the atmospheric temperature T is given in terms of the infrared optical depth τ and several tunable free parameters. The infrared optical depth τ is related to the atmospheric pressure P and gravity g by

$$\tau(P) = \frac{\kappa_{\mathrm{th}} P}{g}. \tag{3.2}$$

For the computation of Equation (3.1), this thesis assumes a negligible change in gravity with pressure as emission spectroscopy only probes a limited pressure range, so τ is linear in P. This TP profile has four free parameters: κ_{th} is the mean infrared opacity, γ is the ratio between the mean visible opacity and the mean infrared opacity, T_{int} is the intrinsic heat flux, and f is a catch-all parameter of order unity that can model the effects of albedo and the redistribution of stellar flux due to atmospheric circulation. Note that when γ is greater than 1 (visible opacity greater than infrared opacity), the profile has a thermal inversion; otherwise, the profile would be non-inverted. T_{irr} is the irradiation temperature defined by

$$T_{\mathrm{irr}} = \Big(\frac{R_{\mathrm{star}}}{a}\Big)^{1/2} T_{\mathrm{star}}, \tag{3.3}$$

where a is the orbital semi-major axis, and R_{star} and T_{star} are the host star radius and temperature, respectively. Table 3.1 lists the free parameters of the Guillot (2010) profile and their priors used in this thesis.

Parameter	Description	Prior	Unit
$\log \kappa_{\mathrm{th}}$	Log_{10} mean infrared opacity	U(-4,2)	$\mathrm{m}^2\mathrm{kg}^{-1}$
$\log \gamma$	Log_{10} ratio of visible and infrared opacities	U(-4,1)	dimensionless
$\log f$	Log_{10} heat redistribution parameter	U(-4,1)	dimensionless
T_{int}	Intrinsic heat flux temperature	U(100,1000)	Kelvin

Table 3.1: Free parameters of the Guillot (2010) TP profile and their priors. $U(a, b)$ denotes a uniform prior distribution between a and b. For κ_{th}, γ, and κ_{v}, the priors are given in the $\log_{10}$ space.

3.1.2 Madhusudhan & Seager (2009) TP Profile

Madhusudhan & Seager (2009) proposed a parametric TP profile motivated by general physical principles and known Solar System planet TP profiles. The Madhusudhan & Seager (2009) TP profile is flexible enough to reproduce a wide range of 1D TP profiles calculated from more sophisticated models for exoplanet atmospheres (see Madhusudhan & Seager, 2009). The profile divides the atmosphere into three representative layers: Layer 1 (upper-most layer), Layer 2 (middle layer), and Layer 3 (bottom-most layer). The profile prescribes that the temperature is isothermal in Layer 3 and that no thermal inversion is possible in Layer 1, so Layer 2 is the only region where a thermal inversion can occur. The TP profile is given by

$$\begin{cases} P = P_0 e^{\alpha_1 (T-T_0)^{\beta_1}} \text{ in Layer 1 } (P_0 < P < P_1), \\ P = P_2 e^{\alpha_2 (T-T_2)^{\beta_2}} \text{ in Layer 2 } (P_1 < P < P_3), \\ T = T_3 \text{ in Layer 3 } (P_3 < P). \end{cases} \tag{3.4}$$

Following Madhusudhan & Seager (2009), β_1 and β_2 are empirically set to 0.5 as the remaining parameters span the space of TP profiles in all generality. For the remaining parameters, two can be eliminated by enforcing continuity at the two layer boundaries, and P_0 is usually specified as the pressure at the top of the atmospheric model. It is convenient to parametrise the profile with the following six parameters: P_1, P_2, P_3, $T_{100\mathrm{mb}}$, α_1, and α_2, where $T_{100\mathrm{mb}}$ is the temperature at 100 millibar (Gandhi & Madhusudhan, 2018). Table 3.2 lists the free parameters of the Madhusudhan & Seager (2009) profile and their priors used in this thesis.

Parameter	Description	Prior	Unit
$T_{100\text{mb}}$	Temperature at 100 mb pressure	U(300,3000)	Kelvin
α_1	Layer 1 exponent	U(0.02,1)	Kelvin$^{-1/2}$
α_2	Layer 2 exponent	U(0.02,1)	Kelvin$^{-1/2}$
log P_1	Log$_{10}$ layer 1 base pressure	U(0,7)	Pa
log P_2	Log$_{10}$ layer 2 base pressure	U(0,7)	Pa
log P_3	Log$_{10}$ layer 3 base pressure	U(2,7)	Kelvin

Table 3.2: Free parameters of the Madhusudhan & Seager (2009) Profile and their priors. $U(a, b)$ denotes a uniform prior distribution between a and b. For P_1, P_2, and P_3, the priors are given in the log$_{10}$ space.

3.2 Yang et al. (2023) 2D Temperature Model

Yang et al. (2023) introduced a novel parametric 2D temperature model that accounts for the spatial variation of the atmospheric thermal structure. The model is given by Model 4 in Yang et al. (2023), which will be termed the Yang et al. (2023) 2D temperature model hereafter. The Yang et al. (2023) 2D temperature model divides the atmosphere into a dayside region and a nightside region that are each described with a representative temperature-pressure (TP) profile, as illustrated by Figure 3.1. The width and the central longitude of the dayside region are free parameters, modelling the effects of atmospheric circulation on heat redistribution. These parameters can also mimic the impact of a cloud distribution across the atmosphere, which may cause an apparent shift in heat redistribution by changing the hot spot offset, as shown by Parmentier et al. (2020).

In the Yang et al. (2023) 2D temperature model, the TP profile can vary with longitude on the dayside but is kept constant with longitude on isobars on the nightside, inspired by GCM studies which show approximately constant-with-longitude meridional mean thermal structures on the nightsides of hot Jupiters (e.g., Figure 10, Kataria et al., 2015; Figure 4, Mendonça et al., 2018a; Figure 7, Yang et al., 2023; Figure 2, Teinturier et al., 2024). Mathematically, the temperature T in the model atmosphere at pressure P, longitude Λ, and latitude Φ is given by

$$T(P, \Lambda, \Phi) = \begin{cases} T_{\text{night}}(P) \text{ if } \Lambda > \delta + 90^\circ \times \epsilon \text{ or } \Lambda < \delta - 90^\circ \times \epsilon, \\ T_{\text{night}}(P) + (T_{\text{day}}(P) - T_{\text{night}}(P)) \cos^n(\frac{\Lambda - \delta}{\varepsilon}) \\ \text{ if } \delta + 90^\circ \times \epsilon \geq \Lambda \geq \delta - 90^\circ \times \epsilon, \end{cases} \tag{3.5}$$

where $T_{\text{day}}(P)$ and $T_{\text{night}}(P)$ are respectively the representative TP profiles for the dayside region and the nightside region, δ is the longitudinal deviation of the centre of the dayside region from the substellar point, and ϵ is a parameter governing the width of the dayside region. The coordinate system is defined such that the sub-stellar point, where the star would be perceived to be directly overhead, is at 0° longitude, and the anti-stellar point is at $-180°$ longitude. The dayside region in the model is bound by the meridians $\Lambda = \delta - 90° \times \varepsilon$ and $\Lambda = \delta + 90° \times \varepsilon$, and the rest of the model is the nightside region (see Figure 3.1). The 'dayside region' in this model can deviate from the illuminated region of the planet. The exponent n of the cosine term in Equation (3.5) additionally prescribes how strongly temperatures vary with longitude on isobars on the dayside.

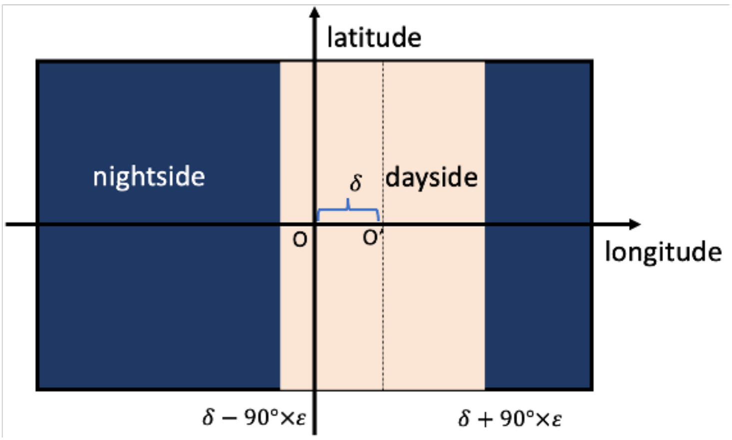

Figure 3.1: Schematics of the parametric 2D temperature model as defined by Equation (3.5). The model divides the atmosphere into a dayside region and a nightside region, each modelled with a representative TP profile. The dayside central longitude and the dayside width are allowed to vary. 'O' marks the substellar point, and 'O$'$' marks the centre of the dayside region. While temperature is constant with longitude on isobars in the nightside region, the variation of temperature with longitude on the dayside can be parametrised. Note that the temperature is constant with latitude and only varies with pressure and longitude. The retrieved thermal structure is interpreted as a latitudinal average.

The temperature model is '2D' in the sense that temperature only varies with pressure and longitude and is held constant with latitude. Of course, physically, we do not expect the temperature to be constant with latitude but should instead fall off towards the poles. We interpret the thermal structure retrieved using this 2D model as a latitudinally-averaged thermal structure, as Chapter 5 shows that the temperature structure retrieved from synthetic phase curve data simulated from a general circulation model (GCM) closely resembles the meridional mean thermal structure of the GCM calculated using cos(latitude) as the weight (see also Yang et al., 2023). The Yang et al. (2023) 2D temperature model does not model the latitudinal temperature variation since we are much more sensitive to longitudinal variation than latitudinal variation with phase curve observations. The central longitude during the observation changes, whereas the central latitude is held constant[1].

To set the representative TP profiles in the Yang et al. (2023) 2D temperature model, i.e., $T_{\rm day}(P)$ and $T_{\rm night}(P)$ in Equation (3.5), one is free to use any 1D TP profile. Chapters 5 and 6, for example, pair the Yang et al. (2023) 2D temperature model with the Guillot (2010) TP profile.

---

[1] The dayside latitudinal variation can be constrained with the eclipse mapping technique; see, for example, Hammond et al. (2024).

Chapter 4

Retrieving Information from Spectra

Chapter 2 demonstrates that the emission spectra of hot Jupiters depend on the physical conditions of their atmospheres. This chapter explores the inverse problem known as atmospheric retrieval, which is the inference of atmospheric properties by fitting a model to spectroscopic observations. The workflow of atmospheric retrievals can be divided into the following steps. Firstly, we must construct a parametric model for the observed region of the atmosphere (dealt with in Chapter 3). Secondly, we need a radiative transfer pipeline that can calculate model spectra from the atmospheric model (dealt with in Chapter 2). Finally, we need to constrain the atmospheric model parameters given the observed data using an appropriate statistical method. The posterior distribution of the atmospheric model parameters constrains the atmospheric properties of the observed planet. Figure 4.1 shows a flowchart of atmospheric retrieval. This chapter focuses on the statistical methods used in atmospheric retrievals. Section 4.1 starts with an overview of Bayesian inference. Three statistical inference methods commonly used in atmospheric retrievals are then introduced, namely Optimal Estimation (Section 4.2.1), Markov Chain Monte Carlo (Section 4.2.2), and Nested Sampling (Section 4.2.3). All atmospheric retrievals in this thesis employ the Nested Sampling algorithm, and Section 4.2.3 justifies this choice in the context of exoplanetary observations. Finally, Section 4.3 reviews Bayesian model comparison.

4.1 Principles of Bayesian Inference

This section outlines the basic principles of Bayesian inference in the context of atmospheric retrievals. Consider an array of observed data points $\boldsymbol{D}$ (e.g., data points in emission spectra), and a parametric model $\boldsymbol{M}(\boldsymbol{\theta})$ for the data (e.g., a model that can

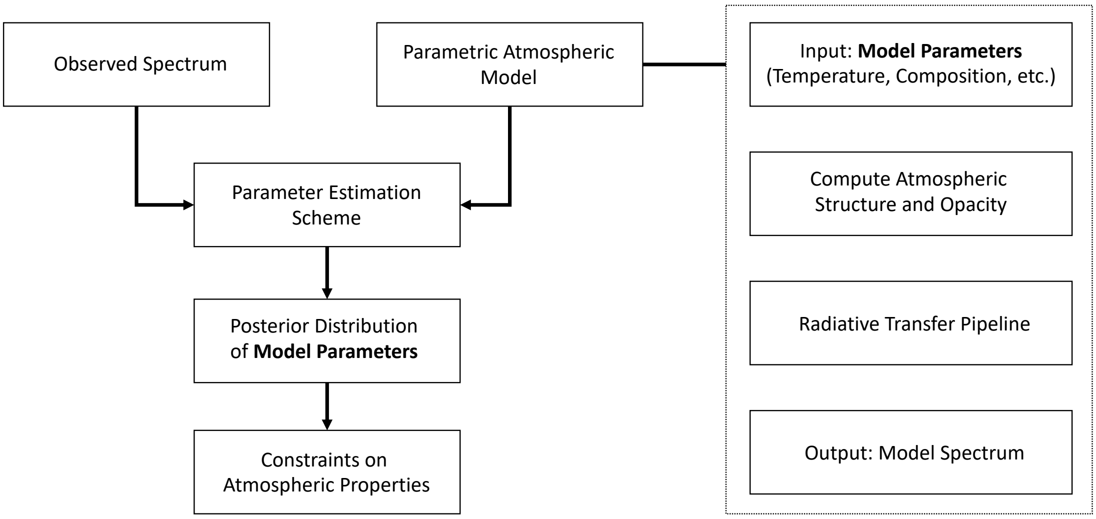

Figure 4.1: Atmospheric retrieval flowchart adapted from Madhusudhan (2018). Note that the parameter estimation step is an iterative process, where many model spectra are compared to the observed spectrum to map out the posterior distribution of the model parameters.

be used to simulate the emission spectra), where $\boldsymbol{\theta}$ are the parameters of the model. We can model the observed data as

$$\boldsymbol{D}_i = M(\boldsymbol{\theta})_i + \boldsymbol{\epsilon}_i, \tag{4.1}$$

where $\boldsymbol{D}_i$ is the ith data point and $\boldsymbol{\epsilon}_i$ the corresponding measurement uncertainty. The key task is to infer the model parameters $\boldsymbol{\theta}$ given the data $\boldsymbol{D}$ and the measurement uncertainties $\boldsymbol{\epsilon}$.

Information about $\boldsymbol{\theta}$ can be extracted from the data using Bayesian inference. By Bayes' theorem, the probability distribution of the parameters $\boldsymbol{\theta}$ given the data $\boldsymbol{D}$ is

$$\Pr(\boldsymbol{\theta}, \boldsymbol{M}|\boldsymbol{D}) = \frac{\Pr(\boldsymbol{D}|\boldsymbol{\theta}, \boldsymbol{M}) \Pr(\boldsymbol{\theta}|\boldsymbol{M})}{\Pr(\boldsymbol{D}|\boldsymbol{M})} = \frac{\mathcal{L}(\boldsymbol{D})\pi(\boldsymbol{\theta})}{Z}, \tag{4.2}$$

where Pr denotes the probability, $P(\boldsymbol{\theta}) \equiv \Pr(\boldsymbol{\theta}, \boldsymbol{M}|\boldsymbol{D})$ is the posterior distribution, $\mathcal{L}(\boldsymbol{D}) \equiv \Pr(\boldsymbol{D}|\boldsymbol{\theta}, \boldsymbol{M})$ is the likelihood, $\pi(\boldsymbol{\theta}) \equiv \Pr(\boldsymbol{\theta}|\boldsymbol{M})$ is the prior, and $Z \equiv \Pr(\boldsymbol{D}|\boldsymbol{M})$ is the evidence. In the context of exoplanet atmospheric retrievals, where the data are spectral observations of an exoplanetary atmosphere and the parameters are the parameters of an atmospheric model, evaluating the posterior distribution is challenging for several reasons. Firstly, the signal-to-noise ratio of the data is usually low, so it is important to robustly propagate the measurement uncertainties to the uncertainties in the inferred parameters to avoid spurious conclusions. Secondly, atmospheric models generally have high-dimensional parameter space, which makes the computation of the posterior distribution complex and time consuming. Thirdly, our theoretical understanding of exoplanetary atmospheres is lacking, so we generally do not have strong priors on the model parameters we wish to infer.

4.2 Statistical Algorithms

This section reviews three statistical inference algorithms commonly used in planetary science and atmospheric retrievals.

4.2.1 The Optimal Estimation Algorithm

The Optimal Estimation algorithm is widely used in Solar System atmospheric sounding (Rodgers, 1976, 2000; Irwin et al., 2008), and the general non-linear case is reviewed here. Consider a vector of data $\boldsymbol{D}$ with associated measurement covariance matrix S_ϵ, and suppose that we have a model $\boldsymbol{M}(\boldsymbol{\theta})$ for the data. As in the previous section, $\boldsymbol{\theta}$ is a vector of model parameters that we wish to estimate. Suppose we have some prior information about $\boldsymbol{\theta}$, represented by an a priori parameter vector $\boldsymbol{\theta}_0$ and an associated a priori covariance matrix $S_{\boldsymbol{\theta}}$. Qualitatively, the Optimal Estimation algorithm minimises the difference between the observed data $\boldsymbol{D}$ and the model $\boldsymbol{M}$ while favouring solutions that are close to the a priori parameter vector $\boldsymbol{\theta}_0$. Mathematically, this is done by minimising the cost function (Rodgers, 2000; Irwin et al., 2008):

$$\phi = (\boldsymbol{D} - \boldsymbol{M}(\boldsymbol{\theta}))^T S_\epsilon^{-1} (\boldsymbol{D} - \boldsymbol{M}(\boldsymbol{\theta})) + (\boldsymbol{\theta} - \boldsymbol{\theta}_0)^T S_{\boldsymbol{\theta}}^{-1} (\boldsymbol{\theta} - \boldsymbol{\theta}_0) . \tag{4.3}$$

Note that the first term in the cost function accounts for the difference between the observation and the model, whereas the second term accounts for the difference between the retrieved parameter vector and the a priori parameter vector. A common solution to the minimisation of Equation (4.3) is Newtonian iteration

$$\boldsymbol{\theta}_{n+1} = \boldsymbol{\theta}_0 + S_{\boldsymbol{\theta}} K_n^T (K_n S_{\boldsymbol{\theta}} K_n^T + S_\epsilon)^{-1} (\boldsymbol{D} - \boldsymbol{M}(\boldsymbol{\theta}_n) - K_n(\boldsymbol{\theta}_0 - \boldsymbol{\theta}_n)), \tag{4.4}$$

where K_n is the Jacobian matrix, i.e., the rate of change of the spectral data with the model parameter elements, calculated at the nth iteration. As pointed in Irwin et al. (2008), K_n can vary greatly between iterations and the simple iteration scheme in Equation (4.4) can become unstable.

A more numerically stable version of Equation (4.4), based on the Marquardt-Levenberg principle, is given in Irwin et al. (2008) as

$$\boldsymbol{\theta}'_{n+1} = \boldsymbol{\theta}_n + \frac{\boldsymbol{\theta}_{n+1} - \boldsymbol{\theta}_n}{1 + \lambda}, \tag{4.5}$$

where the parameter λ is initially set to 1. During the iterations, if the model $\boldsymbol{M}$ calculated from $\boldsymbol{\theta}_{n+1}$ reduces ϕ, then $\boldsymbol{\theta}_n$ is set to $\boldsymbol{\theta}'_{n+1}$ and λ is multiplied by 0.3; otherwise, $\boldsymbol{\theta}_n$ is kept the same, λ is multiplied by 10, and a new $\boldsymbol{\theta}'_{n+1}$ is calculated. As the algorithm converges on a solution, λ tends to 0, and the model tends to the optimal estimate with errors given by

$$\hat{S} = (S_{\boldsymbol{\theta}}^{-1} + K_n^T S_{\epsilon}^{-1} K_n)^{-1}. \tag{4.6}$$

The above iterative procedure is very efficient, especially when the a priori $\boldsymbol{\theta}_0$ is relatively well-constrained; for example, in retrievals of Solar System planetary atmospheres (Irwin et al., 2008; Teanby et al., 2012; James et al., 2023). However, this is not the case in exoplanetary observations, and we often need to explore a broad parameter space. Furthermore, Optimal Estimation assumes Gaussian posteriors for model parameters, which cannot be justified in exoplanet modelling. For these reasons, this thesis does not use Optimal Estimation to perform retrievals.

4.2.2 The Markov Chain Monte Carlo Algorithm

Markov Chain Monte Carlo (MCMC) methods are a class of algorithms commonly used in Bayesian parameter estimation. These methods work by drawing a sequence of samples from the parameter space under certain constraints such that the sequence forms a Markov chain with the property that the equilibrium distribution of the chain is the desired posterior distribution. Once the chain has stabilised in the neighbourhood of the best-fit parameters, previous steps of the chain are discarded as the 'burn in' phase of the chain. Afterwards, the number of iterations the chain spends at different parameter values can be used to infer the posterior. The term 'Monte Carlo' describes a broad class of computational algorithms that obtain numerical results by repeated random sampling of the parameter space.

As an example, this section introduces the Metropolis-Hastings algorithm (Cornish & Littenberg, 2007), which is a common MCMC-type algorithm. To begin with, the chain starts at some random initial parameter vector $\boldsymbol{\theta}_0$ in the model parameter space Θ. The algorithm then finds the next position to adopt by first drawing a new parameter vector $\boldsymbol{\theta}_1$ from some proposal distribution[1] $q(\boldsymbol{\theta}_0|\boldsymbol{\theta}_1)$. The algorithm decides whether to stay put or move to $\boldsymbol{\theta}_1$ by computing the Hastings ratio (transition probability)

$$\alpha = \min\left\{1, \frac{\Pr(\boldsymbol{\theta}_1)\mathcal{L}(\boldsymbol{\theta}_1)q(\boldsymbol{\theta}_1|\boldsymbol{\theta}_0)}{\Pr(\boldsymbol{\theta}_0)\mathcal{L}(\boldsymbol{\theta}_0)q(\boldsymbol{\theta}_0|\boldsymbol{\theta}_1)}\right\}, \tag{4.7}$$

and compares α to a random number β drawn from a uniform distribution $U(0,1)$. If $\alpha > \beta$, then the chain moves to $\boldsymbol{\theta}_1$; otherwise, the chain stays put for the current step, and a new parameter vector is drawn from the proposal distribution. The algorithm repeats until some convergence criterion is met.

It is proven that an MCMC such as the one outlined above will eventually perfectly map out the posterior distribution, although its convergence can be problematic in some cases, for example, when there are strong degeneracies between model parameters, a problem commonly encountered in exoplanetary retrievals. While there are remedies for this issue, this thesis employs the Nested Sampling algorithm, which is less affected by the convergence issues. MCMC methods can also be used to evaluate the Bayesian evidence, although such endeavours are usually much more computationally demanding, whereas Nested Sampling can compute the Bayesian evidence as a by-product of evaluating the posterior distribution.

4.2.3 The Nested Sampling Algorithm

For high-dimensional parameter spaces, MCMC can be inefficient if the posterior is multimodal or has large curving degeneracies. Such degeneracies often arise when analysing low resolution spectra, as multiple gases can contribute to the opacity in a particular channel, and temperature can be degenerate with molecular abundance. The Nested Sampling algorithm is an alternative Monte Carlo algorithm that circumvents these issues (Skilling, 2006; Feroz & Hobson, 2008). It is an efficient way of evaluating the Bayesian evidence. The algorithm can also approximate the posterior with no additional computation cost, making it a convenient choice when we need to perform model comparisons in addition to parameter estimation. To start, we define the log-likelihood function as

$$\log \mathcal{L}(\boldsymbol{\theta}) = -\frac{1}{2}\sum_{i=1}^{N_{\rm obs}} \frac{(\boldsymbol{D}_i - \boldsymbol{M}(\boldsymbol{\theta})_i)^2}{\sigma_i^2}, \tag{4.8}$$

where $N_{\rm obs}$ is the total number of data points in the data vector $\boldsymbol{D}$ and σ_i is the associated measurement uncertainty. As before, $\boldsymbol{M}(\boldsymbol{\theta})$ is our model evaluated at

---

[1] Note that the proposal distribution is independent of the past history of the chain as it only depends on the current position, thus making sure that the chain is indeed Markovian.

the parameter vector $\boldsymbol{\theta}$. Recall from Equation (4.2) that the Bayesian evidence is defined by $Z = \Pr(\boldsymbol{D}|\boldsymbol{M})$, i.e., the probability of the data given a particular model. It follows that the Bayesian evidence can be written as the integral of the product of the likelihood and the prior over the model parameter space:

$$Z = \int_{\Theta} \mathcal{L}(\boldsymbol{\theta})\pi(\boldsymbol{\theta})d^n\theta, \tag{4.9}$$

where the integral is over the n-dimensional parameter space Θ, $\mathcal{L}(\boldsymbol{\theta})$ is the likelihood, and $\pi(\boldsymbol{\theta})$ is the prior. We can approximately calculate the posterior distribution and the evidence by sampling the parameter space Θ, which is a computationally expensive task for retrievals because Θ is usually high-dimensional and $\boldsymbol{M}(\boldsymbol{\theta})$ can be expensive to calculate.

The Nested Sampling algorithm (Skilling, 2006; Feroz & Hobson, 2008) calculates the evidence by first rewriting the evidence in terms of the prior volume X, defined as

$$X(\lambda) = \int_{\mathcal{L}(\boldsymbol{\theta})>\lambda} \pi(\boldsymbol{\theta})d^n\theta. \tag{4.10}$$

The evidence is then given by

$$\int_0^1 \mathcal{L}(X)dX, \tag{4.11}$$

where $\mathcal{L}(X)$ is a monotonic function and can be evaluated with simple quadrature schemes, and the likelihood contours $\mathcal{L}(X_i)$ are approximated by sampling the parameter space within nested ellipsoids. Numerically, the evidence is given by

$$Z \approx \sum_{i=1}^{N_{\text{iter}}} \mathcal{L}(X_i)w_i, \tag{4.12}$$

where $X_i \in [0, 1]$ is a decreasing sequence of quadrature points (starting from 1) and w_i the corresponding weights, and N_{iter} is determined by some convergence criterion. The Nested Sampling algorithm discards the point with the lowest likelihood at each iteration, so the posterior can be generated by assigning weights to those points by

$$p_i = \frac{\mathcal{L}(X_i)w_i}{Z}. \tag{4.13}$$

The retrievals in this thesis use the Python interface PyMultiNest (Buchner et al., 2014) to implement the Nested Sampling algorithm of Feroz & Hobson (2008) with 1000 sampling live points, which is standard in the retrievals of exoplanetary spectra (e.g., Bell et al., 2024).

p-value	B	ln B	sigma	Interpretation
0.05	2.5	0.9	2.0	
0.04	2.9	1.0	2.1	weak detection at best
0.01	8.0	2.1	2.6	
0.006	12	2.5	2.7	moderate detection at best
0.003	21	3.0	3.0	
0.001	53	4.0	3.3	
0.0003	150	5.0	3.6	strong detection at best
6×10^{-7}	43000	11	5.0	

Table 4.1: Translation from Bayes factor to detection significance from Trotta (2008).

4.3 Bayesian Model Comparison

When several models could potentially explain the observed data, Bayesian model comparison can help identify the model most favoured by the data. This thesis uses the Bayes factor to compare two competing models. The Bayes factor is the ratio of the Bayesian evidence of two competing models and can be used to quantify the support for one model over the other (Morey et al., 2016). Recall that the Bayesian evidence for a model M with a N dimensional parameter space Θ is given by

$$\mathcal{Z}_M(\boldsymbol{D}) = \mathcal{P}(\boldsymbol{D}|\boldsymbol{M}) = \int_\Theta \pi(\theta|\boldsymbol{M})\mathcal{L}(\boldsymbol{D}|\boldsymbol{M},\boldsymbol{\theta})d^N\theta, \tag{4.14}$$

where π is the prior and $\mathcal{L}$ is the likelihood, as defined in Section 4.1. The Bayes factor of two models, M_0 and M_1, are simply given by

$$B_{M_1,M_0}(\boldsymbol{D}) = \frac{Z_{M_1}}{Z_{M_0}}. \tag{4.15}$$

The numerical value of $B_{M_1,M_0}(\boldsymbol{D})$ can then be used to compare two models: if Z_{M_1} is greater than Z_{M_0}, then Z_{M_1} is favoured over Z_{M_0}. The larger the Bayes factor, the more favoured Z_{M_0} is.

This thesis uses Bayesian model comparison to evaluate the detection significance of a molecule, following Trotta (2008) and Benneke & Seager (2013). As an example, suppose that a model M_A contains the molecule CO and is being used to fit the data, and we want to find the detection significance of CO. Let us define a new model M_B, which is identical to M_A except that M_B does not include CO. The next step is to calculate the Bayesian evidence of M_B (the model without CO) and the Bayesian evidence of M_A (the model with CO). We treat M_B as the 'null' model, and M_A as the more complex alternative model, and define the Bayes factor B as

$$B = \frac{Z_{M_A}}{Z_{M_B}}, \tag{4.16}$$

which is simply the evidence ratio of M_A and M_B. Finally, B can be related to the significance of the detection with the following steps. The Bayes factor is related to the p-value (Sellke et al., 2001) by

$$B \leq -\frac{1}{e \cdot p \cdot \ln p}, \tag{4.17}$$

where p denotes the p-value. Then, the significance is related to the p-value by the following equation

$$p = 1 - \mathrm{erf}\left(\frac{n_\sigma}{\sqrt{2}}\right), \tag{4.18}$$

where erf is the error function. Table 4.1 lists a correspondence between the Bayes factor and detection significance. Note that the conversion of Bayesian evidence is only valid if the models are nested, which is the case in this thesis as it is used to ascertain the significance of molecular detections: the model with an additional molecule nests the model without the additional molecule.

Chapter 5

Testing 2D Temperature Models with *HST* and *Spitzer* Phase Curves of WASP-43b

Contents of this chapter have been published in Monthly Notices of the Royal Astronomical Society under Yang et al. (2023).

Chapters 2, 3, and 4 introduce the tools with which we can retrieve information from phase-resolved emission spectra of hot Jupiters. The following chapters apply those tools to characterise the atmospheres of the hot Jupiter WASP-43b. This chapter first tests several 2D temperature models using synthetic data of two instruments: (1) the Wide Field Camera 3 (WFC3) onboard the Hubble Space Telescope (*HST*) and (2) the InfraRed Array Camera (IRAC) onboard the Spitzer Space Telescope (*Spitzer*). This chapter then performs atmospheric retrievals on real *HST*/WFC3 + *Spitzer*/IRAC data.

As discussed in Chapter 4, it is necessary to construct appropriate parametric atmospheric models to retrieve information from observations. Suppose we want to analyse emission spectra at several orbital phases simultaneously. In that case, the atmospheric models must describe the whole observable atmosphere to generate disc-averaged emission spectra at multiple orbital phases. In other words, we need multidimensional temperature models that capture the longitudinal variation of thermal structure in the pressure ranges probed by emission spectroscopy. The models should also contain as few parameters as possible to ensure parameter estimation can be done in a reasonable time and to avoid overfitting.

There are two main approaches to constructing multidimensional parametric temperature models in atmospheric retrieval studies. The first approach is to split the atmosphere into disjoint regions, with the thermal structure in each region modelled with a one-dimensional TP model. For example, Feng et al. (2020) split the atmosphere into a dayside and a nightside, whereas Changeat et al. (2021) further modelled an additional hot spot within the dayside, and Irwin et al. (2020) divided the atmosphere into meridian bands with linearly interpolated temperature maps between the band centres. A variation of this approach is given in Taylor et al. (2020), where the atmosphere is split into a dominant hot region and a negligible cold region using a dilution parameter (see also Chapter 7.2.1). The second approach is to construct highly-simplified three-dimensional analytical atmospheric models. For example, Dobbs-Dixon & Blecic (2022) proposed a 3D model by separating the radiative and the convective components in Global Circulation Model (GCM) outputs, whereas Chubb & Min (2022) prescribed a 3D model by restricting heat transfer to diffusion and zonal winds.

This chapter applies the Yang et al. (2023) 2D Temperature Model (introduced in Section 3.2) to retrieve chemical abundance and thermal structure from phase curves[1] of hot Jupiters. In this model, the temperature is a function of pressure and longitude, representing a latitudinally-averaged temperature profile. The model is split into a dayside and a nightside: on the dayside, the temperature varies with $\cos^n(\text{longitude}/\epsilon)$ on isobars, where n and ϵ are free parameters, and on the nightside, the temperature is constant on isobars. This chapter uses this scheme, together with several other simpler 2D retrieval schemes for comparison, to retrieve molecular abundance and latitudinally-averaged thermal structure from phase curves of WASP-43b observed with *HST*/WFC3 and *Spitzer*/IRAC. This chapter first tests the performance of the various 2D schemes by retrieving atmospheric properties from synthetic phase curves generated from a GCM of WASP-43b, where the 'ground truth' is known, so we can assess the accuracy of the retrieved properties. This chapter then applies the 2D schemes to the observed *HST*/WFC3 and *Spitzer*/IRAC phase curves of WASP-43b. This chapter also compares the 2D approach to the phase-by-phase approach, where the spectrum at each orbital phase is analysed separately, in Section 5.6.2.

This chapter is structured as follows. Section 5.1 presents the *HST*/WFC3 + *Spitzer*/IRAC data set. Section 5.2 describes the methodology of the retrievals, including the routine for simulating spectroscopic phase curves, the 2D temperature models, and the retrieval setup. Section 5.3 demonstrates that simplified atmospheric models can reproduce the synthetic data generated from a GCM. Section 5.4 presents

---

[1] The term 'phase curves' in this thesis refers to spectroscopic phase curves unless otherwise stated, and is used interchangeably with 'phase-resolved emission spectra', as this thesis only works with the phase-resolved emission spectra derived from the phase curve observations.

the mock retrieval results on synthetic GCM phase curves using the 2D temperature models, followed by application to the observed phase curves in Section 5.5. Section 5.6 discusses the implications of the retrieval results and compares them with past studies. Section 5.7 ends the chapter with a summary.

5.1 The *HST*/WFC3 + *Spitzer*/IRAC Observation

The observed data set of WASP-43b analysed in this chapter is taken from Table 5 of Stevenson et al. (2017). The data set consists of observations from two different instruments: the Wide Field Camera 3 (WFC3) onboard the Hubble Space Telescope (*HST*) and the InfraRed Array Camera (IRAC) onboard the Spitzer Space Telescope (*Spitzer*).

The *HST*/WFC3 observation (Program GO-13467, PI: Jacob Bean, see Stevenson et al., 2014) was taken with the G141 grism (1.1 to 1.7 μm) in the bidirectional spatial scan mode from 4 to 7 November 2013. The phase-resolved emission spectra derived from the observation were binned into 15 0.035-μm-wide channels, as described in Stevenson et al. (2014). The *Spitzer*/IRAC observation (Programs 10169 and 11001, PI: Kevin Stevenson, see Stevenson et al., 2017) was taken using the subarray mode with two-second frame times (Fazio et al., 2004) and used two broadband channels at 3.6 μm and 4.5 μm. The 3.6 μm observation was taken over 7-8 March 2015, whereas the 4.5 μm observation was taken on two separate visits: visit one over 7-8 March 2015 and visit two over 4-5 September 2015.

The data reduction procedures used to derive phase-resolved emission spectra from the *HST*/WFC3 observation and the *Spitzer*/IRAC observation are described in Stevenson et al. (2014) and Stevenson et al. (2017), respectively. This chapter works directly on the phase-resolved emission spectra presented in Stevenson et al. (2017), as shown in Table 5.1. The phase-resolved emission spectra contain 17 wavelength channels in total at 15 different orbital phases, made up of the 15 *HST*/WFC3 channels and the two *Spitzer*/IRAC broad channels.

5.2 Methodology

The primary aim of this chapter is to assess the performance of the Yang et al. (2023) 2D temperature model in retrieving atmospheric properties from low-resolution spectroscopic phase curves, which is also referred to as Model 4 in this chapter. This

Orbital Phase	1.1425 (μm)	1.1775 (μm)	1.2125 (μm)	1.2475 (μm)	1.2825 (μm)	1.3175 (μm)	1.3525 (μm)	1.3875 (μm)	1.4225 (μm)	1.4575 (μm)	1.4925 (μm)	1.4275 (μm)	1.5625 (μm)	1.5975 (μm)	1.6325 (μm)	3.6 (μm)	4.5 (μm)
0.0625	60(66)	55(61)	66(58)	86(56)	53(57)	90(53)	2(55)	29(52)	35(56)	-3(56)	24(56)	-3(55)	22(58)	48(58)	87(63)	-13(103)	95(133)
0.125	103(67)	105(61)	125(59)	154(56)	92(57)	144(53)	19(55)	74(52)	71(56)	33(56)	74(56)	50(55)	91(58)	116(58)	167(63)	235(105)	524(133)
0.1875	161(71)	176(65)	201(62)	242(60)	158(61)	219(57)	60(58)	132(55)	124(60)	95(59)	149(59)	129(58)	195(62)	218(61)	283(67)	735(103)	1302(136)
0.25	224(63)	253(58)	278(55)	330(53)	235(54)	298(50)	117(52)	192(48)	181(53)	169(53)	233(52)	221(52)	309(55)	331(54)	413(60)	1458(103)	2242(134)
0.3125	283(69)	326(64)	347(61)	407(59)	314(59)	373(56)	183(57)	247(54)	236(59)	246(58)	315(58)	311(57)	422(61)	443(60)	539(66)	2245(100)	3145(119)
0.375	329(66)	383(61)	396(58)	464(56)	384(57)	433(53)	249(55)	288(51)	281(56)	315(55)	383(55)	388(55)	515(58)	536(57)	644(63)	2909(79)	3768(103)
0.4375	355(59)	417(53)	419(52)	491(49)	433(50)	467(47)	303(48)	309(44)	309(49)	364(49)	426(48)	439(48)	575(51)	595(51)	708(56)	3281(77)	4000(103)
0.5	367(45)	431(39)	414(38)	482(36)	460(37)	473(33)	353(34)	313(30)	320(36)	394(36)	439(33)	458(35)	595(36)	614(37)	732(42)	3231(60)	3827(84)
0.5625	335(61)	399(55)	375(53)	441(51)	445(52)	444(48)	349(50)	280(46)	298(51)	379(51)	420(50)	437(50)	563(52)	583(52)	691(58)	2881(80)	3389(103)
0.625	293(65)	349(59)	316(57)	373(55)	405(55)	391(52)	335(53)	236(50)	262(55)	343(54)	370(54)	384(53)	493(56)	514(56)	610(61)	2285(121)	2799(109)
0.6875	237(71)	281(65)	242(63)	289(61)	342(61)	317(57)	295(59)	179(56)	211(60)	283(59)	298(60)	307(59)	393(62)	415(62)	497(67)	1625(103)	2204(133)
0.75	174(66)	204(61)	164(58)	200(56)	266(57)	238(53)	237(55)	119(51)	154(56)	209(55)	214(55)	215(55)	278(58)	301(57)	368(63)	1054(103)	1640(134)
0.8125	115(68)	131(63)	96(60)	121(58)	186(58)	162(55)	171(56)	64(53)	99(57)	132(57)	131(57)	124(56)	165(59)	189(59)	242(64)	617(103)	1126(134)
0.875	67(63)	71(57)	45(55)	63(52)	114(53)	100(50)	103(51)	22(48)	52(53)	61(52)	61(52)	45(51)	68(54)	94(54)	135(59)	299(103)	645(133)
0.9375	41(70)	36(64)	22(62)	37(59)	66(60)	67(56)	47(58)	1(55)	25(59)	12(58)	17(59)	-5(58)	9(61)	36(61)	70(66)	83(103)	247(133)

Table 5.1: Phase-resolved emission spectra of WASP-43b observed with *HST*/WFC3 and *Spitzer*/IRAC as published in Stevenson et al. (2017). The first row from the top denotes the wavelength channels, and the first column from the left denotes the orbital phases. Fluxes are given as planet-to-star flux ratios and expressed as parts per million (ppm), whereas the values within the parentheses represent uncertainties. This table is the same as Table 5 in Stevenson et al. (2017).

Molecule	VMR	Opacity Data
H_2O	4.8×10^{-4}	Barber et al. (2006)
CO_2	7.4×10^{-8}	Tashkun & Perevalov (2011)
CO	4.6×10^{-4}	Rothman et al. (2010)
CH_4	1.3×10^{-7}	Yurchenko & Tennyson (2014)
He	0.162	Borysow & Frommhold (1989) & Borysow et al. (1989)
H_2	0.837	Borysow & Frommhold (1989) & Borysow et al. (1989)

Table 5.2: Gas volume mixing ratios (VMRs) and opacity data used to simulate synthetic phase curves. The VMRs are uniform with longitude, latitude, and altitude. The coefficients from Borysow & Frommhold (1989) and Borysow et al. (1989) are used for H_2-H_2 and H_2-He collision-induced absorption opacity.

chapter also tests three simpler models (Models 1, 2, and 3 in Section 5.2.3) for comparison. In addition to the real phase curve observation of WASP-43b presented in Section 5.1, this chapter also uses synthetic phase curves of the same resolution simulated from a GCM-based model to perform mock retrievals. Section 5.2.1 describes the GCM used to simulate the synthetic phase curves, Section 5.2.2 describes the procedure for calculating disc-averaged spectra, Section 5.2.3 describes the 2D atmospheric temperature models, and Section 5.2.4 describes the retrieval setup.

5.2.1 GCM Data

This chapter uses a GCM of WASP-43b to simulate synthetic phase curves, which are then used to validate retrieval schemes with different 2D temperature models in mock retrievals. We can directly assess the performance of the retrieval schemes by comparing the atmospheric properties retrieved from the synthetic data with the input GCM data. The GCM selected is a cloud-free solar metallicity model calculated using SPARC/MITgcm (Showman et al., 2009) based on the set-up of Parmentier et al. (2016) and was used for validating the 2.5D retrieval scheme by Irwin et al. (2020). The temperature as a function of longitude and latitude at three pressure levels of the GCM is shown in Figure 5.1, and the transmission weighting function at the substellar point of the GCM as a function of pressure and wavelength channel number is shown in Figure 5.2.

The GCM atmosphere is H_2/He-dominated and contains four spectrally active gas species: H_2O, CO, CO_2 and CH_4, which are expected to be the dominant opacity sources in the atmosphere of WASP-43b in the observed wavelengths. The chemical abundance in the GCM is initially set according to chemical equilibrium, resulting

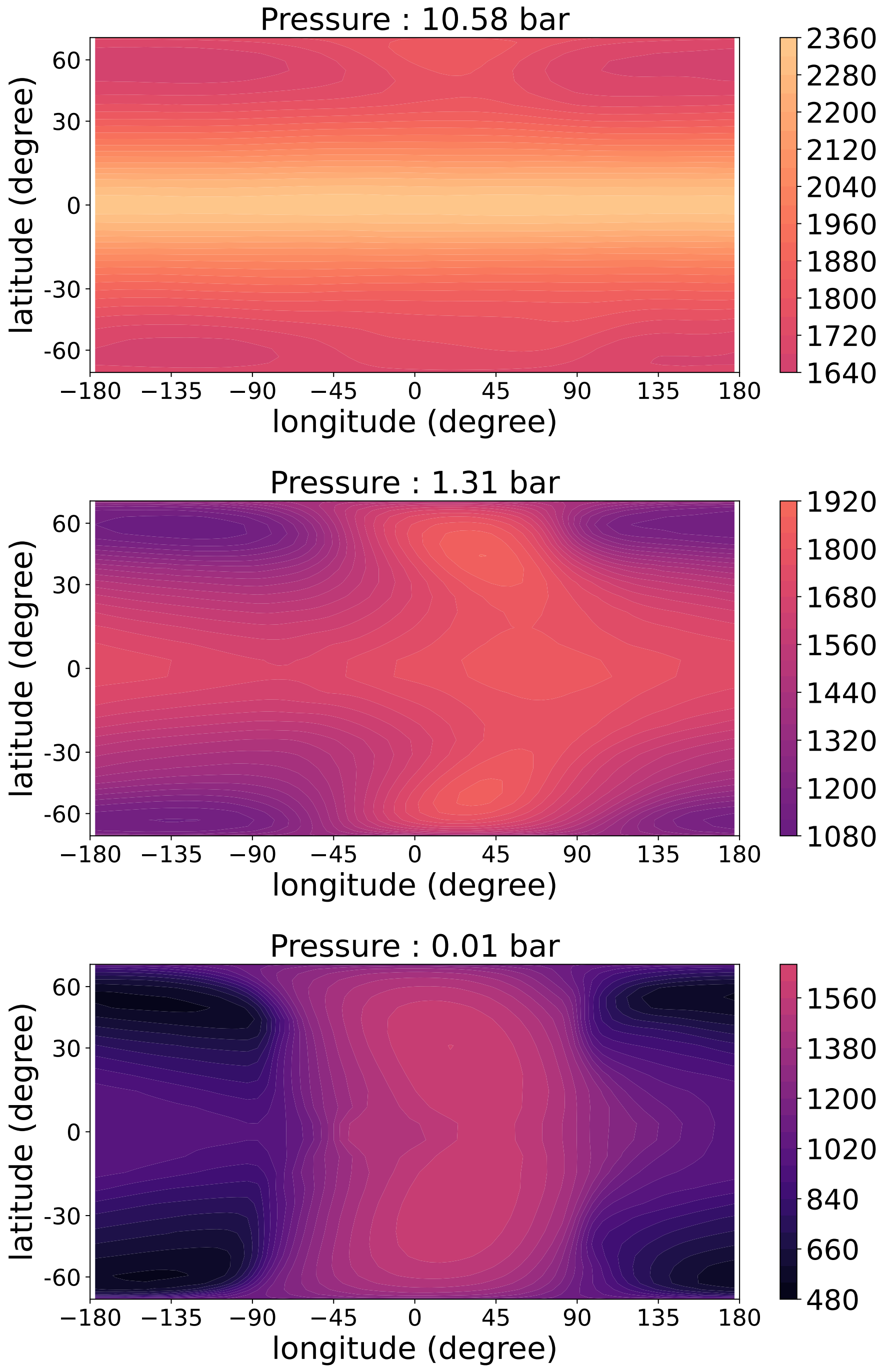

Figure 5.1: Temperature (Kelvin) as a function of longitude and latitude at three pressure levels in the WASP-43b GCM. The super-rotating equatorial jet is clearly visible and shifts the 'hot spot' eastward of the substellar point (where the star would be perceived to be directly overhead). Note that the substellar point is set at 0° longitude. Such jet-like features would cause the phase curve amplitudes to peak before secondary eclipses. Note that the latitudinal distance is weighted by cos(latitude) to mimic the effect that polar latitudes would appear foreshortened to us because we observe WASP-43b from above the equator.

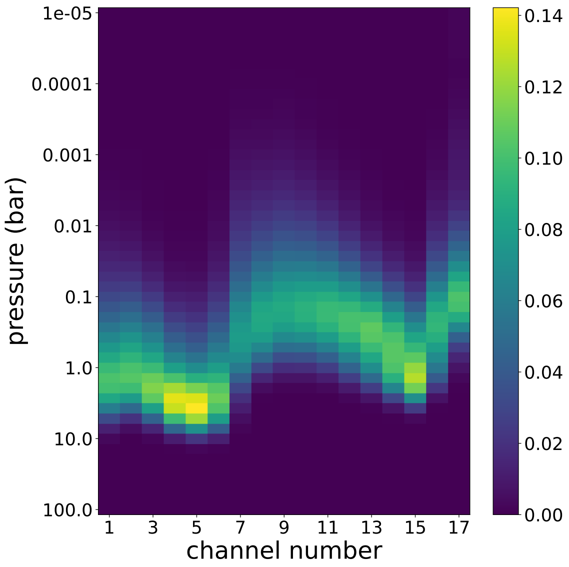

Figure 5.2: Transmission weighting function of the WASP-43b GCM atmosphere at the substellar point as a function of pressure and wavelength channel. The first 15 *HST*/WFC3 channels are in equally spaced bins of width 0.035 μm spanning the wavelength range 1.1425-1.6325 μm, and the last two *Spitzer*/IRAC broad channels are centred at 3.6 and 4.5 μm, respectively.

in significant variation in CH_4 abundance from dayside to nightside in the photospheric pressures. However, disequilibrium chemistry processes such as horizontal quenching are expected to smooth out such inhomogeneity (Cooper & Showman, 2006; Agúndez et al., 2014). Hence, the abundance of all molecules at all location is reset to be the latitudinally-averaged abundances in the 0.1 to 1-bar pressure region (using cos(latitude) as the weight) at the sub-stellar meridian at the end of the GCM run, following Irwin et al. (2020). This model is then used to simulate the synthetic data. By resetting the chemical abundance to uniform values, this chapter isolates the effect of temperature parameterisation in retrievals. The volume mixing ratios (VMRs) in the GCM-based model are presented in Table 5.2.

In summary, the synthetic phase curves are generated from the thermal structure of the GCM and assuming the uniform chemical abundance listed in Table 5.2. The chemical abundance and thermal structure of this GCM-based model are seen as the 'ground-truths' for the mock retrievals in Section 5.4.

5.2.2 Radiative Transfer Calculation

As in the rest of this thesis, the emission spectra in this chapter are calculated using the NEMESISPY software (Yang et al., 2024a) described in Section 2.5, which

Parameter	Value	Reference
$T_{\rm star}$	4500 K	Gillon et al. (2012)
$R_{\rm star}$	0.667 $R_{\rm Sun}$	Gillon et al. (2012)
$[\rm Fe/H]_{\rm star}$	-0.01 dex	Gillon et al. (2012)
a	0.0153 AU	Gillon et al. (2012)
$M_{\rm plt}$	2.034 $M_{\rm Jup}$	Gillon et al. (2012)
$R_{\rm plt}$	1.036 $R_{\rm Jup}$	Gillon et al. (2012)

Table 5.3: WASP-43b stellar and planetary parameters used in this chapter.

employs the correlated-k method (Lacis & Oinas, 1991; Irwin et al., 2008) and the disc-integration scheme of Irwin et al. (2020) to calculate disc-integrated emission spectra. This chapter uses k-distribution look-up tables ('k-tables') with $N_g = 20$ (see Section 2.3) generated from the spectral line data summarised in Table 5.2. To speed up calculations, this chapter uses channel-averaged k-tables for the 15 channels of *HST*/WFC3 and the two channels of *Spitzer*/IRAC, following Irwin et al. (2020). As found in Irwin et al. (2020), such an approach produces an excellent approximation, resulting in residuals much less than typical measurement uncertainties. Apart from the above molecular opacity, the radiative transfer calculation additionally includes collision-induced absorption of H_2-H_2 pairs and H_2-He pairs using the coefficients of Borysow & Frommhold (1989) and Borysow et al. (1989). To convert the calculated emission spectra to the planet-to-star flux ratios, this chapter uses a stellar spectrum from the Kurucz ATLAS model atmospheres (Castelli & Kurucz, 2004) interpolated to the WASP-43 stellar parameters from Gillon et al. (2012) as listed in Table 5.3, following Irwin et al. (2020).

Note that the setup of the radiative transfer calculation in this chapter, which follows that of Irwin et al. (2020), is slightly different from the setup of Chapters 6, 7, and 8. Firstly, the stellar spectrum used Chapters 6, 7, and 8 is a PHOENIX stellar model (Allard & Hauschildt, 1995; Hauschildt et al., 1999; Husser et al., 2013), generated assuming an effective temperature of 4300 K. The updating of the stellar spectrum is informed by the work of Bell et al. (2024) published after the work in this chapter. Secondly, the opacity data used for Chapters 6, 7, and 8 are all taken from the ExoMol database (Chubb et al., 2021), while the opacity data used in this chapter are the same as those used in Irwin et al. (2020) and are listed in Table 5.2. However, the differences between the two stellar spectra and the two sets of opacity data are insignificant for the spectral resolution and photometric precision of the spectra analysed in this chapter. Reassuringly, the abundance constraints on H_2O retrieved in this chapter agree well with those retrieved in Chapters 6, 7, and 8.

5.2.3 2D Models

This section describes four parametric temperature models for the atmospheres of hot Jupiters. Model 4 is the Yang et al. (2023) 2D temperature model introduced in Section 3.2 and is seen as the fiducial model. The other three simpler models are included for comparison. All 2D models in this chapter use the one-dimensional analytical TP profile of Guillot (2010) introduced in Section 3.1.1 to describe temperature as a function of pressure[2]. For ease of reference, the Guillot (2010) TP profile is given again:

$$T^4 = \frac{3T_{\rm int}^4}{4}\Big(\frac{2}{3}+\tau\Big) + \frac{3T_{\rm irr}^4}{4} f\Big[\frac{2}{3} + \frac{1}{\gamma\sqrt{3}} + \Big(\frac{\gamma}{\sqrt{3}} - \frac{1}{\gamma\sqrt{3}}\Big)\mathrm{e}^{-\gamma\tau\sqrt{3}}\Big], \tag{5.1}$$

where the infrared optical depth τ is related the pressure P by

$$\tau(P) = \frac{\kappa_{\rm th} P}{g}. \tag{5.2}$$

All 2D models place the sub-stellar point at the origin in the longitude-latitude coordinate system. All 2D models describe the thermal structure with two TP profiles: a representative dayside profile and a representative nightside profile. Note that temperature is set to be uniform as a function of latitude on isobars, and the retrieved temperature profiles are treated as latitudinally-averaged temperature profiles. In these models, the centres of 'dayside' and the 'nightside' can shift away from the substellar point and the anti-stellar point, respectively.

5.2.3.1 Model 1

Model 1 (Figure 5.3, top panel) is the simplest model. The dayside and nightside are set to span 180° in longitude. The centre of the dayside region (O') is allowed to shift eastward or westward by some longitude δ relative to the substellar point (O), representing the effect of atmospheric dynamics (for example, equatorial jets) on redistributing heat around the atmosphere. The dayside is thus bound by the meridians $\Lambda = \delta - 90°$ and $\Lambda = \delta + 90°$. Within each region, temperature is only a function of pressure. Note that in all the temperature models in this chapter, the 'dayside' denotes the region of the atmosphere modelled by the dayside TP profile and does not necessarily coincide with the physically illuminated dayside. The temperature model alone contains 9 parameters: 4 parameters for each of the two TP profiles

---

[2] These 2D models can also be easily interfaced with other 1D parametric TP profiles.

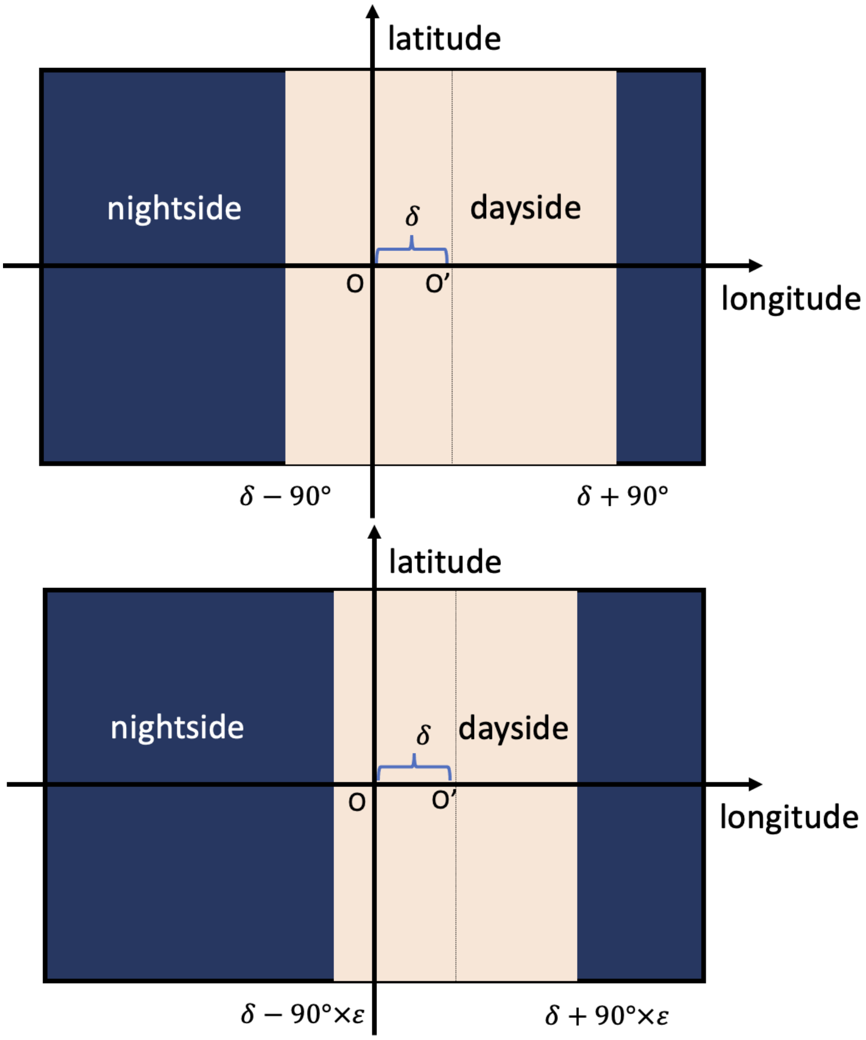

Figure 5.3: Schematics of Model 1 and Model 2. Model 1 (top panel) is defined by Equation (5.3) and divides the atmosphere into a dayside and a nightside. Each region is then modelled with a single representative TP profile. The dayside central longitude δ is allowed to vary, and the dayside width (longitudinal extent) is fixed to be 180°. Model 2 (bottom panel) is defined by Equation (5.4) and generalises Model 1 by allowing the dayside width to vary, which now spans $180^\circ \times \varepsilon$ in longitude.

and 1 parameter δ for the longitudinal offset. Model 1 is equivalent to the '2TP-Crescent' approach of Feng et al. (2020) when applied to all phases simultaneously. Mathematically, Model 1 is given by the following equation:

$$T = \begin{cases} T_{\text{night}}(P) & \text{if } \Lambda > \delta + 90^\circ \text{ or } \Lambda < \delta - 90^\circ, \\ T_{\text{day}}(P) & \text{otherwise.} \end{cases} \tag{5.3}$$

5.2.3.2 Model 2

Model 2 (Figure 5.3, lower panel) is similar to Model 1, with the only difference being that the 'width' (longitudinal extent) of the dayside is now a free parameter. Model 2 contains a scaling parameter ε, so that the dayside is now bounded by the meridians $\Lambda = \delta - 90^\circ \times \varepsilon$ and $\Lambda = \delta + 90^\circ \times \varepsilon$ and spans $180^\circ \times \varepsilon$ in longitude. The temperature model alone contains 10 parameters: 4 parameters for each TP profile, 1 parameter δ for the longitudinal offset, and 1 parameter ε for the dayside width. Parameterising the dayside area fraction has been shown to be effective in analysing disc-averaged emission spectrum of tidally-locked hot Jupiters by Taylor et al. (2020), and this approach has been applied to phase curve analysis by Feng et al. (2020) in their '2TP-Free' model, albeit only in the phase-by-phase approach. Model 2 is a way of implementing the dayside area fraction parameterisation self-consistently when fitting all phases of phase curves simultaneously. Mathematically, Model 2 is given by the equation:

$$T = \begin{cases} T_{\text{night}}(P) & \text{if } \Lambda > \delta + 90^\circ \times \varepsilon \text{ or } \Lambda < \delta - 90^\circ \times \varepsilon, \\ T_{\text{day}}(P) & \text{otherwise.} \end{cases} \tag{5.4}$$

5.2.3.3 Model 3

Model 3 (Figure 5.4, upper panel) is an extension of Model 2, where the temperature is now a continuous function of longitude across the dayside boundary. The dayside is bound by the meridians $\Lambda = \delta - 90^\circ \times \varepsilon$ and $\Lambda = \delta + 90^\circ \times \varepsilon$. Within the dayside, temperatures at each pressure level vary with the cosine of longitude. The TP is set to be a single nightside profile outside the dayside. The temperature model alone contains 10 parameters: 4 parameters for each of the dayside/nightside TP profiles, 1 parameter δ for the longitudinal offset, and 1 parameter ε for the dayside width. Mathematically, Model 3 is given by the equation:

$$T = \begin{cases} T_{\text{night}}(P) \text{ if } \Lambda > \delta + 90^\circ \times \varepsilon \text{ or } \Lambda < \delta - 90^\circ \times \varepsilon, \\ T_{\text{night}}(P) + (T_{\text{day}}(P) - T_{\text{night}}(P)) \cos(\frac{\Lambda-\delta}{\varepsilon}) \text{ otherwise.} \end{cases} \tag{5.5}$$

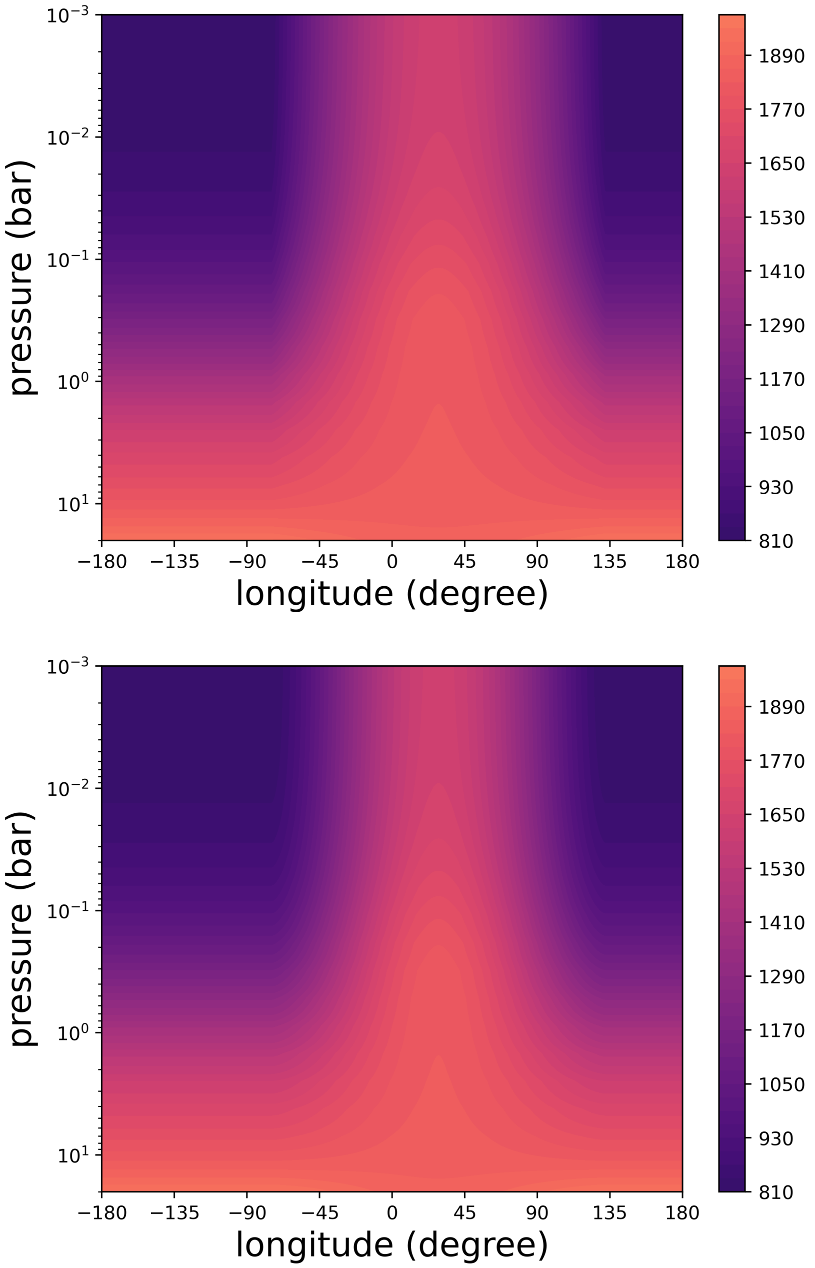

Figure 5.4: Temperature as a function of pressure and longitude in two examples of Model 3 and Model 4. Model 3 (top panel) is defined by Equation (5.5). Model 4 (bottom panel) is defined by Equation (5.6); in this example, n is set to be 1.75. Note that Model 4 is equivalent to Model 3 if n is set to 1.

Parameter	Description	Model Usage	Range
δ	Dayside longitudinal offset	all	[-45°,45°]
ε	Dayside longitudinal width scaling	2,3,4	[0.5,1.2]
n	Dayside longitudinal variation exponent	4	[0,2]
$\log \kappa_{\mathrm{th,day}}$	Mean infrared opacity (dayside)	all	[-4,2]
$\log \gamma_{\mathrm{day}}$	Ratio of visible and infrared opacities (dayside)	all	[-4,1]
$\log f_{\mathrm{day}}$	Heat redistribution parameter (dayside)	all	[-4,1]
$\mathrm{T}_{\mathrm{int,day}}$	Internal heat flux (dayside)	all	[100,1000]
$\log \kappa_{\mathrm{th,nigtht}}$	Mean infrared opacity (nightside)	all	[-4,2]
$\log \gamma_{\mathrm{night}}$	Ratio of visible and infrared opacities (nightside)	all	[-4,1]
$\log f_{\mathrm{night}}$	Heat redistribution parameter (nightside)	all	[-4,1]
$\mathrm{T}_{\mathrm{int,night}}$	Internal heat flux (nightside)	all	[100,1000]
$\log \mathrm{VMR}_{\mathrm{H_2O}}$	Log_{10} volume mixing ratio of $\mathrm{H_2O}$	all	[-8,-2]
$\log \mathrm{VMR}_{\mathrm{CO_2}}$	Log_{10} volume mixing ratio of $\mathrm{CO_2}$	all	[-8,-2]
$\log \mathrm{VMR}_{\mathrm{CO}}$	Log_{10} volume mixing ratio of CO	all	[-8,-2]
$\log \mathrm{VMR}_{\mathrm{CH_4}}$	Log_{10} volume mixing ratio of $\mathrm{CH_4}$	all	[-8,-2]

Table 5.4: Parameters of our atmospheric models. All models have 4 parameters for gas VMRs, with the other parameters specifying the thermal structure. Model 1 has 13 parameters in total, whereas Model 2 and Model 3 have 14 parameters in total. Model 4 has 15 parameters in total.

5.2.3.4 Model 4

Model 4 is the Yang et al. (2023) 2D temperature model introduced in Section 3.2. It is a generalisation of Model 3, where the exponent of the cosine term in Equation (5.5) is a variable so that we parametrise how strongly temperatures vary with longitude on isobars:

$$T = \begin{cases} T_{\mathrm{night}}(P) \text{ if } \Lambda > \delta + 90^\circ \times \varepsilon \text{ or } \Lambda < \delta - 90^\circ \times \varepsilon, \\ T_{\mathrm{night}}(P) + (T_{\mathrm{day}}(P) - T_{\mathrm{night}}(P)) \cos^n(\frac{\Lambda - \delta}{\varepsilon}) \text{ otherwise.} \end{cases} \tag{5.6}$$

The temperature model alone contains 11 parameters: 4 parameters for each of the dayside/nightside TP profiles, 1 parameter δ for the longitudinal offset, 1 parameter ε for the dayside width, and 1 parameter n to parametrise the variation of temperature with longitude on the dayside. The parameters for the temperature models, together with the other parameters of the atmospheric models, are summarised in Table 5.4.

5.2.4 Retrieval Setup

This chapter performs atmospheric retrievals on two sets of data: (1) synthetic *HST*/WFC3 and *Spitzer*/IRAC phase curves simulated from the GCM-based model described in Section 5.2.1, and (2) observed *HST*/WFC3 and *Spitzer*/IRAC phase curves of WASP-43b as presented in Stevenson et al. (2017). For each set of data, four retrievals are performed using each of the atmospheric models described in Section 5.2.3. The retrievals fit the spectra at all phases simultaneously using spectra generated from the parametric atmospheric models. The retrievals use Nested Sampling (Feroz & Hobson, 2008) to calculate the posterior distribution of the atmospheric model parameters and the Bayesian evidence of the model, following the procedure described in Chapter 4. Section 5.6.2 compare the retrieval results to the phase-by-phase retrieval approach, where the spectrum at each orbital phase is analysed independently.

In all retrievals, the atmospheric model is defined from 20 to 10^{-3} bar, on 20 points equally spaced in log pressure. The atmospheric models have two components: a temperature model and a chemical abundance model. In each of the retrieval schemes, a different temperature model described in Section 5.2.3 is used. On the other hand, all of the retrieval schemes share the same chemical abundance model, which assumes a H_2/He-dominated atmosphere and contains four spectrally active gases: H_2O, CO_2, CO, CH_4. The abundance model is parametrised by the volume mixing ratios (VMRs) of the spectrally active gases, assumed to be constant with respect to pressure, longitude and latitude. Furthermore, none of the models include clouds/hazes, and it is assumed that aerosols with no significant spectral features to be degenerate with the other components of the atmospheric models. The model parameters and their prior ranges are listed in Table 5.4, and uniform priors are prescribed for all of the model parameters.

5.3 Preliminary Tests

Before testing retrieval schemes on synthetic *HST*/WFC3 and *Spitzer*/IRAC phase curves, this section investigates if simplified atmospheric models can reproduce the phase curves generated from the more complex GCM described in Section 5.2.1. This section will show that we can reproduce these GCM phase curves well within realistic measurement uncertainties if: (1) the TP profiles in the GCM at all locations are replaced with best-fit 1D Guillot profiles; (2) the TP profiles in the GCM on the same meridian are replaced with the latitudinally-averaged TP profile of that meridian; and (3) the volume mixing ratios of all gases are replaced with a uniform profile. These results justify the use of 2D models coupled with the Guillot profile in the retrievals. Indeed, Section 5.4 later shows that such 2D models can adequately model synthetic *HST*/WFC3 and *Spitzer*/IRAC phase curves.

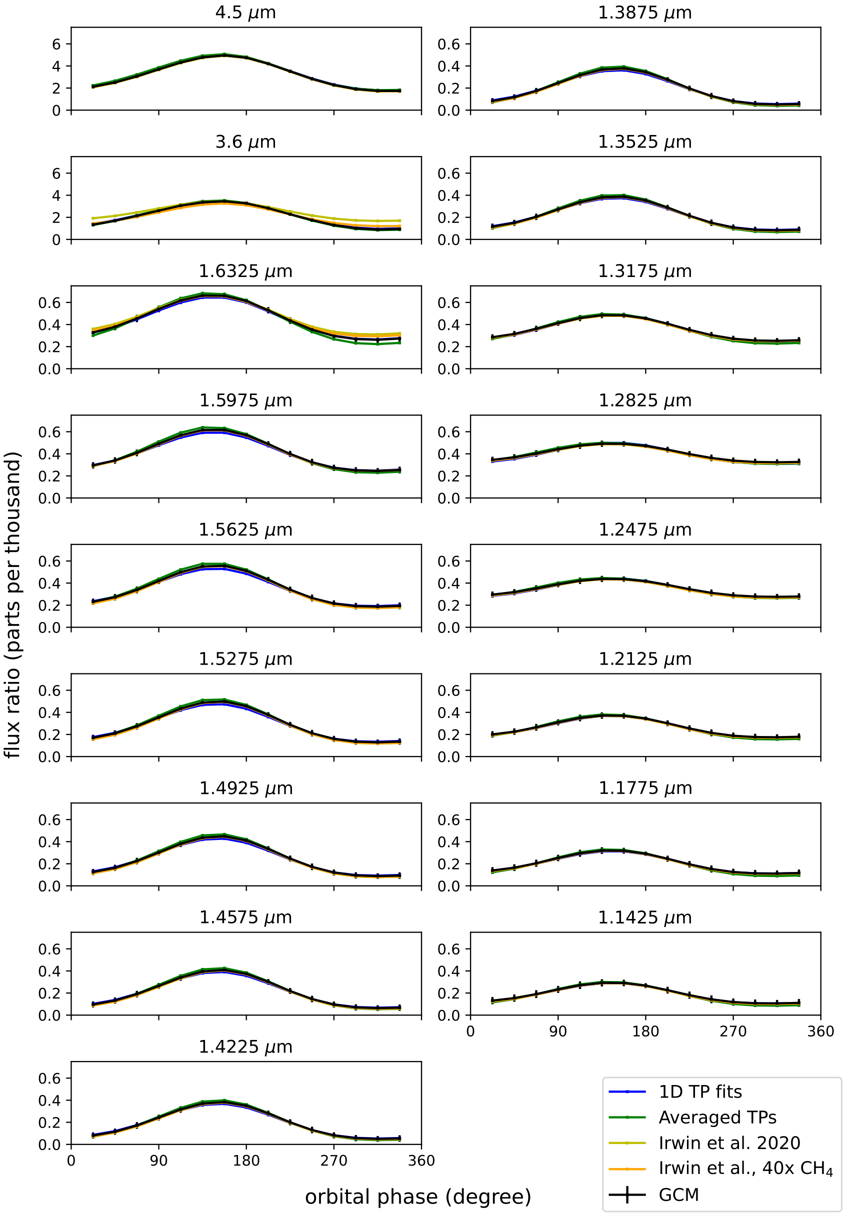

Figure 5.5: Comparison of the phase curves calculated from simplified models to the phase curves calculated from the original WASP-43b GCM (black), where abundance is set by chemical equilibrium. The blue curves are simulated from the best-fit Guillot profiles. The green curves are simulated from latitudinally-averaged TP profiles from 0° to 45°, using cos(latitude) as the weight. The yellow curves are simulated with uniform abundance listed in Table 5.2, which are the synthetic data we retrieve on in Section 5.4. The orange curves are simulated with the abundance listed in Table 5.2, but with the methane abundance multiplied by 40, which illustrates the fact that models with uniform gas abundance can match the phase curves produced from a chemical equilibrium model. Note that the error bars on the GCM phase curves are the estimated observational uncertainties of Stevenson et al. (2017).

5.3.1 Replace GCM TP Profiles with 1D model fits

The 2D temperature models described in Section 5.2.3 use the Guillot (2010) TP profile. The following procedure will show that this profile is flexible enough to approximate the range of TP profiles found in the WASP-43b GCM. First, the 1D TP profile is directly fit to the TP profiles of the GCM on all longitude-latitude grid points in the pressure range 20-10^{-3} bar, which covers the support of the transmission weighting function. Extending the pressure range has negligible effects on the spectra. The total collection of best-fit 1D profiles (one at each GCM grid point) are then used to generate phase curves and compared to those generated directly from the GCM. Both sets of phase curves are simulated using the volume mixing ratios of the original GCM, which are set via chemical equilibrium. Figure 5.5 compares the phase curves simulated from the best-fit 1D profiles (blue curves) with the phase curves simulated directly from the GCM (black curves). The measurement errors of Stevenson et al. (2017) are plotted on the phase curves simulated directly from the GCM. It can be seen that the phase curves simulated from the 1D best-fit profiles can match the GCM phase curves to within error at almost all phases.

5.3.2 Replace GCM Thermal Structure with Latitudinal Average

In the 2D models described in Section 5.2.3, the atmospheric temperature varies with longitude and pressure only, and is held constant with respect to latitudinal variation. The key point is that one should interpret the retrieved thermal structure as a latitudinally-averaged thermal structure, as we have very limited sensitivity to the latitudinal variation of atmospheric properties in the data. The following procedure will demonstrate that the latitudinally-averaged thermal structure of the GCM can reproduce the synthetic data, which justifies the choice of 2D temperature models. Firstly, let us replace all the TP profiles on the same meridian with some latitudinally-averaged TP structure. I find that if the TP profile is averaged from 0° latitude to 45° latitude using cos(latitude) as the weight, the resulting 2D temperature model could produce phase curves (green curves, Figure 5.5) that agree best with the phase curves simulated directly from the GCM (black curves, Figure 5.5) to measurement uncertainties quoted in Stevenson et al. (2017). Note that both sets of phase curves are simulated using the chemical equilibrium VMRs of the original GCM. In conclusion, a 2D temperature model can reproduce *HST*/WFC3 and

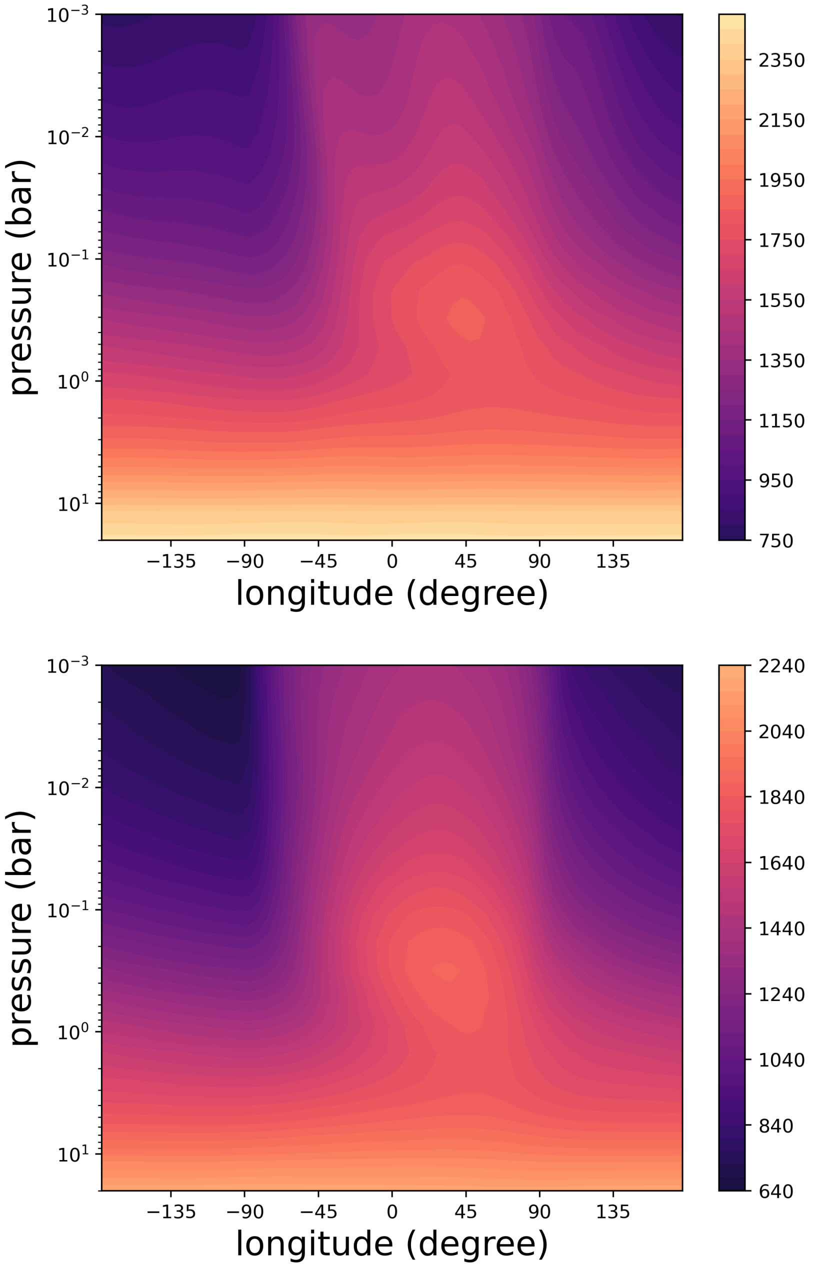

Figure 5.6: Top panel: temperature as a function of longitude and pressure in the WASP-43b GCM at the equator. Lower panel: latitudinally-averaged TP profiles from 0° to 45° latitude, using cos(latitude) as the weight. Since the retrieved thermal structure resembles the latitudinally-averaged profiles, one would under-predict the hot spot offset at the equator for typical hot Jupiter GCMs from synthetic data.

Spitzer/IRAC quality phase curves simulated from the WASP-43b GCM. Furthermore, one would expect the retrieved thermal structure using a 2D model to resemble the latitudinally-averaged thermal structure of the atmosphere. Figure 5.6 plots the GCM temperature as a function of pressure and longitude at the equator on the top, compared to the latitudinally-averaged temperature (from 0° latitude to 45° latitude using cos(latitude) as the weight) on the bottom. For the mock retrievals in Section 5.4, the retrieved thermal structures from the synthetic data are compared with this latitudinally-averaged GCM thermal structure.

5.3.3 Replace Chemical Equilibrium with Constant Chemistry

As mentioned in Section 5.2.1, the chemical equilibrium abundance of the original WASP-43b GCM is expected to be homogenised by horizontal quenching (Cooper & Showman, 2006; Agúndez et al., 2014), and Irwin et al. (2020) reset the GCM gas abundances at all altitudes and locations to be the latitudinally-averaged abundances in the 0.1-1-bar pressure region (using cos(latitude) as the weight) at the sub-stellar meridian. Figure 5.5 compares the phase curves simulated using uniform abundance as those used by Irwin et al. (2020) (yellow curves) with those simulated using the chemical equilibrium abundance (black curves). The main difference is that the different distributions of CH_4 result in significantly different phase curves at 3.6 μm. This effect has been investigated by Steinrueck et al. (2019), who explored if disequilibrium effects such as the quenching of CH_4 can explain why GCMs systematically overestimate phase curve amplitudes compared to observations. The result here echos the finding of Steinrueck et al. (2019) that phase curves observed in the wavelength range covered by the 3.6 μm *Spitzer* channel are an effective diagnostic for disequilibrium methane chemistry on hot Jupiters.

The synthetic phase curves used to validate the retrieval schemes are simulated from uniform gas VMRs as listed in Table 5.2 and are the same synthetic phase curves in Irwin et al. (2020). To further justify the use of uniform gas abundance in my model, Figure 5.5 shows that if we multiply the CH_4 abundance of Irwin et al. (2020) by a factor of 40, the resultant phase curves (orange curves) agree well with the phase curves simulated from the equilibrium chemistry VMRs (black curves). This suggests that while using uniform VMRs can adequately fit *HST*/WFC3 and *Spitzer*/IRAC quality phase curves, this approach can lead to significantly biased CH_4 abundance when the uniform chemistry assumption is not valid.

5.4 Application to Synthetic Phase Curves

This section validates the four retrieval schemes with synthetic data simulated from the full GCM of WASP-43b described in Section 5.2.1. Each retrieval scheme is identified with one of the temperature models described in Section 5.2.3, while all other aspects of the retrieval schemes are identical, so each retrieval scheme is referred to by the temperature model used. The synthetic phase curves are simulated at the same wavelengths as those presented in Stevenson et al. (2017), and their measurement uncertainties are used to set the uncertainties of the synthetic data. No additional random noise is added to the synthetic phase curves. This section assesses the retrieval schemes on three criteria: (1) the goodness of fit to the synthetic phase curves; (2) the accuracy of the retrieved chemical abundance; (3) the goodness of fit of the retrieved thermal structure to the latitudinally-averaged GCM thermal structure in Figure 5.6. Overall, apart from Model 1, all other models can fit the synthetic phase curves within measurement uncertainties at almost all wavelengths and all orbital phases and can accurately constrain the abundance of H_2O and CH_4, as well as retrieve the latitudinally-averaged thermal structure of the GCM.

Figure 5.8 shows the phase curves generated from the medians of the posterior distributions of the model parameters. It is clear that Model 1, where the dayside[3] width is fixed at 180°, gives the worst spectral fit to the synthetic data. The phase curve amplitudes retrieved by Model 1 are too small at most wavelengths, whereas the other models mostly retrieve the correct phase curve amplitudes. It can be seen in Figure 5.7 that Model 1 is not flexible enough to approximate the thermal structure of the GCM, which has a hot region significantly narrower than 180° in longitude. This also leads Model 1 to retrieve a biased high H_2O abundance, as the model tries to match the amplitudes of the synthetic phase curves by pushing the photosphere higher, where the day/night flux contrast is larger. It follows that the dayside area fraction is an important parameter in phase curve retrievals, and the exclusion of its implementation can lead to significant biases in retrieved molecular abundance.

Figure 5.9 shows the posterior distributions of gas VMRs using different retrieval schemes. As mentioned previously, Model 1 retrieves biased H_2O abundance due to the inflexibility of the temperature parameterisation, namely the fixed dayside fraction. The other models produce precise and accurate constraints on H_2O, as well as accurate upper bounds on CH_4. None of the models can constrain CO and CO_2

---

[3] Note again that the ‘dayside’ in the models denotes the region of the atmosphere modelled by the dayside profile and does not necessarily coincide with the permanently illuminated ‘physical dayside’.

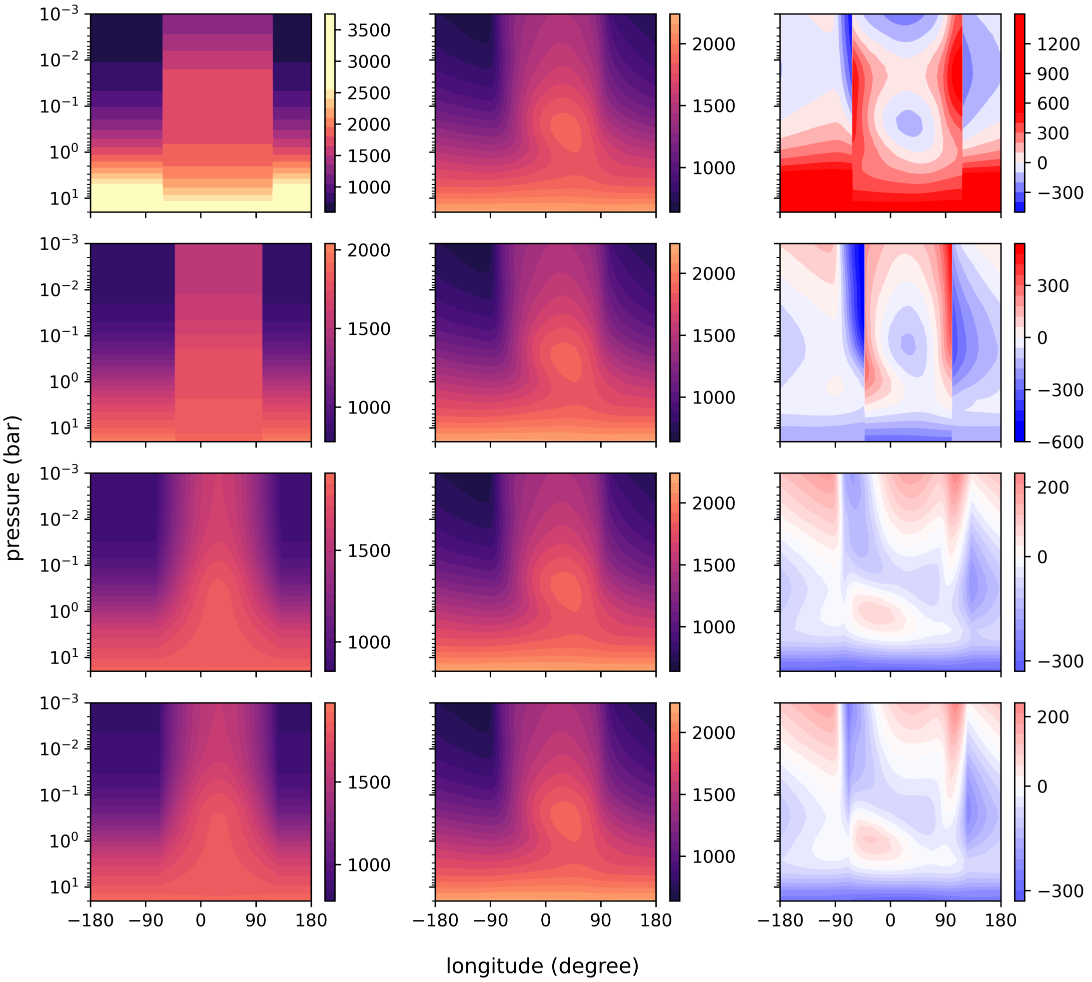

Figure 5.7: Results from the retrievals of synthetic phase curves generated from the WASP-43b GCM. The rows from top to bottom correspond to Model 1, Model 2, Model 3, and Model 4, respectively. Left column: retrieved temperature structures, which are calculated using the median parameters of the posterior distributions. Middle column: latitudinally-averaged TP profile of the GCM from 0° to 45° latitude, using cos(latitude) as the weight. Right column: difference between right and middle columns. Note that the residuals for Models 3 and 4 are generally much smaller than for Models 1 and 2.

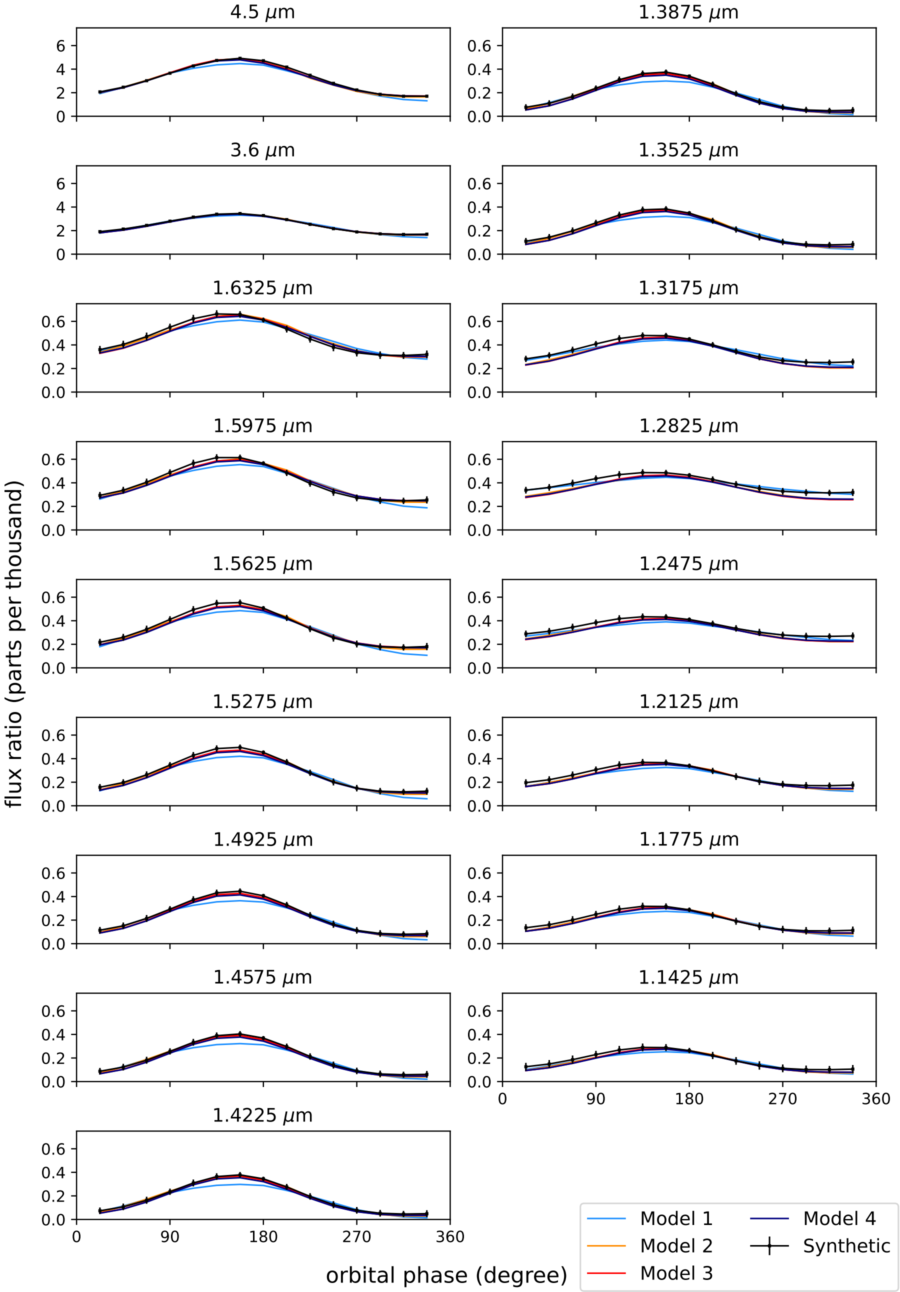

Figure 5.8: Results from the retrievals of synthetic phase curves generated from the WASP-43b GCM. This plot shows the best-fit model phase curves calculated from the posterior medians and compared them to the synthetic data. The synthetic data is shown with the measurement uncertainties of Stevenson et al. (2017). The models are described in Section 5.2.3.

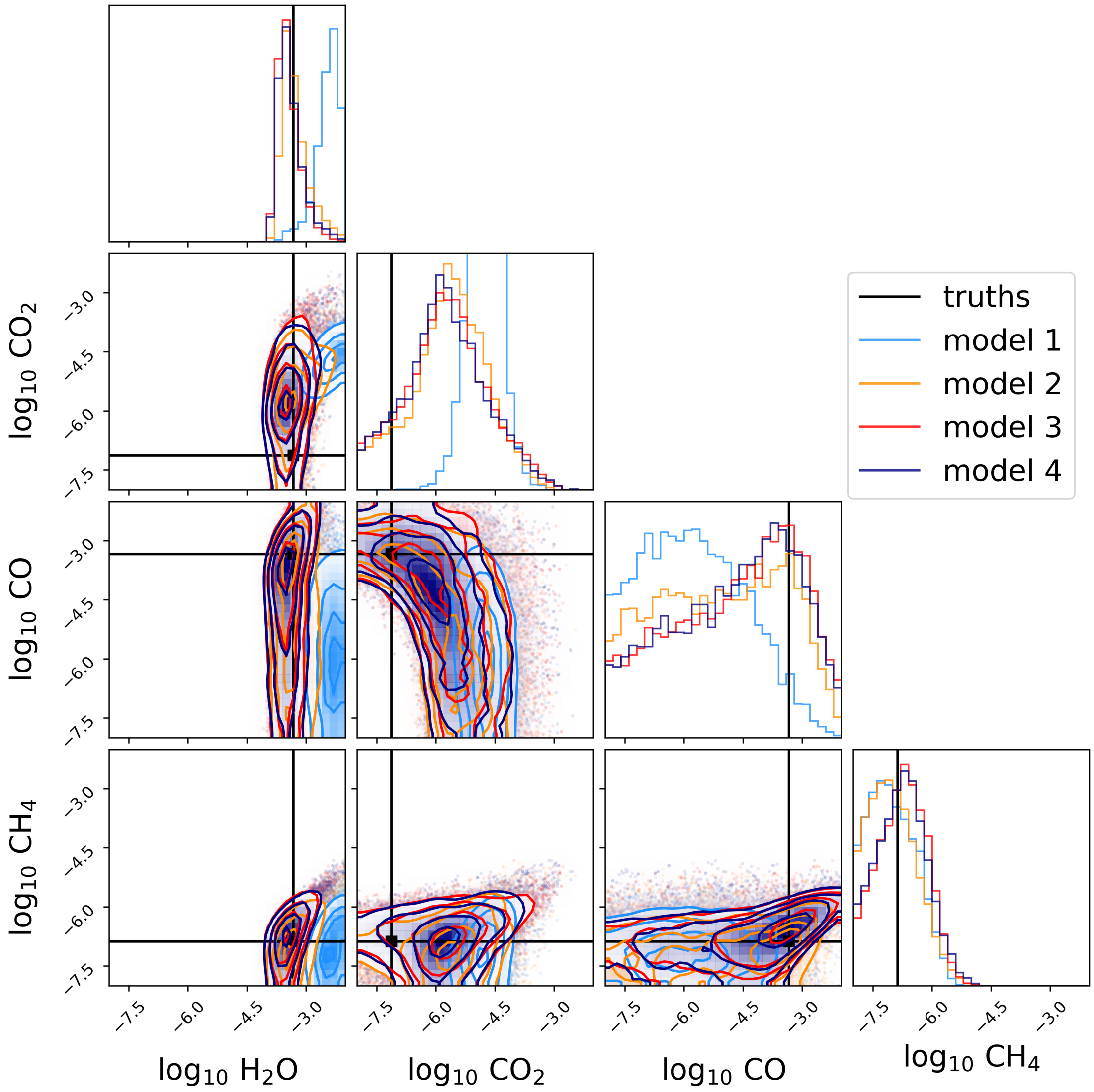

Figure 5.9: Results from the retrievals of synthetic phase curves generated from the WASP-43b GCM. The posterior distributions of the retrieved gas VMRs using different retrieval schemes are shown, and the abundance used to simulated the synthetic data are marked with black lines ('truths').

from the data, as CO and CO_2 have weak opacities in the *HST*/WFC3 wavelengths, and their retrieved abundance are mainly driven by the two *Spitzer* wavelengths. Hence, their abundance are more susceptible to degeneracy with the thermal structure and are therefore poorly constrained.

Figure 5.7 shows the retrieved thermal structures, calculated with the median parameters of the posterior distributions. Figure 5.7 compares the retrieved thermal structures to the latitudinally-averaged TP structure of the GCM, since Section 5.3.2 has shown that the appropriately averaged GCM TP structure can reproduce the synthetic phase curves generated directly from the GCM. As described in Section 5.3.2, the average is between 0° and 45° latitude and with cos(latitude) as the weight. It is now clear that Model 1 performs badly because the width of the hot region in the GCM is significantly narrower than the dayside width prescribed by Model 1. Model 2 can accurately approximate the typical dayside and nightside TP profiles; however, since Model 2 contains a discontinuity at the dayside/nightside boundary, there are large jumps in temperature on isobars around the day/night boundary. Hence, the fits at those regions deviate significantly from the GCM. Models 3 and 4, by virtue of being continuous models, avoid this problem and can approximate the latitudinally-averaged GCM structure to well within ± 300 K at most pressures and longitudes. However, both models perform relatively poorly in the deep atmosphere as the retrieved deep atmosphere temperatures are too low (right column, Figure 5.7). This leads to incorrectly retrieved phase curve amplitudes at the wavelengths with the deepest photospheres. By computing the transmission weighting function in Figure 5.2, we can see that the three channels at 1.2475 μm, 1.2825 μm, 1.3175 μm are sensitive mainly to the deep atmosphere at close to 10 bar, whereas most other channels are sensitive to lower pressure levels. In Figure 5.8, we can see that the phase curve fits at these three channels by Model 3 and Model 4 have lower flux than the synthetic phase curves. The retrieved deep atmosphere temperature is biased because there are more data points constraining the TP profile at lower pressure levels, and the TP profile used cannot satisfy all constraints equally well. One would expect that the biased deep atmosphere temperature can be resolved using a more sophisticated TP profile. However, this issue does not lead to significantly biased retrieved abundance, and our precision is still in line with past studies.

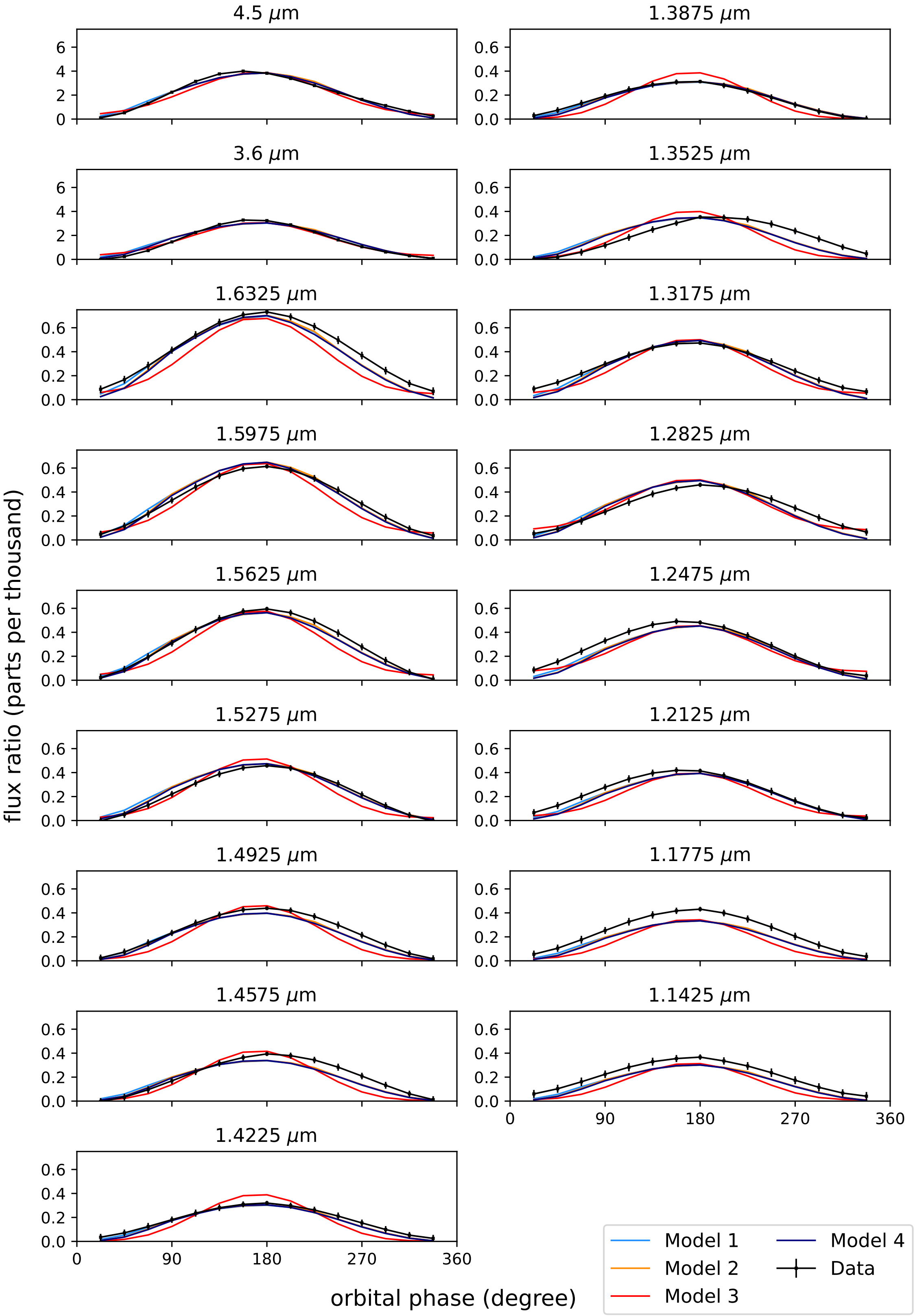

Figure 5.10: Retrieval results of the real phase curves. The retrieved phase curves are calculated from the posterior medians and compared to the real data. The models are described in 5.2.3.

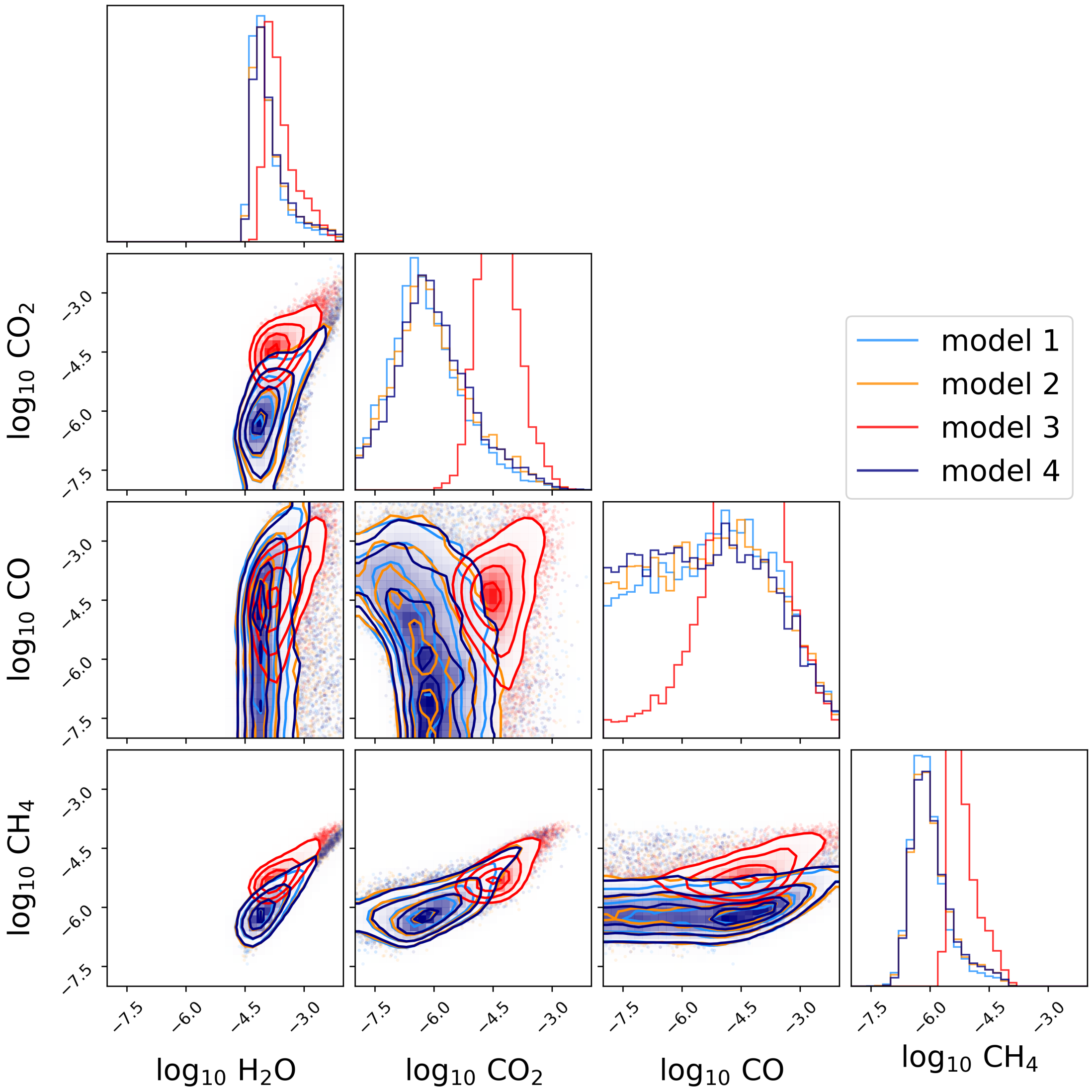

Figure 5.11: Retrieval results of the real phase curves. Posterior distributions of the retrieved gas VMRs.

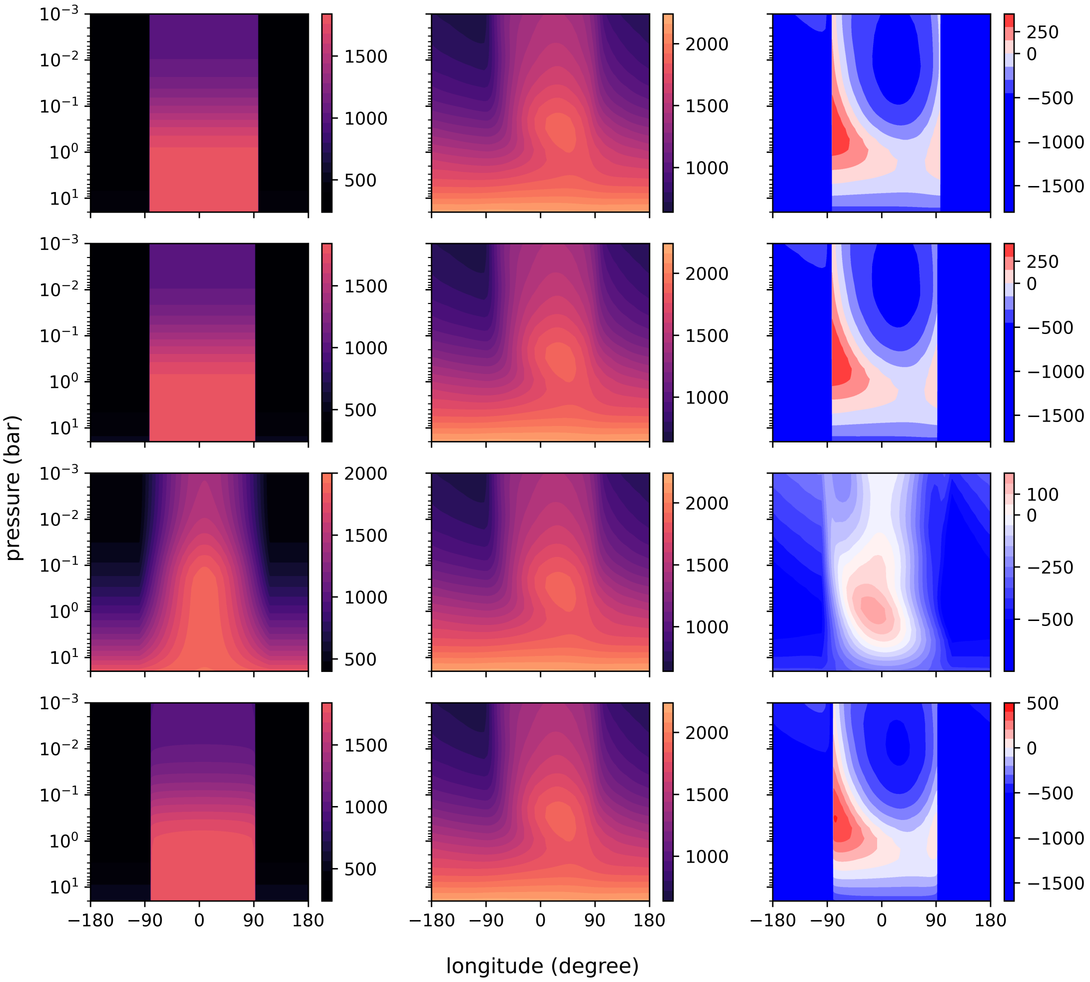

Figure 5.12: Retrieval results of the real phase curves. The rows from top to bottom correspond to Model 1, Model 2, Model 3, and Model 4, respectively. Left column: retrieved temperature structures, which are calculated using the median parameters of the posterior distribution. Middle column: latitudinally-averaged TP profile of the GCM from 0° to 45° latitude, using cos(latitude) as the weight. Right column: difference between right and middle columns.

5.5 Application to Real Phase Curves

Section 5.4 tested the performance of the 2D retrieval schemes against synthetic data. It was shown that 2D retrieval schemes can accurately constrain the abundance of H_2O and CH_4 from synthetic data simulated from a GCM, provided that the temperature model is flexible enough to approximate the thermal structure of the GCM atmosphere. This section applies the retrieval schemes to the observed *HST*/WFC3 and *Spitzer*/IRAC phase curves of Stevenson et al. (2017). This section again looks at the spectral fits, the retrieved chemical abundance, and the retrieved thermal structure.

Figure 5.10 shows the phase curves generated from the medians of the posterior distributions of model parameters. The model fits to the real data are worse than the model fits to the synthetic data, partly because no additional random noise was added onto the synthetic data. Furthermore, there are two interesting points of comparison with the fits to synthetic data. First, in the case of real data, Model 1 can fit the phase curves almost as well as Model 2, whereas in the case of synthetic data, Model 1 fits the phase curves markedly worse than Model 2. The reason that Model 1 cannot fit the synthetic data is that the GCM used to generate the data has a hot region that is significantly narrower in longitudinal extent than the width of the dayside region in Model 1, which is fixed at 180°. However, the thermal structure retrieved from the real data by both models is consistent with a hot dayside region that spans approximately 180° in longitude. This is the reason why Model 1 could perform as well as Model 2 on the real data while failing to do so on the synthetic data. Second, Model 3 produces the poorest fits to the real data and often produces phase curve maxima that are too large while simultaneously under-producing the amplitudes of the intermediate phases. Since Model 3 prescribes that temperatures on isobars vary sinusoidally with longitude on the dayside, the misfits suggest that temperature must vary less strongly with longitude on isobars. This is confirmed by the retrieved thermal structure of Model 4.

Figure 5.11 shows the posterior distributions of gas VMRs using different retrieval schemes. The retrieved H_2O abundances are consistent across models. Taking Model 4 as the fiducial model gives the constraints of 5.6×10^{-5}–4.0×10^{-4} at 1σ. As with the synthetic data, the model cannot constrain the abundance of CO and CO_2, but can place an upper bound on the VMR of CH_4 at $\sim 10^{-6}$. Figure 5.12 plots the retrieved thermal structures, calculated with the median parameters of the posterior distributions. The retrieved dayside temperatures of Model 4 suggest that the dayside

Reference	Data	H_2O 1σ Range	Notes
Kreidberg et al. (2014)	transmission	3.3×10^{-5}–1.4×10^{-3}	
Kreidberg et al. (2014)	emission	3.1×10^{-4}–4.4×10^{-3}	
Kreidberg et al. (2014)	transmission + emission	2.4×10^{-4}–2.1×10^{-3}	
Stevenson et al. (2017)	phase curves, nightside	2.5×10^{-5}–1.1×10^{-4}	phase-by-phase
Stevenson et al. (2017)	phase curves, dayside	1.4×10^{-4}–6.1×10^{-4}	phase-by-phase
Irwin et al. (2020)	phase curves	2×10^{-4}–1×10^{-3}	'2.5D model'
Feng et al. (2020)	phase curves	1.1×10^{-4}–3.9×10^{-3}	2D model
Changeat et al. (2021)	phase curves + transmission		'1.5D model'
Chubb & Min (2022)	phase curves + transmission		3D model
This chapter	phase curves	5.6×10^{-5}–4.0×10^{-4}	2D model

Table 5.5: Summary of previous retrieval studies of WASP-43b. The emission data analysed by Kreidberg et al. (2014) refer to the *HST*/WFC3 secondary eclipse data as presented in Kreidberg et al. (2014) and the *Spitzer* secondary eclipse data from Blecic et al. (2014). The transmission data refer to the *HST*/WFC3 primary transit data as presented in Kreidberg et al. (2014). The phase curves refer to the *HST*/WFC3 and *Spitzer* phase curves as presented in Stevenson et al. (2017). The constraints on the abundance of H_2O at 1σ are shown for the studies that publish such a result. For the studies that analysed phase curves, the retrieval methods are noted.

thermal structure of WASP-43b is relatively homogeneous, meaning that temperature does not vary strongly as a function of longitude on isobars. On the other hand, the retrieved temperatures on the nightside are extremely cold, likely due to thick cloud coverage that lifts the photosphere to lower pressure levels.

5.6 Discussion

This section compares the retrieval results presented in the previous section to past retrieval studies of WASP-43b and to the phase-by-phase retrieval approach, and discusses the effects of nightside clouds,

5.6.1 Comparison with Previous Retrievals

Table 5.5 presents a summary of past retrieval studies of WASP-43b, focusing on the studies which analysed the *HST* transmission, secondary eclipse and phase curve data (GO Program 13467, PI: Jacob Bean, Kreidberg et al., 2014), *Spitzer* secondary eclipse data (Program ID 70084, Blecic et al., 2017), and *Spitzer* phase curve data (Programs 10169 and 11001, PI: Kevin Stevenson, Stevenson et al., 2017). Table 5.5 shows the 1σ constraints on the abundance of H_2O for the studies that publish such a result. The H_2O constraints retrieved in this chapter are on the lower end compared to past studies, though all of the H_2O abundance constraints overlap.

5.6.2 Comparison with Phase-by-Phase Retrievals

Some studies found variable H_2O abundance as a function of longitude in the atmosphere of hot Jupiters (e.g., Stevenson et al., 2017). However, this might be the result of the 1D 'phase-by-phase' approach used by these studies, where the spectrum at each orbital phase was retrieved independently, assuming uniform abundance and TP structure for each phase. For example, Stevenson et al. (2017) analysed the same *HST*/WFC3 and *Spitzer* phase curves of WASP-43b as in this chapter and found the retrieved H_2O abundance varied between the dayside and the nightside phases. For the nightside, they constrained the H_2O abundance to be 2.5×10^{-5}–1.1×10^{-4} at 1σ, whereas for the dayside, they constrained the H_2O abundance to be 1.4×10^{-4}–6.1×10^{-4} at 1σ. However, the 1D retrieval approach, where uniform atmospheric condition is assumed for the visible atmosphere under observation, is now known to give biased results in the analysis of disc-averaged hot Jupiter spectra (Blecic et al., 2017; Taylor et al., 2020). Furthermore, the phase-by-phase approach is not geometrically self-consistent and under-utilises the constraints from the fact that hemispheres observed at neighbouring phases overlap (Irwin et al., 2020).

To illustrate that the phase-by-phase approach cannot reliably constrain the variation of molecular abundance as a function of planetary longitude, this subsection presents phase-by-phase retrieval results of the synthetic data analysed in Section 5.4. In keeping with Stevenson et al. (2017), the spectrum at each orbital phase is independently analysed with a uniform TP and abundance profile. Figure 5.13 shows the retrieved molecular abundance from the synthetic phase curves, where the truths (the molecular abundance used to calculate the synthetic data) are marked by horizontal black lines. The retrieved H_2O abundance varies as a function of orbital phase even though the abundance is uniform in the input GCM-based model used to simulate the synthetic data. Furthermore, the retrieved H_2O abundance is biased at several orbital phases, echoing the findings of past studies (Blecic et al., 2017; Taylor et al., 2020) that the 1D phase-by-phase approach could lead to significantly biased molecular abundance. The abundance constraints from Model 4 are plotted in Figure 5.13 for comparison. We can see from Figure 5.13 that Model 4 performs markedly better than the 1D approach on synthetic phase curves both in terms of accuracy and precision in retrieved molecular abundance. I also apply the phase-by-phase approach to the real data analysed in Section 5.5, which are the same data presented in Stevenson et al. (2017). Figure 5.14 presents the retrieved molecular abundance, which shows a similar trend as Stevenson et al. (2017) that the H_2O abundance is higher for the dayside phases than for the nightside phases.

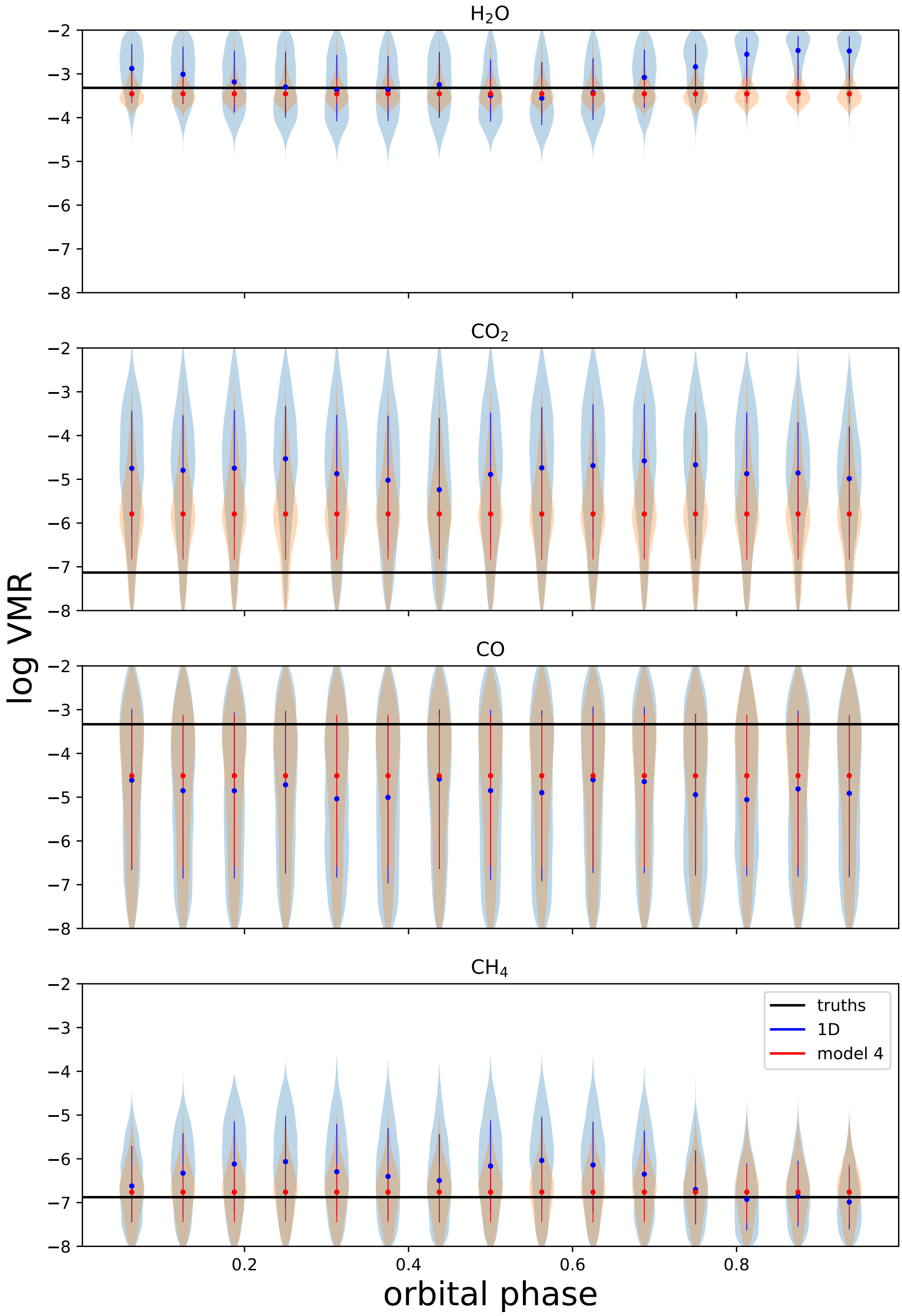

Figure 5.13: Retrieved molecular abundance from the synthetic phase curves using the 1D phase-by-phase approach (blue), compared to the retrieved abundance using Model 4 (red). The shaded areas represent the marginalised posterior distributions. The vertical lines mark the 1 σ confidence intervals. The true abundances used to generate the data are marked by the black horizontal lines.

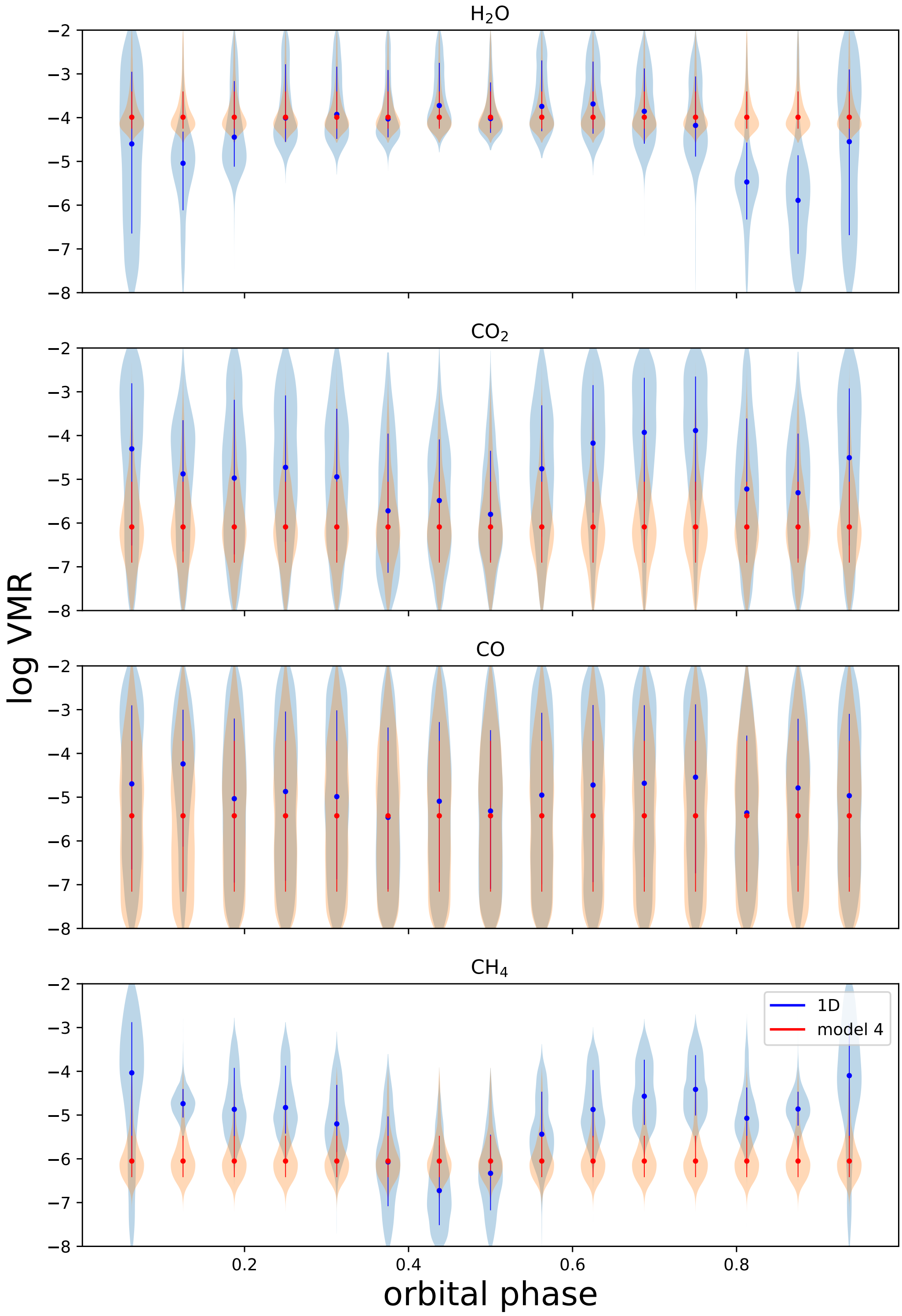

Figure 5.14: Retrieved molecular abundance from the observed phase curves presented in Stevenson et al. (2017) using the 1D phase-by-phase approach (blue), compared to the retrieved abundance using Model 4 (red). The shaded areas represent the marginalised posterior distributions. The vertical lines mark the 1 σ confidence intervals.

5.6.3 Clouds on WASP-43b

Multiple studies support the hypothesis that WASP-43b has no optically thick clouds on the dayside. Kreidberg et al. (2014) analysed the transmission spectrum observed with *HST*/WFC3 and found that the day-night terminator of WASP-43b contained no significant clouds at the pressure levels probed by transmission spectroscopy. Since the dayside is hotter than the terminator region and likely has a comparable chemical inventory, it should also be free from significant cloud coverage. More directly, Fraine et al. (2021) found a very low dayside geometric albedo (<0.06) using *HST* WFC3/UVIS secondary eclipse data in the optical wavelengths, and reported a non-detection of clouds on the dayside at $P > 1$ bar. Furthermore, Stevenson et al. (2014) estimated the Bond albedo of WASP-43b to be $0.18^{+0.07}_{-0.12}$ by computing the day-and nightside bolometric fluxes from the model spectra retrieved from the *HST*/WFC3 phase curves. These findings justify using a cloud-free retrieval scheme on the dayside, in accordance with the prediction from modelling work that a cloud-free hot spot should dominate the dayside of hot Jupiters (Parmentier et al., 2016).

By comparing the synthetic phase curves simulated from the cloud-free WASP-43b GCM with the observed phase curves (Figures 5.8 and 5.10), we can see that the GCM phase curves under-predict the phase curve amplitudes and over-predict the phase curve maximum offsets. The mismatch in phase curve offsets suggests that the strength of heat circulation on WASP-43b is weaker than predicted by the GCM, and the low nightside brightness temperatures further suggest significant nightside cloud coverage. According to Parmentier et al. (2020), when nightside clouds are present, the day-to-night heat transport becomes extremely inefficient, and the nightside photosphere is lifted to a higher altitude. This could explain the low nightside temperatures and small phase curve offsets observed on WASP-43b.

5.7 Summary

This chapter tests the Yang et al. (2023) 2D temperature model introduced in Section 3.2 against several simpler 2D temperature models. All 2D temperature models are built on two TP profiles, which signify the representative dayside and nightside profiles. In these models, the temperature is a function of pressure and longitude and can be used to retrieve the chemical composition and latitudinally-averaged thermal structure of hot Jupiter atmospheres from phase curves.

The 2D temperature models are validated in retrievals using synthetic phase curves simulated from a cloud-free GCM of WASP-43b, representing a more realistic atmospheric model than the typically simple models used for validating retrieval schemes in the literature. This chapter finds that the models that allow variable dayside longitudinal extent can fit synthetic *HST*/WFC3 and *Spitzer*/IRAC phase curves within typical measurement uncertainties, as well as accurately and precisely constraining the water and methane abundance. The retrieved thermal structures using these models are good approximations to the latitudinal average of the GCM thermal structure weighted towards the low latitude regions.

This chapter applies the 2D temperature models to retrieve information from the observed phase curves of WASP-43b presented in Stevenson et al. (2017). Retrievals using the Yang et al. (2023) 2D temperature model constrain the abundance of water to be 5.6×10^{-5}–4.0×10^{-4} at 1σ using Model 4, as well as an upper bound on CH_4 at $\sim 1 \times 10^{-6}$. The results show that the latitudinally-averaged dayside TP structure of WASP-43b does not vary strongly as a function of longitude on the dayside and is non-inverted.

Chapter 6

JWST/MIRI Phase Curve of WASP-43b

The contents of this chapter have been published in Monthly Notices of the Royal Astronomical Society under Yang et al. (2024b).

This chapter continues the atmospheric characterisation of WASP-43b by analysing four phase-resolved emission spectra observed with the Mid-Infrared Instrument (MIRI) onboard the *JWST*. Atmospheric retrievals using these spectra were first published in Bell et al. (2024), though the retrievals were performed 'phase-by-phase', i.e., the spectrum at each orbital phase was retrieved independently, assuming a uniform temperature-pressure (TP) profile. Instead, this chapter uses the Yang et al. (2023) 2D temperature model introduced in Section 3.2 to retrieve the atmospheric properties of WASP-43b by simultaneously fitting the four emission spectra, with the assumption that atmospheric dynamics effectively homogenise the abundance of the most abundant molecular species in the pressure range probed by the observation (see Chapter 9.2 for an in depth discussion of this assumption, as well as Cooper & Showman, 2006; Agúndez et al., 2014; Drummond et al., 2018a,b; Mendonça et al., 2018b; Venot et al., 2020; Baeyens et al., 2021). By analysing the four spectra together, the retrievals in this chapter better constrain the molecular abundances than the phase-by-phase analysis in Bell et al. (2024).

This chapter is structured as follows. Section 6.1 describes the *JWST*/MIRI observation. Section 6.2 details the methodology of the atmospheric retrievals. Section 6.3 presents the retrieval results, including the spectral fits, the abundance constraints, and the thermal structure constraints. Section 6.4 discusses the retrieval results, where they are compared to the findings of Bell et al. (2024) in Section 6.4.1 and to the findings of Chapter 5 in Section 6.4.2. Section 6.4.3 additionally compares the retrieved H_2O abundance to past studies of WASP-43b. Section 6.5 concludes the chapter with a summary.

6.1 The *JWST*/MIRI Observation

The data analysed in this chapter are four phase-resolved disc-integrated emission spectra derived from a phase curve observation of WASP-43b with the Mid-Infrared Instrument (MIRI) onboard the *JWST*. The data were collected between December 1 and 2, 2022, with *JWST*/MIRI in Low Resolution Spectrometer (LRS) slitless mode, as part of the Transiting Exoplanet Community Early Release Science Program JWST-ERS-1366 (PI: Natalie Batalha, see Bell et al., 2024). The original observation spans 5 to 12 μm and contains a full phase curve with two eclipses and one transit, lasting 26.5 hours at a cadence of 10.34 s (Bell et al., 2024). However, the retrievals in this chapter only fit the observation in the 5-10.5 μm region due to unresolved systematic effects in the 10.6-11.8 μm region, known as the 'shadowed region effect', following the retrieval analysis in Bell et al. (2024)[1]. The so-called 'shadowed region effect' of the MIRI instrument has not yet been robustly separated from the astrophysical phase variations, making the observation in this wavelength range unreliable for this particular observation (not all MIRI/LRS observations are affected, see Bell et al., 2024). The spectra analysed in this chapter are the final 'fiducial spectra' presented in Bell et al. (2024), which are the mean average of the spectra reduced using the four different data reduction pipelines in Bell et al. (2024): Eureka! v1, Eureka! v2, TEATRO, and SPARTA. Bell et al. (2024) set the uncertainties as the mean uncertainty per wavelength bin, and then adding in quadrature the root mean square between the individual reductions and the mean spectrum. Table 6.1 lists the MIRI phase-resolved emission spectra as presented in Bell et al. (2024).

6.2 Methodology

This section outlines the atmospheric retrieval procedure, which is divided into three parts. Firstly, the atmosphere of WASP-43b is modelled using the Yang et al. (2023) 2D temperature model defined in Section 3.2 assuming uniform molecular abundances, as described by Section 6.2.1. Secondly, a correlated-k radiative transfer pipeline is

---

[1] The exclusion of the 10.6-11.8 μm region naturally reduces the information content of the data set, particularly because this wavelength region contains strong NH_3 features. Therefore, a better understanding of the 'shadowed region effect' in the future will allow us to more confidently constrain the NH_3 abundance of WASP-43b and other hot Jupiters.

Orbital Phase	5.25 (μm)	5.75 (μm)	6.25 (μm)	6.75 (μm)	7.25 (μm)	7.75 (μm)	8.25 (μm)	8.75 (μm)	9.25 (μm)	9.75 (μm)	10.25 (μm)	10.75 (μm)	11.25 (μm)	11.75 (μm)
0	1132(71)	1128(62)	1239(77)	1149(65)	1401(79)	1889(80)	2171(90)	2389(87)	2583(103)	2902(112)	2901(142)	2069(303)	2804(457)	3476(394)
0.25	2945(65)	3280(50)	3465(67)	3121(63)	3650(66)	3995(66)	4401(71)	4633(80)	4934(96)	5351(94)	5262(123)	4860(272)	5336(328)	5549(356)
0.5	4844(43)	5216(45)	5453(44)	5141(48)	5506(55)	6023(56)	6265(70)	6388(74)	7239(84)	7508(108)	7261(119)	7542(164)	7679(248)	7430(287)
0.75	2453(66)	2511(58)	2826(69)	2422(71)	3074(73)	3462(77)	3738(76)	3933(88)	4058(96)	4445(95)	4372(118)	5161(270)	5829(344)	6086(371)

Table 6.1: Phase-resolved emission spectra of WASP-43b observed with *JWST*/MIRI as published in Bell et al. (2024). The first row from the top denotes the wavelength channels, and the first column from the left denotes the orbital phases. Fluxes are in units of parts per million (ppm), whereas the values within the parentheses represent uncertainties.

used to generate phase-resolved disc-integrated emission spectra from atmospheric models, as described by Section 6.2.2. Thirdly, a Bayesian parameter inference algorithm is used to constrain the parameters of the atmospheric model given the observed spectra and calculate the significance of the molecular detections from Bayesian evidence, as described by Section 6.2.3.

6.2.1 Atmospheric Modelling

The atmospheric model used in the retrievals combines the Yang et al. (2023) parametric 2D temperature model in Section 3.2 with a simple chemistry model that assumes uniform gas volume mixing ratios (VMRs). The thermal structure retrieved using this 2D model is interpreted as a latitudinally-averaged thermal structure, as Section 5.3 shows that the temperature structure retrieved from synthetic phase curve data closely resembles the meridional mean of the input temperature structure between ±45° latitude calculated using cos(latitude) as the weight. The model does not prescribe the latitudinal temperature variation since phase curve observations are much more sensitive to longitudinal variation than latitudinal variation: the central longitude during the observation changes, whereas the central latitude is held constant[2].

For the chemistry component of the atmospheric model, the retrievals assume the atmosphere is H_2/He-dominated, with a fixed Jupiter-like H_2 to He VMR ratio at 86:14 (Von Zahn & Hunten, 1996; Niemann et al., 1998). The model includes five spectrally active molecules whose VMRs are free parameters: H_2O, CO_2, CO, CH_4, and NH_3 (see Table 6.4 for the molecular opacity data). These molecules are expected at potentially detectable abundance in the atmosphere of WASP-43b from chemical modelling (Mendonça et al., 2018b; Figure 5, Venot et al. 2020; Figure 18, Baeyens et al. 2021) and given their significant opacities in the MIRI wavelengths (Figure 6.2). The VMRs of the spectrally active molecules are set to be constant with altitude, longitude and latitude based on previous modelling work (e.g., Cooper & Showman, 2006; Agúndez et al., 2014; Baeyens et al., 2021), which suggest that atmospheric circulation should effectively homogenise the molecular abundances in hot Jupiters in the pressure range (10-10^{-3} bar) typically probed by low-resolution emission spectroscopy.

---

[2] Note that the dayside latitudinal thermal structure of WASP-43b can be constrained with the eclipse mapping technique, albeit with large uncertainties (e.g., Hammond et al., 2024; Challener et al., 2024).

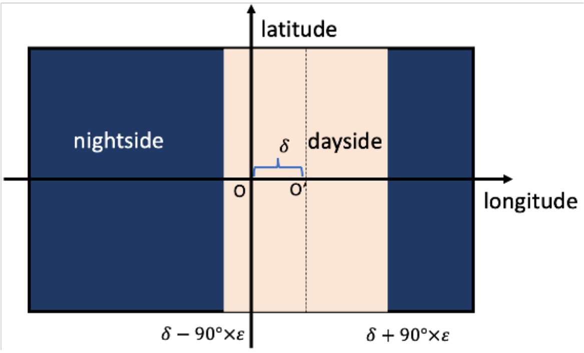

Figure 6.1: Schematics of the parametric 2D temperature model as defined by Equation (3.5). The model divides the atmosphere into a dayside region and a nightside region, each modelled with a representative TP profile. The dayside central longitude and the dayside width are allowed to vary. 'O' marks the substellar point, and 'O$'$' marks the centre of the dayside region. While temperature is constant with longitude on isobars in the nightside region, the variation of temperature with longitude on the dayside can be parameterised. Note that the temperature is constant with latitude and only varies with pressure and longitude. The retrieved thermal structure is interpreted as a latitudinal average.

Table 6.2 lists the free parameters of the atmospheric retrievals, and Table 6.3 lists the fixed stellar and planetary parameters used in this chapter.

6.2.2 Radiative Transfer

As in the rest of this thesis, the emission spectra in this chapter are calculated using the NEMESISPY software (Yang et al., 2024a) described in Section 2.5, which is a Python development of the Fortran NEMESIS library (Irwin et al., 2008). The radiative transfer calculations are done with the correlated-k method (Lacis & Oinas, 1991), following Irwin et al. (2008). The molecular opacity data for the radiative transfer calculations in this chapter are taken from the ExoMol database (Chubb et al., 2021) and are listed in Table 6.4. Channel-integrated k-tables are generated at the resolution of the spectra (constant 0.5-μm bins) from the original ExoMol k-tables, which were computed at a resolving power of R=1000. The radiative transfer calculation models the molecular absorption due to the five spectrally active molecules in the model and the collision-induced absorption due to H_2–H_2 pairs and H_2–He pairs (Borysow & Frommhold, 1989; Borysow et al., 1989). The full list of opacity data is given in Table 6.4. NEMESISPY calculates the disc-integrated emission spectra at arbitrary orbital phase using the method of Irwin et al. (2020) described in Section 2.4, which takes into account the variation of emission angle and optical path across the atmosphere. As in

Parameter	Description	Prior	Unit
δ	Dayside longitudinal offset	U(-45,45)	degree
ε	Dayside longitudinal width scaling	U(0.5,1.2)	dimensionless
n	Dayside longitudinal variation exponent	U(0,2)	dimensionless
$\log \kappa_{\mathrm{th,day}}$	Log_{10} mean infrared opacity (dayside)	U(-4,2)	$\mathrm{m}^2\mathrm{kg}^{-1}$
$\log \gamma_{\mathrm{day}}$	Log_{10} ratio of visible and infrared opacities (dayside)	U(-4,1)	dimensionless
$\log f_{\mathrm{day}}$	Log_{10} heat redistribution parameter (dayside)	U(-4,1)	dimensionless
$\mathrm{T}_{\mathrm{int,day}}$	Internal heat flux temperature (dayside)	U(100,1000)	Kelvin
$\log \kappa_{\mathrm{th,nigtht}}$	Log_{10} mean infrared opacity (nightside)	U(-4,2)	$\mathrm{m}^2\mathrm{kg}^{-1}$
$\log \gamma_{\mathrm{night}}$	Log_{10} ratio of visible and infrared opacities (nightside)	U(-4,1)	dimensionless
$\log f_{\mathrm{night}}$	Log_{10} heat redistribution parameter (nightside)	U(-4,1)	dimensionless
$\mathrm{T}_{\mathrm{int,night}}$	Internal heat flux temperature (nightside)	U(100,1000)	Kelvin
b	Error inflation parameter	U(1,5)	dimensionless
$\log \mathrm{VMR}_{\mathrm{H_2O}}$	Log_{10} volume mixing ratio of H_2O	U(-10,-2)	dimensionless
$\log \mathrm{VMR}_{\mathrm{CO_2}}$	Log_{10} volume mixing ratio of CO_2	U(-10,-2)	dimensionless
$\log \mathrm{VMR}_{\mathrm{CO}}$	Log_{10} volume mixing ratio of CO	U(-10,-2)	dimensionless
$\log \mathrm{VMR}_{\mathrm{CH_4}}$	Log_{10} volume mixing ratio of CH_4	U(-10,-2)	dimensionless
$\log \mathrm{VMR}_{\mathrm{NH_3}}$	Log_{10} volume mixing ratio of NH_3	U(-10,-2)	dimensionless

Table 6.2: Free parameters of the retrieval model and their priors. Compared to the retrievals in Chapter 5, this chapter additionally includes NH_3 as a free parameter, an error inflation parameter b, and extend the priors for the $\log_{10}$ VMRs from $(-8,-2)$ to $(-10,-2)$ to account for the generally higher opacities in the MIRI bandpass compared to the *HST*/WFC3 bandpass modelled in Chapter 5.

Parameter	Value	Reference
T_{star}	4300 K	Bell et al. (2024)
R_{star}	0.667 R_{Sun}	Gillon et al. (2012)
$[\mathrm{Fe/H}]_{\mathrm{star}}$	-0.01 dex	Gillon et al. (2012)
a	0.0153 AU	Gillon et al. (2012)
M_{plt}	2.034 M_{Jup}	Gillon et al. (2012)
R_{plt}	1.036 R_{Jup}	Gillon et al. (2012)

Table 6.3: WASP-43b stellar and planetary parameters used in this chapter.

Molecule	Opacity Data
H_2O	Polyansky et al. (2018)
CO_2	Yurchenko et al. (2020)
CO	Li et al. (2015)
CH_4	Yurchenko et al. (2017)
NH_3	Coles et al. (2019)
He	Borysow & Frommhold (1989) & Borysow et al. (1989)
H_2	Borysow & Frommhold (1989) & Borysow et al. (1989)

Table 6.4: Opacity data used to calculate emission spectra in this chapter. Apart from the H_2-H_2 and H_2-He collision-induced absorption opacity, all data are downloaded from the ExoMol database (Chubb et al., 2021).

the rest of this thesis, five zenith angle quadratures are used for the disc-integration scheme, i.e., setting $N_\mu = 5$ in Equation (2.22). The disc-integrated spectrum at a given orbital phase is computed assuming a circular, tidally locked, and edge-on orbit, using the parameters in Table 6.3. The planetary emission is converted to planet-to-star flux ratio using a stellar spectrum computed using the PHOENIX stellar model (Allard & Hauschildt, 1995; Hauschildt et al., 1999; Husser et al., 2013), generated assuming an effective temperature of 4300 K, a surface gravity of log(g)= 4.50, and a solar metallicity. The choice of stellar model is informed by the work done in Bell et al. (2024).

6.2.3 Retrieval Setup

This chapter performs atmospheric retrievals on the phase-resolved MIRI emission spectra of WASP-43b at four different orbital phases simultaneously. As in Bell et al. (2024), the spectra are binned to eleven 0.5-μm wavelengths bins in the 5-10.5 μm wavelength range. The four orbital phases are phase 0 (nightside), phase 0.25 (observer facing the evening terminator), phase 0.5 (dayside) and phase 0.75 (observer facing the morning terminator). The retrievals fit the four spectra simultaneously using spectra calculated from the atmospheric model described in Section 6.2.1 via the radiative transfer procedure described in Section 6.2.2.

The atmospheric model is defined from 20 to 10^{-5} bar, on 40 points equally spaced in log pressure. The retrievals retrieve the eleven free temperature model parameters, the five molecular VMRs, and an error inflation parameter that is described in Section 6.2.3.1. The priors of these parameters are listed in Table 6.2. The posterior distribution of these parameters given the data is estimated using the Nested Sampling algorithm (Feroz & Hobson, 2008), as described in Section 4.2.3. This thesis uses the PyMultiNest software package (Buchner et al., 2014) to implement the algorithm, using 1000 sampling live points. For each molecule, its detection significance is calculated via Bayesian model comparison by performing five additional retrievals, each omitting one of the five molecules in our fiducial model, as described in Section 4.3. The detection significance of a molecule can be calculated by computing the Bayes factor of the fiducial model over the model without the particular molecule, following Trotta (2008) and Benneke & Seager (2013).

6.2.3.1 Error inflation

The retrievals in this chapter include an error inflation parameter to account for underestimated measurement and forward modelling uncertainties, following the approach used in, for example, Line et al. (2015) and Bell et al. (2024). The error inflation is implemented by modifying the likelihood term in Bayesian inference with a constant-with-wavelength multiplicative factor. The log likelihood function with error inflation is given by

$$\ln L(\boldsymbol{D}|\boldsymbol{\theta}) = -\frac{1}{2}\sum_{i=1}^{n}\frac{(D_i - F_i(\boldsymbol{\theta}))^2}{s_i^2} - \frac{1}{2}\ln(2\pi s_i^2), \tag{6.1}$$

where $\boldsymbol{D}$ is the set of data points in the observed spectra, $F_i(\boldsymbol{\theta})$ is the ith data point in the model spectra given model parameters $\boldsymbol{\theta}$, and s_i is defined as

$$s_i = b * \sigma_i, \tag{6.2}$$

where σ_i is the uncertainty for the ith data point, and b is a free error inflation parameter between 1 and 5.

6.3 Results

This section describes the results of the atmospheric retrievals. Section 6.3.1 shows that the Yang et al. (2023) parametric 2D temperature model can fit the observation. Section 6.3.2 shows that there is statistically significant evidence of H_2O, NH_3, CO, statistically weak evidence of CO_2, and no detectable level of CH_4. Section 6.3.3 plots the transmission weighting function of the best-fit model atmosphere and the best-fit thermal structure.

6.3.1 Spectral Fit

Figure 6.2 shows the model fit to the observed emission spectra. Subplots a) - d) show the best-fit model spectra calculated from the maximum a posteriori parameters. The $1\sigma/2\sigma$ central credible intervals are propagated to show the spread of the posterior distribution. The best-fit model can fit almost all observed data points within the original uninflated error bars in Bell et al. (2024), which is also reflected by the fact that the error inflation parameter retrieved is only around 1.65 (see Section 6.2.3.1 for an explanation of error inflation). The only exception is the 8.75 μm bin at phase 0.5, which cannot be accounted for by any of the opacity sources in the atmospheric model[3].

For ease of reference, subplots e) and f) of Figure 6.2 show the cross-sections of the molecules included in the retrievals in the MIRI/LRS wavelength range. H_2O opacity is significant throughout the MIRI range, and there are visible H_2O spectral features between ∼5 and ∼8 μm in the observed spectra. The absence of strong CH_4 absorption features in ∼7-9 μm in the observed spectra allows us to rule out CH_4 at high abundance. The constraints on CO can only be derived from the 5.25 μm bin due to its negligible cross-section elsewhere in the MIRI range, and the constraints on CO_2 can only be driven by the 9-10.5 μm region for the same reason. While NH_3 has strong opacities throughout the MIRI/LRS bandpass, its expected abundance is about two orders of magnitude lower than H_2O. This means that the spectral features of H_2O would dominate over those of NH_3 in the wavelength regions where H_2O has higher or similar opacity compared to NH_3. The notable exception is the wavelength

---

[3] The feature at 8.75 μm may be indicative of SiO_2 crystals in the atmosphere, see, e.g., Grant et al. (2023).

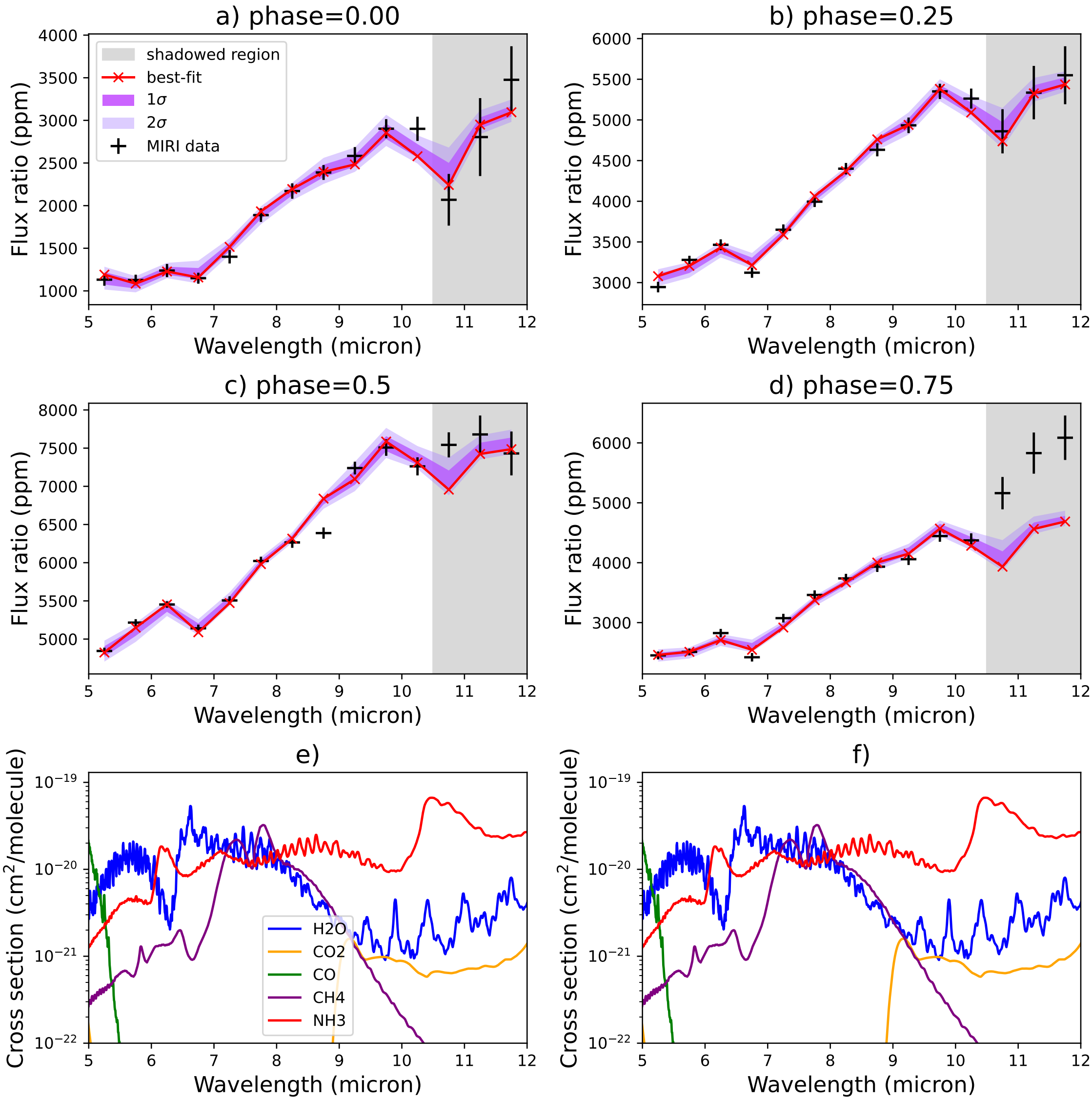

Figure 6.2: a) - d): Best-fit model spectra at the four orbital phases. The 1σ and 2σ central credible intervals are plotted with dark and light purple shading, respectively. The data in the grey shaded region (10.5-12 μm) are affected by the 'shadowed region' systematics and are not included in the retrievals (see Section 6.1). Interestingly, the best-fit model, when extended to 12 μm, is consistent with the current reduction of the 'shadowed region' data for all phases except at phase 0.75. Since NH_3 has strong spectral features in the 'shadowed region', a reliable reduction of the 'shadowed region effect' in the future can refine the abundance constraints on NH_3. Note the absorption feature at the 8.75 μm bin at phase 0.5, which the model cannot explain. e) - f): Cross-sections of the spectrally active molecules included in the retrievals, computed at a spectral resolution of R= 1000 at 1 bar pressure and 1500 K temperature. f) is identical to e) except for the omission of legend for clarity.

region greater than $\sim$8 μm, where the H_2O opacity is generally much lower than the NH_3 opacity, allowing us to constrain the abundance of NH_3.

Recall that the retrievals exclude the data in the 'shadowed region', i.e., the wavelength region longer than 10.5 μm (the grey region in Figure 6.2). Therefore, the retrieval analysis excludes most of the strong NH_3 features centred around 10.5 μm. Interestingly, the best-fit model, when extended to the 10.5-12 μm 'shadowed region', seems consistent with the current reduction of the 'shadowed region' data for three out of four orbital phases (phases 0, 0.25, and 0.5). Because the severity of the 'shadowed region effect' (see Section 6.1) decreased as a function of time since the beginning of the MIRI observation, phases 0.5 and 0.75 are expected to be more severely affected as the observation started just before a secondary eclipse, where phase=0.5 (see Figure 1, Bell et al., 2024). However, since phase 0.5 was observed again at the end of the observation, we may expect it to be more reliable than phase 0.75, which was only observed once. On the other hand, phases 0 and 0.25 are expected to be least affected since they were observed later when much of the 'shadowed region effect' had decayed away (Bell et al., 2023a). Therefore, if the best-fit model is representative of the true atmosphere of WASP-43b and the 'shadowed region' data is more reliable at phases 0, 0.25, and 0.5 than at phase 0.75, then we expect the best-fit model to be more consistent with the 'shadowed region' data at phases 0, 0.25 and 0.5 than at phase 0.75. As shown in Figure 6.2, the best-fit model agrees well with the data in the 'shadowed region' for phase 0 and phase 0.25, and slightly less so at phase 0.5. In contrast, the best-fit model does not agree with the 'shadowed region' data at phase 0.75. Considering the time dependence of the 'shadowed region effect', the data in the 'shadowed region' is consistent with the best-fit model and the presence of NH_3. The important caveat is that the poorly fit systematic noise due to the 'shadowed region effect' could unexpectedly impact the data reduction in Bell et al. (2024), so I do not want to draw any definitive conclusions from the affected data until the systematics issue is fully resolved. Further observations of WASP-43b using other *JWST* instruments at other wavelengths, re-observations of WASP-43b using MIRI after the (still unknown) cause of the 'shadowed region effect' has been mitigated, or a robust reduction of the 'shadowed region effect' can all be used to confirm the NH_3 signal and tighten the constraints on its abundance. In Chapter 8, a significant detection of NH3 is again reported using the combined dayside emission spectrum from *JWST*/MIRI, *JWST*/NIRSpec, and *HST*/WFC3.

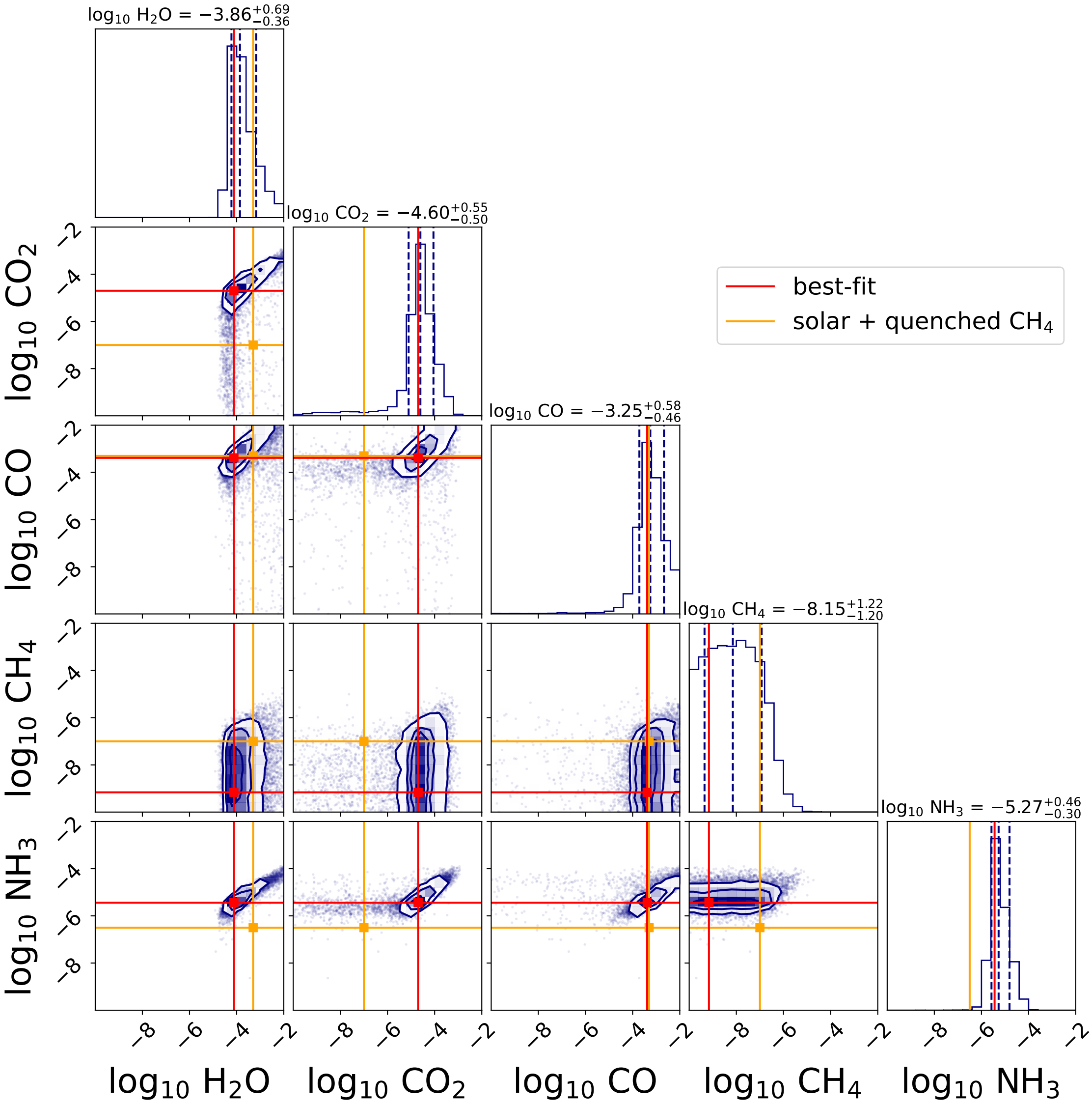

Figure 6.3: Posterior distribution of the molecular abundances. The histograms on the diagonal show the marginalised posterior distributions of each molecular VMR, where the blue dashed lines give the 16%, 50% and 84% percentiles (the percentile values are given at the top of each panel). The off-diagonal plots show the joint posterior distributions of any pairs of parameters. The red solid lines mark the retrieved best-fit parameters (maximum a posteriori parameters). The orange solid lines mark the expected $\log_{10}$ VMR of the molecules in a solar metallicity atmosphere, taking horizontal and vertical mixing into account: -3.3 for H_2O and CO, -7 for CO_2 and CH_4, and -6.5 for NH_3 (Venot et al., 2020; Baeyens et al., 2021). While the abundances of H_2O, CO and CO_2 in the chemical models of Baeyens et al. (2021) and Venot et al. (2020) are approximately constant with altitude, there are some vertical variations in the abundances of CH_4 and NH_3 in the pressure region probed by our observation. I take the 'solar abundances' of CH_4 and NH_3 to be roughly the values at 1 bar.

Molecule	Detection Significance	$\log_{10}$(VMR)
H_2O	6.5σ	$-3.86^{+0.69}_{-0.36}$
CO_2	2.5σ	$-4.60^{+0.55}_{-0.50}$
CO	3.1σ	$-3.25^{+0.58}_{-0.46}$
CH_4	NA	< -6.39
NH_3	4σ	$-5.27^{+0.46}_{-0.30}$

Table 6.5: Detection significance and abundance constraints for the molecules included in the retrieval model. For all molecules apart from CH_4, the constraints are quoted as the medians of the marginalised posterior distributions, with the uncertainties showing the 1σ central credible intervals. For CH_4, the constraints are quoted as the 95% upper limit.

6.3.2 Abundance Constraints

Figure 6.3 shows the retrieved posterior distribution of the molecular abundance. The best-fit model is marked with red solid lines and a solar-metallicity GCM-based chemistry model is marked in orange solid lines for reference (Venot et al., 2020; Baeyens et al., 2021). A Bayesian evidence ratio test as described in Section 4.3 reveals statistically significant evidence of H_2O at 6.5σ, NH_3 at 4σ, and CO at 3.1σ. There is weak evidence of CO_2 (2.5σ) and no detectable level of CH_4 (95% VMR upper limit at $10^{-6.39}$). This analysis is one of the first studies to report evidence of NH_3 in the atmosphere of an exoplanet (MacDonald & Madhusudhan, 2017a,b; Giacobbe et al., 2021; Dyrek et al., 2024). Table 6.5 lists the detection significance and the abundance constraints.

Figure 6.4 shows the constraints on the metallicity and C/O ratio of WASP-43b derived using the posterior distribution of the molecular VMRs, taking the reference solar abundances from Lodders (2010), where the solar C/O ratio is assumed to be 0.457. The metallicity estimate is calculated taking into account all of the molecules included in the retrievals, as listed in Table 6.5, thus taking into account O, C, and N elemental abundances. I tentatively estimate the metallicity of WASP-43b at $1.6^{+4.9}_{-1.0}\times$ solar and its C/O ratio at $0.8^{+0.1}_{-0.2}$. The retrieved abundance constraints and the inferred metallicity and C/O ratio are very similar to the results of Lesjak et al. (2023), who constrained the metallicity at 0.4-7.9× solar and the C/O ratio at 0.78±0.09. The results of Lesjak et al. (2023) were based on high-resolution dayside emission spectra observed with VLT/CRIRES+, thus providing validation to the retrieval results in this chapter with a different observational method.

The metallicity and C/O ratio estimations constrained from the MIRI observation are only tentative for the following reasons. Firstly, constraints on the abundance of CO, which is the dominant carrier of carbon, come only from the shortest 5.25 μm wavelength bin (see Figure 6.2). Since the shortest 1-2 wavelength bins are much more strongly illuminated, they may suffer more from poorly modelled non-linearity effects (Argyriou et al., 2023) in the data reduction stage of Bell et al. (2024). Furthermore, the detection significance of the carbon-bearing molecules is relatively low, as the MIRI/LRS wavelengths are not optimal for constraining the abundances of CO and CO_2. Note also that the gaseous C/O ratio and metallicity may be significantly different from the total atmospheric C/O ratio and metallicity due to cloud formation. As pointed out by Lodders & Fegley (2002) and Woitke et al. (2018), the formation of silicate clouds can take oxygen away from gas-phase molecules. Therefore, if there is a significant level of silicate cloud formation on the nightside of WASP-43b, then the C/O ratio estimation would be an overestimate and the metallicity estimation would be an underestimate[4]. The NIRSpec observation covering the 2.9-5.2 μm region analysed in Chapter 7 more robustly constrains the abundances of both CO and CO_2, which will lead to a more reliable estimation of the C/O ratio and metallicity.

6.3.3 Thermal Structure

Figure 6.5 shows the transmission weighting function of the best-fit model at the sub-stellar point and the nightside. It is apparent that the retrieval is primarily sensitive to pressures in the 1 bar to 1 millibar pressure range. Figure 6.6 plots the retrieved best-fit temperature profile as a function of pressure and longitude in the 1 bar to 1 millibar pressure range, as the temperature profile outside this pressure range is not constrained by the data directly, but rather a consequence of the temperature model parameterisation. The retrieved temperature profile should be interpreted as a latitudinally-averaged thermal structure. As shown in Section 5.3, the retrieved thermal structure from GCM-simulated phase curves using the retrieval scheme employed in this chapter closely resemble the latitudinally-averaged GCM thermal structure using cos(latitude) as the weight. In Irwin et al. (2020), the authors also found that the retrieved thermal structure from GCM-simulated phase curves using a different method closely resembles the latitudinally-averaged GCM thermal structure using cos(latitude) as the weight. This weighting scheme is also commonly used in GCM

---

[4] Assuming an oxygen to silicon elemental ratio of about 15:1 in the atmosphere, and that all of the silicon forms enstatite ($MgSiO_3$) clouds, then silicate cloud formation may remove about 25% of the oxygen from the gas phase. This is, of course, an upper bound.

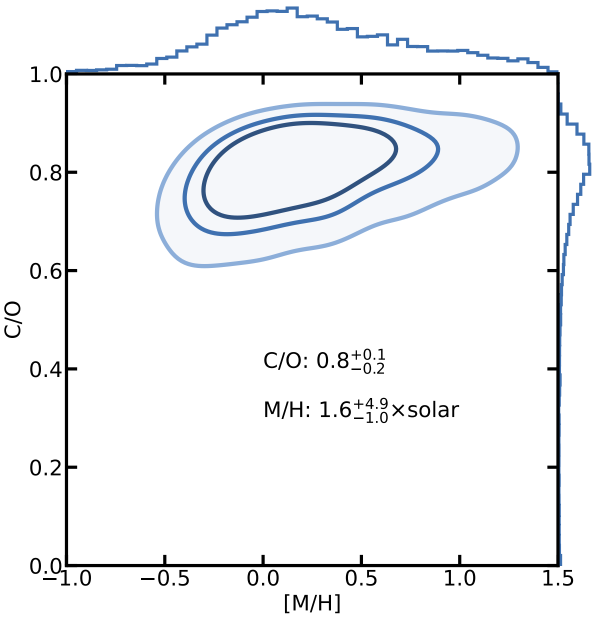

Figure 6.4: Joint distribution of metallicity and C/O ratio derived from the posterior distribution of all molecular VMRs in the retrieval model. The plot was generated using a Python code developed by Adina Feinstein, Luis Welbanks, and Michael Line.

studies to calculate meridionally averaged temperature structure (e.g., Kataria et al., 2015; Mendonça et al., 2018a; Carone et al., 2020).

The best-fit thermal structure, as shown in Figure 6.6, consists of a hot dayside region and a cooler nightside region, where the centre of the hot dayside region is moderately offset to the east. The eastward shift of the retrieved thermal structure is due to the fact that the peak of the phase curve occurred before the secondary eclipse (Bell et al., 2024), and similar phase curve maximum offsets have been observed in numerous hot Jupiters (e.g., Parmentier & Crossfield, 2017, Figure 4). The eastward shift has been predicted and explained by GCM studies (Showman & Guillot, 2002; Showman et al., 2009; Showman & Polvani, 2011), which proposed that strong equatorial super-rotating (eastward) jets would develop in the atmospheres of hot Jupiters and act to transport heat eastwards, so the hottest region of the atmosphere is displaced eastward of the substellar point. This offset is also seen in numerous GCM simulations specific to the planetary parameters of WASP-43b (Kataria et al., 2015; Mendonça et al., 2018a,b; Carone et al., 2020; Schneider et al., 2022; Teinturier et al., 2024). The retrieval constraints an eastward hotspot offset of $8.68^{+0.96}_{-1.14}$ degrees, consistent with the $7.34^{+0.38}_{-0.38}$ degrees eastward offset in Bell et al. (2024). Note that the offset of the phase curve maximum does not necessarily correspond to the

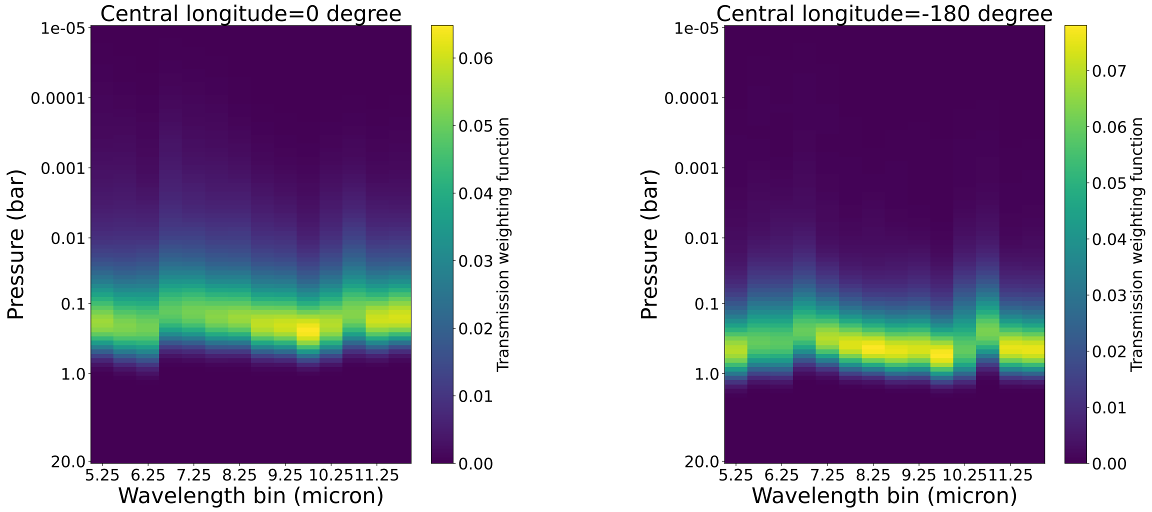

(a) Substellar point.

(b) Nightside.

Figure 6.5: Transmission weighting function of the retrieved best-fit model at the substellar point and on the nightside.

longitudinal offset of the hottest atmospheric region if there are clouds, latitudinal thermal variation, or more complex longitudinal thermal variation than permitted by the retrieval model (Parmentier et al., 2020). The best-fit model in Figure 6.6 resembles some GCM simulations of WASP-43b, for example, Figure 10 in Kataria et al. (2015) and Figure 4 in Mendonça et al. (2018a).

Figure 6.7 shows the retrieved representative nightside and dayside TP profiles T_{night} and T_{day}. There are large day-night temperature contrasts of at least 700 K at all pressure levels. As shown by Figure 6.7, the retrieved temperature profiles are broadly consistent with the TP profiles retrieved in Bell et al. (2024) (see their Figure 4). While the retrievals do not include clouds, past studies (e.g., Burningham et al., 2017; Mollière et al., 2020) have shown that flexible TP profiles can mimic the spectral effects of clouds by becoming more isothermal. The retrieved large day-night temperature contrast and relatively isothermal nightside TP profile are consistent with the presence of clouds on the nightside, which echo the results of Bell et al. (2024) that cloudy GCMs can match the nightside emission of WASP-43b better than cloudless GCMs. However, we cannot rule out or confirm the presence of nightside clouds directly with the retrieval model in this chapter.

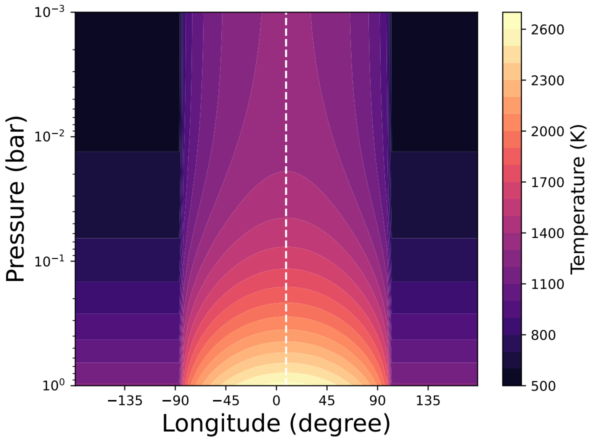

Figure 6.6: Best-fit 2D thermal structure calculated from the maximum a posteriori parameters. The white vertical dashed line marks the position of the hot spot offset.

6.3.4 Full Posterior

Figure 6.8 shows the full posterior distribution of the retrieval model parameters listed in Table 6.2.

6.4 Discussion

This section discusses the retrieval results presented in the previous section in more detail.

6.4.1 Comparison with Bell et al. (2024)

Figure 6.9 compares the retrieved H_2O abundance constraints in Section 6.3.2 to those in Bell et al. (2024), which were obtained by performing retrievals on the spectrum at each orbital phase separately and using a dilution parameter to account for spatial inhomogeneity in thermal structure (Taylor et al., 2020). The retrieval results in this chapter confirm the detection of H_2O at a much higher significance level (6.5σ) than the analysis in Bell et al. (2024), which reported significance ranging from 1.8σ to 4.1σ depending on the orbital phase and the retrieval pipeline. Additionally, the abundance constraints in this chapter are more precise than those in Bell et al. (2024). For the retrievals in Bell et al. (2024) that included H_2O abundance as a free parameter, none of the three retrieval pipelines found any variation of H_2O abundance with orbital phase, which is consistent with the assumption of this thesis that the H_2O abundance is constant across all orbital phases. The retrievals in this chapter also confirm the

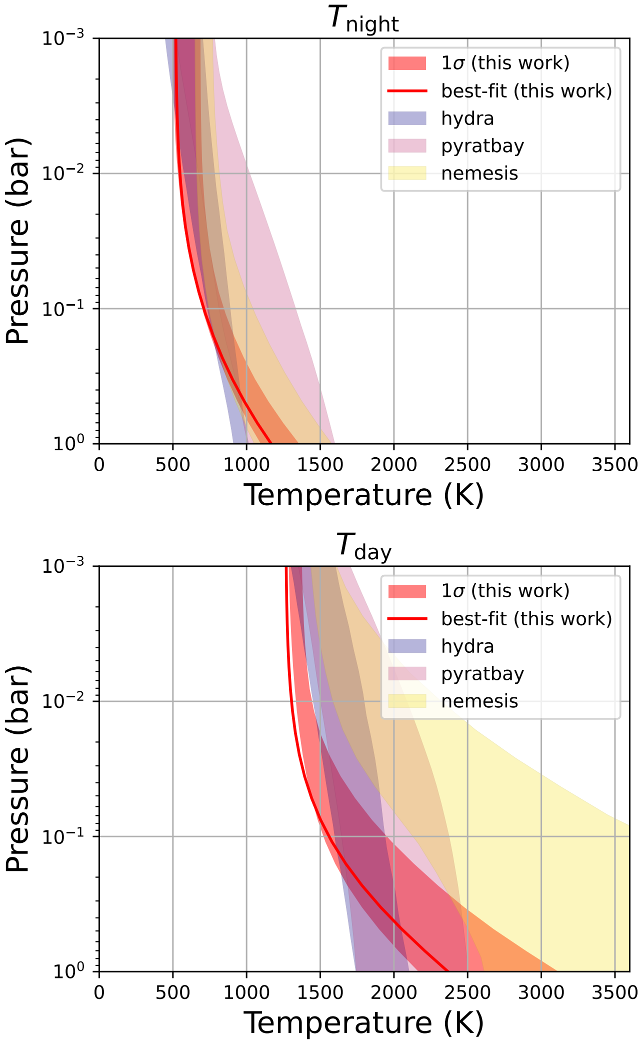

Figure 6.7: Comparison of the retrieved representative dayside/nightside TP profiles in this work to the retrieved dayside/nightside TP profiles in Bell et al. (2024). The best-fit model (red line) is calculated from the maximum a posteriori parameters, whereas the 1σ credible intervals (red shaded areas) are propagated from the 1σ central credible intervals of our posterior distribution. The blue, purple, yellow shaded regions represent the 1σ credible intervals of the TP profiles retrieved using three different retrieval pipelines in Fig. 4 of Bell et al. (2024). I only include the retrievals in which the chemical abundances were free parameters. This plot was generated using a Python code developed by Patricio Cubillos.

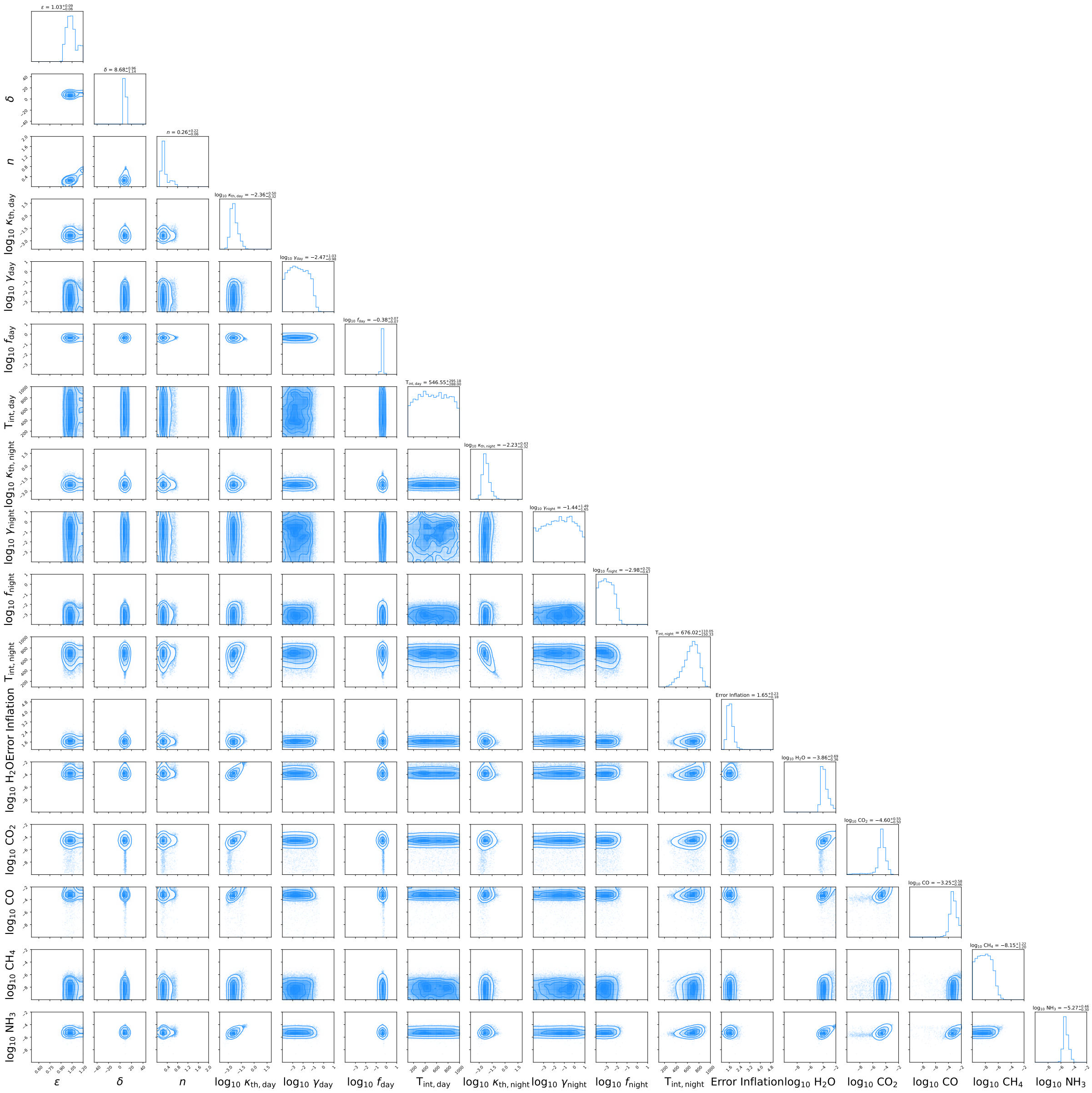

Figure 6.8: Posterior distribution of all the model parameters listed in Table 6.2. The diagonal plots are the marginalised posterior distributions, and the labels above show the posterior medians and 1σ central credible intervals.

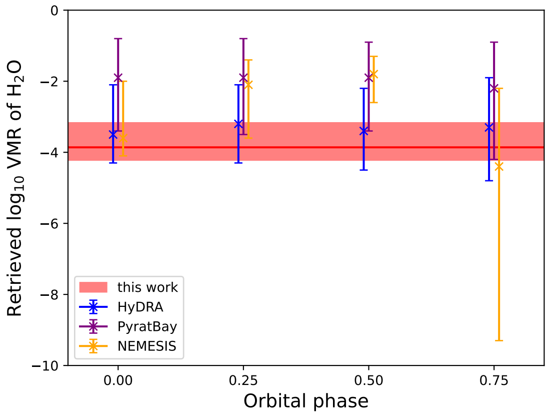

Figure 6.9: Comparison of the retrieved constraints on H_2O VMR in this chapter to those retrieved in Bell et al. (2024). The horizontal red solid line shows the median of the marginalised posterior distribution, and the red shaded region around it shows the 1σ central credible interval. I only include the retrievals in which the abundance of H_2O was a free parameter.

non-detection of CH_4 in Bell et al. (2024) at a 95% upper limit of $10^{-6.39}$. In addition to tightening the abundance constraints reported in Bell et al. (2024), the retrievals in this chapter reveal statistically significant evidence of two additional molecules, namely NH_3 and CO. These results demonstrate the power of fitting phase-resolved emission spectra at multiple orbital phases simultaneously.

6.4.2 Comparison with *HST*/WFC3 + *Spitzer*/IRAC Observation

Figure 6.10 compares the constraints on molecular abundances retrieved from the *JWST*/MIRI observation in this chapter to the abundance constraints retrieved from the *HST*/WFC3 + *Spitzer*/IRAC data set presented in Chapter 5 (Stevenson et al., 2017; Yang et al., 2023). The abundance constraints on H_2O retrieved from the MIRI/LRS data set are entirely consistent with those retrieved from the *HST*/WFC3 + *Spitzer*/IRAC data set. Moreover, as shown in Chapter 5, the *HST*/WFC3 observation probes deeper in the atmosphere (to pressure levels as high as ~10 bar) than the MIRI/LRS observation analysed in this chapter (Yang et al., 2023; Irwin et al., 2020). The consistent H_2O abundance retrieved from the two data sets reaffirms the assumption that the abundance of H_2O is constant with pressure in the observable pressure levels of WASP-43b.

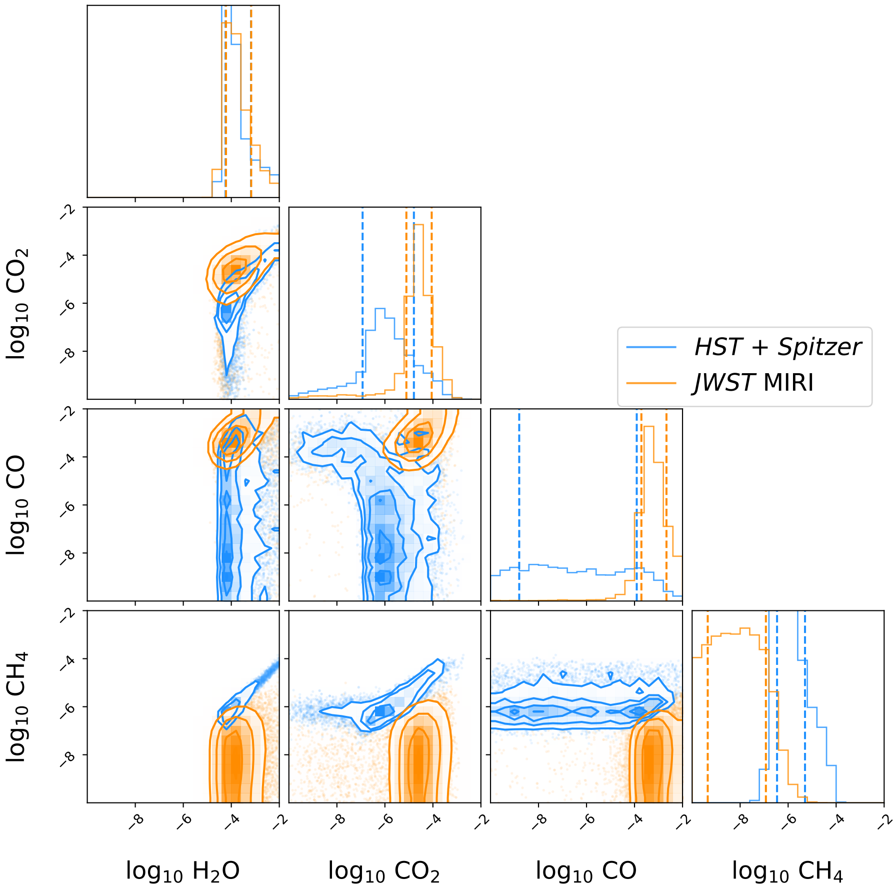

Figure 6.10: Comparison of posterior distributions of the molecular abundances retrieved from (1) the *HST*/WFC3 and *Spitzer*/IRAC data set analysed in Chapter 5; (2) the *JWST* MIRI/LRS data set analysed in this chapter. The histograms on the diagonal show the marginalised posterior distributions of each molecular VMR, where the dashed lines give the 16%, 50% and 84% percentiles. The off-diagonal plots show the joint posterior distributions of any pairs of parameters.

6.4.3 Comparison of H_2O Abundance to Past Studies

Figure 6.11 compares the retrieved H_2O abundance in this chapter to past studies that retrieved H_2O abundance for WASP-43b. Apart from Lesjak et al. (2023), who analysed ground-based high-resolution spectra observed with VLT/CRIRES+, all other studies analysed low-resolution space telescope data. For Bell et al. (2024), Figure 6.11 lists the phase-by-phase retrieval results from the three retrieval pipelines that included H_2O as a free parameter (see also Figure 6.9). The list of studies included is as follows: K14: Kreidberg et al. (2014); S17: Stevenson et al. (2017); F18: Fisher & Heng (2018); W19: Welbanks et al. (2019); C20: Chubb et al. (2020); I20: Irwin et al. (2020); F20: Feng et al. (2020); C21: Cubillos et al. (2021); W22: Welbanks & Madhusudhan (2022); T23: Taylor & Parmentier (2023); Y23: Yang et al. (2023); L23: Lesjak et al. (2023); B24: Bell et al. (2024); Y24: this work. Note that K14, S17, F18, W19, C20, I20, F20, C21, W22, T23, Y23 analysed subsets of *HST*/WFC3 and *Spitzer*/IRAC data, L23 analysed VLT/CRIRES+ data, and B24 and Y24 analysed *JWST*/MIRI data. Note that both C21 and B24 performed phase-by-phase retrievals. Hence, there are multiple error bars for those studies to show the constraints from all phases in Figure 6.11. The constraints for T23 are taken from the Scat.Cloud model in their Table A6. In general, the results of this Chapter agree with previous work.

6.4.4 1D Chemical Modelling

The contents of Section 6.4.4 are work done in collaboration with Dr Shang-Min Tsai as part of Yang et al. (2024b).

This section examines if the retrieved representative dayside TP profile in Section 6.3.3, which should approximate the thermal structure of the dayside hot spot of WASP-43b, can produce the retrieved molecular abundances in Section 6.3.3, assuming the tentatively estimated metallicity and C/O ratio in Section 6.3.2. This is motivated by the assumption that the atmospheric chemical abundances are homogenised to the dayside values by circulation in the pressure region probed by the observation (Cooper & Showman, 2006; Agúndez et al., 2014; Mendonça et al., 2018b; Venot et al., 2020; Baeyens et al., 2021). The remainder of this section is the work done in collaboration with Dr Shang-Min Tsai as part of Yang et al. (2024b).

We employ a 1D chemical model (Tsai et al., 2017, 2021), which simultaneously takes into account thermochemistry, photochemistry and vertical mixing. In particular, we want to explore if we can produce the level of NH_3 retrieved in Section 6.3.2,

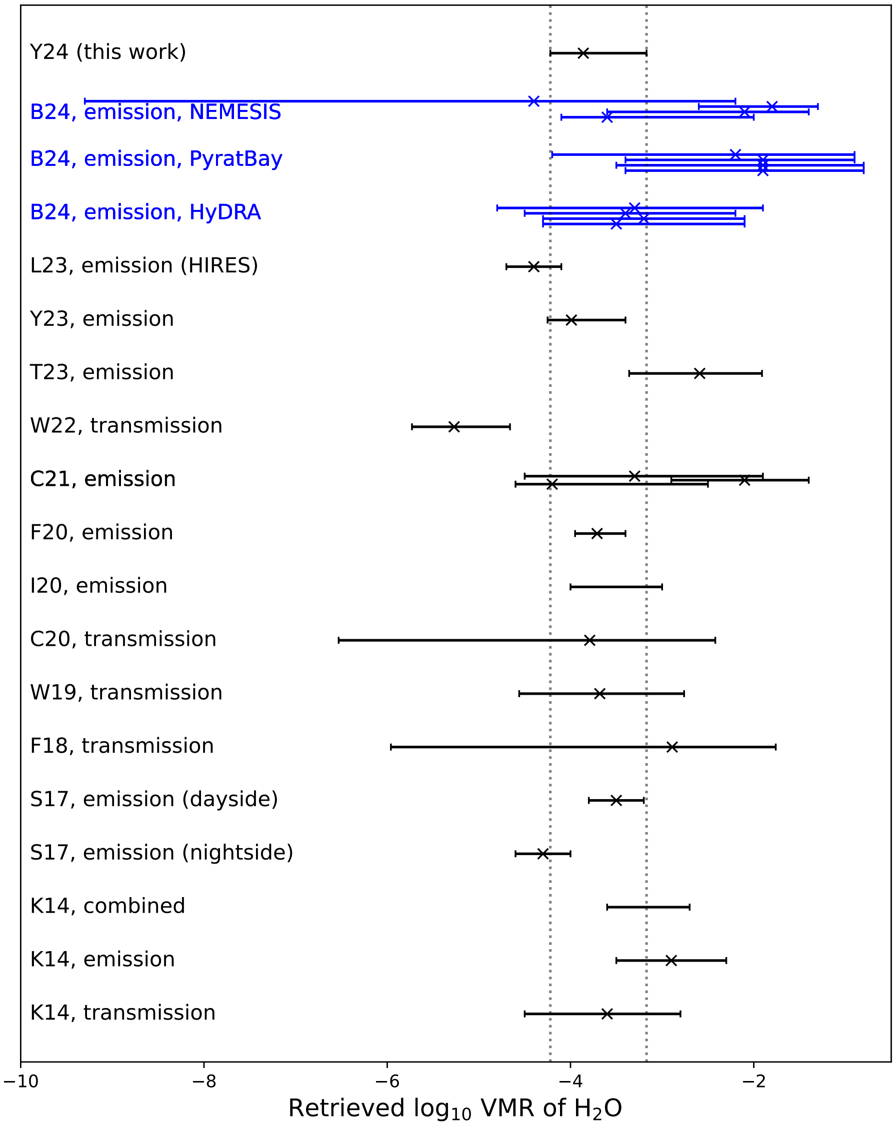

Figure 6.11: Comparison to past studies of WASP-43b that retrieved H_2O abundance. The error bars represent the 1σ credible intervals, and the crosses mark the posterior medians for studies that quoted such values. The vertical dashed lines mark the 1σ credible interval retrieved in this work. See the main text in 6.4.3 for the list of studies included in the plot.

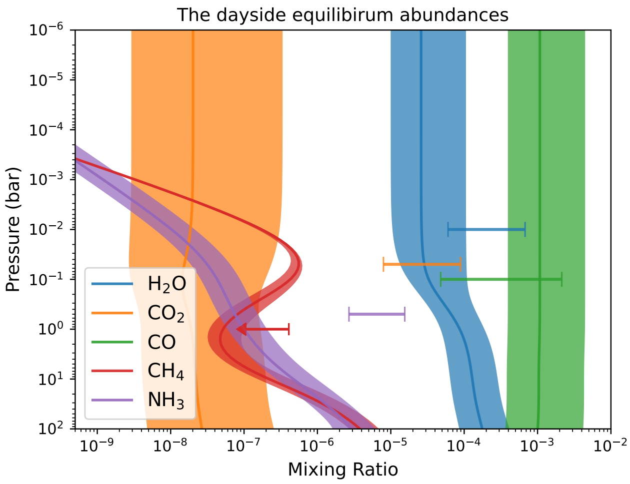

(a) Comparison of dayside thermochemical equilibrium abundances with the retrieved chemical abundances. The shaded regions represent a range of 1D thermochemical equilibrium models consistent with the estimated metallicity in 6.3.2. The horizontal error bars show the 1σ credible intervals of the retrieved molecular abundances. The right edge of the red horizontal arrow shows the 95% upper limit of CH_4 abundance. Note that the vertical positions of the error bars and the arrow are arbitrary.

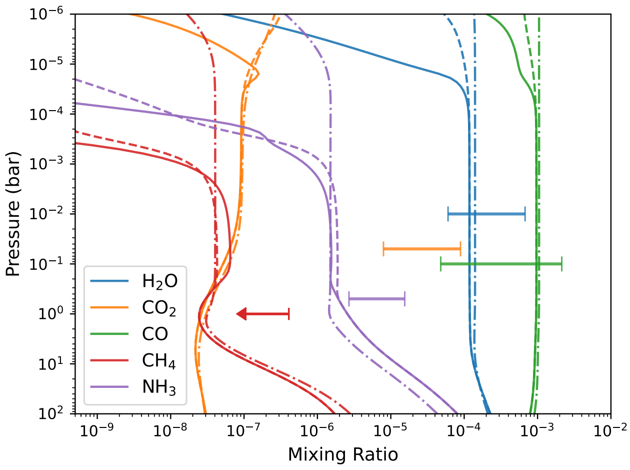

(b) Dayside chemical abundances with vertical mixing and photochemistry. The solid and dashed lines show the model with 1000× enriched N elemental abundance, with the solid lines showing $K_{zz} = 10^8$ cm^2/s and the dashed lines showing $K_{zz} = 10^{10}$ cm^2/s. The dash-dotted lines show the model with 200× enriched N elemental abundance and $K_{zz} = 10^{13}$ cm^2/s.

Figure 6.12: 1D atmospheric chemistry modelling of WASP-43b.

which is more than one order of magnitude higher than several model predictions for a WASP-43b like planet (Venot et al. 2020; Baeyens et al. 2021; Figures 14 and 21 of Fortney et al. 2020). We extend the retrieved representative dayside TP profile in Section 6.3.3 down to 100 bar using the double-grey analytical expression of Heng et al. (2014) to model the chemistry in the deep atmosphere, exploring a range of values for the intrinsic heat flux. We find that the temperature of the retrieved dayside profile T_{day} at 1 bar is so high that the vertical quenching of chemical abundances happens at approximately 1 bar for all the models that we have tested. Therefore, the thermal structure below the 1 bar pressure level does not impact the photospheric composition, and the results of our 1D chemical modelling are insensitive to the particular value of intrinsic heat flux that we choose since we always have to match the deep atmosphere TP profile to the retrieved TP profile at around 1 bar. We then test three different metallicities corresponding to the median and the 1σ central credible interval bounds of the estimated metallicity while keeping the input C/O ratio at 0.8. We also experiment with different values of vertical eddy diffusion coefficient K_{zz} (e.g., Parmentier et al., 2013) and N/H ratios to see if we can produce our retrieved NH_3 abundance using the 1D chemical model.

Figure 6.12 shows the results of our 1D chemical modelling. We first examine the dayside chemical abundances under thermochemical equilibrium without vertical mixing and photochemistry. As shown in Figure 6.12a, our retrieved H_2O and CO abundances are consistent with their equilibrium abundances, which are roughly uniform with pressure. Our retrieved CH_4 upper bound is also consistent with the dayside equilibrium abundance, which is lower than 10^{-6} for pressures lower than 10 bar. However, our retrieved abundances for CO_2 and NH_3 are much higher than the equilibrium abundances. We defer the investigation of CO_2 as its detection significance is relatively low; however, as Chapter 7 will show, the NIRSpec observation does confirm the presence of CO_2 at a slightly lower abundance, which is still much higher than the equilibrium abundance. We include the effect of photochemistry and vertical mixing on the equilibrium abundances in Figure 6.12b. We show three models that can increase the level of NH_3 compared to the equilibrium model: (1) 200× enhanced N/H, $K_{zz} = 10^{13}$ cm^2/s (dash-dotted lines); (2) 1000× enhanced N/H, $K_{zz} = 10^{8}$ cm^2/s (solid lines); (3) 1000× enhanced N/H, $K_{zz} = 10^{10}$ cm^2/s (dashed lines). In these models, the value of K_{zz} sets the strength of vertical mixing, e.g, $K_{zz} = 10^{13}$ cm^2/s corresponds to stronger mixing than $K_{zz} = 10^{10}$ cm^2/s. We illustrate two pathways of increasing the NH_3 abundance in the context of a one-dimensional model: invoking stronger vertical mixing to quench the NH_3 abundance to deeper pressure levels (i.e., increasing K_{zz}) or increasing the overall N abundance in the atmosphere (i.e., increasing N/H). In the context of our 1D chemical modelling, an improbably strong enhancement of N/H (at least >200× enhanced N/H) is necessary to obtain the retrieved NH_3 abundance, even with unlikely high vertical mixing, as illustrated by model (1). This indicates that other effects, such as 3D circulation, must be at play if the retrieved NH_3 abundance is accurate.

6.5 Summary

Atmospheric retrievals using four emission spectra observed at different orbital phases using the MIRI/LRS on the *JWST* reveal evidence of H_2O (6.5σ), NH_3 (4σ), CO (3.1σ), CO_2 (2.5σ) and no evidence of CH_4 in the atmosphere of the hot Jupiter WASP-43b. The abundance constraints yield tentative estimates of the metallicity of WASP-43b at $1.6^{+4.9}_{-1.0}\times$ solar and its C/O ratio at $0.8^{+0.1}_{-0.2}$.

The retrievals fit the spectra simultaneously by employing the Yang et al. (2023) 2D temperature model accounting for a non-uniform temperature profile across the dayside and assuming uniform chemical abundances. This approach more confidently and precisely constrains the molecular abundances than the previous retrievals in Bell et al. (2024), which analysed each orbital phase separately.

Chapter 7

JWST/NIRSpec Phase Curve of WASP-43b

This chapter retrieves the atmospheric properties of WASP-43b from four phase-resolved disc-integrated emission spectra observed with the Near Infrared Spectrograph (NIRSpec) onboard the *JWST*. The spectral resolution of the NIRSpec spectra is roughly between $R = 300$ and $R = 500$, far exceeding the *JWST*/MIRI data analysed in Chapter 6 ($R \leq 20$) and the *HST*/WFC3 + *Spitzer*/IRAC data analysed in Chapter 5 ($R \leq 40$). Consequently, calculating model spectra for the NIRSpec observation is much more computationally expensive. Due to the more than ten-fold increase in computation time, this chapter does not fit the emission spectra at different orbital phases simultaneously, in contrast to the retrievals in Chapters 5 and 6. Instead, this chapter applies a 1D phase-by-phase approach, where the emission spectrum at each orbital phase is analysed independently, assuming a single temperature-pressure (TP) profile and uniform chemistry for each phase. Due to the broad wavelength coverage and high spectral resolution of the NIRSpec data set, the retrievals confidently detect H_2O, CO_2, CO and H_2S even without the boost in the signal-to-noise ratio from analysing multiple orbital phases simultaneously. This chapter further tests multiple temperature models in the retrievals to explore the effect of thermal structure parameterisation on the retrieval results. The retrieval results consistently point to a metal-enriched atmosphere with a super-solar C/O ratio.

This chapter is structured as follows. Section 7.1 describes the *JWST*/NIRSpec observation. Section 7.2 outlines the methodology of the retrievals. Section 7.3 presents the 1D phase-by-phase retrieval results. Section 7.4 discusses the retrieval results, and Section 7.5 concludes the chapter with a summary.

7.1 The *JWST*/NIRSpec Observation

Figure 7.1 shows the four disc-integrated emission spectra derived from the phase curve observation of WASP-43b with the G395H grating of *JWST*/NIRSpec. The data were collected between May 14 and 15, 2023, as part of the *JWST* Cycle 1 GTO-1224 program (PI: Stephan Birkmann). The raw observational data were reduced to the current form by Dr Nicolas Crouzet using the TEATRO pipeline[1]. The emission spectra are binned to constant 0.01-μm bins in the 2.86-5.16 μm wavelength range. There is a $\sim$0.1 μm gap in the spectra located at roughly 3.7-3.8 μm because G395H observations are observed by two physically separate detectors, NRS1 and NRS2 (Birkmann et al., 2022). The emission spectra are generated at four orbital phases: phase = 0 (nightside), phase = 0.25 (evening), phase = 0.5 (dayside), and phase = 0.75 (morning), identical to the MIRI phase-resolved spectra analysed in Chapter 6.

---

[1] `https://github.com/ncrouzet/TEATRO`

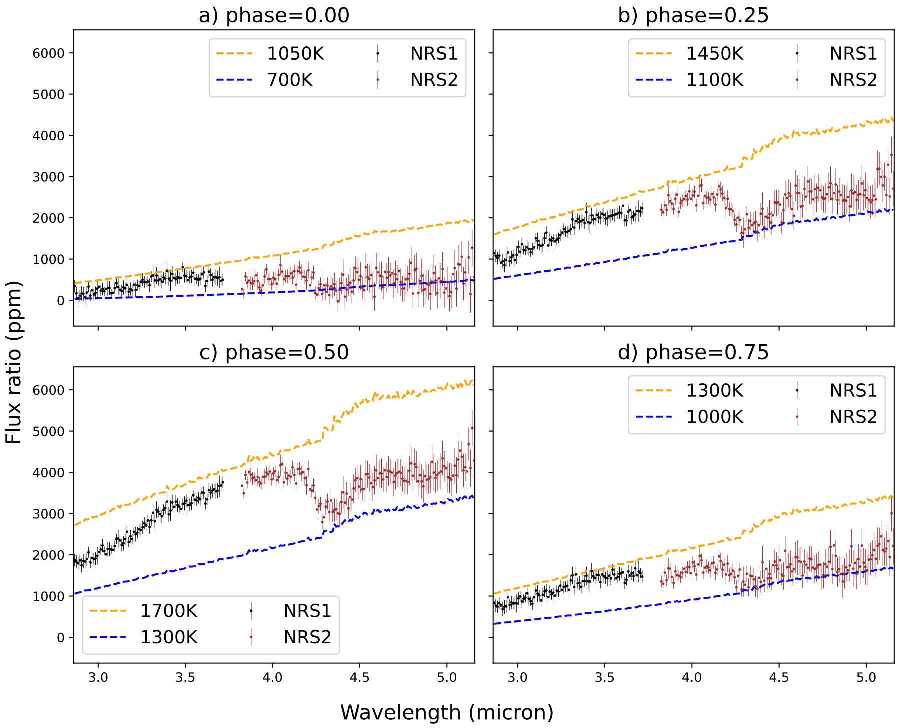

Figure 7.1: *JWST* NIRSpec/G395H emission spectra of WASP-43b at four orbital phases: 0.00 (nightside), 0.25 (evening), 0.50 (dayside), and 0.75 (morning). The spectra are in units of planet-to-star flux ratio. There is a gap at roughly 3.7-3.8 μm between the data observed by the NRS1 and NRS2 collectors. Blackbody emission curves are plotted with dashed lines for comparison. The strong absorption features due to CO_2 and CO between 4-5 μm, and the lack of CH_4 absorption features between 3-4 μm, are apparent in the spectra.

7.2 Methodology

This section describes the retrieval setup. Section 7.2.1 explains the two retrieval approaches employed in this chapter: the '1D phase-by-phase retrieval' and the 'GCM dayside retrieval'. Section 7.2.2 describes the calculation of model emission spectra, which, as in Chapters 5 and 6, is implemented by the NEMESISPY pipeline. Section 7.2.3 reviews the statistical methods used for the retrievals, which are identical to Chapters 5 and 6.

7.2.1 Atmospheric Modelling

This chapter applies two different approaches of atmospheric retrievals on the four NIRSpec spectra: the '1D phase-by-phase retrieval' and the 'GCM dayside retrieval'. The 1D phase-by-phase retrieval approach independently fits the spectrum at each orbital phase. For the retrieval at each orbital phase, a single 1D TP profile and uniform chemistry is assumed. This chapter experiments with two 1D TP profiles: the Guillot (2010) TP profile introduced in Section 3.1.1 and the Madhusudhan & Seager (2009) TP profile introduced in Section 3.1.2. Furthermore, this chapter experiments with a 'dilution parameter' introduced in Taylor et al. (2020), which is a simplistic way of modelling the thermal emission from an inhomogeneous atmosphere: suppose that the observed atmosphere is made up of a hot region and a cold region with average spectral radiances of $\bar{I}_{\text{hot}}(\lambda)$ and $\bar{I}_{\text{cold}}(\lambda)$, respectively. The average spectral radiance of the entire observed atmosphere, $\bar{I}(\lambda)$, can then be written as the weighted sum of the average spectral radiance of the two regions:

$$\bar{I}(\lambda) = s\bar{I}_{\text{hot}}(\lambda) + (1-s) \times \bar{I}_{\text{cold}}(\lambda), \tag{7.1}$$

where s is the fraction of the visible disc covered by the hot region. If we assume that the contribution from the cold region is negligible, then we can approximately fit the observed spectrum with a scaled hot region spectral radiance,

$$\bar{I}(\lambda) \approx s\bar{I}_{\text{hot}}(\lambda). \tag{7.2}$$

Effectively, retrievals using the dilution parameter scale the model spectrum by a free parameter s valued between 0 and 1. In total, this chapter contains phase-by-phase retrievals with four different setups: (1) Guillot (2010) TP profile; (2) Guillot (2010) TP profile + Dilution Parameter; (3) Madhusudhan & Seager (2009) TP profile; (4) Madhusudhan & Seager (2009) TP profile + Dilution parameter. By fitting the spectra with two different TP profiles with and without the dilution parameter, we can explore how the assumed atmospheric temperature model affects the retrieved atmospheric properties.

This chapter also performs a 'GCM dayside retrieval', where we fit the dayside emission spectrum at phase 0.5 (the eclipse spectrum) assuming the fixed thermal structure of the WASP-43b GCM introduced in Section 5.2.1, calculated by Vivien Parmentier using the setup of Parmentier et al. (2016). This test further explores the dependence of the retrieved molecular abundances on the assumed thermal structure parameterisation. The reason that this chapter only fits the dayside spectrum with the GCM thermal structure is that while the dayside of GCM roughly agrees with the observed emission of WASP-43b, the nightside of the GCM is too hot compared with the observation, as was found by Irwin et al. (2020) for the *HST*/WFC3 + *Spitzer*/IRAC data set. The GCM dayside retrieval assumes a uniform chemistry for each orbital phase, as in the phase-by-phase retrievals.

All retrievals include seven spectrally active molecules with uniform volume mixing ratios (VMRs) in a H_2/He-dominated model atmosphere: H_2O, CO_2, CO, CH_4, NH_3, HCN, and H_2S (see Table 7.2 for the corresponding molecular opacity data). The atmospheric model is defined from 20 to 10^{-5} bar, on 40 points equally spaced in log pressure. Table 7.1 gives the full list of free parameters of the retrievals and their priors. Note that an 'offset' parameter is included between the NRS1 data and NRS2 data, which is an additive constant on the model NRS2 spectra to account for potential photometric offsets between data observed with the two detectors. The offset parameters retrieved are around 200 ppm, which is insignificant as those values are on par with typical error bars of the NIRSpec data, as shown by the figures in Chapter 7.3.4.

7.2.2 Radiative Transfer

As in the rest of the thesis, the radiative transfer calculations are implemented by the NEMESISPY package (Yang et al., 2024a) described in Section 2.5, which is a Python development of the Fortran NEMESIS library of Irwin et al. (2008). The NEMESISPY package uses the correlated-k method for radiative transfer (Lacis & Oinas, 1991; Irwin et al., 2008) described in Section 2.3 and the disc-integration method of Irwin et al. (2020) described in 2.4 to calculate the disc-integrated emission spectra at arbitrary orbital phases. Five zenith angle quadratures are used for the Irwin et al. (2020) disc-integration scheme, i.e., setting $N_\mu = 5$ in Equation (2.22). The disc-integrated spectra are computed assuming a circular, tidally locked, and edge-on orbit,

Parameter	Description	Prior	Unit
$\log \kappa_{\text{th}}$	Log_{10} mean infrared opacity (Guillot, 2010)	U(-4,2)	m^2kg^{-1}
$\log \gamma$	Log_{10} ratio of visible and infrared opacities (Guillot, 2010)	U(-4,1)	dimensionless
$\log f$	Log_{10} heat redistribution parameter (Guillot, 2010)	U(-4,1)	dimensionless
T_{int}	Intrinsic heat flux temperature (Guillot, 2010)	U(100,1000)	Kelvin
T_{100mb}	Temperature at 100 mb (Madhusudhan & Seager, 2009)	U(300,3000)	Kelvin
α_1	Layer 1 exponent (Madhusudhan & Seager, 2009)	U(0.02,1)	$\text{Kelvin}^{-1/2}$
α_2	Layer 2 exponent (Madhusudhan & Seager, 2009)	U(0.02,1)	$\text{Kelvin}^{-1/2}$
$\log P_1$	Log_{10} layer 1 base pressure (Madhusudhan & Seager, 2009)	U(0,7)	Pa
$\log P_2$	Log_{10} layer 2 base pressure (Madhusudhan & Seager, 2009)	U(0,7)	Pa
$\log P_3$	Log_{10} layer 3 base pressure (Madhusudhan & Seager, 2009)	U(2,7)	Kelvin
$\log \text{VMR}_{\text{H}_2\text{O}}$	Log_{10} volume mixing ratio of H_2O	U(-10,-1)	dimensionless
$\log \text{VMR}_{\text{CO}_2}$	Log_{10} volume mixing ratio of CO_2	U(-10,-1)	dimensionless
$\log \text{VMR}_{\text{CO}}$	Log_{10} volume mixing ratio of CO	U(-10,-1)	dimensionless
$\log \text{VMR}_{\text{CH}_4}$	Log_{10} volume mixing ratio of CH_4	U(-10,-1)	dimensionless
$\log \text{VMR}_{\text{NH}_3}$	Log_{10} volume mixing ratio of NH_3	U(-10,-1)	dimensionless
$\log \text{VMR}_{\text{HCN}}$	Log_{10} volume mixing ratio of HCN	U(-10,-1)	dimensionless
$\log \text{VMR}_{\text{H}_2\text{S}}$	Log_{10} volume mixing ratio of H_2S	U(-10,-1)	dimensionless
Δ_{NRS2}	Offset of NRS2 data relative to NRS1 data	U(-500,500)	ppm
s	Dilution parameter	U(0,1)	dimensionless

Table 7.1: Free parameters of the retrieval model and their priors. The phase-by-phase retrievals with different setups have different temperature parameters, which are indicated by the parentheses. All phase-by-phase retrievals and the GCM dayside retrieval share the same VMR parameters and the same offset parameter. There are no free temperature parameters in the GCM dayside retrieval as the temperature structure is assumed to be the fixed GCM thermal structure.

using the parameters in Table 6.3. The planetary emission is converted to planet-to-star flux ratios using a stellar spectrum computed from the PHOENIX stellar model (Allard & Hauschildt, 1995; Hauschildt et al., 1999; Husser et al., 2013), generated assuming an effective temperature of 4300 K, a surface gravity of log(g)= 4.50, and a solar metallicity. The choice of stellar model is informed by the work done for Bell et al. (2024). Note that the above setup is identical to the MIRI analysis presented in Chapter 6.

The input molecular opacity data for the radiative transfer calculations in this chapter are taken from the ExoMol database (Chubb et al., 2021). Channel-integrated k-tables are generated at the resolution of the spectra (constant 0.01 μm bins) from the original ExoMol k-tables, which were computed at a resolving power of R=1000. The radiative transfer calculation models the molecular absorption due to the seven spectrally active molecules in the model and the collision-induced absorption due to H_2–H_2 pairs and H_2–He pairs with data from Borysow & Frommhold (1989) and Borysow et al. (1989). The full list of opacity data is given in Table 7.2, and Figure 7.2 plots the absorption cross-sections of the molecules in the NIRSpec wavelength range.

Molecule	Opacity Data
H_2O	Polyansky et al. (2018)
CO_2	Yurchenko et al. (2020)
CO	Li et al. (2015)
CH_4	Yurchenko et al. (2017)
NH_3	Coles et al. (2019)
HCN	Barber et al. (2014)
H_2S	Azzam et al. (2016)
He	Borysow & Frommhold (1989) & Borysow et al. (1989)
H_2	Borysow & Frommhold (1989) & Borysow et al. (1989)

Table 7.2: Opacity data used to calculate emission spectra in this chapter. Apart from the H_2-H_2 and H_2-He collision-induced absorption opacity, all data are downloaded from the ExoMol database (Chubb et al., 2021).

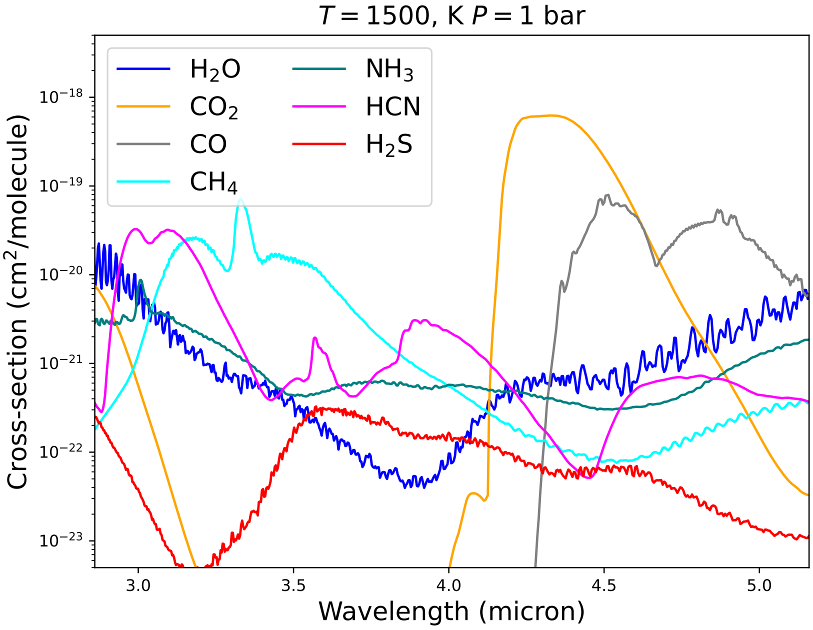

Figure 7.2: Absorption cross-sections of the molecules included in the retrievals in the NIRSpec/G395H wavelength range computed using the opacity data listed in Table 7.2.

7.2.3 Statistical Method

The retrievals find the posterior distribution of the free parameters listed in Table 7.1 given the NIRSpec data using the Nested Sampling algorithm (Feroz & Hobson, 2008), as described in Section 4.2.3. As in the rest of the thesis, this chapter uses the PyMultiNest software package (Buchner et al., 2014) to implement the algorithm, using 1000 sampling live points. For each molecule, the significance of its detection is calculated via Bayesian model comparison by performing seven additional retrievals, each omitting one of the seven molecules in the fiducial model, as described in Section 4.3. The detection significance of a molecule is then calculated by computing the Bayes factor of the fiducial model over the model without the particular molecule, following Trotta (2008) and Benneke & Seager (2013).

7.3 Results

The wide wavelength coverage and high spectral resolution of the NIRSpec spectra enable confident detection of key molecular species. Section 7.3.1 lists the molecular detection significance of the retrievals. Section 7.3.2 presents the constraints on molecular abundances and compares them to those retrieved from the MIRI data set presented in Chapter 6. Section 7.3.3 explores the retrieved thermal structure from the NIRSpec data. Section 7.3.4 includes supplementary results of the phase-by-phase retrievals.

7.3.1 Molecular Detections

The retrievals give confident constraints on the presence of carbon-bearing molecules in the atmosphere of WASP-43b, which is to be expected since CO_2, CO, and CH_4 all have prominent spectral features in the wavelengths covered by NIRSpec/G395H, as shown in Figure 7.2. Indeed, the strong features of CO_2 and CO between 4-5 μm are clearly visible in the observed spectra, as shown in Figure 7.1. Table 7.3 and 7.4 list the molecular detection significance for the phase-by-phase retrievals, where a molecule is considered detected when its detection significance is greater than or equal to 3σ. Furthermore, if the inclusion of a molecule reduces the Bayesian evidence of the model, then it is considered to be not favoured by the data.

The phase-by-phase retrievals show clear detections of CO_2 and CO. CO_2 is detected at all orbital phases for all phase-by-phase retrieval setups. CO is also detected for all phase-by-phase retrieval setups at all orbital phases, except for the retrieval at phase 0.75 using Guillot (2010) TP Profile with the dilution parameter. Even for that exception, the detection significance for CO is 1.97σ, so the data weakly prefer the presence of CO. These results mark the first confident detection of CO_2 in the atmosphere of WASP-43b in the literature, as well as the first confident detection of CO in WASP-43b using a space telescope (in addition to the detection of CO in WASP-43b using the ground-based *VLT*/CRIRES+ instrument by Lesjak et al. 2023), confirming the weak detections from the MIRI data set in Chapter 6. On the other hand, the phase-by-phase retrievals rule out CH_4 at detectable levels at all orbital phases for all retrieval setups, except for the retrieval using the Guillot (2010) TP profile at phase 0.5, where it is only weakly favoured by the data with a detection significance of 1.43σ. The detections of CO, CO_2, and the non-detection of CH_4 in the phase-by-phase retrievals are backed up by the GCM dayside retrieval, as shown by Table 7.5, which is a testament that these results are robust to the choice of thermal structure parameterisation. Furthermore, these results are also consistent with the *JWST*/MIRI retrieval results in Chapter 6. For HCN, the retrievals do not give a definitive verdict. It is not detected at any orbital phase with any retrieval setup in the phase-by-phase retrievals, and it is disfavoured by exactly half of the retrievals and weakly favoured by the other half. It is also not detected in the GCM dayside retrieval.

In addition to the detections of CO and CO_2 across orbital phases, the retrievals also show detections of H_2O and H_2S at some orbital phases. Referring again to Tables 7.3 and 7.4, H_2O is detected at greater than 5σ at phase 0.5 for all phase-by-phase retrieval setups, which is backed up by the 5.3σ detection in the GCM dayside retrieval, as shown in Table 7.5. H_2S is also detected for at least one orbital phase for all phase-by-phase retrieval setups. However, the GCM dayside retrieval only showed weak evidence of H_2S at 2.6σ. The detection of H_2O is consistent with the *JWST*/MIRI retrieval results in Chapter 6 and the *HST* + *Spitzer* retrievals in Chapter 5, whereas the detection of H_2S is the first evidence of sulphur chemistry in the atmosphere of WASP-43b in the literature. In contrast to the *JWST*/MIRI retrieval results in Chapter 6, NH_3 is not detected in the NIRSpec data in any of the retrievals. Nonetheless, the NIRSpec data also does not rule out the presence of NH_3, as it is favoured by more than 75% of the phase-by-phase retrievals. In particular, as shown by Figure 7.3, the NIRSpec data in this chapter do not rule out the NH_3 abundance retrieved from the MIRI data in Chapter 6.

Guillot (2010) TP Profile								
	Without Dilution				With Dilution			
Phase	0.00	0.25	0.50	0.75	0.00	0.25	0.50	0.75
H_2O	1.06	3.58	5.65	1.34	N.F.	3.36	6.43	N.F.
CO_2	4.34	8.58	8.84	4.84	4.77	9.05	9.04	4.99
CO	4.86	9.04	10.32	8.25	3.27	4.36	6.40	1.97
CH_4	N.F.	N.F.	1.43	N.F.	N.F.	N.F.	N.F.	N.F.
NH_3	1.76	1.20	1.33	N.F.	2.42	1.52	N.F.	2.21
HCN	N.F.	1.47	1.82	N.F.	N.F.	1.54	2.04	N.F.
H_2S	3.01	3.06	4.52	N.F.	2.87	3.36	6.43	3.61

Table 7.3: Molecular detection significance (σ) in the phase-by-phase retrievals using the Guillot (2010) TP profile with and without the dilution parameter at the four orbital phases. Molecules not favoured by the data at an orbital phase are denoted by 'N.F.'. Significant detections ($\geq 3\sigma$) are coloured in blue.

Madhusudhan & Seager (2009) TP Profile								
	Without Dilution				With Dilution			
Phase	0.00	0.25	0.50	0.75	0.00	0.25	0.50	0.75
H_2O	N.F.	2.30	5.68	1.00	1.45	2.69	6.01	N.F.
CO_2	4.86	9.64	9.64	6.11	5.01	9.62	8.82	5.58
CO	5.10	9.76	11.53	8.96	5.77	12.89	16.43	7.56
CH_4	N.F.	N.F.	N.F.	N.F.	N.F.	N.F.	N.F.	N.F.
NH_3	1.68	1.71	1.78	1.42	2.13	1.91	N.F.	2.07
HCN	N.F.	N.F.	2.02	1.56	1.50	N.F.	N.F.	1.38
H_2S	1.83	3.02	2.23	1.70	2.06	3.26	N.F.	1.57

Table 7.4: Molecular detection significance (σ) in the phase-by-phase retrievals using the Madhusudhan & Seager (2009) TP profile with and without the dilution parameter at the four orbital phases. See Table 7.3 for further detail.

GCM Dayside Retrieval (Phase 0.50)						
H_2O	CO_2	CO	CH_4	NH_3	HCN	H_2S
5.3	12.8	13.8	N.F.	1.5	2	2.6

Table 7.5: Molecular detection significance (σ) in the retrieval of the dayside spectrum assuming a GCM thermal structure. See Table 7.3 for further detail.

7.3.2 Molecular Abundance

Based on the abundance constraints retrieved from the *JWST*/MIRI observation in Chapter 6, which are consistent with the constraints retrieved from the *HST*/WFC3 + *Spitzer*/IRAC observation in Chapter 5, we expect that the atmospheric metallicity of WASP-43b should range from moderately sub-solar to moderately super-solar ($1.6^{+4.9}_{-1.0}\times$ solar from MIRI retrievals). From a theoretical standpoint, the core accretion model of planet formation also predicts that more massive planets should have lower metallicity, a trend which is well supported by the Solar System planets. Following the above arguments, we would expect the volume mixing ratio of CO in the atmosphere of WASP-43b to be around 10^{-3}, which is roughly the predicted value by chemistry models assuming a solar metallicity.

The retrieval results of the NIRSpec data dramatically differ from the above expectation. Figure 7.3 shows the constraints on the molecular abundances retrieved from the NIRSpec data, which are also listed in Tables 7.6, 7.7, and 7.8. The key result is that CO is detected at extremely high abundance: the volume mixing ratio of CO is constrained roughly between 10^{-1} and 10^{-3} depending on the orbital phase and retrieval setup. If we focus on the abundance constraints retrieved from the dayside spectrum (phase=0.50), which are more precise as it is the phase with the highest signal-to-noise ratio, then the VMR of CO is constrained roughly between 10^{-1} and 10^{-2}, close to the upper limit of the prior on molecular abundance. Figures 7.8, 7.9, 7.10, and 7.11 in Section 7.3.4, which contain the marginalised posterior distribution of the molecular abundances for the phase-by-phase retrievals, will further show that the phase-by-phase retrievals can only retrieve a lower bound for the CO abundance, as the posterior distributions significantly overlap with the upper limit of the prior (10^{-1}). The dayside GCM retrieval, which is the only retrieval that yields bounded constraints on CO, constrains the CO abundance at roughly $10^{-1.6}$ (Table 7.8), that is, between 1% and 4%. These values indicate a metallicity of 10× solar or more. This is intriguing, given that the stellar metallicity of WASP-43 is approximately solar.

The VMR of CO_2, constrained between 10^{-5} and 10^{-6}, supports the argument that WASP-43b has an elevated metallicity, as chemistry models predict the VMR of CO_2 at between 10^{-7} and 10^{-6} for a solar metallicity. The VMR of H_2S, constrained at between $10^{-2.5}$ and $10^{-4.0}$, also supports the high metallicity hypothesis, though caution is needed as the detection of H_2S varies with both orbital phase and retrieval setup, and the detection significances are relatively low. Note that the retrieved constraints on CO are somewhat higher than the $10^{-3.71} - 10^{-2.67}$ constraints retrieved from the MIRI data, whereas the retrieved constraints on CO_2 are broadly consistent with the $10^{-5.10} - 10^{-4.05}$ constraints retrieved from MIRI. However, as mentioned in Chapter 6, MIRI/LRS data are not optimised for constraining these molecules, and the constraints on CO and CO_2 derived from NIRSpec should take precedence over those retrieved from MIRI. The H_2O VMR constrained from the NIRSpec data is between 10^{-2} and 10^{-3}, which is higher than the $10^{-4.22} - 10^{-3.17}$ constraints retrieved from MIRI. While this disagreement seems significant, in Chapter 8, where we fit the *HST*/WFC3, *JWST*/MIRI and *JWST*/NIRSpec dayside emission spectra simultaneously, it will be evident that a H_2O abundance closer to that retrieved from MIRI and *HST*/WFC3 can fit all observations simultaneously.

Table 7.8 additionally shows the molecular constraints retrieved assuming a GCM thermal structure at phase 0.5. The point of this exercise is to explore the effect that thermal structure parameterisation has on the retrieved abundance. For CO and CO_2, the abundances retrieved assuming a GCM thermal structure agree nicely with those retrieved using 1D TP profiles. In contrast, the abundance of H_2O and H_2S are both significantly lower than those retrieved using 1D TP profiles. This illustrates that thermal structure parameterisation is a dominant source of uncertainty in the retrievals of hot Jupiter emission spectra. Interestingly, the H_2O abundance retrieved assuming the GCM thermal structure agrees better with that retrieved from MIRI.

Figure 7.4 and Figure 7.5 show the constraints on the metallicity and C/O ratio of WASP-43b derived from the NIRSpec spectra using the posterior distribution of the molecular VMRs, taking the reference solar abundances from Lodders (2010). The metallicity estimate is calculated taking into account all of the molecules included in the retrievals, as listed in Table 6.5, thus taking into account O, C, S, and N elemental abundances. It is evident that the metallicity of WASP-43b is super-solar. If we take values at the highest signal-to-noise phase (phase 0.5), then the metallicity is roughly constrained to be at least 10× solar. The C/O ratio, due to the high CO abundance, is estimated to be close to unity. Taking the dayside value again, the C/O ratio is constrained to be between 0.8 and 1. For the dayside retrievals, Figure 7.6 shows the joint posterior distribution of the C/O ratio and metallicity retrieved from the data.

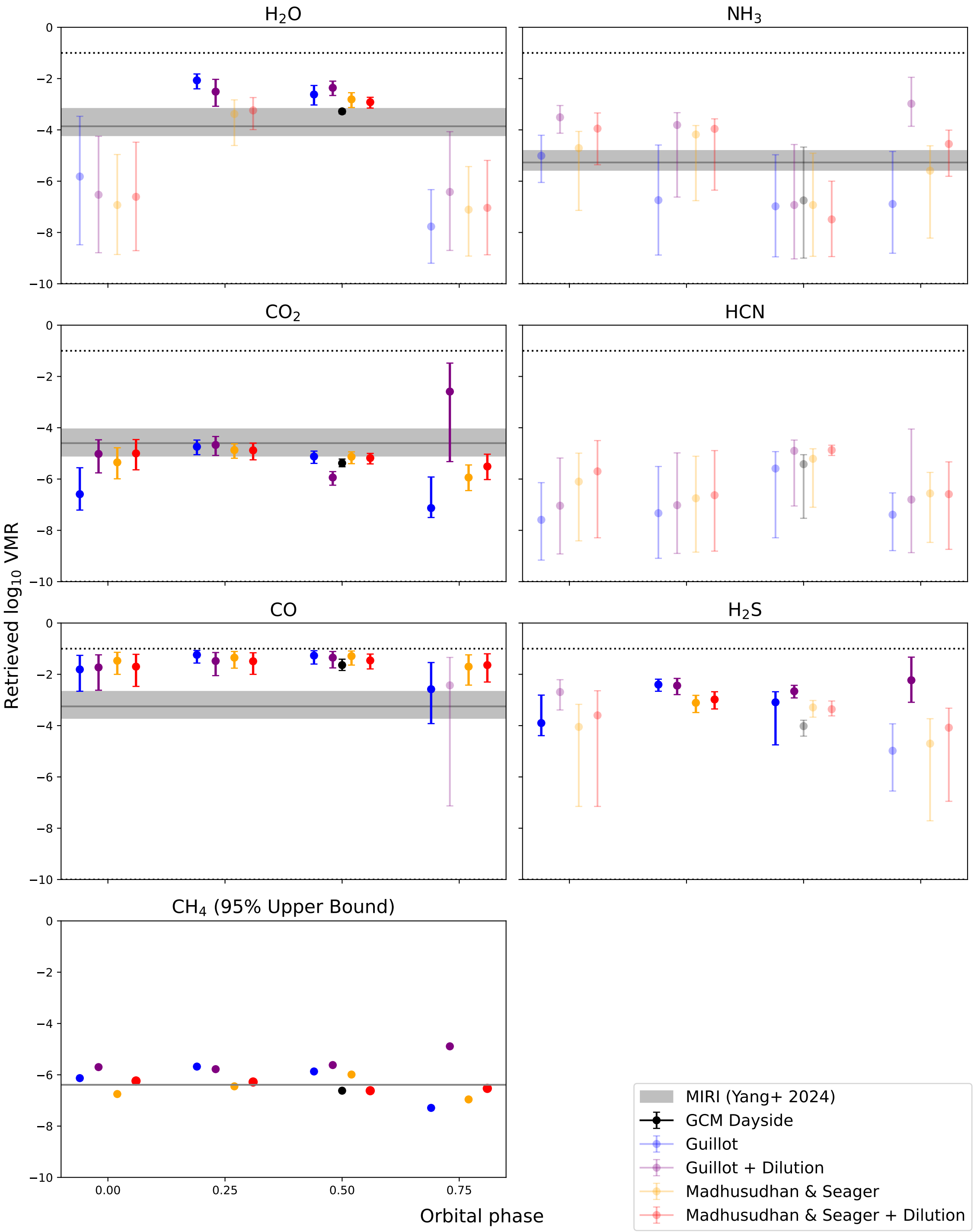

Figure 7.3: Retrieved molecular abundances for each molecule at different orbital phases. For all molecules apart from CH_4, the error bars show the 1σ central credible interval around the median of the marginalised posterior distribution. For CH_4, 95% upper limits are shown. The data points are slightly offset from each other in orbital phase for clarity. Significant detections ($\geq 3\sigma$) are indicated with more opaque markers. The data can be found in Tables 7.6, 7.7, and 7.8. For comparison, the MIRI results from Chapter 6 are plotted in grey.

Guillot (2010) Profile								
	Without Dilution				With Dilution			
Phase	0.00	0.25	0.50	0.75	0.00	0.25	0.50	0.75
H_2O	$-5.82^{+2.35}_{-2.66}$	$-2.07^{+0.25}_{-0.33}$	$-2.62^{+0.35}_{-0.41}$	$-7.77^{+1.44}_{-1.34}$	$-6.53^{+2.28}_{-2.26}$	$-2.51^{+0.48}_{-0.57}$	$-2.36^{+0.26}_{-0.30}$	$-6.42^{+2.35}_{-2.28}$
CO_2	$-6.59^{+1.03}_{-0.62}$	$-4.74^{+0.26}_{-0.31}$	$-5.12^{+0.21}_{-0.27}$	$-7.13^{+1.21}_{-0.37}$	$-5.02^{+0.55}_{-0.74}$	$-4.67^{+0.33}_{-0.41}$	$-5.04^{+0.23}_{-0.30}$	$-2.59^{+1.11}_{-2.73}$
CO	$-1.81^{+0.55}_{-0.85}$	$-1.24^{+0.17}_{-0.32}$	$-1.27^{+0.19}_{-0.33}$	$-2.58^{+1.04}_{-1.34}$	$-1.73^{+0.49}_{-0.89}$	$-1.48^{+0.33}_{-0.57}$	$-1.35^{+0.24}_{-0.40}$	$-2.43^{+1.09}_{-4.70}$
CH_4	$-8.22^{+1.30}_{-1.08}$	$-7.71^{+1.49}_{-1.52}$	$-7.97^{+1.49}_{-1.31}$	$-8.78^{+0.89}_{-0.76}$	$-7.83^{+1.44}_{-1.35}$	$-7.84^{+1.45}_{-1.38}$	$-7.67^{+1.49}_{-1.55}$	$-7.41^{+1.65}_{-1.69}$
NH_3	$-5.01^{+0.80}_{-1.04}$	$-6.74^{+2.15}_{-2.14}$	$-6.98^{+2.01}_{-1.97}$	$-6.89^{+2.05}_{-1.92}$	$-3.51^{+0.46}_{-0.62}$	$-3.81^{+0.48}_{-2.81}$	$-6.93^{+2.36}_{-2.10}$	$-2.98^{+1.03}_{-0.88}$
HCN	$-7.59^{+1.45}_{-1.57}$	$-7.33^{+1.82}_{-1.76}$	$-5.59^{+0.66}_{-2.70}$	$-7.39^{+0.85}_{-1.40}$	$-7.04^{+1.86}_{-1.88}$	$-7.02^{+2.04}_{-1.88}$	$-4.90^{+0.42}_{-2.15}$	$-6.80^{+2.75}_{-2.07}$
H_2S	$-3.90^{+1.09}_{-0.49}$	$-2.40^{+0.21}_{-0.26}$	$-3.09^{+0.41}_{-1.66}$	$-4.98^{+1.05}_{-1.57}$	$-2.69^{+0.48}_{-0.70}$	$-2.44^{+0.28}_{-0.35}$	$-2.66^{+0.23}_{-0.26}$	$-2.23^{+0.90}_{-0.86}$

Table 7.6: Molecular abundance constraints retrieved using the Guillot (2010) TP profile with and without the dilution parameter at the four orbital phases, quoted as the medians of the marginalised posterior distributions, with the uncertainties showing the 1σ central credible intervals. Significant detections are coloured in blue.

Madhusudhan & Seager (2009) TP Profile								
	Without Dilution				With Dilution			
Phase	0.00	0.25	0.50	0.75	0.00	0.25	0.50	0.75
H_2O	$-6.93^{+1.97}_{-1.93}$	$-3.38^{+0.55}_{-1.23}$	$-2.81^{+0.26}_{-0.32}$	$-7.11^{+1.68}_{-1.81}$	$-6.61^{+2.13}_{-2.10}$	$-3.24^{+0.50}_{-0.75}$	$-2.92^{+0.19}_{-0.23}$	$-7.04^{+1.85}_{-1.83}$
CO_2	$-5.35^{+0.57}_{-0.64}$	$-4.87^{+0.24}_{-0.32}$	$-5.13^{+0.19}_{-0.27}$	$-5.94^{+0.49}_{-0.51}$	$-5.00^{+0.54}_{-0.64}$	$-4.88^{+0.28}_{-0.37}$	$-5.18^{+0.18}_{-0.23}$	$-5.51^{+0.48}_{-0.51}$
CO	$-1.47^{+0.33}_{-0.53}$	$-1.35^{+0.24}_{-0.41}$	$-1.29^{+0.20}_{-0.35}$	$-1.70^{+0.46}_{-0.72}$	$-1.70^{+0.48}_{-0.77}$	$-1.49^{+0.33}_{-0.51}$	$-1.46^{+0.25}_{-0.33}$	$-1.64^{+0.44}_{-0.66}$
CH_4	$-8.47^{+1.09}_{-0.97}$	$-8.24^{+1.21}_{-1.18}$	$-7.92^{+1.37}_{-1.36}$	$-8.56^{+1.02}_{-0.91}$	$-8.12^{+1.18}_{-1.15}$	$-8.13^{+1.25}_{-1.19}$	$-8.30^{+1.08}_{-0.96}$	$-8.31^{+1.13}_{-1.06}$
NH_3	$-4.71^{+0.65}_{-2.43}$	$-4.18^{+0.35}_{-2.58}$	$-6.93^{+2.02}_{-2.00}$	$-5.59^{+0.97}_{-2.63}$	$-3.95^{+0.61}_{-1.41}$	$-3.96^{+0.39}_{-2.39}$	$-7.49^{+1.49}_{-1.45}$	$-4.55^{+0.54}_{-1.26}$
HCN	$-6.10^{+1.11}_{-2.31}$	$-6.75^{+1.64}_{-2.10}$	$-5.21^{+0.39}_{-1.89}$	$-6.59^{+0.82}_{-1.91}$	$-5.70^{+1.20}_{-2.59}$	$-6.63^{+1.74}_{-2.18}$	$-4.87^{+0.19}_{-0.21}$	$-6.59^{+1.26}_{-2.15}$
H_2S	$-4.05^{+0.88}_{-3.10}$	$-3.11^{+0.29}_{-0.38}$	$-3.29^{+0.27}_{-0.38}$	$-4.70^{+0.97}_{-3.01}$	$-3.60^{+0.96}_{-3.55}$	$-2.98^{+0.30}_{-0.37}$	$-3.36^{+0.21}_{-0.26}$	$-4.08^{+0.76}_{-2.87}$

Table 7.7: Molecular abundance constraints retrieved using the Madhusudhan & Seager (2009) TP profile with and without the dilution parameter at the four orbital phases, quoted as the medians of the marginalised posterior distributions, with the uncertainties showing the 1σ central credible intervals. Significant detections are coloured in blue.

GCM Dayside Fit						
H_2O	CO_2	CO	CH_4	NH_3	HCN	H_2S
$-3.28^{+0.08}_{-0.09}$	$-5.38^{+0.16}_{-0.14}$	$-1.64^{+0.23}_{-0.21}$	$-8.38^{+1.24}_{-1.08}$	$-6.74^{+2.08}_{-2.25}$	$-5.42^{+0.37}_{-2.11}$	$-4.02^{+0.23}_{-0.39}$

Table 7.8: Molecular abundances retrieved using the WASP-43b GCM thermal structure at phase 0.5, quoted as the medians of the marginalised posterior distributions, with the uncertainties showing the 1σ central credible intervals.

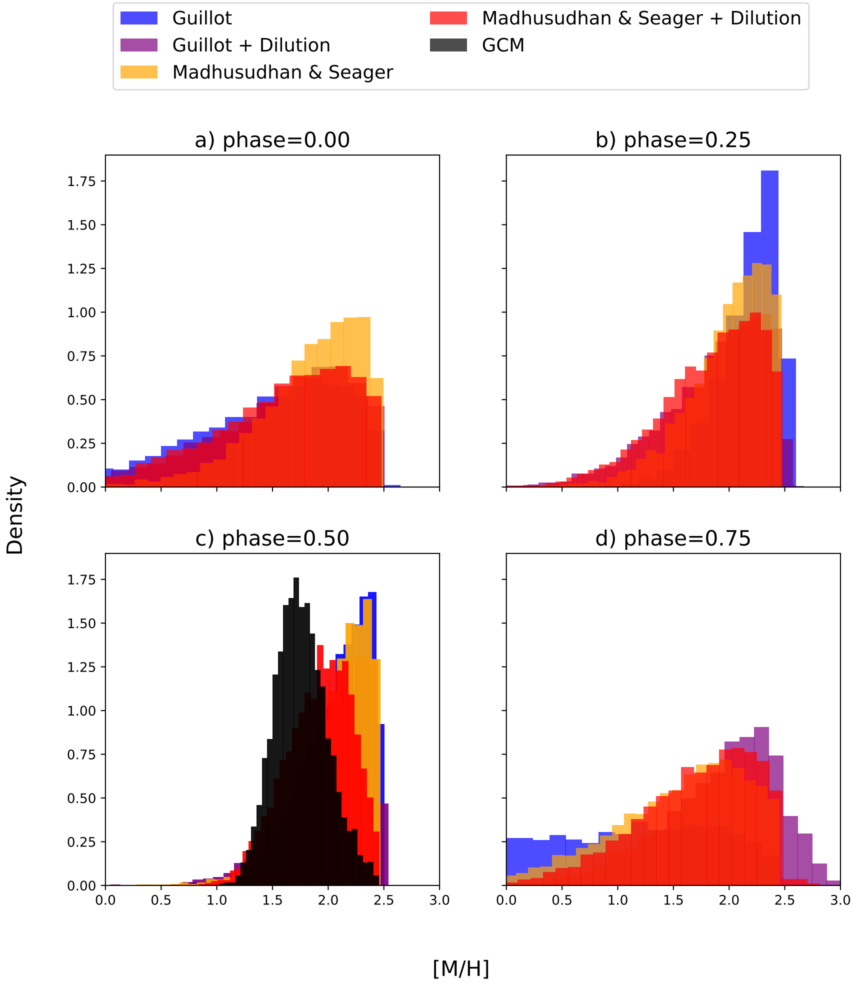

Figure 7.4: Retrieved metallicity using the different retrieval setups: (1) Guillot (2010) TP profile; (2) Guillot (2010) TP profile + Dilution Parameter; (3) Madhusudhan & Seager (2009) TP profile; (4) Madhusudhan & Seager (2009) TP profile + Dilution parameter. The metallicity estimate is calculated taking into account all of the molecules included in the retrievals. [M/H] denotes the logarithm (base 10) of the ratio of the retrieved metallicity relative to the solar metallicity.

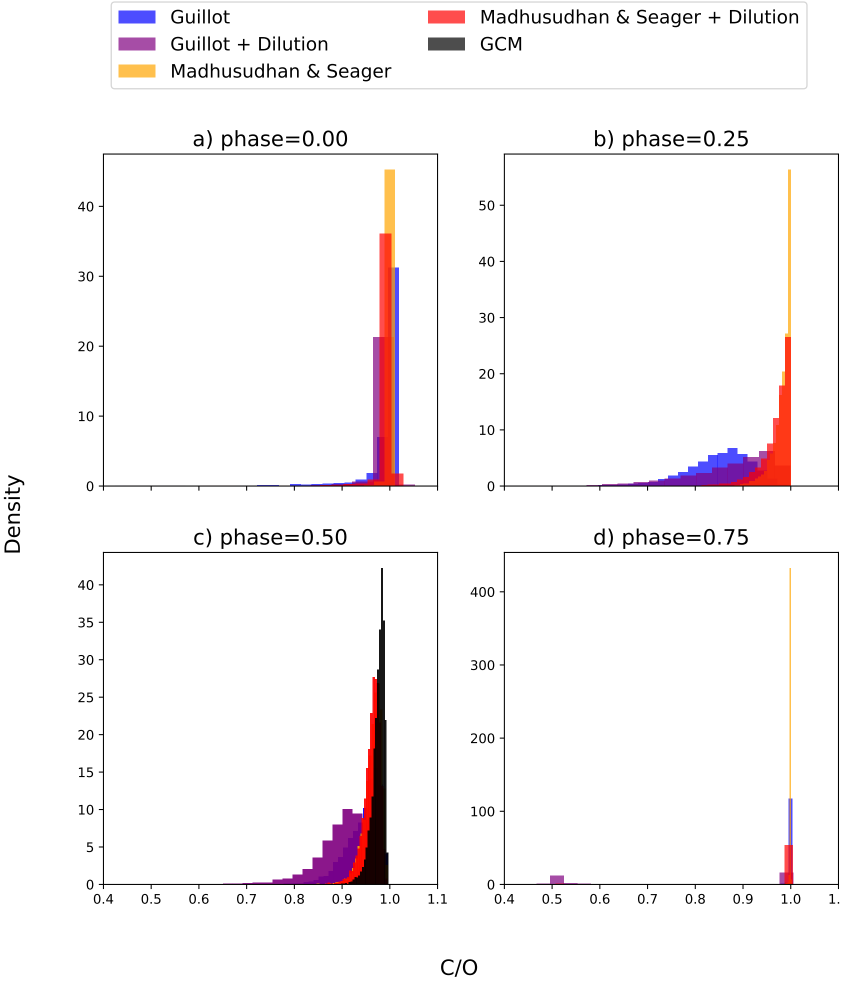

Figure 7.5: Retrieved C/O ratio using the different retrieval setups: (1) Guillot (2010) TP profile; (2) Guillot (2010) TP profile + Dilution Parameter; (3) Madhusudhan & Seager (2009) TP profile; (4) Madhusudhan & Seager (2009) TP profile + Dilution parameter. Note that the C/O ratio is close to unity when the CO abundance dominates over other molecules (consider the limit where the atmosphere has only CO, in which case the C/O ratio is exactly one).

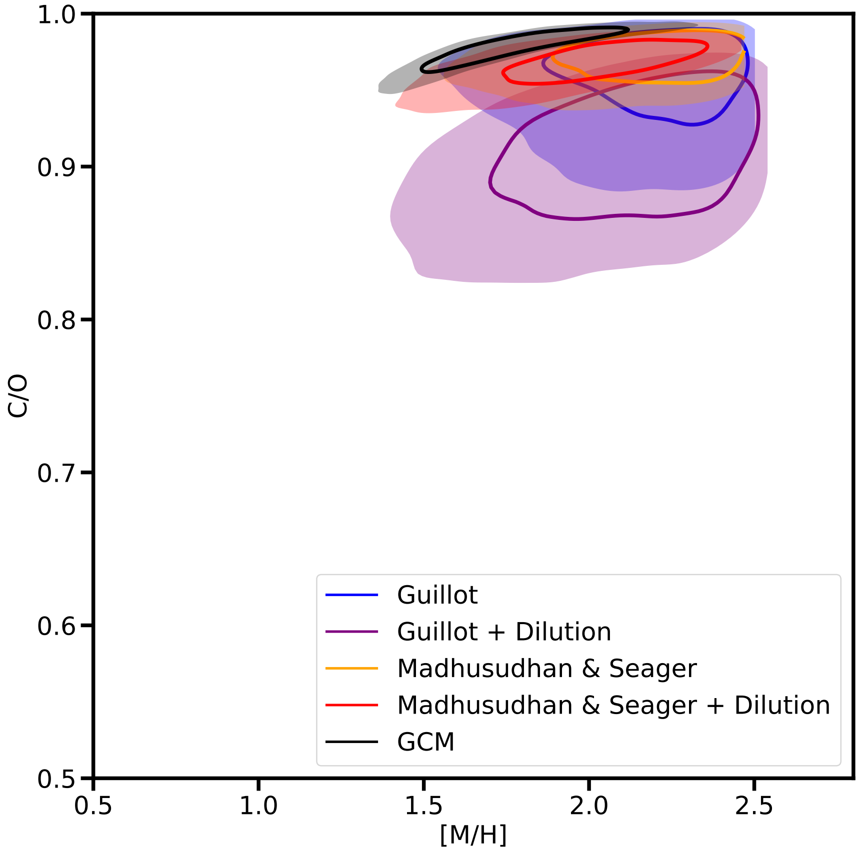

Figure 7.6: Joint posterior distribution of C/O ratio and metallicity retrieved from the dayside emission spectrum (phase=0.5) using the different retrieval setups: (1) Guillot (2010) TP profile; (2) Guillot (2010) TP profile + Dilution Parameter; (3) Madhusudhan & Seager (2009) TP profile; (4) Madhusudhan & Seager (2009) TP profile + Dilution parameter; (5) dayside retrieval assuming the GCM thermal structure. The solid lines show the 1σ contours, whereas the shadings show the 3σ contours. Note that metallicity is given as the logarithm of the ratio of retrieved metallicity relative to the solar metallicity

7.3.3 Thermal Structure

Figure 7.7 plots the retrieved TP profiles using the different setups of the phase-by-phase retrieval approach, with the TP profiles from the WASP-43b GCM shown for comparison. When the dilution parameter is not included, the thermal structure retrieved using the Guillot (2010) TP profile agrees well with the thermal structure retrieved using the Madhusudhan & Seager (2009) TP profile at all orbital phases, which suggests that the retrieved thermal structure is robust to the choice of 1D TP profile. Furthermore, the retrieved TP profiles using the Guillot (2010) and the Madhusudhan & Seager (2009) TP profiles without the dilution parameter are consistent with the latitudinally-averaged GCM TP profile on the dayside, which is not surprising as both the GCM thermal structure and the retrieved 1D TP profiles can match the observation. In contrast, the retrieved 1D TP profiles on the nightside without the dilution parameter are significantly colder than the latitudinally-averaged GCM TP profile on the nightside, echoing the picture from previous studies that cloud-free GCMs tend to give nightside temperatures that are too high to match observations (Parmentier et al., 2020; Irwin et al., 2020; Bell et al., 2024).

Figure 7.7 also demonstrates the effect of including the dilution parameter in the retrievals: the retrieved TP profiles using the Guillot (2010) and the Madhusudhan & Seager (2009) TP profiles with the dilution parameter are generally hotter than the TP profiles retrieved without the dilution parameter. This is due to the fact that the TP profile retrieved using the dilution parameter represents the thermal structure of the 'hot region' in the atmosphere, as explained in Section 7.2.1. Crucially, this assumes that the flux contribution from the 'cold region' is negligible. As such, the dilution parameter retrieval setup is more applicable to the dayside phase, where a hot spot dominates the outgoing flux, than to the other phases. This is evidenced by the comparison between the TP profiles on the dayside phase, where the retrieved TP profiles with the dilution parameter agree well with the hottest latitudinally-averaged GCM TP profile. For the other orbital phases, the retrieved TP profiles using the dilution parameter are generally hotter than the hottest latitudinally-averaged GCM TP profile, which suggests that the employment of the dilution parameter is not physical for any orbital phase other than the dayside phase.

Finally, referring again to Figure 7.7, let us compare the retrieved TP profiles from the NIRSpec data with the representative dayside and nightside profiles retrieved from the MIRI data using the 2D retrieval in Chapter 6. On the dayside, the representative dayside TP profile retrieved from MIRI agrees well with the TP profiles retrieved from NIRSpec without the dilution parameter in the MIRI photosphere (between 1 and

10^{-3} bar). On the nightside, the representative nightside TP profile retrieved from MIRI is somewhat cooler than the TP profiles retrieved from NIRSpec without the dilution parameter.

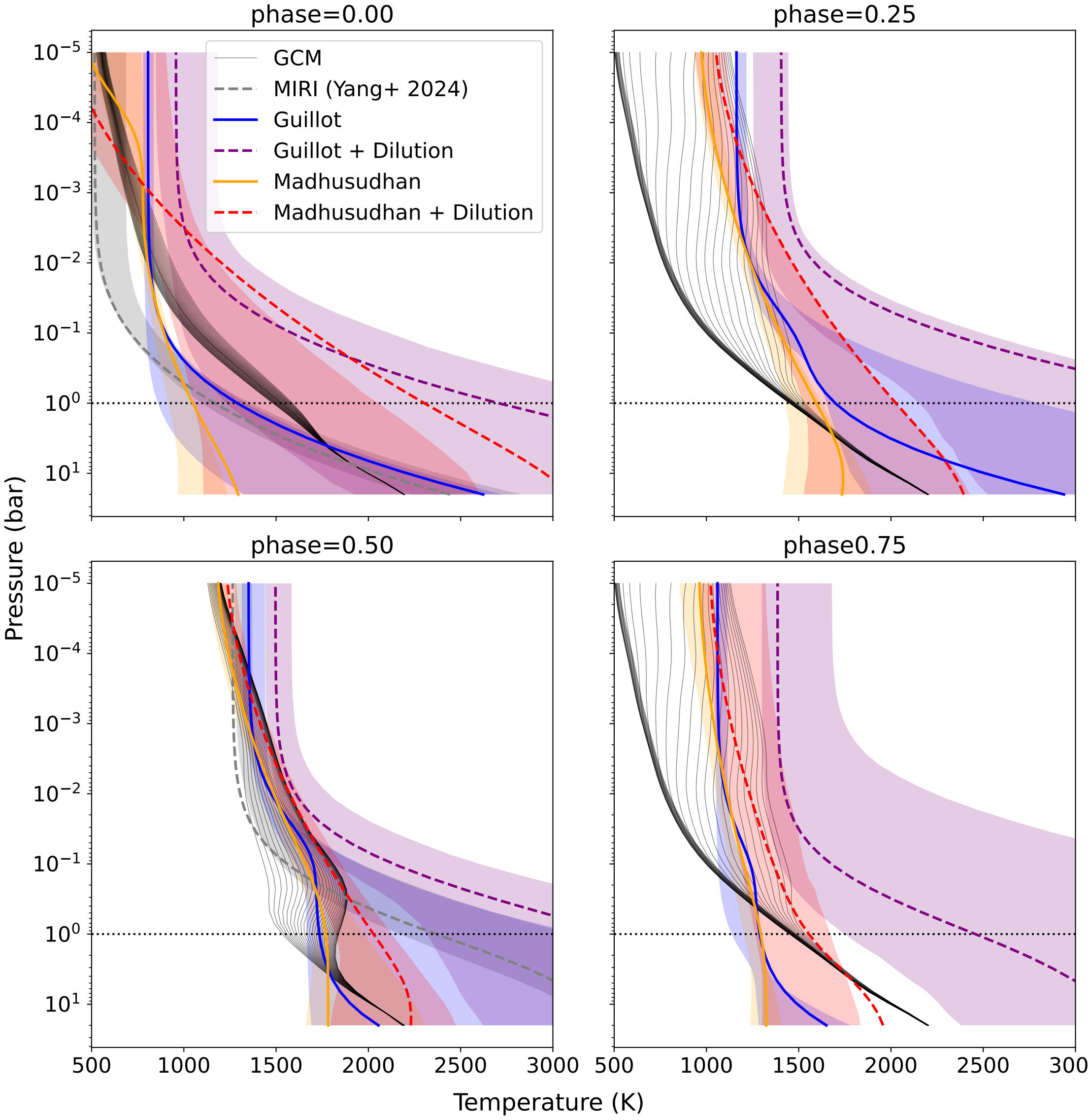

Figure 7.7: Best-fit (maximum a posteriori) TP profiles retrieved from the NIRSpec spectra using either the Guillot (2010) TP profile or the Madhusudhan & Seager (2009) TP profile, with or without the dilution parameter. The shading around the best-fit profiles denote the 1σ central credible interval. A collection of latitudinally-averaged GCM TP profiles at 30 equally spaced longitudes, averaged between ±45° using cos(latitude) as weight, are plotted for each orbital phase for comparison. The representative dayside and nightside TP profiles retrieved from the MIRI data set using the 2D model in Chapter 6 are also included for comparison. The dashed line marked 1 bar pressure, which is approximately the lower limit of the MIRI and NIRSpec photospheres.

7.3.4 Further Results of Phase-by-Phase Retrievals

This section presents supplementary results of the phase-by-phase retrievals. Figures 7.8, 7.9, 7.10, and 7.11 respectively show more results from: (1) retrievals using the Guillot (2010) TP profile without the dilution parameter; (2) retrievals using the Guillot (2010) TP profile with the dilution parameter; (3) retrievals using the Madhusudhan & Seager (2009) TP without the dilution parameter; (4) retrievals using the Madhusudhan & Seager (2009) TP profile with the dilution parameter. The first row of these figures shows the best-fit (maximum a posteriori) spectra at each orbital phase plotted in terms of flux ratio, and the second row shows the best-fit spectra plotted in terms of luminosity. The third row shows the marginalised posterior distribution of the molecular abundance at each orbital phase, and the fourth row shows the transmission weighting function at each orbital phase. The fifth and last row of the figures shows the retrieved temperature profiles.

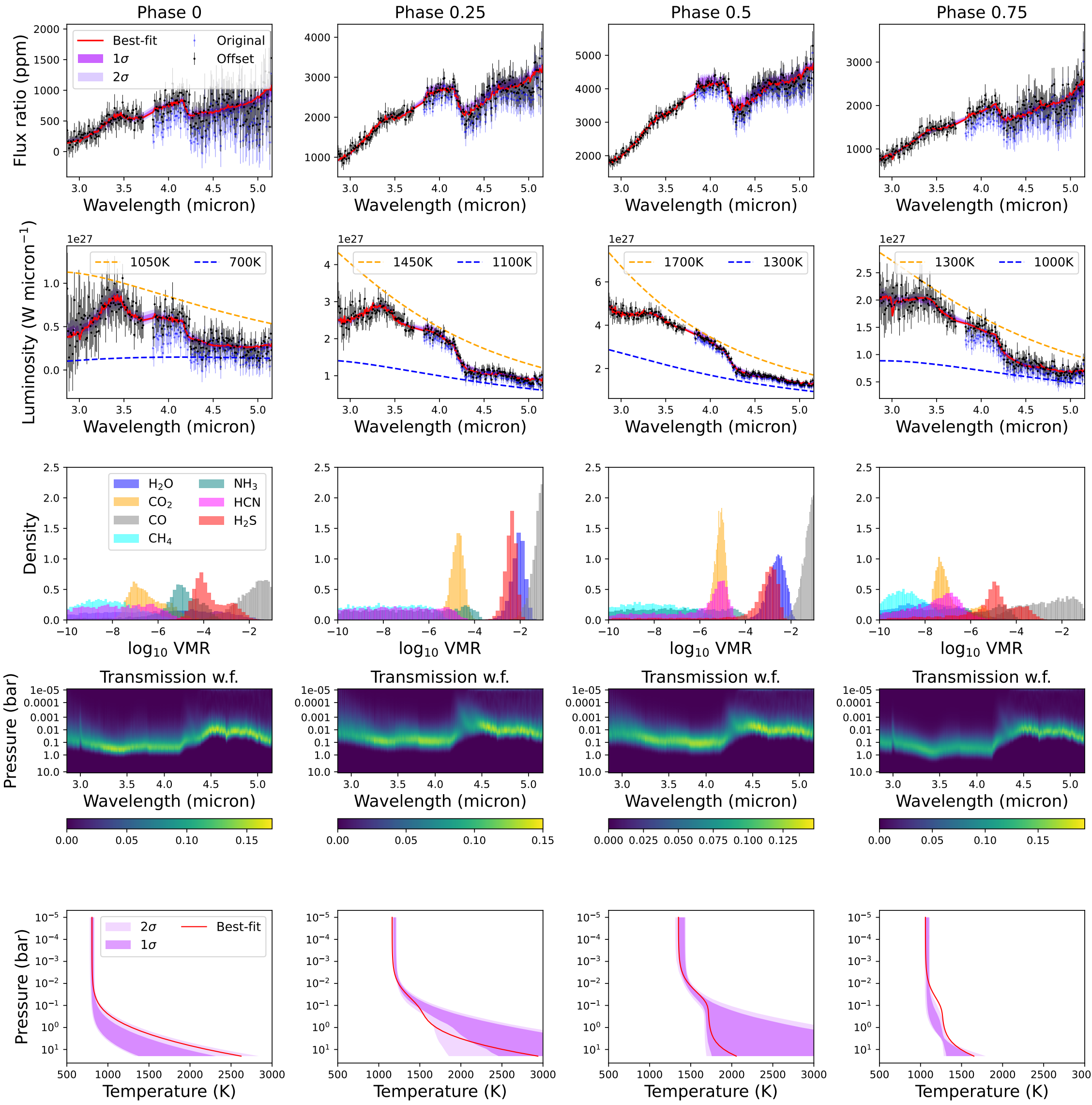

Figure 7.8: Retrieval results using the Guillot (2010) TP profile. 1st row: best-fit model spectra with 1σ and 2σ central credible intervals plotted with dark and light purple shading, respectively. The original NRS2 data are plotted in blue, whereas the offseted NRS data are plotted in black. 2nd row: same as first row, but plotted in terms of luminosity. Blackbody emissions are plotted for comparison. 3rd row: marginalised posterior distribution of molecular abundances. 4th row: transmission weighting function. 5th row: best-fit TP profile. The 1σ and 2σ central credible intervals are plotted with dark and light purple shading, respectively.

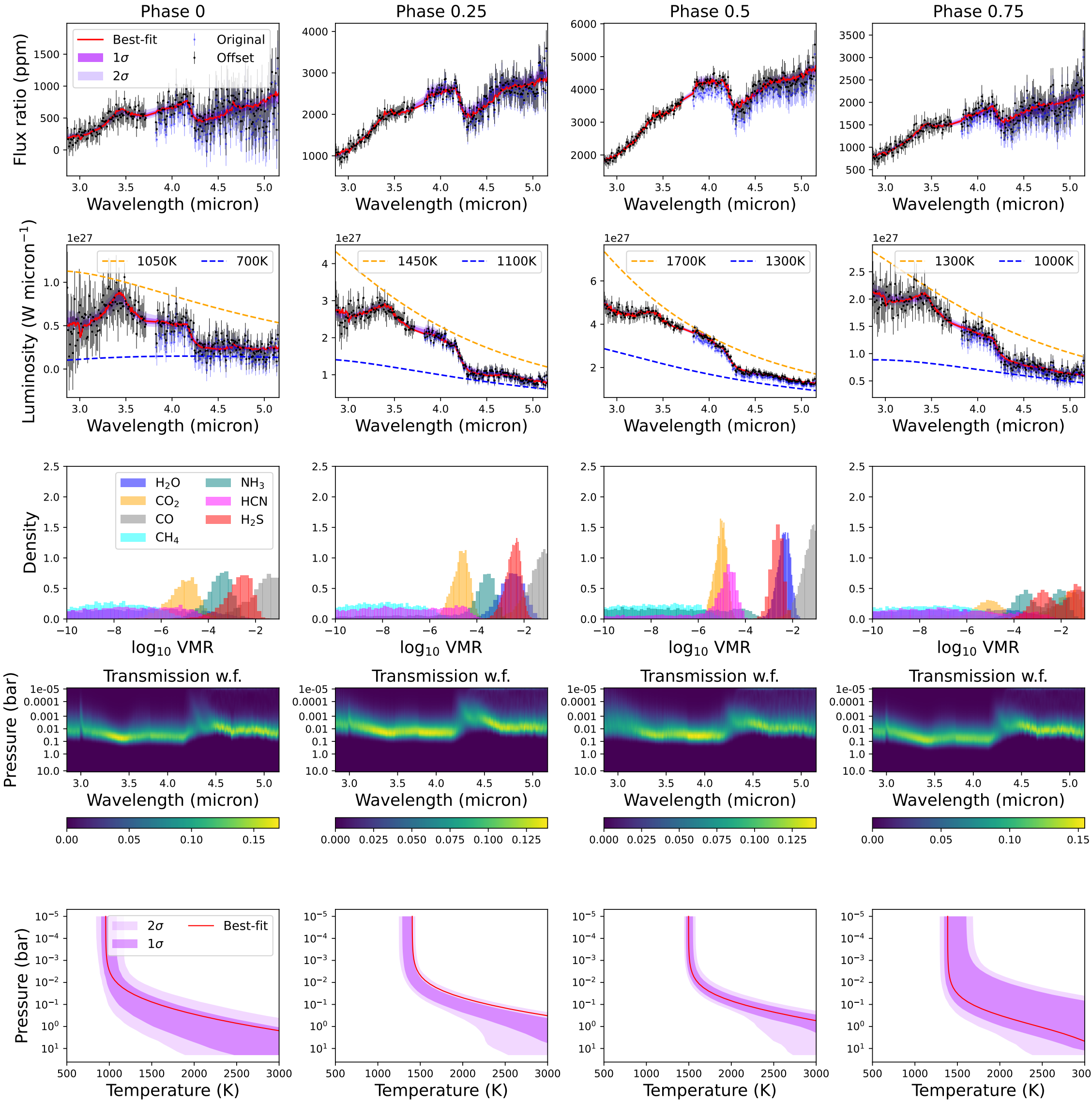

Figure 7.9: Retrieval results using the Guillot (2010) TP profile with the dilution parameter. Rows and columns are the same as Figure 7.8.

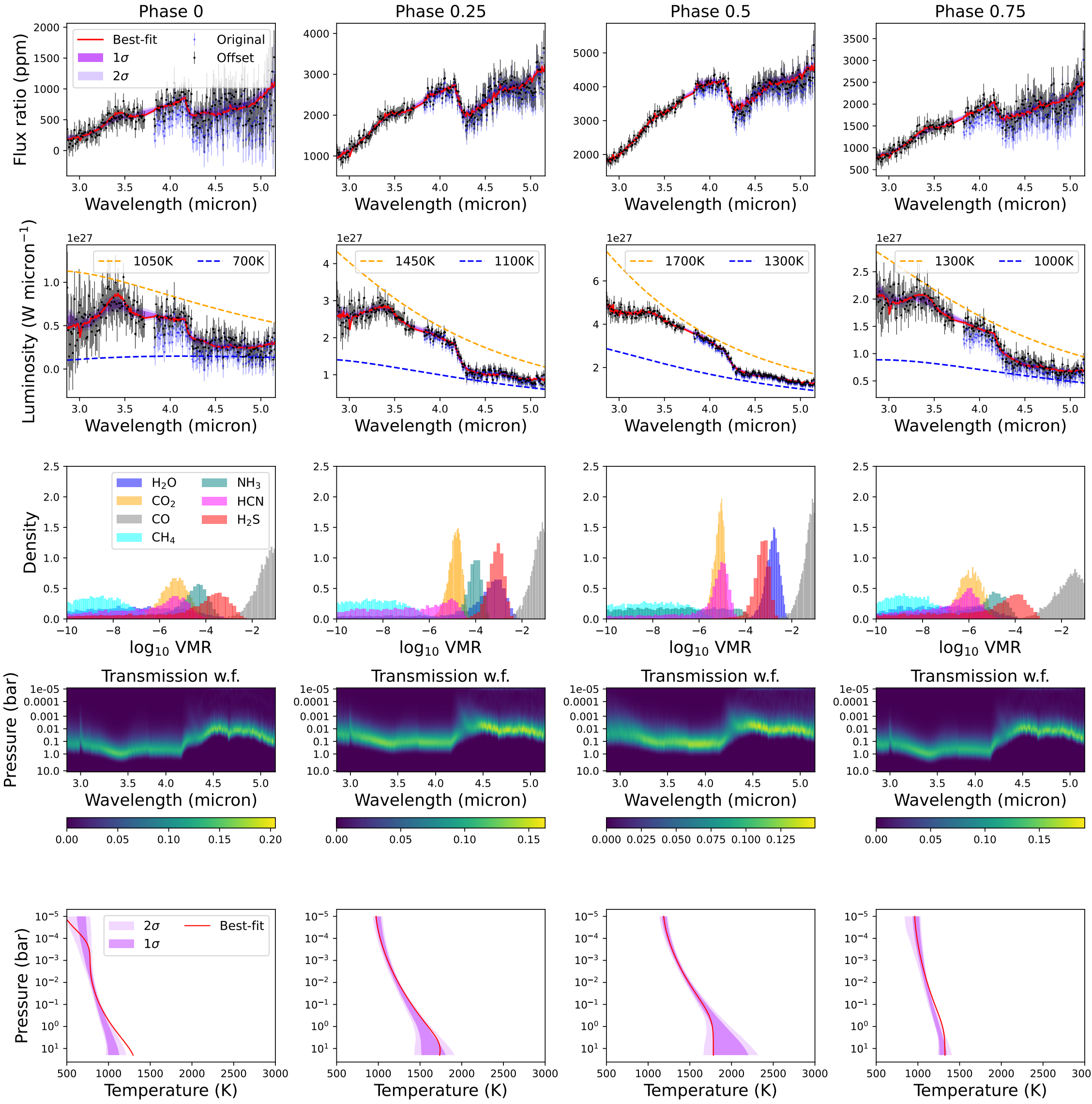

Figure 7.10: Retrieval results using the Madhusudhan & Seager (2009) TP without the dilution parameter. Rows and columns are the same as Figure 7.8.

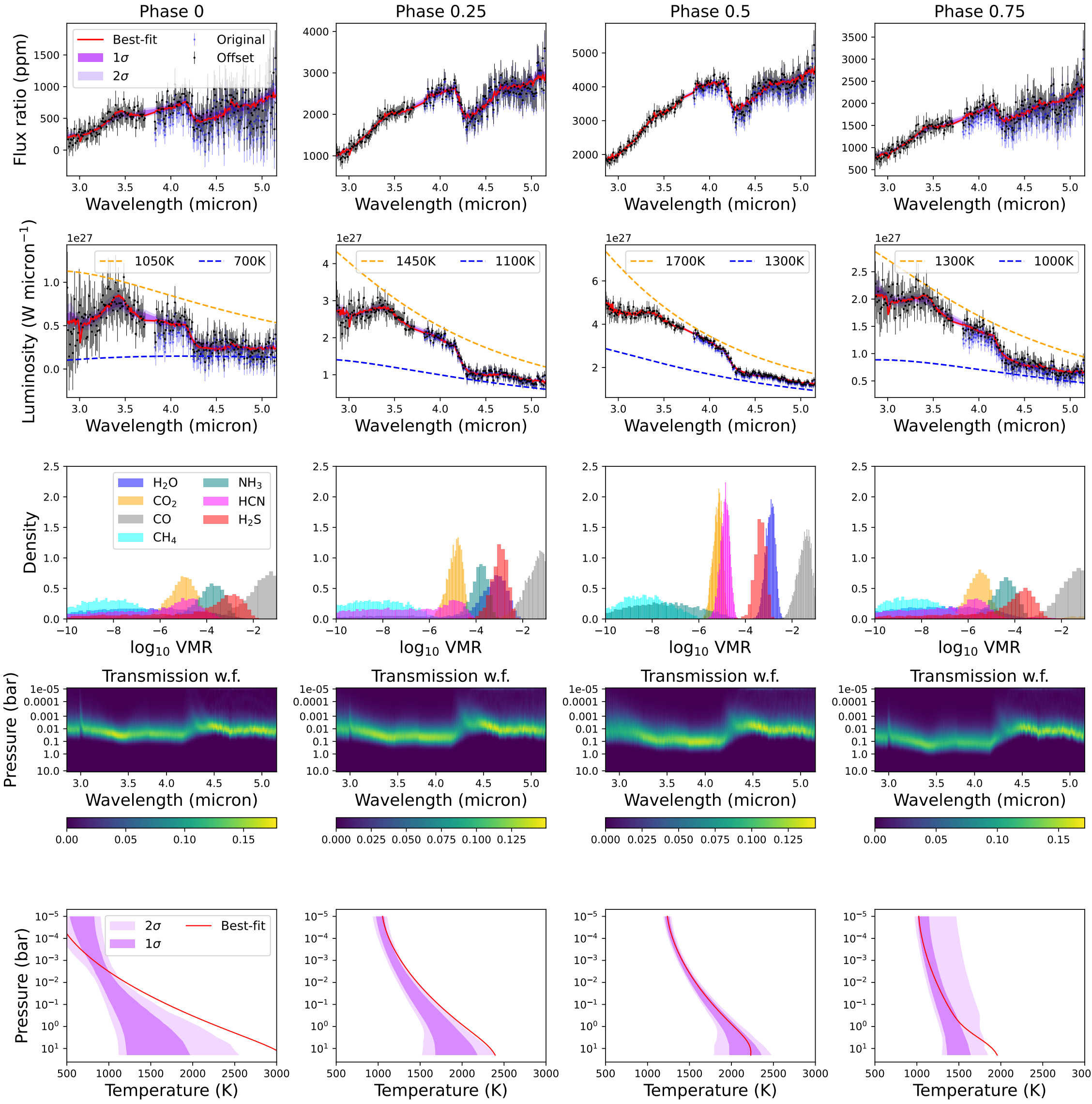

Figure 7.11: Retrieval results using the Madhusudhan & Seager (2009) TP with the dilution parameter. Rows and columns are the same as Figure 7.8.

7.4 Discussion

The retrieval results in this chapter demonstrate, with a real-world data set, that different thermal structure parameterisation and assumptions can provide similarly adequate fits to the data. While the molecular detections in this chapter are robust to the choice of thermal structure parameterisation, the abundance constraints can vary depending on the assumed temperature structure in the retrievals. In the *JWST* era, where the data quality has dramatically improved from previous space telescopes, model uncertainty is replacing data uncertainty as the dominant source of error on the retrieved atmospheric properties of hot Jupiters.

Furthermore, for any given TP profile, there can be significant uncertainty in the molecular abundance. The temperature structure is degenerate with the molecular abundance in the retrieval of low resolution emission spectra typically collected with space telescopes. For example, for a non-inverted atmosphere, if we increase the opacity across wavelength by increasing the molecular abundance, then the resultant emission spectrum from the atmosphere should exhibit a lower spectral radiance, as the spectrum would be probing higher up in the atmosphere, where it is cooler, due to the increased opacity. However, if we also increase the atmospheric temperature accordingly, then the resultant emission spectrum may be indistinguishable from that of the original atmosphere. This is well-demonstrated in the phase-by-phase retrievals, which cannot give an upper bound on the CO abundance. The counterexample is the GCM dayside retrieval, which, by assuming a fixed thermal structure, gives the only bounded constraints on the CO abundance. However, by fixing the thermal structure, the GCM dayside retrieval also fails to properly explore the possible atmospheric structures that could fit the data.

Overall, the above arguments suggest that a thorough investigation of the hot Jupiter atmospheric temperature structure parameterisation is of the utmost importance if we want to infer precise and accurate atmospheric molecular abundances from emission spectra.

7.5 Summary

H_2O, CO_2, CO, and H_2S are detected in WASP-43b's atmosphere using the NIRSpec data. There are strong detections of CO_2 and CO at all orbital phases, strong detection of H_2O at the dayside phase, and H_2S is detected at some orbital phases. The NIRSpec data clearly rules out the presence of CH_4 at detectable levels. The presence of HCN and NH_3 are ill-constrained using the NIRSpec data alone. The retrieved molecular abundances indicate a significantly super-solar metallicity and a super-solar C/O ratio.

Chapter 8

Panchromatic Picture of WASP-43b

This chapter combines the constraints from the three data sets analysed in Chapters 5, 6, and 7 with atmospheric retrievals on a 'panchromatic dayside emission spectrum' of WASP-43b, made up of the eclipse spectra observed with three instruments: *HST*/WFC3, *JWST*/MIRI, and *JWST*/NIRSpec. The wavelength range covered by this panchromatic dayside emission spectrum, from roughly 1 μm to 10 μm, is one of the broadest for an exoplanet to date.

This chapter is organised as follows. Section 8.1 shows the panchromatic dayside emission spectrum of WASP-43b. Section 8.2 details the retrieval methodology. Section 8.3 presents the retrieval results, which suggest that the atmosphere of WASP-43b is enriched in heavy elements[1] and has an elevated C/O ratio relative to its host star, broadly consistent with the retrieval results in Chapters 6 and 7. Section 8.4 investigates the constraints on the formation history of WASP-43b from the retrieved atmospheric properties. Section 8.5 concludes the chapter with a summary.

8.1 The Panchromatic Dayside Spectrum

Figure 8.1 displays the panchromatic dayside emission spectrum, which includes the dayside emission spectra observed with *HST*/WFC3 (1.1-1.6 μm, see Chapter 5), *JWST* NIRSpec/G395H (2.8-5.3 μm, see Chapter 7), and *JWST* MIRI/LRS (5-12 μm, see Chapter 6). As in Chapter 6, the MIRI data beyond 10.5 μm are excluded from the retrieval analysis due to the shadowed region effect (see Section 6.1). Figure 8.1 also shows the absorption cross-sections of the molecules included in the retrievals

---

[1] All elements except H and He are considered 'heavy elements', or 'metals', in this thesis, following common astronomy terminology.

computed at a pressure of 1 bar and a temperature of 1500 K using the opacity data from the ExoMol database listed in Section 8.2.2 (Chubb et al., 2021).

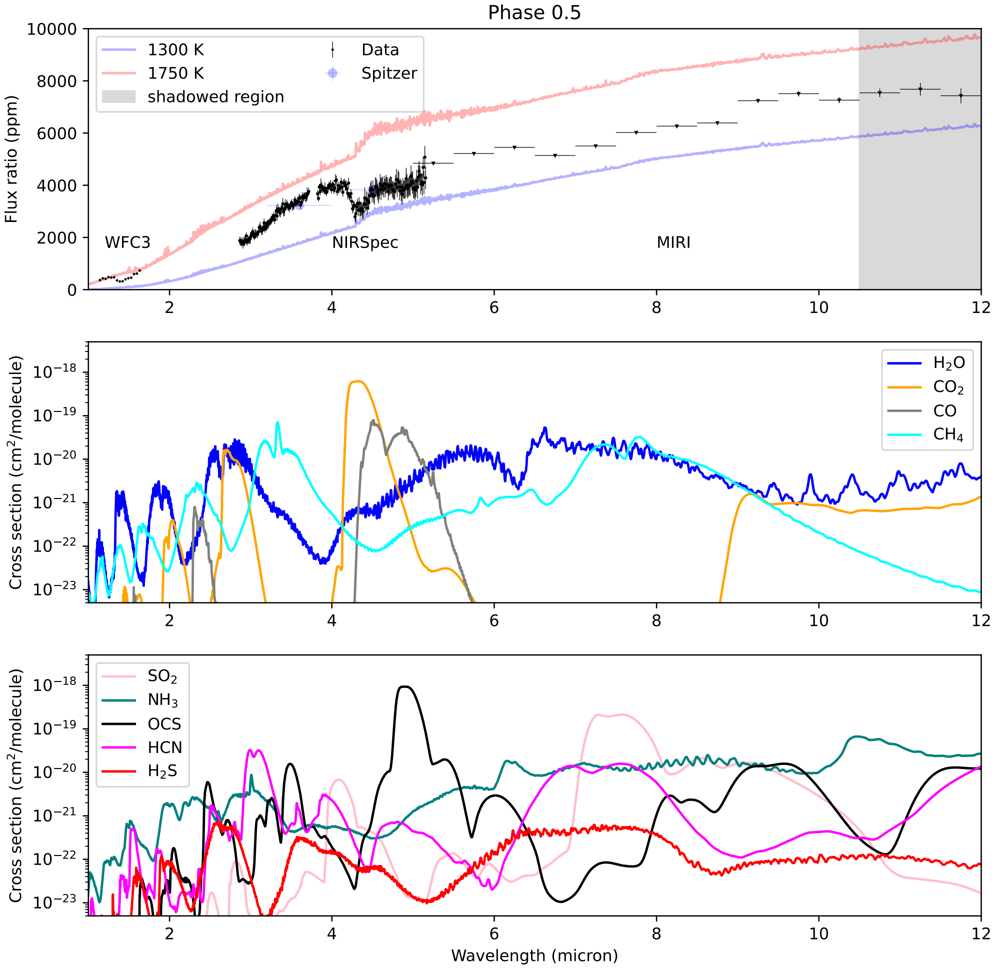

Figure 8.1: Top panel: Panchromatic dayside emission spectrum of WASP-43b observed with *HST*/WFC3, *JWST*/NIRSpec, and *JWST*/MIRI. Blackbody emission curves and Spitzer data are plotted for comparison. As described in Section 6.1, the MIRI data in the shadowed region are not reliable and are excluded from the retrievals. Middle and lower panels: absorption cross-sections of the molecules included in the retrievals.

8.2 Methodology

Section 8.2.1 outlines the atmospheric models used for the retrievals. Section 8.2.2 describes how the model spectra are calculated. Section 8.2.3 explains how an error inflation parameter is included to account for forward modelling errors and potential photometric offsets between the different data sets.

8.2.1 Atmospheric Modelling

This chapter retrieves the panchromatic dayside spectrum presented in Figure 8.1 with three different assumptions about the temperature-pressure (TP) structure of the atmosphere, similar to Section 7.2. The first approach assumes a single TP profile for the entire dayside atmosphere, parametrised using the Guillot (2010) TP profile introduced in Section 3.1.1. The second approach also assumes a single TP profile but instead parametrises the TP structure using the more flexible Madhusudhan & Seager (2009) TP profile introduced in Section 3.1.2. The third approach assumes a fixed thermal structure given by the WASP-43b GCM used in Chapters 5 and 7.

While the three retrieval methods assume different temperature models, all share the uniform chemistry assumption, i.e., the volume mixing ratios (VMRs) of molecules are constant in the observed atmosphere. All retrievals include nine spectrally active molecules uniformly mixed in a H_2/He-dominated model atmosphere: H_2O, CO_2, CO, CH_4, SO_2, NH_3, OCS, HCN, and H_2S. The two additional sulphur-bearing molecules (OCS and SO_2) compared to Chapter 7 are included due to the detection of the sulphur-bearing H_2S in Chapter 7 to probe the sulphur chemistry in WASP-43b further. The atmospheric model is defined from 20 to 10^{-5} bar, on 40 points equally spaced in log pressure. Table 8.1 gives the full list of free parameters of the retrievals and their priors.

8.2.2 Radiative Transfer

As in the rest of the thesis, the radiative transfer calculations are implemented by the NEMESISPY package (Yang et al., 2024a) described in Section 2.5, which is a Python development of the Fortran NEMESIS library of Irwin et al. (2008). The NEMESISPY package uses the correlated-k method for radiative transfer (Lacis & Oinas, 1991; Irwin et al., 2008) described in Section 2.3 and the disc-integration method of Irwin et al. (2020) described in 2.4 to calculate disc-integrated emission spectra at arbitrary orbital phases. Five zenith angle quadratures are used for the disc-integration scheme, i.e., setting $N_\mu = 5$ in Equation (2.22). The disc-integrated

Parameter	Description	Prior	Unit
$\log \kappa_{\mathrm{th}}$	Log_{10} mean infrared opacity (Guillot, 2010)	U(-4,2)	$\mathrm{m^2kg^{-1}}$
$\log \gamma$	Log_{10} ratio of visible and infrared opacities (Guillot, 2010)	U(-4,1)	dimensionless
$\log f$	Log_{10} heat redistribution parameter (Guillot, 2010)	U(-4,1)	dimensionless
$\mathrm{T_{int}}$	Intrinsic heat flux temperature (Guillot, 2010)	U(100,1000)	Kelvin
$T_{100\mathrm{mb}}$	Temperature at 100 mb (Madhusudhan & Seager, 2009)	U(300,3000)	Kelvin
α_1	Layer 1 exponent (Madhusudhan & Seager, 2009)	U(0.02,1)	$\mathrm{Kelvin}^{-1/2}$
α_2	Layer 2 exponent (Madhusudhan & Seager, 2009)	U(0.02,1)	$\mathrm{Kelvin}^{-1/2}$
$\log P_1$	Log_{10} layer 1 base pressure (Madhusudhan & Seager, 2009)	U(0,7)	Pa
$\log P_2$	Log_{10} layer 2 base pressure (Madhusudhan & Seager, 2009)	U(0,7)	Pa
$\log P_3$	Log_{10} layer 3 base pressure (Madhusudhan & Seager, 2009)	U(2,7)	Kelvin
$\log \mathrm{VMR_{H_2O}}$	Log_{10} volume mixing ratio of H_2O	U(-10,-1)	dimensionless
$\log \mathrm{VMR_{CO_2}}$	Log_{10} volume mixing ratio of CO_2	U(-10,-1)	dimensionless
$\log \mathrm{VMR_{CO}}$	Log_{10} volume mixing ratio of CO	U(-10,-1)	dimensionless
$\log \mathrm{VMR_{CH_4}}$	Log_{10} volume mixing ratio of CH_4	U(-10,-1)	dimensionless
$\log \mathrm{VMR_{SO_2}}$	Log_{10} volume mixing ratio of SO_2	U(-10,-1)	dimensionless
$\log \mathrm{VMR_{NH_3}}$	Log_{10} volume mixing ratio of NH_3	U(-10,-1)	dimensionless
$\log \mathrm{VMR_{OCS}}$	Log_{10} volume mixing ratio of OCS	U(-10,-1)	dimensionless
$\log \mathrm{VMR_{HCN}}$	Log_{10} volume mixing ratio of HCN	U(-10,-1)	dimensionless
$\log \mathrm{VMR_{H_2S}}$	Log_{10} volume mixing ratio of H_2S	U(-10,-1)	dimensionless
b	Error inflation parameter	U(1,5)	dimensionless

Table 8.1: Free parameters of the retrieval models and their priors. All retrievals share the same VMR parameters and error inflation parameter. There are no free temperature parameters in the GCM dayside retrieval as the temperature structure is assumed to be the fixed GCM thermal structure. $U(a, b)$ denotes a uniform distribution between a and b.

spectra are computed assuming a circular, tidally locked, and edge-on orbit, using the parameters in Table 6.3. The planetary emission is converted to planet-to-star flux ratios using a stellar spectrum computed using the PHOENIX stellar model (Allard & Hauschildt, 1995; Hauschildt et al., 1999; Husser et al., 2013), generated assuming an effective temperature of 4300 K, a surface gravity of log(g)= 4.50, and a solar metallicity. The choice of stellar model is informed by the work done for Bell et al. (2024). Note that the above setup is identical to the analysis presented in Chapters 6 and 7.

The molecular opacity data for the radiative transfer calculations in this chapter are taken from the ExoMol database (Chubb et al., 2021). Channel-integrated k-tables are generated at the resolution of the spectra from the original ExoMol k-tables, which were computed at a resolving power of R=1000. The radiative transfer calculation models the molecular absorption due to the nine spectrally active molecules in the atmospheric model and the collision-induced absorption due to H_2–H_2 pairs and H_2–He pairs with data from Borysow & Frommhold (1989) and Borysow et al. (1989). The full list of opacity data is given in Table 8.2, and Figure 8.1 plots the absorption cross-sections of the molecules in the panchromatic dayside emission spectrum wavelength range.

Molecule	Opacity Data
H_2O	Polyansky et al. (2018)
CO_2	Yurchenko et al. (2020)
CO	Li et al. (2015)
CH_4	Yurchenko et al. (2017)
SO_2	Underwood et al. (2016)
NH_3	Coles et al. (2019)
OCS	Owens et al. (2024)
HCN	Barber et al. (2014)
H_2S	Azzam et al. (2016)
He	Borysow & Frommhold (1989) & Borysow et al. (1989)
H_2	Borysow & Frommhold (1989) & Borysow et al. (1989)

Table 8.2: Opacity data used to calculate emission spectra in this chapter. Apart from the He-H_2 and H_2-H_2 collision-induced absorption opacity, all data are downloaded from the ExoMol database (Chubb et al., 2021).

8.2.3 Error Inflation

The retrievals in this chapter include an error inflation parameter to account for underestimated measurement and forward modelling uncertainties, following the approach used in, for example, Line et al. (2015) and Bell et al. (2024). The error inflation is implemented by modifying the likelihood term in Bayesian inference with a constant-with-wavelength multiplicative factor. The log likelihood function with error inflation is given by

$$\ln L(\boldsymbol{D}|\boldsymbol{\theta}) = -\frac{1}{2}\sum_{i=1}^{n}\frac{(D_i - F_i(\boldsymbol{\theta}))^2}{s_i^2} - \frac{1}{2}\ln(2\pi s_i^2), \tag{8.1}$$

where $\boldsymbol{D}$ is the set of data points in the observed spectrum, $F_i(\boldsymbol{\theta})$ is the ith data point in the model spectrum given model parameters $\boldsymbol{\theta}$, and s_i is defined as

$$s_i = b * \sigma_i, \tag{8.2}$$

where σ_i is the uncertainty for the ith data point, and b is a free error inflation parameter between 1 and 5.

8.3 Results

This section presents the retrieval results. Section 8.3.1 shows the model fits to the panchromatic dayside emission spectrum using different retrieval approaches. Section 8.3.2 describes the retrieved constraints on molecular abundance. Section 8.3.3 explores the constraints on the thermal structure of WASP-43b.

8.3.1 Spectral Fit

As shown by Figure 8.2, all three retrieval approaches outlined in Section 8.2 can adequately fit the panchromatic dayside emission spectrum. The reduced χ^2 is 0.99 for the best-fit model using the GCM thermal structure, 0.96 for the best-fit model using the Guillot (2010) TP profile, and 0.93 for the best-fit model using the Madhusudhan & Seager (2009) TP profile.

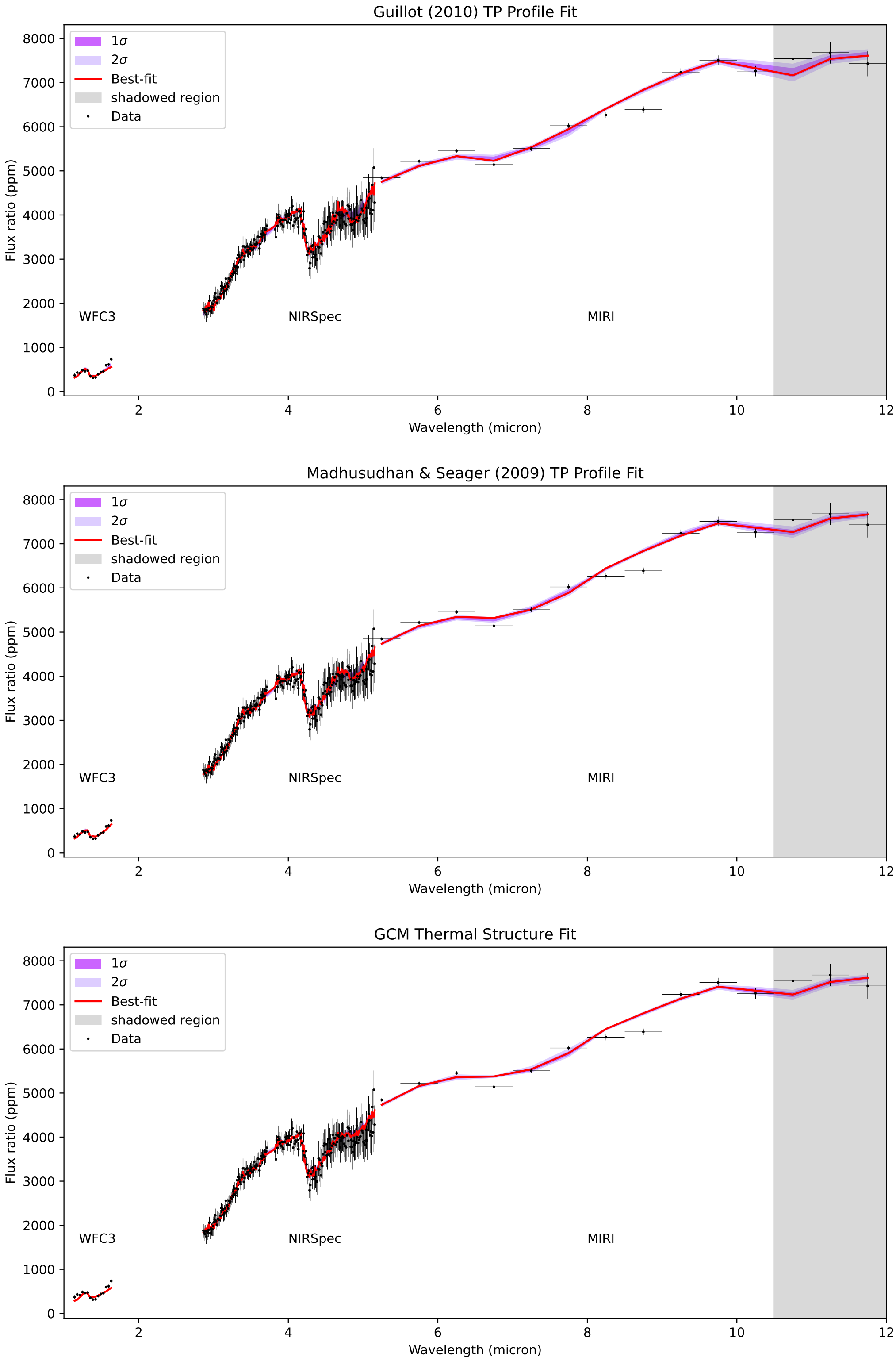

Figure 8.2: Best-fit models to the panchromatic dayside emission spectrum using the different retrieval approaches. The best-fit models are calculated from the maximum a posteriori parameters. $1\sigma/2\sigma$ central credible intervals are plotted around the best-fit models.

8.3.2 Molecular Detections and Abundance Constraints

	H_2O	CO_2	CO	CH_4	SO_2	NH_3	OCS	HCN	H_2S
GCM	12.2	14.5	8.1	N.F.	3.1	7.4	N.F.	4.6	3.7
Guillot (2010) Profile	12.0	13.5	7.3	N.F.	1.2	6.0	N.F.	4.2	2.8
Madhusudhan & Seager (2009) Profile	12.6	14.0	8.9	N.F.	1.6	6.5	N.F.	4.6	5.3

Table 8.3: Molecular detection significance (σ) using the different retrieval setups. Molecules not favoured by the data at an orbital phase are denoted by 'N.F.'. Significant detections ($\geq 3\sigma$) are coloured in blue.

	H_2O	CO_2	CO	CH_4	SO_2	NH_3	OCS	HCN	H_2S	M/H	C/O
GCM	$-3.48^{+0.07}_{-0.07}$	$-5.03^{+0.09}_{-0.09}$	$-1.54^{+0.16}_{-0.18}$	≤ -6.64	≤ -5.44	$-4.69^{+0.10}_{-0.10}$	≤ -6.22	$-4.91^{+0.13}_{-0.16}$	$-3.79^{+0.13}_{-0.17}$	$70.9^{+34.8}_{-24.7}$	$0.99^{+0.01}_{-0.01}$
Guillot	$-4.06^{+0.84}_{-0.50}$	$-5.90^{+0.86}_{-0.48}$	$-2.79^{+1.16}_{-0.69}$	≤ -6.72	≤ -5.40	$-5.34^{+0.56}_{-0.34}$	≤ -6.49	$-5.54^{+0.58}_{-0.38}$	$-3.99^{+0.81}_{-0.67}$	$3.9^{+54.4}_{-3.1}$	$0.95^{+0.05}_{-0.03}$
Madhu.	$-3.65^{+0.36}_{-0.36}$	$-5.47^{+0.35}_{-0.36}$	$-2.11^{+0.53}_{-0.53}$	≤ -6.70	≤ -5.62	$-4.96^{+0.33}_{-0.33}$	≤ -6.23	$-5.19^{+0.30}_{-0.32}$	$-3.61^{+0.34}_{-0.34}$	$18.5^{+46.2}_{-13.0}$	$0.97^{+0.01}_{-0.03}$

Table 8.4: Log_{10} VMRs, M/H and C/O retrieved from the panchromatic dayside emission spectrum. For H_2O, CO_2, CO, NH_3, HCN, H_2S, M/H and C/O, the constraints are quoted as the medians of the marginalised posterior distributions, with the uncertainties showing the 1σ central credible intervals. For CH_4, SO_2, and OCS, the constraints are quoted as the 95% upper bound.

Table 8.3 lists the detection significances of the molecules included in the retrievals. As in Chapter 7, CO, CO_2 and H_2O are detected at high significances on the dayside ($> 5\sigma$) for all retrieval approaches, and CH_4 is not favoured by the data in any of the retrievals. On the other hand, the retrievals consistently show significant detections of HCN and NH_3, in contrast to the retrievals in Chapter 7 using only the NIRSpec data, which were inconclusive on the presence of these two molecules. This is due to the much extended wavelength coverage of the panchromatic data set. For the sulphur-bearing molecules, the retrievals show evidence for H_2S, similar to the results in Chapter 7, though the detection significance of H_2S using the Guillot (2010) TP profile is just short of a 3σ detection. OCS is not favoured by the data in any of the retrievals. As for SO_2, it is significantly detected only for the GCM retrieval but not detected for the other two retrieval approaches. To summarise, the significant detections are CO_2 ($> 13\sigma$), H_2O ($> 12\sigma$), CO ($> 7\sigma$), NH_3 ($> 6\sigma$), HCN ($> 4\sigma$), H_2S ($> 2.8\sigma$). The retrievals consistently rule out CH_4 and OCS at detectable levels and remain inconclusive on the presence of SO_2.

Table 8.4 lists the constraints on molecular abundance retrieved from the panchromatic dayside emission spectrum using the three different retrieval models. Figure 8.3 plots the molecular abundance constraints for visualisation. The molecular constraints retrieved using the Guillot (2010) TP profile are entirely consistent with the molecular constraints retrieved using the Madhusudhan & Seager (2009) TP profile. The molecular constraints retrieved using the fixed GCM thermal structure are much more precise than those retrieved using the two parametric TP profiles since assuming a fixed thermal structure removes the degeneracy between thermal structure and chemical abundance inherent in low-resolution emission spectra.

The molecular abundance constraints retrieved from the panchromatic dayside emission spectrum are qualitatively consistent with the constraints retrieved from the NIRSpec data set in Chapter 7: (1) CO is the most abundant molecule in the atmosphere, resulting in C/O ratio close to unity; (2) CO_2 VMR is constrained at 10^{-5}–10^{-6}; (3) H_2S VMR is constrained at 10^{-3}–10^{-4}. The agreement in the constraints on the carbon-bearing molecules retrieved from the panchromatic dayside emission spectrum and the NIRSpec data set is to be expected since the constraints on CO and CO_2 are mostly driven by the NIRSpec data set. On the other hand, the H_2O abundance retrieved from the panchromatic dayside emission spectrum is lower than that retrieved from the NIRSpec data set and more consistent with that retrieved from the MIRI data set and *HST* data set.

Figure 8.4 shows the joint posterior distribution of the retrieved molecular abundances. For the retrievals using the parametric TP profiles, there are significant degeneracies between the retrieved molecular abundances, as the abundances of CO_2, CO, H_2O, H_2S and NH_3 are all positively correlated, reflecting the well-known degeneracy between thermal structure and molecular abundance, i.e., a hotter atmosphere with a higher photosphere (with higher molecular abundances) is degenerate with a colder atmosphere with a lower photosphere (with lower molecular abundances). This degeneracy is a dominant limiting factor in the precision of the retrieved molecular abundances. In contrast, the constraints on molecular abundances are much more precise when the thermal structure is fixed to the GCM thermal structure. The uncertainties in the retrieved abundances propagate to the uncertainties in the retrieved metallicity, as shown in Figure 8.5, though the C/O ratio is precisely constrained. This is because the relative abundance between molecules is roughly preserved since the molecular abundances are all positively correlated.

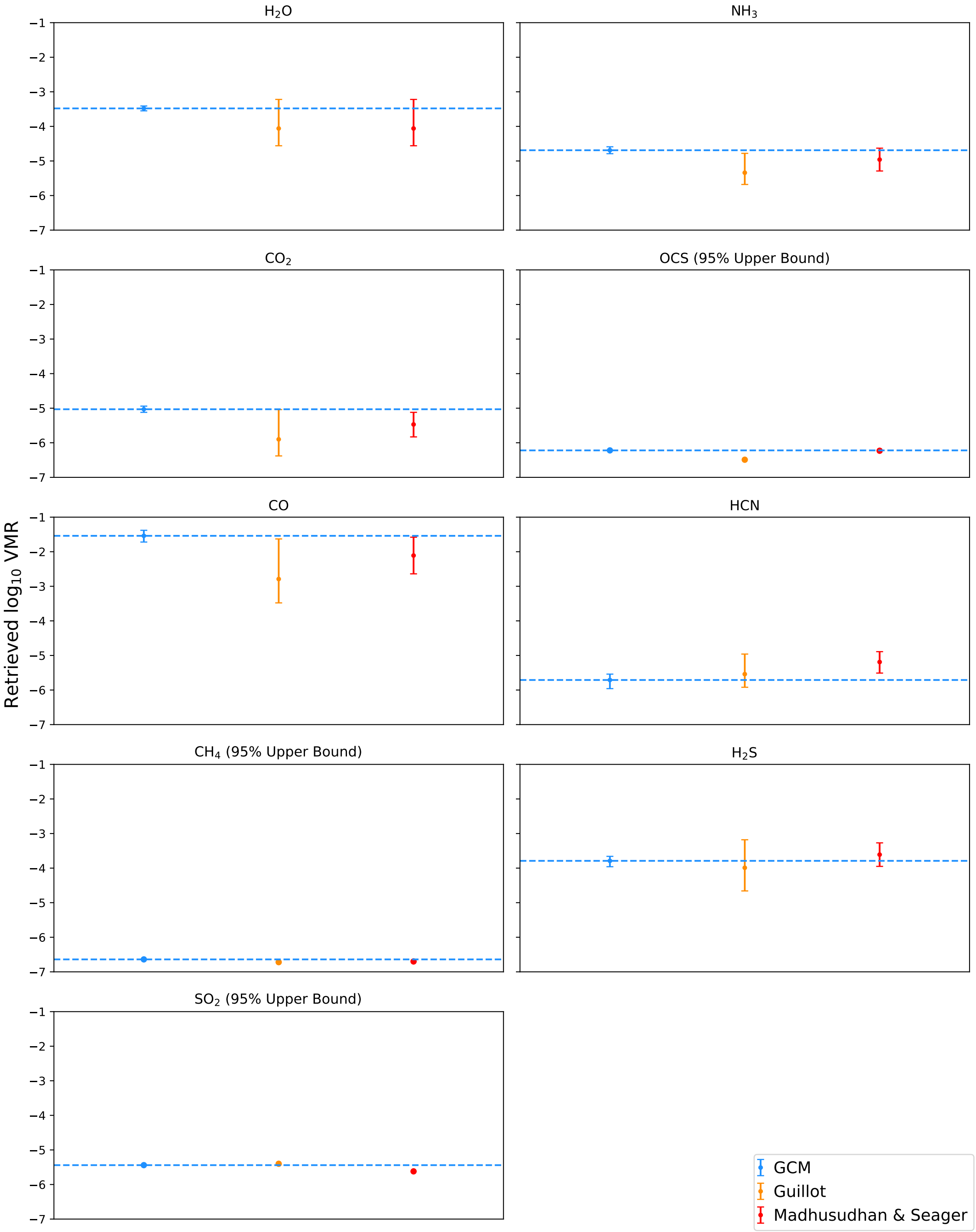

Figure 8.3: Molecular abundances retrieved from the panchromatic dayside emission spectrum using the three different retrieval models. For H_2O, CO_2, CO, NH_3, HCN, H_2S, the constraints are quoted as the medians of the marginalised posterior distributions, with the uncertainties showing the 1σ central credible intervals. For CH_4, SO_2, and OCS, the constraints are quoted as the 95% upper bound. The horizontal dashed line mark the GCM retrieval values for ease of comparison.

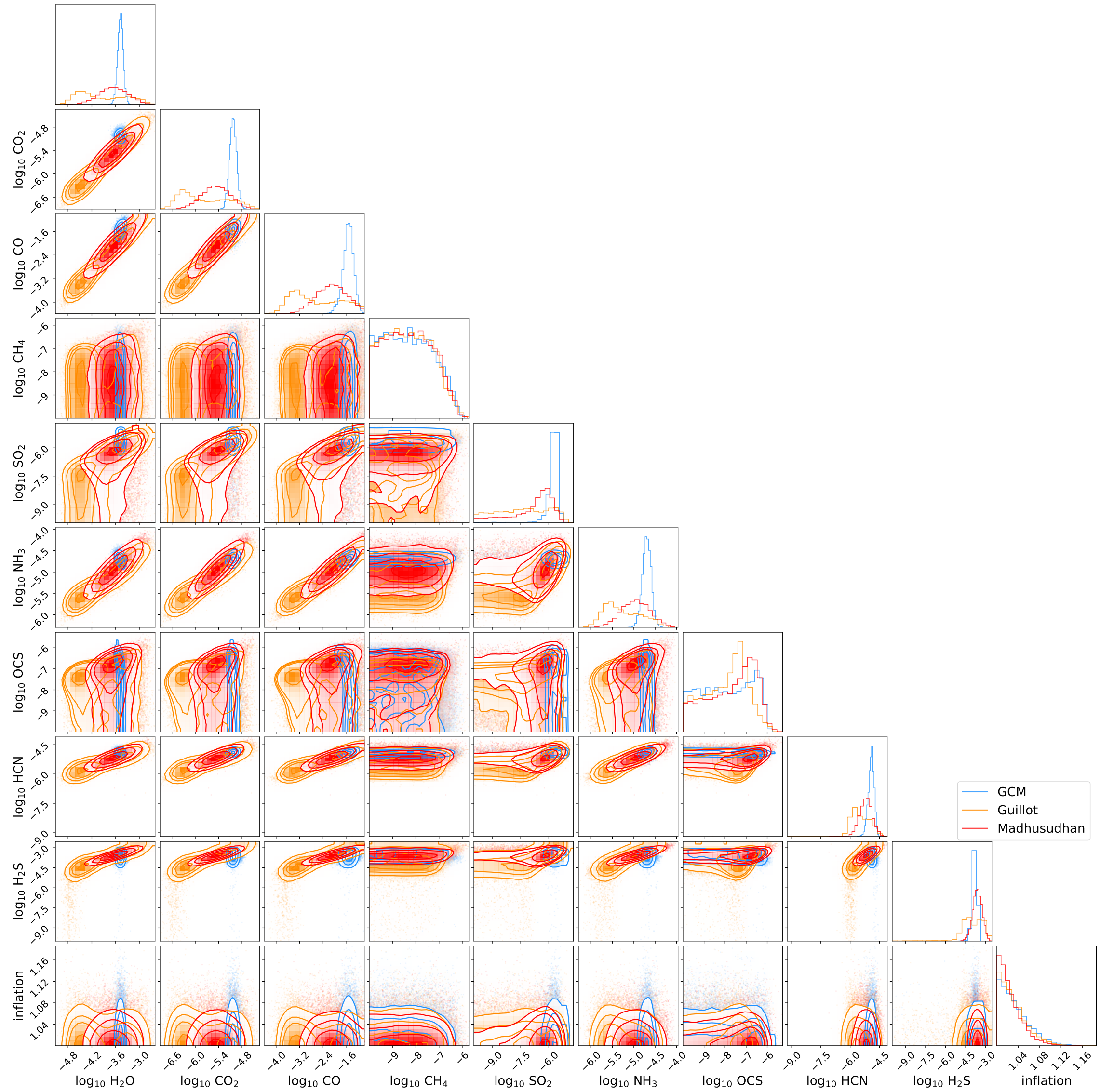

Figure 8.4: Posterior distribution of the molecular abundances. The histograms on the diagonal show the marginalised posterior distributions of each molecular VMR. The off-diagonal plots show the joint posterior distributions of any pairs of parameters. The constraints on the error inflation parameter is also shown here.

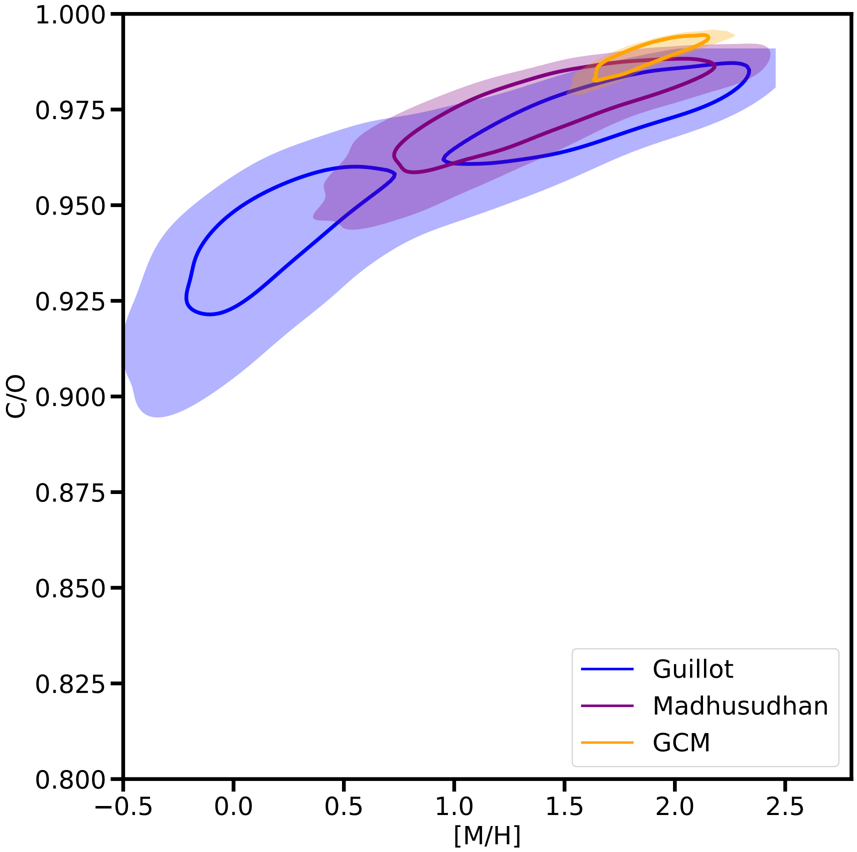

Figure 8.5: Joint posterior distribution of C/O ratio and metallicity retrieved from the dayside emission spectrum (phase=0.5) using the different retrieval set-ups: (1) Guillot (2010) TP profile; (2) Madhusudhan & Seager (2009) TP profile; (3) retrieval assuming the GCM thermal structure. The solid lines show the 1σ contours, whereas the shadings show the 3σ contours.

8.3.3 Thermal Structure

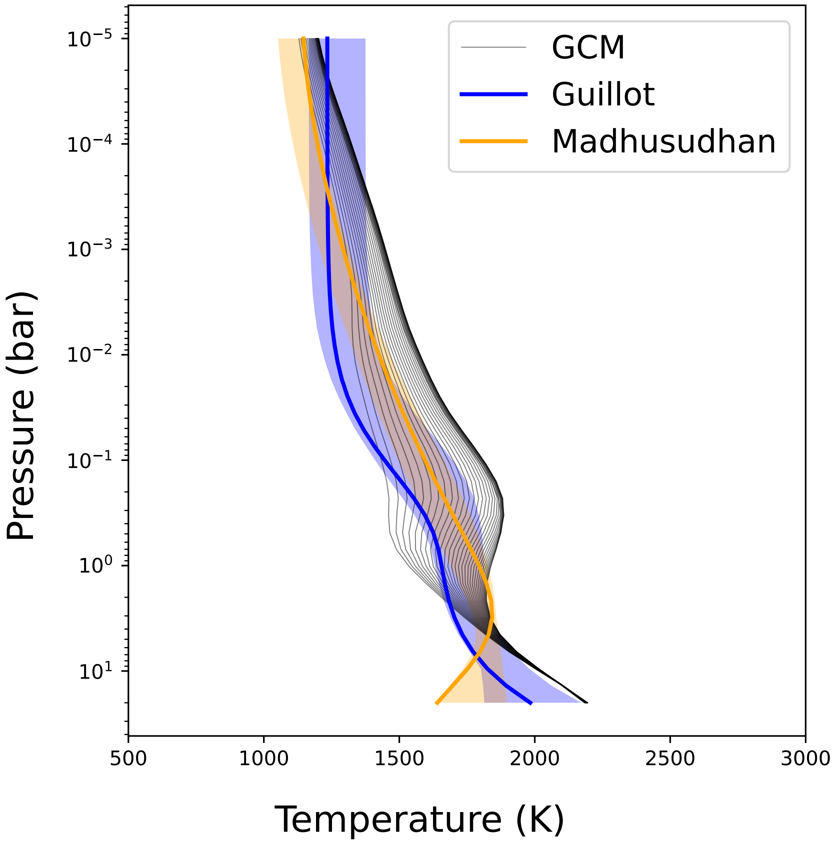

Figure 8.6: Retrieved best-fit TP profiles compared to the GCM dayside thermal structure. A total of 30 latitudinally-averaged GCM TP profiles, computed at 30 equally spaced longitudes from −90° to 90°, are shown on the plot. The GCM TP profiles are latitudinally-averaged between ±45° latitudes, using cos(latitude) as the weight. The best-fit Guillot (2010) and Madhusudhan & Seager (2009) TP profiles are calculated from the retrieved maximum a posteriori parameters. The shaded regions around the best-fit TP profiles represent the 1σ central credible intervals.

Figure 8.6 compares the retrieved thermal structure using the Guillot (2010) TP profile and the Madhusudhan & Seager (2009) TP profile to the latitudinally-averaged GCM dayside thermal structure, computed at 30 equally spaced longitudes from −90° to 90°, with the substellar point being the origin. While the 1σ central credible intervals of the retrieved TP profiles overlap with each other and with some of the latitudinally-averaged GCM thermal structure, we can still see that the GCM thermal structure is in general hotter than the TP profile retrieved using the Madhusudhan & Seager (2009) TP profile, which is in turn generally hotter than the TP profile retrieved using the Guillot (2010) TP profile. This lines up nicely with the metallicity constraints shown in Figure 8.5, where the metallicity retrieved assuming the GCM thermal structure is towards the higher end compared to the metallicity retrieved using the Madhusudhan & Seager (2009) TP profile, which is in turn towards the higher end of the metallicity retrieved using the Guillot (2010) TP profile. The correlation between atmospheric temperature and metallicity is due to the degeneracy between photospheric temperature and atmospheric opacity (which is determined by molecular abundance).

Large uncertainties in the average thermal structure still remain, even given the broad wavelength coverage of the dayside panchromatic emission spectrum. This illustrates that the uncertainty in thermal structure is a dominant source of uncertainty in the retrievals of emission spectra. See Chapter 9.1 for details on future work.

8.4 Constraining the Formation of WASP-43b

The present-day atmospheric composition of hot Jupiters may help us constrain their formation and evolution pathway. Despite the considerable uncertainties in the retrieved metallicity presented in Section 8.3.2, the results generally point to a metal-enriched atmosphere and a super-solar C/O ratio close to unity. In this section, we explore the implication of these constraints on the formation and evolution history of WASP-43b.

Let us first assume that the initial elemental composition of the planet-forming protoplanetary disc is identical to that of the host star (Madhusudhan, 2019), so that the disc is a H/He dominated mixture with trace species such as H_2O and CO_2 in either solid or gaseous form. As the temperature in the disc decreases radially from the star, the major volatile molecules start to condense at increasing radial distances: first H_2O, then CO_2, followed by CO, as shown by Figure 8.7. The location where these molecules start to condense, known as 'snowlines' or 'icelines', also migrates inward with time as the disc cools and eventually dissipates. The make-up of solid materials and gas materials in the disc changes drastically across these ice lines. Therefore, as argued in Öberg et al. (2011), the composition of a planet depends on the time and location of its formation, as well as the relative importance of gas-accretion and solid-accretion in its formation history.

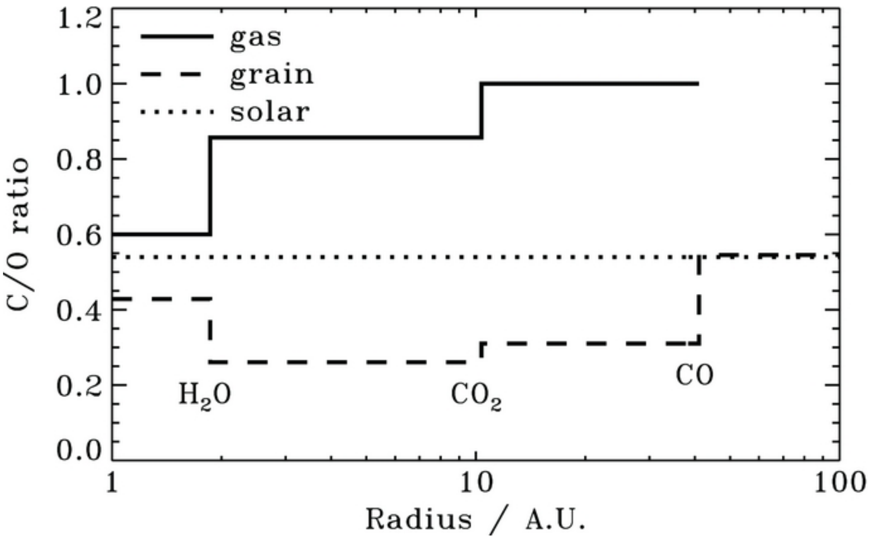

Figure 8.7: Figure 1 from Öberg et al. (2011) showing the C/O ratio in the gaseous phase and in the solid phase (grains) of the disc as a function of distance from the star. The figure shows the C/O profile taken from the disc mid plane, for a model protoplanetary disc around a solar-type star. The horizontal dashed line mark the solar C/O ratio. The locations of H_2O, CO_2, and CO snowlines are also marked for reference. Note that in this model, the C/O ratio in the gas is increasing as a function of radial distance, and that the C/O ratio in grains is mostly sub-solar.

Two parameters are important in constraining the formation history of hot Jupiters using atmospheric observations. The first parameter is metallicity, which is the abundance of heavy elements (elements other than H and He), often expressed relative to a solar composition gas . Since the gas phase of the disc is dominated by the H/He mixture, it is relatively metal-poor. In contrast, the solid phase of the disc is dominated by elements such as C and O and is relatively metal-rich. The metallicity of the planet thus contains information about the relative importance of gas accretion and solid accretion in a planet's formation history. The second parameter is the C/O ratio, i.e., the carbon-to-oxygen elemental abundance ratio. The C/O ratio is a tracer for the formation location, as the C/O ratios in the gas phase and solid phase change dramatically across ice lines, as illustrated by Figure 8.7 (Öberg et al., 2011). In general, C/O ratio in the gas phase increases with radial distance and can be super-stellar beyond H_2O ice line, whereas the C/O ratio in the solid phase is generally sub-stellar or stellar beyond H_2O ice line.

Let us now assume that WASP-43b formed in a protoplanetary disc similar to the disc model described in Öberg et al. (2011) and depicted in Figure 8.7. It will become apparent that it is difficult for the Öberg et al. (2011) disc model to produce a planet that matches the super-solar metallicity and super-solar C/O ratio retrieved for WASP-43b in this chapter. Consider two formation pathways. First, if WASP-43b formed beyond the CO/CO_2 snowlines and then migrated inward after the disc dissipation, then it should have sub-stellar metallicities and carbon-rich compositions with C/O approaching 1 (Madhusudhan et al., 2017; Madhusudhan, 2019), reflecting the low metallicity and high C/O ratio of the gas phase beyond the CO/CO_2 snowlines. This is inconsistent with the metal enrichment seen in the retrievals of WASP-43b (recall that WASP-43 has a solar metallicity). Second, suppose that WASP-43b formed via core accretion with significant planetesimal accretion and migrate inward before disc dissipation, in which case it should have super-stellar metallicities and sub-stellar C/O ratio (Madhusudhan et al., 2017; Madhusudhan, 2019). This is inconsistent with the close-to-unity C/O seen in the retrievals.

The difficulty in creating a high metallicity and high C/O ratio planet using the Öberg et al. (2011) disc model is interesting and suggest that other formation mechanisms might have played a part in the formation of WASP-43b. One possible mechanism is pebble drift and accretion. First, centimetre-sized, carbon-rich pebbles can form at large radial distance. These pebbles experience headwind from the gas phase of the disc since the gas phase orbit at sub-Keplerian velocity due to the pressure support, so the pebbles would drift inward rapidly (Johansen & Lambrechts, 2017; Madhusudhan et al., 2017; Mollière et al., 2022). As these pebbles drift inward, they can either be accreted directly by a forming gas giant, or evaporate in the inner disc and enrich the gas phase of the disc with carbon-rich species. Notably, Mollière et al. (2022) explored a range of giant planet formation scenarios and argued that the combination of super-solar metallicity and super-solar C/O ratio is difficult to explain without significant pebble drift and accretion. Another potential mechanism is in situ heavy element enrichment of hot Jupiters at short orbital radius by dust grains, which as argued by Morbidelli et al. (2023) an be significant in increasing the metallicity of hot Jupiters. A third potential mechanism is in situ enrichment by planetesimal accretion, though the accretion rate of this mechanism may not be significant (Johansen & Lambrechts, 2017). Therefore, the retrieval results suggest that a combination of pebble drift/accretion and in situ heavy element enrichment probably occurred in the formation of WASP-43b.

8.5 Summary

The retrievals of the panchromatic dayside emission spectrum consisting of the spectra observed with *HST*/WFC3, *JWST* NIRSpec/G395H and *JWST* MIRI/LRS confirm the detection of H_2O, CO and CO_2 reported in Chapters 6 and 7. The retrievals of this chapter also confirm the non-detection of CH_4 in Chapters 6 and 7. The panchromatic retrievals also show detection of NH_3, agreeing with Chapter 6, and detection of H_2S, agreeing with Chapter 7. Furthermore, the retrievals in this chapter show the detection of HCN and rule out the presence of OCS at detectable abundance.

The retrieved molecular abundances suggest that the atmosphere of WASP-43b is metal-enriched and has a close-to-unity C/O ratio, though the uncertainty on the metallicity is large. The metallicity and C/O ratio suggest that pebble accretion and in situ heavy element enrichment likely played important roles in the formation of WASP-43b.

Chapter 9

Limitations and Future Work

Constraining the atmospheric properties of hot Jupiters can be challenging because planetary atmospheres are physically complicated, and exoplanet observations are technically difficult. On the atmospheric physics side, many interacting physical processes affect the observed characteristics of atmospheres, such as radiative transfer, dynamical circulation, thermochemistry, photochemistry, and cloud formation. Disentangling these processes can be tricky as their effects on the observed spectra may be degenerate. On the astronomical observation side, exoplanets are faint objects compared to their stars, and hot Jupiters, in particular, cannot be spatially resolved from their host stars with current telescopes. Consequently, there are limitations on how well we can characterise the atmosphere of WASP-43b with the retrieval analysis presented in this thesis. This section explores the assumptions and limitations of this thesis and discusses avenues for future work. This chapter is structured as follows: Chapter 9.1 details the modelling of atmospheric thermal structure, Chapter 9.2 elaborates on the modelling of atmospheric chemistry, Chapter 9.3 discusses the modelling of aerosols, Chapter 9.4 expands on the limitation of the radiative transfer calculations in this thesis, and Chapter 9.5 explores the topic of data reduction. Finally, Chapter 9.6 summarises future work that can be done on the characterisation of hot Jupiters via emission spectroscopy.

9.1 Thermal Structure

The parametrisation of the atmospheric thermal structure and the degeneracy between thermal structure and molecular abundance in emission spectroscopy are a significant source of uncertainties in the retrieved atmospheric properties presented in this thesis. The retrievals in Chapters 5 and 6 employ the Yang et al. (2023) 2D temperature model introduced in Section 3.2 to fit emission spectra at different orbital phases simultaneously, which comes with various assumptions. The first assumption is that a latitudinally-averaged structure can effectively model the phase curve data. In the Yang et al. (2023) 2D temperature model, temperature varies as a function of longitude and pressure while being held constant as a function of latitude on isobars, as shown by Equation (3.5) and Figure 3.1. The retrieved temperature map is then interpreted as a meridional mean temperature map, using cos(latitude) as the weight. This interpretation is based on the fact that Irwin et al. (2020) and Yang et al. (2023) find the temperature structure retrieved from synthetic phase curve data simulated from a GCM closely resembles the latitudinally-averaged thermal structure of the GCM using cos(latitude) as the weight, which was also demonstrated in Section 5.4 of this thesis. The Yang et al. (2023) 2D temperature model further assumes that the thermal structure is symmetric about the equator (north-south symmetry) and about the meridian going through the centre of the dayside region (east-west symmetry, though the centre of the dayside in the model can shift from the substellar point) and that the thermal structure on the nightside is more homogeneous than that on the dayside. As discussed in Section 3.2, this meridional mean structure is inspired by GCM studies. However, the model cannot explore more complex mean thermal structures seen in GCM simulations, such as pressure-dependent hot spot offset.

The parametric modelling presented is only one of the first steps in understanding the thermal structure of hot Jupiters through observations. As more *JWST* data become available, a more sophisticated model setup may be necessary. Looking ahead, there are two promising avenues for a more detailed modelling of the thermal structure of hot Jupiters. First, we can observationally constrain the dayside latitudinal thermal variation using the eclipse mapping method, where high cadence flux measurements are taken as the star gradually eclipses the planet (e.g., Majeau et al., 2012). During the ingress, the star blocks off the planet slice by slice, whereas during egress, the planet emerges from behind the star slice by slice. By analysing the ingress and egress light curves, we can construct a 2D brightness temperature map for the planet under observation (e.g., Rauscher et al., 2007; Boone et al., 2024). Eclipse mapping of WASP-43b has recently been carried out using the data from the *JWST*/MIRI observation (Hammond et al., 2024) and the *JWST*/NIRSpec observation (Challener et al., 2024), though there are still large uncertainties in the derived dayside brightness temperature maps. A future study could combine the eclipse mapping data and the spectroscopic phase curve data of WASP-43b from both the *JWST*/MIRI observation and the *JWST*/NIRSpec observation to better characterise its thermal structure. By fitting these two data sets simultaneously, we can combine the latitudinal constraints from eclipse mapping with the longitudinal and vertical constraints from spectroscopic phase curves to create a 3D atmospheric temperature map of WASP-43b on the dayside. Secondly, from a modelling perspective, it has been shown in Chapters 7 and 8 that a general circulation model of WASP-43b can fit the dayside observations well, though the model struggles to reproduce the low observed nightside flux of WASP-43b. This points to the feasibility of directly fitting hot Jupiter observations with a grid of pre-computed GCMs, for example, those computed in Roth et al. (2024) or Roman et al. (2021). Atmospheric retrievals with a GCM grid will confine the exploration of atmospheric models to more physically self-consistent thermal structures, and a future study can explore if GCMs with stronger atmospheric drag (hence lower heat circulation efficiency) and/or nightside clouds can better fit the observations of WASP-43b.

9.2 Uniform Chemistry

There are two limitations in constraining atmospheric chemistry using the retrievals in this thesis: (1) the observations in this thesis are not spatially resolved; (2) molecular abundance and thermal structure are degenerate in low-resolution emission spectroscopy. In particular, it is difficult to constrain the spatial distribution of molecules observationally. A major assumption made in the retrievals in this thesis is that the chemical abundance of the atmosphere is constant with longitude, latitude, and pressure in the pressure region probed by the observations. This uniform chemistry assumption is based on previous chemical and dynamical modelling work, which showed that atmospheric dynamics can effectively homogenise the abundance of the most significant molecular species in the atmospheres of hot Jupiters in the pressure region probed by emission spectra (Cooper & Showman, 2006; Agúndez et al., 2014; Baeyens et al., 2021, 2022). The physical mechanism behind this homogenisation is atmospheric quenching. In a static atmosphere with negligible photochemistry, the atmospheric chemical abundance is set by thermochemical equilibrium (Venot et al., 2020), which is illustrated in the top panel of Figure 9.1. In other words, the chemical abundance in a static atmosphere is set by the temperature structure of the atmosphere. In the presence of atmospheric mixing, consider a parcel of gas in equilibrium in one region of the atmosphere. As it is transported to another region with a different temperature, it is driven out of thermochemical equilibrium. The timescale on which chemical reactions can restore the parcel to equilibrium is dependent on the temperature: chemical reactions generally happen faster at higher temperatures.

Therefore, when a parcel of air from a hot region is transported to a much colder region, it roughly retains the equilibrium abundance of the hot region as the reaction rate slows down, i.e., the parcel is ‘quenched’. Therefore, in the atmosphere of hot Jupiters, where strong equatorial jets are expected to drive vigorous atmospheric mixing (Cooper & Showman, 2006), it is expected that the atmospheric abundance is quenched to the equilibrium abundance of the hot substellar region in the 1 bar to 1 mbar pressure range probed by emission spectra, as illustrated by the bottom panel of Figure 9.1.

The validity of the uniform chemistry assumption depends on the gas species, the characteristics of the planetary atmosphere and the relevant pressure range. The chemical and dynamical modelling work of Venot et al. (2020) showed that for H_2O and CO, which are predicted to be two of the most abundant spectrally active molecules on hot Jupiters in the pressure ranges probed by low-resolution emission spectroscopy, the constant chemistry assumption is valid. Both thermochemical equilibrium models and models that include atmospheric mixing predict their abundances to be approximately uniform in the observable pressure region for a WASP-43b-like planet (see Figure 9.1). The assumption of uniform H_2O abundance on WASP-43b is also consistent with the retrieval analysis in Bell et al. (2024), which showed no significant phase variation in H_2O abundance, as illustrated in Figure 6.9. As a result, since the metallicity and C/O ratio constraints in this thesis (see Chapter 8) are largely based on the retrieved H_2O and CO abundances, they are robust to the assumption of different atmospheric chemistry models.

The spatial distributions of some less abundance molecules such as CH_4, NH_3, HCN and CO_2 in thermochemical equilibrium can vary significantly with longitude and pressure in hot Jupiter atmospheres, especially in the case of CH_4, as shown by the top panel of Figure 9.1. Under thermochemical equilibrium, CH_4 is expected to be detectably abundant on the nightside of WASP-43b but remain undetectable on the dayside. However, by coupling a simplified chemical kinetics network to a GCM of the hot Jupiter HD 209458b, Cooper & Showman (2006) showed that the CH_4 abundance should be homogenised between 1 bar and 1 millibar to be representative of the low dayside abundance when strong zonal circulation is present in the atmosphere of a hot Jupiter. The uniform CH_4 prediction was later corroborated by Agúndez et al. (2014), who coupled a more realistic chemical network to a simplified circulation scheme that included both vertical mixing and a uniform zonal wind. Modelling specific to the planetary parameters of WASP-43b showed that dynamical timescale dominates over chemical timescale between 1 bar and 1 millibar (Mendonça et al., 2018b; Venot et al., 2020; Baeyens et al., 2021), and there should be no significant longitudinal variation in the abundances of CO_2, CH_4 and NH_3. The assumption of constant-with-longitude CH_4 abundance is consistent with the non-detection of CH_4 at all orbital phases in Bell et al. (2024). There is also circumstantial evidence of strong zonal circulation on WASP-43b. For example, Bell et al. (2024) found a $\sim 8^\circ$ eastward hot spot shift that could be explained by an equatorial super-rotating jet, and Lesjak et al. (2023) inferred a wind speed of 3-8 kms^{-1} from high-resolution emission spectroscopy of WASP-43b. Nonetheless, the assumption that molecules such as CH_4, NH_3, HCN and CO_2 are uniform in the atmosphere of WASP-43b is weaker than the assumption that H_2O and CO are uniform in the atmosphere, as there are can also be vertical variation in their abundances, as shown by Figure 9.1. As a result, the errors on their retrieved abundances may be underestimated by the retrievals in this thesis.

Apart from the interplay between circulation and equilibrium chemistry, photochemistry and molecular dissociation can also affect the spatial distribution of molecular abundance. This is particularly relevant for sulphur species. However, one would only expect dissociation to be significant in much more strongly irradiated planets than WASP-43b, and one would expect photochemical products to be insignificant in the pressure region probed by emission spectroscopy. The assumption that photochemistry is insignificant is consistent with the non-detection of SO_2, which is produced by photochemistry, in Chapter 8.

For future study, there are two potential extensions to the work done in this thesis. Firstly, we can add parameterisation of variable chemistry into the retrievals, so that molecular abundance can vary as a function of location. This can allow us to more robustly estimate the uncertainties of the molecular constraints. Secondly, we can explore the chemistry of WASP-43b from a more self-consistent modelling approach by calculating chemistry models on a grid of GCMs such as those from Roth et al. (2024). We can then compare these chemistry models to the observations to better understand the chemical profile of WASP-43b.

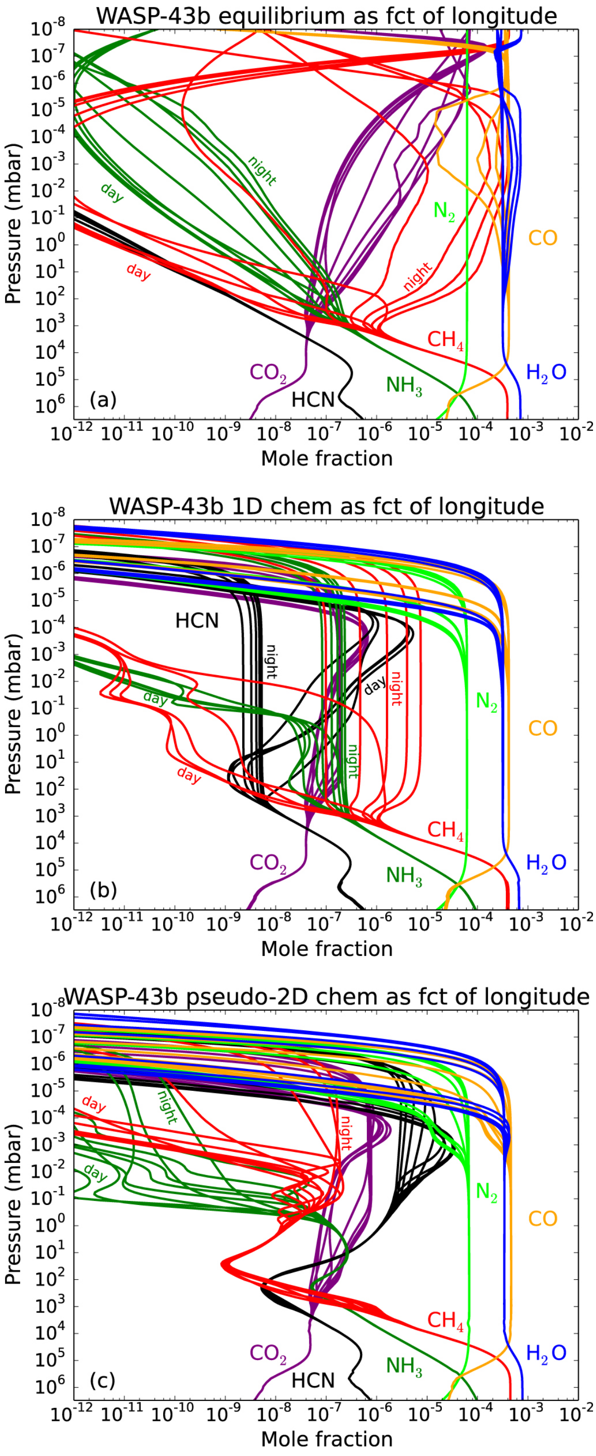

Figure 9.1: Figure 5 from Venot et al. (2020) displaying three atmospheric chemistry models of WASP-43b. In the top panel, the chemical abundance is set purely by thermochemical equilibrium. The middle panel extends the model in the top panel by adding vertical mixing and photochemistry. The bottom panel extends the model in the middle panel further by taking horizontal mixing into account. Note that the different profiles corresponding to the same molecules represent profiles taken from a range of different latitudes.

9.3 Aerosols

The lack of explicit cloud modelling is a major limitation of this thesis, as the retrievals of WASP-43b in this thesis include no aerosol models. The errors introduced by this assumption depend, of course, on whether there are significant aerosols in the atmosphere of WASP-43b in the pressure range probed by the emission spectra analysed in this thesis. The hypothesis that the dayside region of WASP-43b contains no optically thick aerosols in the pressure range probed by emission spectroscopy is supported by numerous studies. Kreidberg et al. (2014) found no evidence of clouds in the day/night terminator of the planet by analysing the transmission spectrum observed with *HST*/WFC3, and Stevenson et al. (2017) inferred a low Bond albedo from *HST*/WFC3 + *Spitzer*/IRAC phase curves that is consistent with insignificant dayside cloud coverage. More recently, Fraine et al. (2021) did not detect clouds using reflected light photometry with *HST* WFC3/UVIS, and a joint analysis of *CHEOPS*, *TESS*, and *HST* WFC3/UVIS data by Scandariato et al. (2022) also found no evidence of clouds. From a modelling perspective, it has been found that cloud-free GCMs can match the dayside observations of WASP-43b (Bell et al., 2024), and Chapter 8 also showed that the thermal structure of a cloud-free GCM can fit the panchromatic dayside emission spectrum and that the retrieved thermal structure using parametric TP profiles resembles that of the cloud-free GCM on the dayside. If the dayside of WASP-43b does contain clouds, then the reflected light from the aerosols may contaminate the spectra and bias the retrieval results. However, Fraine et al. (2021) estimated the geometric albedo of WASP-43b to be less than 0.06 at 3σ, which correspond to a negligible reflected stellar light contribution compared to the measurement uncertainties of the data analysed in this thesis. Even using the larger indirect estimate of the Bond albedo at $0.19^{+0.08}_{-0.09}$ from Stevenson et al. (2017), the contribution from reflected stellar light is at most 150 ppm (Figure 6, Irwin et al., 2020), which is only likely to be significant for the shortest *HST* wavelengths analysed in Chapter 5. Reassuringly, the retrieval results in Chapter 5 are in good agreement with the retrievals in the other Chapters that analysed longer wavelengths. In conclusion, the dayside of WASP-43b is unlikely to contain clouds that can significantly bias the retrieval results.

The nightside of WASP-43b, on the other hand, may be cloudy, though there are no direct observational evidence of any aerosols. A cloudy nightside has been inferred from the large day-night brightness temperature contrast (Stevenson et al., 2017; Kataria et al., 2015; Mendonça et al., 2018a; Morello et al., 2019; Irwin et al., 2020). Bell et al. (2024) also found that some cloudy GCMs can fit the MIRI phase curve at nightside phases better than cloudless GCMs, though no GCM could fit the observation within measurement uncertainties at all orbital phases. Notably, both the retrieval analysis in Bell et al. (2024) and the retrieval analysis in this thesis show that the observed nightside spectra can be adequately fit with cloud-free parametric atmospheric models. As discussed in Section 6.3.3, it has been shown that a more isothermal temperature profile can mimic the effects of cloud opacity in low-resolution spectral retrievals (Burningham et al., 2017; Mollière et al., 2020), which can explain the ability of simple models to fit the observation without invoking cloud opacity. This is a key reason why low-resolution emission spectra are not optimal at constraining aerosol properties.

The main error introduced by the omission of clouds from the retrievals is that the retrieved nightside thermal structure presented in Chapters 5, 6 and 7 would not be reliable if the nightside of WASP-43b is cloudy, which in turn bias the retrieved molecular abundance. However, the cloud-free dayside still anchors the retrieved chemical abundances. On the other hand, as mentioned in Section 6.3.2, even though the abundance constraints may not be biased in the presence of nightside clouds, a significant amount of oxygen may be removed from the gas-phase molecules if the cloud composition is rich in silicates (Woitke et al., 2018). Consequently, based on the retrieved gas-phase abundance constraints, one would underestimate the metallicity and overestimate the C/O ratio of WASP-43b.

For future work, it would be crucial to quantify the potential bias introduced by clouds. One approach is to simulate emission spectra using cloudy GCMs, for example those calculated in Parmentier et al. (2020) and Roman et al. (2021). By performing mock retrievals on these cloudy spectra with a range of parametric cloud models such as those outlined in Barstow (2020) and Ma et al. (2023), we can then quantitatively assess the effects of clouds on the retrieved atmospheric properties.

9.4 Radiative Transfer

The accuracy of the radiative transfer calculation that computes the model spectra limits the accuracy of the atmospheric properties retrieved from observations. There are two sources of errors in radiative transfer calculation: the errors in the radiative transfer model itself and the errors in the input opacity data. On the radiative transfer model side, this thesis employs the correlated-k approximation (Lacis & Oinas, 1991) to speed up radiative transfer calculation as the retrievals performed in this thesis typically requires the computation of hundreds of thousands of model spectra. Studies have shown that the correlated-k method introduces negligible errors in modelling exoplanet spectra (Mollière et al., 2015; Irwin et al., 2020; Leconte, 2021), especially compared to the large uncertainties introduced by the degeneracy between thermal structure and molecular abundances inherent in the analysis of emission spectra. On the opacity data side, the accuracy of the molecular opacity data may be a significant source of errors, as argued by Niraula et al. (2022), though most atmospheric retrieval studies ignore this source of errors at present. As data quality advances in the *JWST* era, future studies need to more carefully assess the errors intrinsic to the assumed opacity data. A particularly important avenue of future study would be to explore the effect of using different opacity data parameters, such as pressure broadening parameter (Niraula et al., 2022) on the retrievals of emission spectra.

9.5 Data Reduction

Data reduction is the procedure by which raw outputs from space telescopes are transformed into science products, such as the emission spectra analysed in this thesis. Steps in data reduction include, for example, removing cosmic ray contamination, correcting for systematic errors introduced by the telescope instruments, and binning flux measurements to improve signal-to-noise ratios. Naturally, the atmospheric retrieval results presented in this thesis are conditional on the reliability of the data reduction that produced the emission spectra. Furthermore, in Chapters 5 and 6, the phase-resolved emission spectra at different orbital phases are treated as independent measurements and retrieved simultaneously to boost the signal-to-noise ratio of the retrievals. In reality, these spectra are correlated through the data reduction process, as phase curves are conventionally extracted by fitting a combination of Fourier series and systematics model to the time-series observations, wavelength by wavelength (Stevenson et al., 2014, 2017; Bell et al., 2024; Changeat et al., 2024). In effect, these chapters assume that the measurement uncertainties of the spectra are Gaussian and independent when, in reality, they are possibly non-Gaussian and correlated. Consequently, the retrieved posterior distribution would be different to the case where the atmospheric retrieval is performed simultaneously with the data reduction on the time-series observations. For the current precisions of molecular abundance constraints, the bias introduced by separating data reduction and atmospheric retrievals should be a secondary effect. For future work, we can perform the atmospheric retrieval at the same time as the data reduction directly on the time-series observations, as done in Changeat et al. (2024).

9.6 Future Work

This section summarises future work that can be done to improve the retrievals of phase-resolved emission spectra of WASP-43b, as well as hot Jupiters in general. An immediate starting point is a more in depth analysis of the panchromatic phase-resolved emission spectra analysed in Chapter 8. The retrievals in Chapter 8 fit only four orbital phases of the panchromatic phase-resolved emission spectra, and each spectrum is retrieved independently. The next step would be to fit multiple orbital phases simultaneously, as done for the *HST*, *Spitzer* and MIRI data sets in Chapters 5 and 6. The simultaneous fitting of the panchromatic data at multiple orbital phases will likely require more sophisticated parametric atmospheric models than those used in this thesis. Furthermore, as mentioned in previously in this chapter, we could also combine the panchromatic phase curve data with eclipse mapping data, which will necessitate the modelling of latitudinal thermal structure. Additionally, an in depth exploration of cloud models in the retrievals of emission spectra can also help quantify the potential bias introduced by aerosols. From a modelling perspective, more work should be done on self-consistent modelling of hot Jupiter atmospheres. This can help us create more realistic parametric atmospheric models for retrievals, as well as assessing the assumptions commonly made in retrievals, such as the uniform chemistry assumption discussed earlier in this chapter.

Chapter 10

Conclusion

This thesis presents new tools for the atmospheric retrievals of hot Jupiters using emission spectra observed with space telescopes, including a novel parametric 2D temperature model (Section 3.2) and an open source radiative transfer and retrieval software (Section 2.5). By using these tools, this thesis retrieves the atmospheric properties of the hot Jupiter WASP-43b from phase-resolved emission spectra observed with four different instruments onboard space telescopes: (1) the Wide Field Camera 3 onboard the Hubble Space Telescope (Chapter 5); (2) the InfraRed Array Camera onboard the Spitzer Space Telescope (Chapter 5); (3) the Mid-Infrared Instrument onboard the *JWST* (Chapter 6); and (4) the Near Infrared Spectrograph onboard the *JWST* (Chapter 7). Atmospheric retrievals using these data sets reveal detections of key molecular species in the atmosphere of WASP-43b (Chapter 8), including H_2O ($> 12\sigma$), CO_2 ($> 13\sigma$), CO ($> 7\sigma$), NH_3 ($> 6\sigma$), HCN ($> 4\sigma$), and H_2S ($> 2.8\sigma$), and place a strict upper bound on the abundance of CH_4. This is the first time carbon-bearing and nitrogen-bearing species have been confidently detected in the atmosphere of WASP-43b using space telescope observations. Furthermore, the retrievals constrain the thermal structure of WASP-43b across the pressure range of 1-10^{-3} bar and show that the dayside temperature structure of WASP-43b is well-approximated by a cloud-free general circulation model (Chapters 7 and 8). The detailed characterisation of the atmospheric properties of WASP-43b presented in this thesis is crucial for future modelling studies on this important target. Furthermore, the molecular abundance constrained in this thesis suggests that the atmosphere of WASP-43b has a super-solar metallicity and a super-solar C/O ratio. The combination of these two constraints suggests that pebble drift/accretion and in situ heavy element enrichment likely played important roles in forming WASP-43b.

References

Agúndez M., Parmentier V., Venot O., Hersant F., Selsis F., 2014, Astronomy & Astrophysics, 564, A73

Alderson L., et al., 2023, Nature, 614, 664

Allard F., Hauschildt P. H., 1995, The Astrophysical Journal, 445, 433

Amundsen D. S., et al., 2016, Astronomy & Astrophysics, 595, A36

Argyriou I., et al., 2023, Astronomy & Astrophysics, 680, A96

Azzam A. A. A., Tennyson J., Yurchenko S. N., Naumenko O. V., 2016, Monthly Notices of the Royal Astronomical Society, 460, 4063

Baeyens R., Decin L., Carone L., Venot O., Agúndez M., Mollière P., 2021, Monthly Notices of the Royal Astronomical Society, 505, 5603

Baeyens R., Konings T., Venot O., Carone L., Decin L., 2022, Monthly Notices of the Royal Astronomical Society, 512, 4877

Banerjee A., et al., 2024, Atmospheric Retrievals Suggest the Presence of a Secondary Atmosphere and Possible Sulfur Species on L 98-59 d from JWST NIRSpec G395H Transmission Spectroscopy (`arXiv:2408.15707`), doi:10.3847/2041-8213/ad73d0

Barber R. J., Tennyson J., Harris G. J., Tolchenov R. N., 2006, Monthly Notices of the Royal Astronomical Society, 368, 1087

Barber R. J., Strange J. K., Hill C., Polyansky O. L., Mellau G. Ch., Yurchenko S. N., Tennyson J., 2014, Monthly Notices of the Royal Astronomical Society, 437, 1828

Barman T. S., Konopacky Q. M., Macintosh B., Marois C., 2015, The Astrophysical Journal, 804, 61

Barstow J. K., 2020, Monthly Notices of the Royal Astronomical Society, 497, 4183

Barstow J. K., Aigrain S., Irwin P. G. J., Hackler T., Fletcher L. N., Lee J. M., Gibson N. P., 2014, The Astrophysical Journal, 786, 154

Barstow J. K., Aigrain S., Irwin P. G. J., Sing D. K., 2016, The Astrophysical Journal, 834, 50

Barstow J. K., Changeat Q., Garland R., Line M. R., Rocchetto M., Waldmann I. P., 2020, Monthly Notices of the Royal Astronomical Society, 493, 4884

Bell T. J., et al., 2023a, A First Look at the JWST MIRI/LRS Phase Curve of WASP-43b (`arXiv:2301.06350`), doi:10.48550/arXiv.2301.06350

Bell T. J., et al., 2023b, Nature, 623, 709

Bell T. J., et al., 2024, Nightside Clouds and Disequilibrium Chemistry on the Hot Jupiter WASP-43b (`arXiv:2401.13027`)

Benneke B., Seager S., 2013, The Astrophysical Journal, 778, 153

Birkmann S. M., et al., 2022, Astronomy & Astrophysics, 661, A83

Blecic J., et al., 2014, The Astrophysical Journal, 781, 116

Blecic J., Dobbs-Dixon I., Greene T., 2017, The Astrophysical Journal, 848, 127

Boone S., Grant D., Hammond M., 2024, Monthly Notices of the Royal Astronomical Society, 528, 596

Borysow A., Frommhold L., 1989, The Astrophysical Journal, 341, 549

Borysow A., Frommhold L., Moraldi M., 1989, The Astrophysical Journal, 336, 495

Brogi M., Line M. R., 2019, The Astronomical Journal, 157, 114

Buchner J., et al., 2014, Astronomy & Astrophysics, 564, A125

Burningham B., Marley M. S., Line M. R., Lupu R., Visscher C., Morley C. V., Saumon D., Freedman R., 2017, Monthly Notices of the Royal Astronomical Society, 470, 1177

Carone L., et al., 2020, Monthly Notices of the Royal Astronomical Society, 496, 3582

Casasayas-Barris N., Palle E., Nowak G., Yan F., Nortmann L., Murgas F., 2017, Astronomy & Astrophysics, 608, A135

Castelli F., Kurucz R. L., 2004, Astronomy & Astrophysics, 419, 725

Chachan Y., Knutson H. A., Lothringer J., Blake G. A., 2023, The Astrophysical Journal, 943, 112

Challener R. C., et al., 2024, The Astrophysical Journal Letters, 969, L32

Changeat Q., Al-Refaie A., 2020, The Astrophysical Journal, 898, 155

Changeat Q., Al-Refaie A. F., Edwards B., Waldmann I. P., Tinetti G., 2021, The Astrophysical Journal, 913, 73

Changeat Q., Ito Y., Al-Refaie A. F., Yip K. H., Lueftinger T., 2024, The Astronomical Journal, 167, 195

Charbonneau D., Brown T. M., Noyes R. W., Gilliland R. L., 2002, The Astrophysical Journal, 568, 377

Cho J. Y.-K., Skinner J. W., Thrastarson H. T., 2021, The Astrophysical Journal Letters, 913, L32

Chubb K. L., Min M., 2022, Astronomy & Astrophysics

Chubb K. L., Min M., Kawashima Y., Helling C., Waldmann I., 2020, Astronomy & Astrophysics, 639, A3

Chubb K. L., et al., 2021, Astronomy & Astrophysics, 646, A21

Coles P. A., Yurchenko S. N., Tennyson J., 2019, Monthly Notices of the Royal Astronomical Society, 490, 4638

Cooper C. S., Showman A. P., 2006, The Astrophysical Journal, 649, 1048

Cornish N. J., Littenberg T. B., 2007, Physical Review D, 76, 083006

Cridland A. J., van Dishoeck E. F., Alessi M., Pudritz R. E., 2020, Astronomy & Astrophysics, 642, A229

Crossfield I. J. M., 2023, The Astrophysical Journal Letters, 952, L18

Cubillos P. E., et al., 2021, The Astrophysical Journal, 915, 45

Cumming A., Butler R. P., Marcy G. W., Vogt S. S., Wright J. T., Fischer D. A., 2008, Publications of the Astronomical Society of the Pacific, 120, 531

Czesla S., Salz M., Schneider P. C., Schmitt J. H. M. M., 2013, Astronomy & Astrophysics, 560, A17

Dawson R. I., Johnson J. A., 2018, Annual Review of Astronomy and Astrophysics, 56, 175

Dobbs-Dixon I., Blecic J., 2022, The Astrophysical Journal, 929, 46

Drummond B., et al., 2018a, The Astrophysical Journal Letters, 855, L31

Drummond B., Mayne N. J., Manners J., Baraffe I., Goyal J., Tremblin P., Sing D. K., Kohary K., 2018b, The Astrophysical Journal, 869, 28

Dyrek A., et al., 2024, Nature, 625, 51

Evans T. M., et al., 2016, The Astrophysical Journal, 822, L4

Fazio G. G., et al., 2004, The Astrophysical Journal Supplement Series, 154, 10

Feng Y. K., Line M. R., Fortney J. J., 2020, The Astronomical Journal, 160, 137

Feroz F., Hobson M. P., 2008, Monthly Notices of the Royal Astronomical Society, 384, 449

Fisher C., Heng K., 2018, Monthly Notices of the Royal Astronomical Society, 481, 4698

Fortney J. J., Visscher C., Marley M. S., Hood C. E., Line M. R., Thorngren D. P., Freedman R. S., Lupu R., 2020, The Astronomical Journal, 160, 288

Fortney J. J., Dawson R. I., Komacek T. D., 2021, Journal of Geophysical Research: Planets, 126, e2020JE006629

Fraine J., et al., 2021, The Astronomical Journal, 161, 269

Fu G., et al., 2024, Nature, 632, 752

Gandhi S., Madhusudhan N., 2018, Monthly Notices of the Royal Astronomical Society, 474, 271

Giacobbe P., et al., 2021, Nature, 592, 205

Gibson N. P., et al., 2020, Monthly Notices of the Royal Astronomical Society, 493, 2215

Gillon M., et al., 2012, Astronomy & Astrophysics, 542, A4

Gladman B., Quinn D. D., Nicholson P., Rand R., 1996, Icarus, 122, 166

Goody R. M., Yung Y. L., 1995, Atmospheric Radiation: Theoretical Basis. Oxford University Press

Grant D., et al., 2023, JWST-TST DREAMS: Quartz Clouds in the Atmosphere of WASP-17b (`arXiv:2310.08637`)

Guillot T., 2010, Astronomy and Astrophysics, 520, A27

Hammond M., et al., 2024, Two-Dimensional Eclipse Mapping of the Hot Jupiter WASP-43b with JWST MIRI/LRS (`arXiv:2404.16488`)

Hauschildt P. H., Allard F., Baron E., 1999, The Astrophysical Journal, 512, 377

Hellier C., et al., 2011, Astronomy & Astrophysics, 535, L7

Helling Ch., Kawashima Y., Graham V., Samra D., Chubb K. L., Min M., Waters L. B. F. M., Parmentier V., 2020, Astronomy & Astrophysics, 641, A178

Heng K., Mendonça J. M., Lee J.-M., 2014, The Astrophysical Journal Supplement Series, 215, 4

Hoeijmakers H. J., et al., 2018, Nature, 560, 453

Huitson C. M., Sing D. K., Vidal-Madjar A., Ballester G. E., Lecavelier des Etangs A., Désert J.-M., Pont F., 2012, Monthly Notices of the Royal Astronomical Society, 422, 2477

Husser T.-O., Berg S. W.-v., Dreizler S., Homeier D., Reiners A., Barman T., Hauschildt P. H., 2013, Astronomy & Astrophysics, 553, A6

Irwin P., et al., 2008, Journal of Quantitative Spectroscopy and Radiative Transfer, 109, 1136

Irwin P. G. J., Parmentier V., Taylor J., Barstow J., Aigrain S., Lee E., Garland R., 2020, Monthly Notices of the Royal Astronomical Society, 493, 106

James A., et al., 2023, Journal of Geophysical Research: Planets, 128, e2023JE007904

Johansen A., Lambrechts M., 2017, Annual Review of Earth and Planetary Sciences, 45, 359

Kataria T., Showman A. P., Fortney J. J., Stevenson K. B., Line M. R., Kreidberg L., Bean J. L., Désert J.-M., 2015, The Astrophysical Journal, 801, 86

Keating D., Cowan N. B., 2017, The Astrophysical Journal Letters, 849, L5

Kreidberg L., et al., 2014, The Astrophysical Journal, 793, L27

Krissansen-Totton J., Garland R., Irwin P., Catling D. C., 2018, The Astronomical Journal, 156, 114

Lacis A. A., Oinas V., 1991, Journal of Geophysical Research, 96, 9027

Lam S. K., Pitrou A., Seibert S., 2015, in Proceedings of the Second Workshop on the LLVM Compiler Infrastructure in HPC. LLVM '15. Association for Computing Machinery, New York, NY, USA, pp 1–6, doi:10.1145/2833157.2833162

Leconte J., 2021, Astronomy & Astrophysics, 645, A20

Lee J.-M., Fletcher L. N., Irwin P. G. J., 2012, Monthly Notices of the Royal Astronomical Society, 420, 170

Lesjak F., et al., 2023, Astronomy & Astrophysics, 678, A23

Li G., Gordon I. E., Rothman L. S., Tan Y., Hu S.-M., Kassi S., Campargue A., Medvedev E. S., 2015, The Astrophysical Journal Supplement Series, 216, 15

Line M. R., Teske J., Burningham B., Fortney J. J., Marley M. S., 2015, The Astrophysical Journal, 807, 183

Line M. R., et al., 2021, Nature, 598, 580

Lodders K., 2010, pp 379–417 (`arXiv:1010.2746`), doi:10.1007/978-3-642-10352-0˙8

Lodders K., Fegley B., 2002, Icarus, 155, 393

Ma S., Ito Y., Al-Refaie A. F., Changeat Q., Edwards B., Tinetti G., 2023, YunMa: Enabling Spectral Retrievals of Exoplanetary Clouds (`arXiv:2301.13708`)

MacDonald R. J., Madhusudhan N., 2017a, Monthly Notices of the Royal Astronomical Society, 469, 1979

MacDonald R. J., Madhusudhan N., 2017b, The Astrophysical Journal Letters, 850, L15

Madhusudhan N., 2018, pp 2153–2182 (`arXiv:1808.04824`), doi:10.1007/978-3-319-55333-7˙104

Madhusudhan N., 2019, Annual Review of Astronomy and Astrophysics, 57, 617

Madhusudhan N., Seager S., 2009, The Astrophysical Journal, 707, 24

Madhusudhan N., Amin M. A., Kennedy G. M., 2014, The Astrophysical Journal Letters, 794, L12

Madhusudhan N., Bitsch B., Johansen A., Eriksson L., 2017, Monthly Notices of the Royal Astronomical Society, 469, 4102

Majeau C., Agol E., Cowan N. B., 2012, The Astrophysical Journal, 747, L20

Mansfield M., et al., 2021, Nature Astronomy, 5, 1224

Mayor M., Queloz D., 1995, Nature, 378, 355

Mendonça J. M., 2020, Monthly Notices of the Royal Astronomical Society, 491, 1456

Mendonça J. M., Malik M., Demory B.-O., Heng K., 2018a, The Astronomical Journal, 155, 150

Mendonça J. M., Tsai S.-M., Malik M., Grimm S. L., Heng K., 2018b, The Astrophysical Journal, 869, 107

Mollière P., van Boekel R., Dullemond C., Henning Th., Mordasini C., 2015, The Astrophysical Journal, 813, 47

Mollière P., et al., 2020, Astronomy & Astrophysics, 640, A131

Mollière P., et al., 2022, The Astrophysical Journal, 934, 74

Morbidelli A., Batygin K., Lega E., 2023, Astronomy & Astrophysics, 675, A75

Mordasini C., van Boekel R., Mollière P., Henning Th., Benneke B., 2016, The Astrophysical Journal, 832, 41

Morello G., Danielski C., Dickens D., Tremblin P., Lagage P.-O., 2019, The Astronomical Journal, 157, 205

Morey R. D., Romeijn J.-W., Rouder J. N., 2016, Journal of Mathematical Psychology, 72, 6

Murphy M. M., et al., 2023, The Astronomical Journal, 165, 107

Niemann H. B., et al., 1998, Journal of Geophysical Research: Planets, 103, 22831

Nikolov N., et al., 2014, Monthly Notices of the Royal Astronomical Society, 437, 46

Nikolov N., et al., 2015, Monthly Notices of the Royal Astronomical Society, 447, 463

Niraula P., de Wit J., Gordon I. E., Hargreaves R. J., Sousa-Silva C., Kochanov R. V., 2022, Nature Astronomy, 6, 1287

Öberg K. I., Murray-Clay R., Bergin E. A., 2011, The Astrophysical Journal, 743, L16

Ohno K., Fortney J. J., 2023a, The Astrophysical Journal, 946, 18

Ohno K., Fortney J. J., 2023b, The Astrophysical Journal, 956, 125

Owens A., Yurchenko S. N., Tennyson J., 2024, Monthly Notices of the Royal Astronomical Society, 530, 4004

Parmentier V., Crossfield I. J. M., 2017, in Deeg H. J., Belmonte J. A., eds, , Handbook of Exoplanets. Springer International Publishing, Cham, pp 1–22, doi:10.1007/978-3-319-30648-3˙116-1

Parmentier V., Showman A. P., Lian Y., 2013, Astronomy & Astrophysics, 558, A91

Parmentier V., Fortney J. J., Showman A. P., Morley C., Marley M. S., 2016, The Astrophysical Journal, 828, 22

Parmentier V., Showman A. P., Fortney J. J., 2020, Monthly Notices of the Royal Astronomical Society, 501, 78

Piso A.-M. A., Pegues J., Öberg K. I., 2016, The Astrophysical Journal, 833, 203

Polyansky O. L., Kyuberis A. A., Zobov N. F., Tennyson J., Yurchenko S. N., Lodi L., 2018, Monthly Notices of the Royal Astronomical Society, 480, 2597

Powell D., et al., 2024, Nature, 626, 979

Rauscher E., Menou K., Seager S., Deming D., Cho J. Y.-K., Hansen B. M. S., 2007, The Astrophysical Journal, 664, 1199

Rodgers C. D., 1976, Reviews of Geophysics, 14, 609

Rodgers C. D., 2000, Inverse Methods for Atmospheric Sounding: Theory and Practice. World Scientific

Rodler F., Kürster M., Barnes J. R., 2013, Monthly Notices of the Royal Astronomical Society, 432, 1980

Roman M. T., Kempton E. M.-R., Rauscher E., Harada C. K., Bean J. L., Stevenson K. B., 2021, The Astrophysical Journal, 908, 101

Roth A., Parmentier V., Hammond M., 2024, Monthly Notices of the Royal Astronomical Society, 531, 1056

Rothman L., et al., 2010, Journal of Quantitative Spectroscopy and Radiative Transfer, 111, 2139

Scandariato G., et al., 2022, Astronomy & Astrophysics, 668, A17

Schneider A. D., Carone L., Decin L., Jørgensen U. G., Mollière P., Baeyens R., Kiefer S., Helling C., 2022, Astronomy & Astrophysics, 664, A56

Sedaghati E., et al., 2016, Astronomy & Astrophysics, 596, A47

Seidel J. V., et al., 2023, Astronomy & Astrophysics, 673, A125

Sellke T., Bayarri M. J., Berger J. O., 2001, The American Statistician, 55, 62

Showman A. P., Guillot T., 2002, Astronomy & Astrophysics, 385, 166

Showman A. P., Polvani L. M., 2011, The Astrophysical Journal, 738, 71

Showman A. P., Fortney J. J., Lian Y., Marley M. S., Freedman R. S., Knutson H. A., Charbonneau D., 2009, The Astrophysical Journal, 699, 564

Sing D. K., Vidal-Madjar A., des Etangs A. L., Désert J.-M., Ballester G., Ehrenreich D., 2008, The Astrophysical Journal, 686, 667

Sing D. K., et al., 2015, Monthly Notices of the Royal Astronomical Society, 446, 2428

Sing D. K., et al., 2016, Nature, 529, 59

Sing D. K., et al., 2024, Nature, 630, 831

Skilling J., 2006, Bayesian Analysis, 1, 833

Snellen I. A. G., Albrecht S., de Mooij E. J. W., Le Poole R. S., 2008, Astronomy & Astrophysics, 487, 357

Steinrueck M. E., Parmentier V., Showman A. P., Lothringer J. D., Lupu R. E., 2019, The Astrophysical Journal, 880, 14

Stevenson K. B., et al., 2014, Science, 346, 838

Stevenson K. B., et al., 2017, The Astronomical Journal, 153, 68

Tashkun S., Perevalov V., 2011, Journal of Quantitative Spectroscopy and Radiative Transfer, 112, 1403

Taylor J., Parmentier V., 2023, Monthly Notices of the Royal Astronomical Society, 526, 2133

Taylor J., Parmentier V., Irwin P. G. J., Aigrain S., Lee E., Krissansen-Totton J., 2020, Monthly Notices of the Royal Astronomical Society, 493, 4342

Teanby N. A., et al., 2012, Nature, 491, 732

Teinturier L., et al., 2024, The Radiative and Dynamical Impact of Clouds in the Atmosphere of the Hot Jupiter WASP-43 b (`arXiv:2401.14083`)

Trotta R., 2008, Contemporary Physics, 49, 71

Tsai S.-M., Lyons J. R., Grosheintz L., Rimmer P. B., Kitzmann D., Heng K., 2017, The Astrophysical Journal Supplement Series, 228, 20

Tsai S.-M., Malik M., Kitzmann D., Lyons J. R., Fateev A., Lee E., Heng K., 2021, The Astrophysical Journal, 923, 264

Turrini D., et al., 2021, The Astrophysical Journal, 909, 40

Underwood D. S., Tennyson J., Yurchenko S. N., Huang X., Schwenke D. W., Lee T. J., Clausen S., Fateev A., 2016, Monthly Notices of the Royal Astronomical Society, 459, 3890

Venot O., et al., 2020, The Astrophysical Journal, 890, 176

Von Zahn U., Hunten D. M., 1996, Science, 272, 849

Wakeford H. R., et al., 2017, The Astronomical Journal, 155, 29

Weaver I. C., et al., 2020, The Astronomical Journal, 159, 13

Welbanks L., Madhusudhan N., 2022, The Astrophysical Journal, 933, 79

Welbanks L., Madhusudhan N., Allard N. F., Hubeny I., Spiegelman F., Leininger T., 2019, The Astrophysical Journal Letters, 887, L20

Winn J. N., Fabrycky D. C., 2015, Annual Review of Astronomy and Astrophysics, 53, 409

Woitke P., Helling C., Hunter G. H., Millard J. D., Turner G. E., Worters M., Blecic J., Stock J. W., 2018, Astronomy & Astrophysics, 614, A1

Wolszczan A., 1994, Science, 264, 538

Wolszczan A., Frail D. A., 1992, Nature, 355, 145

Wright J. T., Marcy G. W., Howard A. W., Johnson J. A., Morton T. D., Fischer D. A., 2012, The Astrophysical Journal, 753, 160

Yang J., Irwin P. G. J., Barstow J. K., 2023, Monthly Notices of the Royal Astronomical Society, 525, 5146

Yang J., Alday J., Irwin P., 2024a, NEMESISPY: A Python Package for Simulating and Retrieving Exoplanetary Spectra, https://arxiv.org/abs/2407.06932v1

Yang J., et al., 2024b, Monthly Notices of the Royal Astronomical Society, p. stae1427

Yurchenko S. N., Tennyson J., 2014, Monthly Notices of the Royal Astronomical Society, 440, 1649

Yurchenko S. N., Amundsen D. S., Tennyson J., Waldmann I. P., 2017, Astronomy & Astrophysics, 605, A95

Yurchenko S. N., Mellor T. M., Freedman R. S., Tennyson J., 2020, Monthly Notices of the Royal Astronomical Society, 496, 5282

de Kok R. J., Brogi M., Snellen I. a. G., Birkby J., Albrecht S., de Mooij E. J. W., 2013, Astronomy & Astrophysics, 554, A82

van Sluijs L., et al., 2023, Monthly Notices of the Royal Astronomical Society, 522, 2145